DGK Veröffentlichungen der DGK

Ausschuss Geodäsie der Bayerischen Akademie der Wissenschaften

Reihe C | Dissertationen | Heft Nr. 916

Annike Knabe

New Concepts for Gravity Field Recovery using Satellites

München 2023

Bayerische Akademie der Wissenschaften

ISSN 0065-5325 ISBN 978-3-7696-5328-1

Diese Arbeit ist gleichzeitig veröffentlicht in:
Wissenschaftliche Arbeiten der Fachrichtung Geodäsie und Geoinformatik der Leibniz Universität Hannover
ISSN 0174-1454, Nr. 391, Hannover 2023

Veröffentlichungen der DGK

Ausschuss Geodäsie der Bayerischen Akademie der Wissenschaften

Reihe C | Dissertationen | Heft Nr. 916

New Concepts for Gravity Field Recovery using Satellites

Von der Fakultät für Bauingenieurwesen und Geodäsie
der Gottfried Wilhelm Leibniz Universität Hannover
zur Erlangung des Grades
Doktor-Ingenieur (Dr.-Ing.)
genehmigte Dissertation

von

Annike Knabe, M. Sc.

Geboren am 03.12.1993 in Cuxhaven

München 2023

Bayerische Akademie der Wissenschaften

ISSN 0065-5325 ISBN 978-3-7696-5328-1

Diese Arbeit ist gleichzeitig veröffentlicht in:
Wissenschaftliche Arbeiten der Fachrichtung Geodäsie und Geoinformatik der Leibniz Universität Hannover
ISSN 0174-1454, Nr. 391, Hannover 2023

Adresse der DGK:

Ausschuss Geodäsie der Bayerischen Akademie der Wissenschaften (DGK)

Alfons-Goppel-Straße 11 ● D – 80 539 München

Telefon +49 - 331 - 288 1685 ● E-Mail post@dgk.badw.de

http://www.dgk.badw.de

Prüfungskommission:

Vorsitzender: Prof. Dr.-Ing. Ingo Neumann

Referent: Prof. Dr.-Ing. habil. Jürgen Müller

Korreferenten: Prof. Dr.techn. Wolf-Dieter Schuh (Rheinische Friedrich-Wilhelms-Universität Bonn)
PD Dr.-Ing. Hamza Alkhatib

Tag der mündlichen Prüfung: 25.07.2023

© 2023 Bayerische Akademie der Wissenschaften, München

Alle Rechte vorbehalten. Ohne Genehmigung der Herausgeber ist es auch nicht gestattet,
die Veröffentlichung oder Teile daraus auf photomechanischem Wege (Photokopie, Mikrokopie) zu vervielfältigen

ISSN 0065-5325 ISBN 978-3-7696-5328-1

Abstract

The Earth's gravity field and its temporal variation reveal important information for many disciplines, especially for geosciences. Satellite gravity missions like GOCE, GRACE and GRACE-FO successfully recovered global gravity field models. But the temporal and spatial resolution of the gravity field solutions have to be improved in order to meet the user requirements. New concepts for future satellite missions to recover the global gravity field are investigated by means of comprehensive simulations. In terms of sensor behavior, accelerometers are one major limiting factor. Thus, this dissertation focuses on them. Cold Atom Interferometry (CAI) accelerometers are promising candidates for future missions due to their long-term stability.

Non-gravitational accelerations are simulated for orbit altitudes between 250 km and 470 km and evaluated, as the magnitude of these accelerations is crucial for the impact of the scale factor on electrostatic measurements. The accelerometer measurements are degraded by the insufficient scale factor knowledge. The precise knowledge of the CAI accelerometer scale factor solves this issue. The absolute scale factor is not important for gradiometry missions, but the differential one. The measured gravity gradient is degraded by the non-zero common mode rejection, which is caused by the non-perfect determination of the differential scale factor. Also in this case, its determination is a critical component. Drag compensation is required in order to reduce this error influence on the gravity gradient. Despite the beneficial long-term stability and the well-known scale factor of CAI, the measurement concept also introduces challenges. A longer measurement cycle time of 12 s in CAI accelerometry yields, on the one hand, a high sensitivity, but on the other hand, an aliasing effect. One option to reduce this effect is drag compensation.

Closed-loop simulations are performed for concepts of low-low Satellite-to-Satellite Tracking (ll-SST) and satellite gradiometry in order to quantify the impact of different components on the gravity field recovery. The combination of an electrostatic accelerometer with a CAI accelerometer (hybrid accelerometer) improves the ll-SST gravity field solution by reducing the striping effects in north-south direction. Beyond that, the cumulative geoid error for a resolution of 200 km can be reduced by 90 % when a laser ranging instrument noise is used and background modeling errors are neglected. Furthermore, the addition of a cross-track gradiometer to a ll-SST mission is simulated. A CAI cross-track gradiometer with a white noise level of 1 mE would largely improve the gravity field solutions in the short wavelengths and secure a more isotropic error pattern. Consequently, the cumulative geoid error for a spatial resolution of 100 km is reduced by around 70 % compared to the ll-SST only solution with GRACE-like instruments.

Keywords: Next Generation Gravity Mission, Closed-loop simulation, Satellite Gradiometry, ll-SST, Cold Atom Interferometry, Accelerometer, Drag-free System

Kurzfassung

Das Erdschwerefeld und seine zeitliche Variation liefern wichtige Informationen für verschiedene Disziplinen, vor allem für die Geowissenschaften. Durch Satellitenmissionen, wie GOCE, GRACE und GRACE-FO, können globale Schwerefeldmodelle bestimmt werden. Allerdings sind die räumliche und zeitliche Auflösung dieser Modelle zu verbessern, um die Nutzeranforderungen zu erfüllen. Deshalb werden neue Konzepte für zukünftige Schwerefeldmissionen umfassend simuliert. Diese Dissertation konzentriert sich auf die Beschleunigungsmesser, da sie eine limitierende Komponente, bezogen auf die Sensoren der bisherigen Missionen, sind. Beschleunigungsmesser, basierend auf dem Prinzip der Kaltatominterferometrie (CAI), sind erfolgversprechende Kandidaten für zukünftige Schwerfeldmissionen, insbesondere aufgrund ihrer Langzeitstabilität.
Nicht-gravitative Beschleunigungen werden für Orbithöhen zwischen 250 km und 470 km untersucht, da deren Größe für den Einfluss des Skalierungsfaktors auf die elektrostatischen Messungen entscheidend ist. Die Beschleunigungsmessungen in aktuellen Missionen werden durch eine unzureichende Bestimmung ihres Skalierungsfaktors beeinträchtigt. Der Skalierungsfaktor der CAI-Messungen ist dagegen sehr genau bekannt, wodurch diese Problematik gelöst wird. Für die Gradiometrie ist der differentielle Skalierungsfaktor entscheidend, da dieser eine nicht perfekte Common-Mode Rejection hervorrufen kann. Auch in diesem Fall ist seine Bestimmung eine kritische Komponente. Ein Drag-free System ist erforderlich, um diesen Fehlereinfluss zu reduzieren. Trotz der vorteilhaften Langzeitstabilität und der guten Kenntnis des Skalierungsfaktors der CAI-Messungen birgt dieses Konzept Herausforderungen. Die CAI-Zykluslänge von 12 s ermöglicht zwar eine hohe Sensitivität, ruft jedoch einen Aliasing-Effekt hervor. Dieser kann ebenfalls durch Drag-Kompensation reduziert werden.
Closed-loop-Simulationen werden für die Konzepte low-low Satellite-to-Satellite Tracking (ll-SST) und Satellitengradiometrie durchgeführt, um die Auswirkung unterschiedlicher Komponenten auf die Schwerefeldbestimmung zu quantifizieren. Hybride Beschleunigungsmesser (elektrostatisch und CAI) bewirken eine Reduktion der Streifeneffekte in Nord-Süd-Richtung in der ll-SST Schwerefeldlösung. Außerdem wird der kumulative Geoidfehler für eine Auflösung von 200 km um 90 % reduziert, wenn ein Laser-Ranging-Instrument genutzt wird und die Hintergrundmodellfehler vernachlässigt werden. Weiterhin wird das Hinzufügen eines Cross-Track-Gradiometers zu einer ll-SST Mission simuliert. Ein CAI-Gradiometer in Cross-Track-Richtung mit weißem Rauschen von 1 mE verbessert die Schwerefeldlösung in den kurzen Wellenlängen signifikant und sorgt für ein isotroperes Fehlermuster. Der kumulative Geoidfehler für eine Auflösung von 100 km wird darüber hinaus um ca. 70 % reduziert im Vergleich zu der ll-SST Einzellösung mit GRACE-ähnlichen Instrumenten.

Schlagwörter: Zukünftige Schwerefeldmissionen, Closed-Loop-Simulation, Satellitengradiometrie, ll-SST, Kaltatominterferometrie, Beschleunigungsmesser, Drag-free System

Contents

1 Introduction **1**

2 Satellite Gravity Missions **3**
2.1 Fundamentals of Gravity Field Recovery with Satellites . . . 3
2.1.1 Motion of a Satellite in Space . . . 3
2.1.2 Representation of the Earth's Gravity Field . . . 4
2.1.3 Orbit Design of Satellite Gravity Missions . . . 6
2.2 Previous Satellite Gravity Missions . . . 7
2.2.1 Missions and Measurement Concepts . . . 7
2.2.2 State-of-the-art Sensors . . . 9
2.2.3 State-of-the-art Control Systems . . . 12
2.2.4 State-of-the-art Accelerometer Calibration . . . 13
2.3 Concepts for Future Satellite Gravity Missions . . . 14
2.3.1 Challenges of Satellite Gravity Missions and Requirements for Future Satellite Missions . . . 14
2.3.2 Developments in the Sensor Technology . . . 16
2.3.3 Concepts for Orbit Design . . . 20

3 Evaluation of Simulation Environment **23**
3.1 Overview of the Simulation Environment . . . 23
3.2 Modeling of Non-gravitational Forces . . . 25
3.3 Modeling of the Sensor Behavior . . . 26
3.3.1 Classical Electrostatic Accelerometer . . . 26
3.3.2 Cold Atom Interferometry Accelerometer . . . 27
3.3.3 Ranging Measurement Instruments . . . 30
3.4 Modeling of Control System Behavior . . . 31
3.4.1 Drag-free Control . . . 31
3.4.2 Attitude Control . . . 34
3.5 Time-variable Background Modeling Errors . . . 35
3.6 Gravity Field Recovery . . . 37
3.6.1 Least-squares Adjustment . . . 37
3.6.2 Range Accelerations . . . 39
3.6.3 Gradiometry . . . 41
3.6.4 Combination of Range Accelerations and Gravity Gradients . . . 44
3.7 Summary . . . 45

4 Impact of New Measurement Concepts on Gravity Field Recovery 47
4.1 Selection of Simulation Scenarios 47
4.2 Drag Compensation Analysis 49
4.2.1 Drag Compensation Requirements due to Accelerometer Imperfections for ll-SST Missions 49
4.2.2 Drag Compensation Requirements for Gradiometry due to Accelerometer Imperfections 54
4.2.3 Saturation of the Accelerometer 60
4.2.4 Propellant Consumption 62
4.3 Cold Atom Interferometry Accelerometer Analysis 63
4.4 Gravity Field Solutions using Different Accelerometer Types for ll-SST Missions 67
4.5 Gravity Field Solutions using Different Accelerometer Types for Gradiometry Missions 81
4.6 Combined Gravity Field Solutions from ll-SST and Cross-track Gradiometry 83
4.7 Summary 97

5 Summary and Outlook 99

A Appendix 103
A.1 Reference Frames 103
A.2 Satellite Reference Attitudes for Attitude Control 104
A.3 Simulation results - Gravity Field Solutions for ll-SST Missions 105
A.3.1 Instrument-only scenarios 105
A.3.2 Scenarios including AOD and Ocean-tide Error 109
A.4 Simulation results - Combined Gravity Field Solutions from ll-SST and Cross-track Gradiometry 113

Bibliography 145

List of Figures 155

List of Tables 157

Acronyms 159

Acknowledgments 161

1 Introduction

The Earth's gravity field has obtained a great relevance in various ways. The knowledge about the time-variable part of the Earth's gravity field gets more important for several disciplines. The signals are of high significance for many fields such as hydrology, glaciology, oceanography, solid Earth physics and geodesy (Pail et al., 2015). Moreover, climate change is currently a major challenge for humanity. According to this aspect, gravity field data helps to understand the dynamics of the Earth (Tapley et al., 2019). Satellite missions are powerful methods for observing the global gravity field model with homogeneous accuracy.
The satellite gravity missions Gravity Recovery and Climate Experiment (GRACE) and Gravity Field and Steady-State Ocean Circulation Explorer (GOCE) successfully mapped the Earth's gravity field (Tapley et al., 2004; Drinkwater et al., 2007). This is currently being continued by GRACE Follow-On (GRACE-FO) (Landerer et al., 2020). GOCE measurements provide a precise, spatial highly resolved static gravity field which is crucial for understanding the Earth's interior and ocean circulation. With the missions GRACE and GRACE-FO it is possible to process monthly gravity fields and thereby learn about temporal changes. Well known highlights are changes in ice sheets and glaciers, underground water storage and sea level rise.
Now, the preparation of the so called Next Generation Gravity Mission (NGGM) is fundamental. Requirements for the mission are fixed in the first preparation step. In Murböck (2015) the key questions for NGGM are classified into science requirements, mission objectives, instrument accuracies and orbit constellations. The main objective is the improvement of the spatial as well as temporal resolution. Both are limited by the number of satellites in orbit being used. In Reubelt et al. (2014) the goal of a future satellite mission for the spatial resolution is given as below 100 km and a weekly temporal resolution. A high temporal resolution is important in order to suppress temporal aliasing.
It is necessary to discuss what is achievable by increasing the accuracy of certain instruments with respect to the science requirements. The main instrument error is caused by the accelerometer. In a GRACE-like mission the accelerometers at the center of mass of each satellite are needed for measuring the non-gravitational accelerations. Consequently, it is obvious to refine the state of this sensor. However, the improvement in sensor technology does not result directly in a better recovered gravity field. Accordingly, the whole concept has to be evaluated, including the interdependence of individual components. One major challenge is temporal de-aliasing which gives information about variations over time, e.g. in atmosphere and ocean. This aspect cannot be solved by the improvement of instruments. Temporal aliasing is caused by undersampling the signal of interest (Daras & Pail, 2017).

In this thesis new concepts for satellite gravity missions are analyzed with main focus on accelerometers. There are several activities in the developments of accelerometers, e.g. using

the principle of Cold Atom Interferometry (CAI). The analysis is based on simulations of different scenarios for low-low Satellite-to-Satellite Tracking (ll-SST) and Satellite Gravity Gradiometry (SGG) missions. Closed-loop simulations are performed and evaluated on the basis of the recovered gravity field itself with respect to the reference gravity field model. The main objectives of this work are:

- quantification of CAI accelerometer benefits for future satellite gravity missions,
- analysis of acceleration variation in one CAI cycle,
- drag compensation system analysis in relation to the accelerometer performance,
- evaluation of an additional cross-track gradiometer on a ll-SST mission.

In chapter 2, fundamentals of gravity field recovery with satellites are briefly addressed. In order to give a state-of-the-art overview, previous satellite gravity field missions are presented. Their measurement concepts, sensors and control systems as well as the mission achievements are specified. In the next section, required improvements for the future are given. In this context, possible new sensor technologies and measurement concepts are introduced. Evaluations and analyses are performed with simulation studies. Therefore, a description of the simulation environment is necessary, which is provided in chapter 3. This includes the simulation of satellite dynamics, models of the sensor behavior and models of the control system behavior. Besides, models for degradation due to temporal aliasing are considered. The parameters of interest, which are Spherical Harmonic (SH) coefficients of the gravity field model, are estimated within a least-squares adjustment. The procedure is explained for two different groups of observations: range accelerations and gradiometry measurements. Chapter 4 shows the results of various simulation studies. It is investigated how a drag compensation system can reduce errors due to accelerometer imperfections, i.e. the scale factors. Beyond that, accelerometer saturation and propellant consumption are examined, which depend on the drag compensation. Another separate study relates to CAI accelerometry. It is investigated how critical an acceleration change within an interferometer cycle impacts the CAI measurement. Further sections of chapter 4 present the resulting gravity field solutions for different scenarios. Different accelerometer and ranging measurement performance models as well as orbit altitudes are tested for a ll-SST mission. Aside from that, several sensitivities for a cross-track gradiometer are analyzed. Based on these solutions, combinations of ll-SST and cross-track gradiometry are then evaluated. Finally, chapter 5 presents the summary of the results and discussion of this thesis as well as outlooks for future work.

2 Satellite Gravity Missions

This chapter introduces fundamentals on gravity field recovery using satellite methods. First, the satellite orbital motion and forces acting on the satellite body are described. The representation of the Earth's gravity field is specified. Additionally, basic principles of past satellite gravity missions are explained. State-of-the-art measurement concepts, sensors and control systems are addressed including their characteristics and drawbacks. Thus, studies of possible improvements on the level of sensor technology and orbit constellation are presented.

2.1 Fundamentals of Gravity Field Recovery with Satellites

2.1.1 Motion of a Satellite in Space

The dynamics of a satellite in space depend on the forces acting on it. Gravitational forces, also called conservative forces, influence the motion because of mutual mass attraction. The orbital satellite motion is described by the equation of motion in a simplified scenario for a point mass as

$$\ddot{\mathbf{r}} = -\frac{GM_{\oplus}}{r^3}\mathbf{r}, \tag{2.1}$$

where G is the constant of gravitation, $M_{\oplus}$ is the mass of the Earth and $\mathbf{r}$ is the geocentric position of the satellite, while $\ddot{\mathbf{r}}$ is its acceleration (Torge & Müller, 2012). The equation of motion is based on several assumptions: the Earth and the satellite are homogeneous point masses, only gravitational forces are present and the mass of the satellite is neglected. The equation describes the two-body problem which only considers the Earth and the satellite (Seeber, 2003).
The description of the satellite motion requires six independent parameters, e.g. initial position and initial velocity of the satellite. According to Kepler's three laws of planetary motion, the satellite orbit can be described by the Keplerian elements. These six Keplerian elements are the semi-major axis a, the eccentricity e, the inclination i, the right ascension of the ascending node Ω, the argument of the perigee ω and mean anomaly M. Instead of M also the true anomaly μ or eccentric anomaly E can be used (Montenbruck & Gill, 2000).
The assumptions for the equation of motion (2.1) deviate from reality. The satellite motion is perturbed by several forces. Instead of a point mass the Earth is an inhomogeneous body, hence the non-spherical parts of the Earth's gravitation need to be considered. In addition, the gravitation of other bodies such as Moon and Sun influences the satellite

motion. Furthermore, there are tidal deformations of the Earth caused by other bodies and variations due to terrestrial mass displacements, e.g. the redistribution of ocean water masses. Besides gravitational forces, non-gravitational forces act on the satellite. They are also known as surface forces and are primarily caused by atmospheric drag, solar radiation pressure and Earth albedo. Equation (2.1) can be extended by these further terms:

$$\ddot{\mathbf{r}} = -\frac{GM_\oplus}{r^3}\mathbf{r} + \ddot{\mathbf{r}}_h + \ddot{\mathbf{r}}_{dis,grav} + \ddot{\mathbf{r}}_{dis,non-grav}, \tag{2.2}$$

where $\ddot{\mathbf{r}}_h$ is the inhomogeneous part of the gravity field, $\ddot{\mathbf{r}}_{dis,grav}$ is the part of other gravitational disturbing forces and $\ddot{\mathbf{r}}_{dis,non-grav}$ is the part due to non-gravitational disturbing forces. The difference between the undisturbed orbit and the actual orbit is caused by the disturbing forces and the inhomogeneous part of the gravity field. Thus, disturbing forces have to be modeled or measured in order to obtain the inhomogeneity of the Earth's gravity field.

2.1.2 Representation of the Earth's Gravity Field

The determination of the Earth's gravity field is a fundamental task of geodesy because the physical figure of the Earth is primarily shaped by the Earth's gravity and most geodetic observations refer to it (Torge & Müller, 2012). The Earth's gravity potential W is composed of the gravitational potential V and the centrifugal potential Φ:

$$W = \Phi + V. \tag{2.3}$$

The centrifugal force is caused by the rotation of the Earth about its axis. The centrifugal acceleration is known with high accuracy from astronomy. Accordingly, the centrifugal potential is obtained through

$$\Phi(x, y, z) = \frac{\omega_\oplus^2}{2}(x^2 + y^2), \tag{2.4}$$

where x and y are the coordinates of a point in the Earth-fixed system and $\omega_\oplus$ is the angular velocity of the Earth's rotation about its axis (Torge & Müller, 2012).
The Earth's gravitational field can be expressed in terms of spherical harmonic functions (Hofmann-Wellenhof & Moritz, 2006):

$$V(r, \Theta, \lambda) = \frac{GM_\oplus}{R}\sum_{n=0}^{N}\left(\frac{R}{r}\right)^{n+1}\sum_{m=0}^{n}[\bar{C}_{nm}\cos m\lambda + \bar{S}_{nm}\sin m\lambda]\ \bar{P}_{nm}(\cos\Theta), \tag{2.5}$$

where V is the gravitational potential, the radius r, the co-latitude Θ and the longitude λ are the spherical coordinates of the calculation point, $GM_\oplus$ is the gravitational constant of the Earth, R is the radius of the Earth, n, m are SH degree and order, respectively. N denotes the maximum degree, $\bar{P}_{nm}$ are fully normalized associated Legendre functions, $\bar{C}_{nm}$ and $\bar{S}_{nm}$ are the normalized SH coefficients, respectively.
The SH coefficients are subdivided into zonal, sectorial and tesseral harmonics for the geometrical interpretation. The zonal harmonics for $m = 0$ are independent of the longitude λ and oscillate in latitudinal direction only. The sectorial harmonics for $m = n$ oscillate only in longitudinal direction. The harmonics are tesseral for $m \neq 0$, which means they oscillate

in latitudinal and longitudinal direction.
Low degree SH coefficients give insight about simple physical properties of the body. The coefficient C_{00} represents the total mass of the Earth. The coordinates of the center of mass are defined by C_{10}, C_{11} and S_{11}. The coefficient C_{20} characterizes the polar flattening of the Earth. The asymmetry of the equatorial mass distribution is given by C_{22}. The torsion of the principal axes of inertia are given by C_{21}, S_{21} and S_{22} (Torge & Müller, 2012).

Error representation

The recovered gravity field needs to be validated and evaluated. The variance-covariance matrix gives information about the formal errors of the estimated SH coefficients. In the spectral domain, there are two categories of error representation:

- the two-dimensional error: The square-root of the diagonal elements of the variance-covariance matrix of the unknowns $\boldsymbol{Q}_{\hat{x}\hat{x}}$ are displayed in a triangle which shows the error for each coefficient,
- the one-dimensional error: The sum of the squares of the error or signal of the coefficients at the same degree.

The error degree variance (one-dimensional error) is obtained by

$$\sigma_n^2 = \sum_{m=0}^{n} (\sigma_{C_{nm}}^2 + \sigma_{S_{nm}}^2), \tag{2.6}$$

where $\sigma_{C_{nm}}$ and $\sigma_{S_{nm}}$ are the formal errors of the estimated coefficients. The error representation can also be calculated by the coefficient differences between reference gravity field and estimated gravity field $\Delta\bar{C}_{nm}$ and $\Delta\bar{S}_{nm}$. The degree Root Mean Square (RMS) is obtained by dividing the degree variance σ_n^2 by the number of coefficients and taking the square root:

$$RMS_n = \sqrt{\frac{\sigma_n^2}{2n+1}}. \tag{2.7}$$

The cumulative or commission error is the sum of errors up to a certain degree:

$$CUM_N = \sqrt{\sum_{n=0}^{N} \sigma_n^2}. \tag{2.8}$$

In order to derive the cumulative geoid error, the eigenvalue λ of the gravitational function is required:

$$CUM_N(geoid\ height) = \sqrt{\sum_{n=0}^{N} \sigma_n^2 \lambda_n^2}, \tag{2.9}$$

where λ is the radius of the Earth with the geoid height as the gravitational functional.
The evaluation in space domain is also often substantial, e.g. patterns due to sampling in

space and the orbit configuration can be identified.
The disturbing potential T is calculated with the coefficient differences $\Delta\bar{C}_{nm}$ and $\Delta\bar{S}_{nm}$:

$$T = \frac{GM_\oplus}{R} \sum_{n=0}^{N} \left(\frac{R}{r}\right)^{n+1} \sum_{m=0}^{n} [\Delta\bar{C}_{nm} \cos m\lambda + \Delta\bar{S}_{nm} \sin m\lambda] \; \bar{P}_{nm}(\cos\Theta), \tag{2.10}$$

with the variables according to equation (2.5). The error can also be expressed in terms of geoid height, gravity anomaly, gravity gradient component or Equivalent Water Height (EWH):

- geoid height

$$N = R \sum_{n=0}^{N} \left(\frac{R}{r}\right)^{n+1} \sum_{m=0}^{n} [\Delta\bar{C}_{nm} \cos m\lambda + \Delta\bar{S}_{nm} \sin m\lambda] \; \bar{P}_{nm}(\cos\Theta), \tag{2.11}$$

- gravity anomaly

$$\Delta g = \frac{GM_\oplus}{Rr} \sum_{n=0}^{N} \left(\frac{R}{r}\right)^{n+1} (n+1) \sum_{m=0}^{n} [\Delta\bar{C}_{nm} \cos m\lambda + \Delta\bar{S}_{nm} \sin m\lambda] \; \bar{P}_{nm}(\cos\Theta), \tag{2.12}$$

- radial gravity gradient component

$$\Gamma_{rr} = \frac{GM_\oplus}{R^2 r} \sum_{n=0}^{N} \left(\frac{R}{r}\right)^{n+1} (n+1)(n+2) \sum_{m=0}^{n} [\Delta\bar{C}_{nm} \cos m\lambda + \Delta\bar{S}_{nm} \sin m\lambda] \; \bar{P}_{nm}(\cos\Theta). \tag{2.13}$$

The EWH is calculated using the following equation (Schrama et al., 2007; Wahr et al., 1998):

$$\Delta EWH = \frac{R\,\rho_e}{3\rho_w} \sum_{n=0}^{N} \frac{2n+1}{1+k_n} \sum_{m=0}^{n} (\Delta\bar{C}_{nm} \cos(m\lambda) + \Delta\bar{S}_{nm} \sin(m\lambda)) \bar{P}_{nm}(\cos(\Theta)), \tag{2.14}$$

where ρ_e is the average density of the Earth, ρ_w the density of water and k_n is the Love number of degree n.

2.1.3 Orbit Design of Satellite Gravity Missions

The orbit parameters of the satellite mission strongly affect the recovered gravity field solution. They determine the coverage of the Earth, the repetition cycle and signal strength of the gravitational signal. In this thesis, satellite dynamics are simulated for different orbit scenarios which are explained in chapter 3.
There are two complimentary arguments for the choice of orbit altitude. On the one hand, satellites with high altitudes are only sensitive to long-wavelength parts of the gravity field. The main reason is the attenuation factor $(a_e/r)^n$ in the spherical harmonic expansion of the gravitational potential (Torge & Müller, 2012). On the other hand, the altitude is a determining factor for the mission duration as the atmospheric drag forces decrease with

increasing altitude. A compromise must be found between these oppositional arguments. In general, altitudes between 200 km and 500 km are suitable for satellite gravity missions.
The inclination specifies the coverage of the Earth. In order to cover the whole Earth, the inclination has to be 90° which is also called polar orbit. An deviation from 90° leads to an observation gap which occurs in the polar regions. The more the inclination deviates from 90°, the bigger is the polar gap. The inclination might differ from the 90° to obtain a sun-synchronous orbit. Thereby, small temperature variation and a rather continuous energy supply using solar panels is guaranteed. The orbit eccentricity should be close to zero. This leads to a virtually constant distance to the Earth over a whole orbit revolution.
In Table 2.1 orbit parameters of the missions GRACE and GOCE are summarized. GOCE was in a sun-synchronous orbit with low altitude which required a drag-free control system. Consequently, the orbit altitude is maintained by the control system. In comparison, the altitude of GRACE steadily decreased during the mission lifetime.
A repeat cycle assures a global coverage after a specific time span. It means, after one repeat cycle the satellite covers the same Earth-fixed position again. The repeat cycle is defined by the ratio β/α, where β is the integer number of orbital revolutions and α is the integer number of nodal days. One nodal day is the period between the recurrence of the ascending node of the satellite orbit over the same Earth-fixed meridian. According to Colombo (1984) the maximum resolvable degree for a particular orbit configuration is given by $n < \frac{\beta}{2}$. If the gravitational field should be estimated up to a certain degree n at the equator, the satellite has to perform $2n$ revolutions per day or a longer observation time is required (Torge & Müller, 2012). An odd parity of $\beta - \alpha$ results in a denser spatial coverage (Weigelt et al., 2013). In Murböck et al. (2013) optimal orbit altitudes for temporal gravity field recovery are designed.
In general, the product of the spatial resolution and the temporal resolution is constant. An improvement of both can only be achieved by increasing the number of satellites.

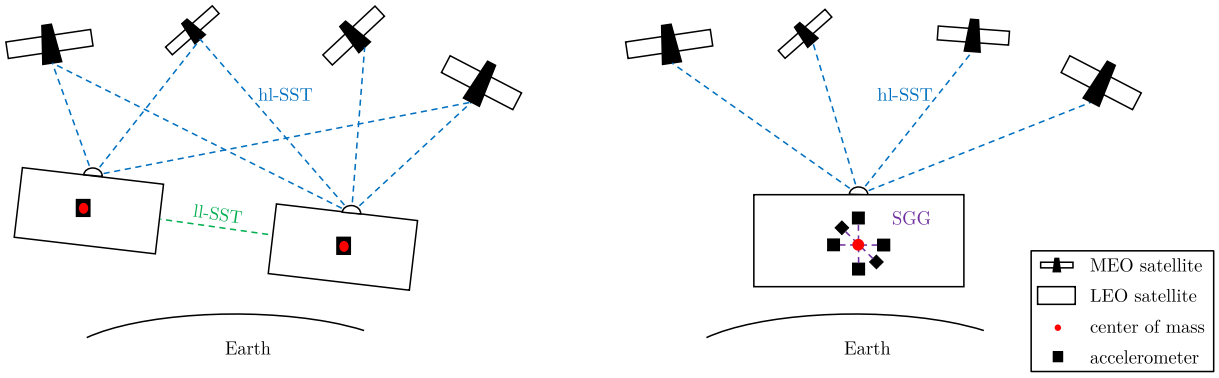
Table 2.1: Orbit parameters of previous satellite gravity missions

	altitude	inclination	repeat cycle
GRACE	485 km - 300 km (decay)	89.0°	30 days (non-repeat ground track)
GOCE	260 km	96.7°	61 days (979 revolutions)
GRACE-FO	491 km (initial altitude)	89.0°	30 days (non-repeat ground track)

2.2 Previous Satellite Gravity Missions

2.2.1 Missions and Measurement Concepts

There are two major measurement concepts for satellite gravity missions: Satellite-to-Satellite Tracking (SST) and satellite gravity gradiometry (SGG). The Challenging Minisatellite Payload (CHAMP) mission realized the SST in high-low mode with Global Positioning System (GPS) satellites. The mission GRACE applied additionally to high-low Satellite-to-Satellite Tracking (hl-SST) the principle of ll-SST with two low-orbiting satellites. The



(a) ll-SST (b) SGG

Figure 2.1: Scheme of the different measurement concepts: ll-SST, hl-SST and SGG

concept of SGG was first realized by the GOCE mission. The three concepts are illustrated in Figure 2.1. The techniques differ not only in their measured quantities but also in their sensitivity to certain wavelengths of the gravitational potential.

CHAMP has demonstrated a new era of global gravity field recovery (Reigber et al., 2005). The mission was active from 2000 to 2010 with the goal to improve observations of the Earth's gravity field, magnetic field, atmosphere and ionosphere. The gravitational orbit perturbations are used for the global gravity field model computation. According to equation (2.2), the difference between the true and the unperturbed orbit gives information about the Earth's gravity field. In order to obtain only perturbations caused by the Earth's gravity field, other disturbances like atmospheric drag have to be measured or modeled and subtracted from the full signal. The true orbit of the satellite is derived from positions using GPS resulting in the hl-SST approach since the GPS satellites are in a much higher orbit (of about 20.000 km, Medium Earth Orbit (MEO)) than the CHAMP satellite (450 km). The achieved geoid accuracy with CHAMP is 10 mm for a spatial resolution of 350 km and 1 mm for 1000 km.

The objective of the **GRACE** mission was to obtain models of the time-variable part of the Earth's gravity field with a much better resolution (Case et al., 2010). The mission operated from 2002 to 2017 and consisted of two almost identical satellites orbiting in an in-line formation with a distance of about 220 km between them. The satellites revolve around the Earth in near circular orbits with inclination of 89° at an altitude of approximately 500 km at mission start. The inter-satellite distance is tracked by the K- and Ka-band microwave ranging system (Tapley et al., 2004). Thanks to the ll-SST constellation the monthly solutions achieve mm-geoid accuracy with a spatial resolution of 350 km (Dahle et al., 2014). Since 2018 the GRACE concept is pursued by the **GRACE-FO** mission. Additionally to the K-band microwave ranging system, an Laser Ranging Interferometer (LRI) is on board in order to improve the ll-SST measurements (Kornfeld et al., 2019).
The distance change in Line-of-Sight (LOS) between the two satellites gives information

about the Earth's gravitational field. It reads at acceleration level:

$$\Delta a_g = \ddot{\rho} - \Delta a_{ng}, \tag{2.15}$$

where Δa_g is the differential gravitational acceleration which depends on the time, the positions of the two satellites and the Earth's gravity field. The second derivative of the range $\ddot{\rho}$ is measured by the ranging instrument. The non-gravitational accelerations Δa_{ng} can be seen as disturbances and are measured by the accelerometers located in the center of the mass of the satellites. The positioning of the GRACE satellites as well as the time synchronization is done by the hl-SST approach using GPS.

GOCE was the first gravitational gradiometry mission which was launched in 2009 in context of the Living Planet program of the European Space Agency (ESA) (Drinkwater et al., 2007). The mission objective was to determine the static part of the Earth's gravity field with high spatial resolution and accuracy. The low altitude of 246 km necessitates drag compensation due to the high atmospheric density at this altitude. The drag-free system compensated the non-gravitational acceleration in along-track direction. Consequently, the fuel budget for the ion propulsion system defined the mission lifetime which ended in 2013. The high spatial resolution is achieved by measuring the second derivative of the gravitational potential. The principle of gradiometry is based on differential acceleration measurements (Rummel et al., 2011). The observed gravity gradient - e.g. for the x-direction - Γ_{xx} is computed from the acceleration difference Δa_{g_x} divided by the length of the baseline L_x between the accelerometers:

$$\Gamma_{xx} = \frac{\Delta a_{g_x}}{L_x}. \tag{2.16}$$

For a spatial scale of 100 km an accuracy of 1.7 cm is obtained (Gruber et al., 2019).

2.2.2 State-of-the-art Sensors

Sensors of a satellite mission are a crucial factor for the quality of the end products. The most relevant sensors and their principles of operation are addressed in this section. This includes their characteristics, measurement accuracies and limitations. The sensor noise models which are included in the simulation are not explained in this section, but in chapter 3.

Accelerometer

The missions CHAMP, GOCE, GRACE and GRACE-FO have accelerometers developed by Office National d'Etudes et de Recherches Aérospatiales (ONERA) on board. However, they are used to measure different signals: gravitational or non-gravitational accelerations. In GOCE, six accelerometers in a so-called diamond configuration around the center of mass form a gradiometer. The measured differential accelerations give a direct link to the gravity potential. In contrast, the other missions need accelerometers to determine the non-gravitational accelerations which are considered as perturbations. Therefore, their accelerometers are located in the center of mass of the satellite, where the gravitational force

and the centrifugal force are in balance. Consequently, only the non-gravitational forces are measured by these accelerometers.
All missions so far have operated with electrostatic accelerometers. The acceleration measurements are based on the electrostatic force which is necessary to maintain the proof mass at the center of the cage. The position of the proof mass is servo-controlled in terms of translation and rotation. The movement of the proof mass leads to capacitance difference between C1 and C2 (cf. Figure 2.2) which is measured by the capacitive sensor and amplified. The corrector determines the drive voltage to be applied to the electrodes in order to reduce the capacitance difference to zero (Johannessen & Aguirre-Martinez, 1999; Touboul et al., 1999). The control voltages are transformed to accelerations by a transfer function (Stummer, 2012).

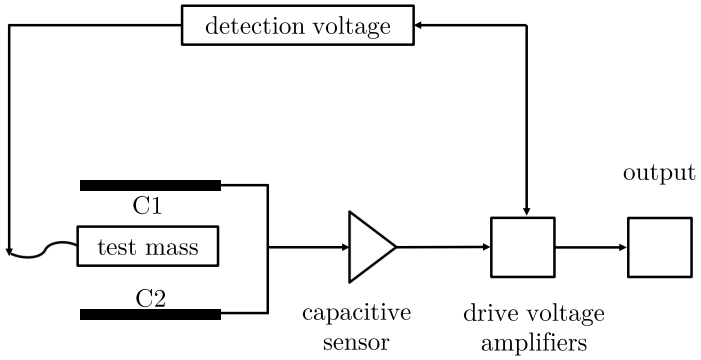


Figure 2.2: Servo-control channel of an electrostatic accelerometer for one axis, Figure modified from (Johannessen & Aguirre-Martinez, 1999; Touboul et al., 1999)

The accelerometers of all satellite gravity missions worked with the same principle, but still differ in their performance due to further developments and different on-board environments. It has to be noted that the verification of the accelerometer performance in space is a challenging task. The main contributions to the noise of an Electrostatic Accelerometer (EA) are (Touboul et al., 2016):

- detector noise,
- wire damping,
- measurement readout and digitalization noise,
- thermal sensitivity of the bias,
- parasitic acceleration inside the accelerometer core.

The detector noise from the electronic noise of the capacitive position sensor increases with frequency. Hence, the detector noise is dominant in high frequencies. The parasitic acceleration inside the accelerometer core are residual acceleration disturbances directly acting on the test mass. This is a limiting factor in the low frequencies. Temperature variations lead to a variation of the electronic bias in low frequencies which is a critical contributor as well. The noise due to the read-out analogue-digital-converter is the dominant factor between the

frequencies of 0.005 Hz and 0.1 Hz. The best trade-off between the required measurement range and noise has to be found. According to Touboul et al. (2016) and Zhu et al. (2013) the wire damping is not a critical factor.
The EAs of CHAMP, GRACE and GOCE provide three linear accelerations along the axes of the instrument frame (x, y and z axis in the following). They have two ultra-sensitive axes and one less sensitive axis due to ground tests under $1g$ conditions (Touboul et al., 2012; Frommknecht, 2007; Johannessen & Aguirre-Martinez, 1999). Their performance parameters are summarized in Table 2.2. EAs include systematic errors and need to be calibrated, which is described in section 2.2.4.
The STAR accelerometer used in CHAMP has a measurement range of $\pm 10^{-4}$ m/s^2. The accelerometer noise is at the level of 3×10^{-9} m/s^2/$\sqrt{\text{Hz}}$ for the y and z axes and 3×10^{-8} m/s^2/$\sqrt{\text{Hz}}$ for the x axis within the measurement bandwidth from 10^{-4} Hz to 10^{-1} Hz (Touboul et al., 2012).
The two Super-STAR accelerometer of GRACE have a reduced full scale range and a better accuracy at the level of 1×10^{-10} m/s^2/$\sqrt{\text{Hz}}$ for the high-sensitive axes x and z and 1×10^{-9} m/s^2/$\sqrt{\text{Hz}}$ for the y axis. The saturation limit for the x and z axes is $\pm 5 \times 10^{-5}$ m/s^2 and $\pm 5 \times 10^{-4}$ m/s^2 for the y axis (Hudson, 2003). The proof mass is a 4 mm $\times$ 4 mm $\times$ 1 mm large titan cube with a mass of 70 g (Frommknecht, 2007). The performance of the GRACE-FO accelerometer is similar to the one of GRACE (Christophe et al., 2015).
The accelerometers of GOCE have an even lower noise level of 2×10^{-12} m/s^2/$\sqrt{\text{Hz}}$ in the Measurement Bandwidth (MBW) from 5×10^{-3} Hz to 0.1 Hz (Touboul et al., 2012). An accelerometer performance of 3×10^{-12} m/s^2/$\sqrt{\text{Hz}}$ was verified in orbit (Christophe et al., 2010). The quiet environment is enabled by the drag-free system and the fine active thermal control of the instrument case which is needed for achieving this high performance (Touboul et al., 2012). The GOCE accelerometer test mass has also a size of 4 mm $\times$ 4 mm $\times$ 1 mm (Johannessen & Aguirre-Martinez, 1999). The measurement range is $\pm 6.5 \times 10^{-6}$ m/s^2 (Marque et al., 2008).

Table 2.2: Accelerometer performances

	accuracy ultra-sensitive axes	measurement bandwidth	saturation limit
CHAMP	3×10^{-9} m/s^2/$\sqrt{\text{Hz}}$	10^{-4} Hz to 10^{-1} Hz	$\pm 1 \times 10^{-4}$ m/s^2
GRACE	1×10^{-10} m/s^2/$\sqrt{\text{Hz}}$	10^{-4} Hz to 10^{-1} Hz	$\pm 5 \times 10^{-5}$ m/s^2
GOCE	2×10^{-12} m/s^2/$\sqrt{\text{Hz}}$	5×10^{-3} Hz to 10^{-1} Hz	$\pm 6.5 \times 10^{-6}$ m/s^2

Inter-satellite Ranging Instrument

The range measurement between the two satellites is fundamental for the missions GRACE and GRACE-FO. The K-band Ranging System (KBR) measures the change of the inter-satellite distance. The microwave ranging system operated with two frequencies, 24 GHz and 32 GHz, to remove variable ionospheric delays. The KBR noise is estimated with 2 µm/$\sqrt{\text{Hz}}$ (Frommknecht, 2007).
With GRACE-FO, an LRI System is demonstrated (Sheard et al., 2012) to measure the change in distance between the two satellites additionally to the KBR. The LRI has a lower

noise compared to KBR of about $1\,\mathrm{nm}/\sqrt{\mathrm{Hz}}$ for frequencies above 100 mHz (Abich et al., 2019).

Star Camera

The determination of the satellite attitude is needed for in-orbit-maneuvers to keep the specified spacecraft orientation and for post-processing and gravity field recovery. Star cameras provide the attitude of the satellite with respect to the inertial frame. The star camera measurements are characterized by their anisotropic accuracies: rotations around the x-axis and y-axis are measured more accurately with an accuracy of 30 µrad. The accuracy of the measured rotations around the z-axis is 240 µrad (Bandikova & Flury, 2014).

GNSS Receiver

The Global Navigation Satellite System (GNSS) receiver is required for the estimation of Low Earth Orbit (LEO) satellite positions. The orbit perturbations give information about the long wavelengths of the gravity field signal following the hl-SST approach. Moreover, the timing of all sensor data captured on board is realized using the GNSS signals.

The reader is referred to Frommknecht et al. (2011), Stummer et al. (2012), Case et al. (2010) and Wen et al. (2019) for further information about inter-satellite ranging instruments, star camera and GNSS receiver.

2.2.3 State-of-the-art Control Systems

Control systems of a satellite mission can be categorized in attitude control systems and drag-free control systems. All control systems consist of sensors and actuators.

Attitude Control System

The attitude control system has to be adapted to the requirements of the mission. The GRACE mission required a precise attitude control to enable the inter-satellite ranging. For GRACE-FO the requirement for the inter-satellite pointing is even higher due to the much smaller area illuminated by the laser beam compared to the cone formed by the K-band signal. However, the stringent pointing requirement of a few mrad for LRI is achieved by a fast steering mirror instead of the attitude control system (Wegener, 2022). Sensors, which contribute to determine the actual attitude and the required attitude, are the Coarse Earth and Sun Sensors for Earth-vector and Sun-vector determination, magnetometer for the magnetic field measurement, Inertial Measurement Unit (IMU) for the angular velocities, star cameras for the spacecraft attitude w.r.t. inertial reference frame and GNSS receiver for orbit determination and timing (Herman et al., 2004). The actuators of the GRACE and GRACE-FO attitude control systems are magnetic torque rods and cold gas thrusters. The magnetic torque rods use the Lorentz force which is generated by a current of the Earth's

magnetic field. The produced mechanical torque $\mathbf{r}_m$ results from the combination of the magnetic dipole moment of the rod $\mathbf{m}$ and the Earth's magnetic field $\mathbf{B}$:

$$\mathbf{r}_m = \mathbf{m} \times \mathbf{B}. \tag{2.17}$$

According to the parameters of GRACE-FO, maximum magnetic control torques of 1.5 mN m for roll, 1.7 mN m for pitch, 0.9 mN m for yaw are possible. The magnetic torques rodes are used primarily for attitude control. However, if the magnetic field lines are parallel to the required torque, the cold gas thrusters are needed. The control force acts in the opposite direction of the outstreaming gas. The corresponding torque $\mathbf{r}_{thr}$ is given by the thrust force vector $\mathbf{F}$ and the position vector $\mathbf{r}$:

$$\mathbf{r}_{thr} = \mathbf{r} \times \mathbf{F}. \tag{2.18}$$

The thruster torque is in the order of 10 mN m (Wegener, 2022).
The pointing requirement in GOCE is less stringent, but nevertheless a very quiet environment is needed. The star cameras, described in 2.2.2, provide the precise attitude information. In GOCE, only magnetic torquers are used as actuators for the 3-axis stabilized attitude control. Reaction wheels or reaction control thrusters are not appropriate because they would not ensure a quite environment (Romanazzo et al., 2011).

Drag-free Control System

GOCE was the first satellite mission with a drag-free control system which compensates disturbances in flight direction caused by non-gravitational forces. The non-gravitational accelerations are measured by the gradiometer. There, the common mode accelerations represent the non-gravitational disturbances. The Ion Propulsion Assembly continuously counteracts these perturbations and consists of two fully redundant assemblies with one storage tank of 41 kg of Xenon propellant. The thrust range is from 0.6 mN to 20 mN (Romanazzo et al., 2011).

2.2.4 State-of-the-art Accelerometer Calibration

Accelerometers perform highly sensitive measurements, but there are still systematic effects which degrade these measurements. Therefore, a calibration is needed in order to reduce these effects. Reasons for these effects are, e.g., that the accelerometer is not at the exact nominal position or the accelerometer axes are not completely orthogonal to each other. The misalignment angles represent the rotational deviation from the nominal orientation and the coupling parameters typify the deviation from orthogonality. The accelerations have quadratic factors, scale factors and biases due to inaccurate knowledge about the transfer function converting the control voltages to accelerations and about the electrostatic gain.
The true acceleration $\boldsymbol{a}_i$ differs from the measured acceleration $\tilde{\boldsymbol{a}}_i$ as follows (Siemes, 2012):

$$\boldsymbol{a}_i = \begin{bmatrix} s_{i,x} & \alpha_i + \zeta_i & \beta_i - \epsilon_i \\ \alpha_i - \zeta_i & s_{i,y} & \gamma_i + \delta_i \\ \beta_i + \epsilon_i & \gamma_i - \delta_i & s_{i,z} \end{bmatrix} \tilde{\boldsymbol{a}}_i + \boldsymbol{b}_i + \boldsymbol{n}_i, \tag{2.19}$$

where $s_{i,x}, s_{i,y}, s_{i,z}$ are the scale factors, $\alpha_i, \beta_i, \gamma_i$ are the shear parameters due to coupling, $\delta_i, \epsilon_i, \zeta_i$ are the rotation parameters due to misalignment, $\boldsymbol{b}$ are the biases, $\boldsymbol{n}$ is the noise vector and i is the index of the accelerometer.
There are different calibration methods for the measurement concepts implemented by GRACE and GOCE. GOCE has six accelerometers on board whereby the calibration can be performed in terms of differential mode and common accelerations. In contrast, one GRACE satellite has only one accelerometer on board. Thus, external information is required.

The calibration method for gradiometer measurements is presented in Siemes (2012) and Siemes et al. (2012). It is based on twelve conditions for accelerometer measurements and star camera measurements. Scale factors, shear parameters and rotation parameters are estimated with this method. The parameters are estimated via least-squares adjustment including a stochastic model for misclosures of the conditions.
For a single satellite the gradiometer calibration procedure is not applicable. In Vielberg et al. (2018) three calibration methods are compared: multi-step numerical estimation approach based on the numerical differentiation of the kinematic orbits of LEO satellites, a calibration within the dynamic precise orbit determination and a comparison of the measured and the modeled non-gravitational forces.
In Klinger and Mayer-Gürr (2016) a two-step calibration using models of non-gravitational accelerations is proposed. The obtained calibration parameters using these models are used as a priori values for the estimation within the gravity field recovery. Scale factors and biases are estimated daily. It has been found that there is a temperature-dependent behavior of the calibration parameters (Klinger & Mayer-Gürr, 2016). In Wöske et al. (2018) a calibration method completely based on precise non-gravitational force modeling is presented.

2.3 Concepts for Future Satellite Gravity Missions

This section presents theoretical concepts for NGGM. First, an overview of the challenges of gravity field determination with satellites is given. The concepts are categorized in improvements in sensor technology and improvements in orbit design.

2.3.1 Challenges of Satellite Gravity Missions and Requirements for Future Satellite Missions

The gravity field recovery using satellites has several advantages. The satellite observations enable global, homogeneous coverage which is an advantage compared to the regional coverage of terrestrial techniques. However, the spatial and temporal resolution achieved by current satellite missions is limited. This has to be improved by future missions. With an increased number of satellites a better temporal resolution could be achieved. However, this also increases the overall costs of a satellite mission. Concerning this, the mission duration is significant as well. In literature a minimum duration of 10 years is recommended (Gruber et al., 2014a; Reubelt et al., 2014).
The choice of the orbit parameter has a large effect on the quality of the recovered gravity

field. LEO satellites are chosen for gravity missions. The orbits should be circular and nearly polar in order to cover the whole Earth with constant accuracy. Aspects of satellite orbit design are described in section 2.1.3 in detail. The satellite orbit has to be tracked continuously using GNSS sensors. An important criteria is the isolation of the gravitational signal. For this reason non-gravitational signals have to be measured by the accelerometers on board of the satellite. Accelerometers are one of the limiting factors when the instrument accuracy is considered.
The major challenge in global gravity field recovery is the time-variable background modeling. With GRACE and GRACE-FO it is possible to detect monthly mass changes with a spatial resolution of 350 km. In Mayer-Gürr et al. (2018) solutions with higher spatial resolution, up to SH degree 120, are estimated, which corresponds to a spatial resolution of approximately 170 km. Signals of processes shorter than this time period, i.e. one month, can not be detected which leads to temporal aliasing. Furthermore, small-scale features can not be measured which results in spatial leakage (Dobslaw et al., 2017).

The main achievement of GOCE is the high spatial resolution of the geoid. The static part of the Earth's gravity field has been determined with a precision of below 2 cm in terms of geoid heights for a resolution of 100 km (Brockmann et al., 2021). In combination with satellite altimetry, which gives information about the sea surface height, dynamic ocean topography can be determined with a resolution of 80 km to 100 km. Beyond that, GOCE contributes to the realization of a global unification of height systems and understanding the Earth's interior (Pail et al., 2015).

GRACE observations enabled the quantification of mass transport processes in the Earth system. Mass transport processes and redistribution of masses are visible in terrestrial water storage, continental aquifers, glaciers and ice sheets (Tapley et al., 2019). The monitoring of changes over time in the Earth's gravity field gives valuable insights, also in the context of the global climate change (Rodell et al., 2018). Application examples are the observations of mass changes of glaciers and ice caps, water storage variations (seasonal, inter-annual and long-term) or the detection of anthropogenic groundwater depletion. The mass loss in Greenland and Antarctica is quantified to 279 Gt/yr and 128 Gt/yr, respectively (Rodell et al., 2018). In addition, GRACE gives relevant insight about the global mean sea level rise. The global sea level rise has two components: the thermal expansion and the mass change. The latter can be measured by GRACE observations. In Eicker et al. (2020) even daily GRACE gravity field solutions up to degree 40 are analyzed to investigate high-frequency hydro-meteorological fluxes over the continents. However, the lower spatial resolution of 500 km causes spatial leakage effects.

In spite of the great achievements by the missions GOCE, GRACE and GRACE-FO improvements are needed for the observation of smaller mass transport processes. In Pail et al. (2015) science and user needs for future satellite gravity mission observations are derived. Joint requirements are set as a compromise of various fields like hydrology, cryosphere, oceans and solid Earth in order to cover a wide range of applications. The required target performance in terms of EWH is stated as 5 cm for monthly solutions and 0.5 cm/yr for long-term trends at a spatial resolution of 150 km. This corresponds to a monthly geoid height error of 0.1 mm for 150 km resolution. In Gruber et al. (2014a) the required monthly geoid height

error is stated with 1 mm for 150 km resolution. In several studies, it is proposed to design the missions with subcycles within one repeat orbit. Thereby, gravity field solutions with higher temporal resolution of one week or even one day can be determined with reduced spatial resolution. Many applications with social benefit would need products with temporal resolution from one to a few days. It is of great interest to extend the available time series of global gravity measurement and increase both spatial and temporal resolution.

2.3.2 Developments in the Sensor Technology

Available and emerging sensor technologies are an important component in the mapping of the Earth's gravity field. In this section, further developments of space accelerometers are summarized. Instruments in space are faced with some challenges. The robustness to the radiation environment, launch vibrations and thermal vacuum are important. The reliability and traceability of the production, maintenance and tests must be demonstrated (Touboul et al., 2016). The classical EAs have already demonstrated their robustness and performance on board of satellites. Beneficial for inertial sensors are the microgravity environment and shielding of the satellite or thermal control (Touboul et al., 2016).

Further Development of Electrostatic Accelerometers

One challenge is the characterization of the space accelerometer performance. The performance is estimated with a combination of the mathematical formulation of the impact of each contributor, tests for assessing the level of this contributor and flight data. The noise of the electronics is precisely measured on ground and converted into acceleration (Touboul et al., 2016). But still these sensors cannot be tested effectually under 1 g conditions. According to Touboul et al. (2016) possible solutions are:

- electrostatic levitation of the test mass in order to enable sensor tests in the horizontal plane,
- mechanical levitation of the test mass with a wire,
- free-fall tests.

The ONERA accelerometers so far used in gravity missions have two high-sensitive axes and one less-sensitive axis due to the calibration on ground (Frommknecht, 2007; Christophe et al., 2018). For the calibration, the proof-mass is levitated under 1 g conditions to verify the accelerometer performance on an anti-seismic pendulum (Christophe et al., 2018). With new catapult drop tower and experiences in the accelerometer design, it is now possible to perform on ground verifications without levitation under $1g$ conditions. This procedure was demonstrated successfully with the Microscope mission (Christophe et al., 2018; Touboul et al., 2017).
The MicroSTAR accelerometer is an enhanced electrostatic accelerometer. It has a cubic test mass which implicates three high-sensitive axes. Moreover, the sensor provides angular accelerations. The test mass is controlled with three pairs of electrode plates, each having

two degrees of freedom. The expected accuracy is 6.6×10^{-12} m/s^2 within the measurement bandwidth from 0.2 mHz to 0.1 Hz. The proof mass has the sizes $30 \times 30 \times 30$ mm and a weight of 218 g. The distance between the test mass and the electrode plates is 400 µm which provides a measurement range of $\pm 6.4 \times 10^{-6}$ m/s^2. In high frequencies, the main noise contributor is the capacitive detector noise. In low frequencies, it is the contact potential noise and the bias thermal fluctuation (Christophe et al., 2018). The accuracy of angular acceleration measurements is $\pm 2.2 \times 10^{-10}$ rad s^{-2} inside the measurement bandwidth from 0.2 mHz to 0.1 Hz. In December 2016, first drop tower experiments have been performed at Zentrum für angewandte Raumfahrttechnologie und Mikrogravitation (ZARM) in Bremen, Germany, with the prototype for testing the control loop.

Electrostatic Accelerometer with Optical Sensing

The development in laser interferometry metrology enables the concept of an EA with optical sensing. The experiences of the Laser Interferometer Space Antenna (LISA) Pathfinder mission are beneficial for the development of this concept. The principle of such an optical accelerometer is very similar to the one of an electrostatic accelerometer. The difference is the detection of the test mass position. Instead of a capacitive detection, the test mass position is measured by laser interferometry. Additionally, the interferometer readout is used for the correction of the electrode voltage output signal (cf. Figure 2.3).
In Alvarez et al. (2022), a new inertial sensor based on the LISA Pathfinder technology is designed and analyzed. The test mass charge is controlled by an UV LED-based charge management system instead of using a grounding wire. This replacement allows an increase of the mass from 100 g to 500 g and an increase of the gap between the electrode housing and the test mass from 100 µm to 1 mm. The estimated acceleration noise model for a mission with drag compensation at 350 km is 5×10^{-13} m/s^2 in the MBW from 0.1 mHz to 3 mHz. The performance is limited by the capacitive sensing noise in the frequencies above 3 mHz. The noise level is at a level of 5×10^{-12} m/s^2 in the frequencies below 8 mHz for a GRACE-FO-like mission at 500 km.

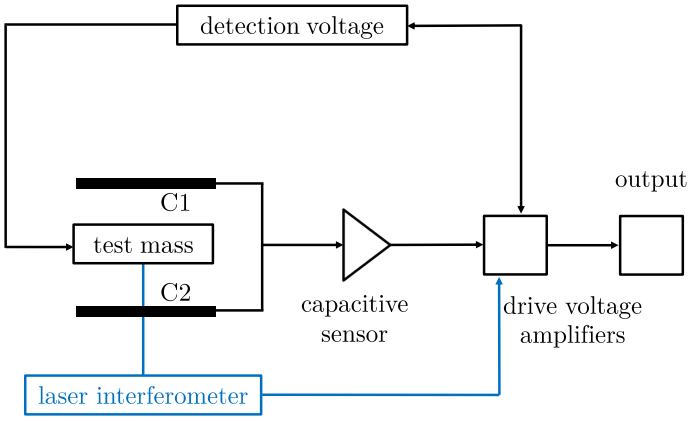


Figure 2.3: Servo-control channel of an electrostatic accelerometer for one axis with addition of a laser interferometer

Cold Atom Interferometry Accelerometer

A new instrument concept which relies on the manipulation of matter waves through atom interferometry offers advantages against the classical EA type. The principle of CAI has already applied to ground sensors like cold atom gravimeters or gravity gradiometers (Tino, 2021).

One measurement cycle of the atom interferometer is divided in three segments: preparation of the atoms, free fall and interferometer sequence and detection of the atomic states. The atom cloud consisting for example of $10^6 - 10^8$ Rubidium ^{87}Rb atoms is prepared by laser cooling and trapping techniques (Carraz et al., 2014).
The principle of atom interferometers is predicated on the interference of matter waves and the superposition principle of atoms (cf. Figure 2.4) . The atoms can be in ground state $|g\rangle$ or in excited state $|e\rangle$ depending on the atomic energy level. The interaction between an atom and a photon causes a change of the atomic energy level. The atomic state change leads to a momentum transfer which results in a spatial separation of the atoms in different states. The atom moves in the direction of the laser beam if the photon is absorbed. If it is emitted, the atom moves in the opposite direction. The momentum transfer $\Delta\mathbf{p}$ depends on the reduced Planck constant $\hbar$ and wave vector of the laser light $\mathbf{k}$: $\Delta\mathbf{p} = \hbar\mathbf{k}$. A two-photon Raman transition using two counter-propagation beams leads to an effective wave vector $\mathbf{k}_{eff}$ which is the difference of the two wave vectors. The stimulation of an atom in the ground state $|g\rangle, \mathbf{p}\rangle$ puts the atom in the excited state $|e, \mathbf{p} + \hbar\mathbf{k}_{eff}\rangle$ (Kasevich & Chu, 1991; Schilling, 2019).
Several approaches exist to implement an atom interferometer. One is the Mach-Zehnder interferometer which consists of three interactions between photons and atoms. The sequence of such an interferometer is: beam splitter - reflector - beam splitter (which is here realized by quantum-optical methods instead of optical component parts). The beam splitter transfers an atom in a different state with a probability of 50 % by a so called $\pi/2$ pulse. After a time interval T the reflector changes the atomic state with a probability of 100 % by a π pulse. After another time interval T a second $\pi/2$ pulse interacts with the atoms. The type of interaction is controlled by the pulse duration of the laser light. The interferometer sequence is illustrated in Figure 2.4.

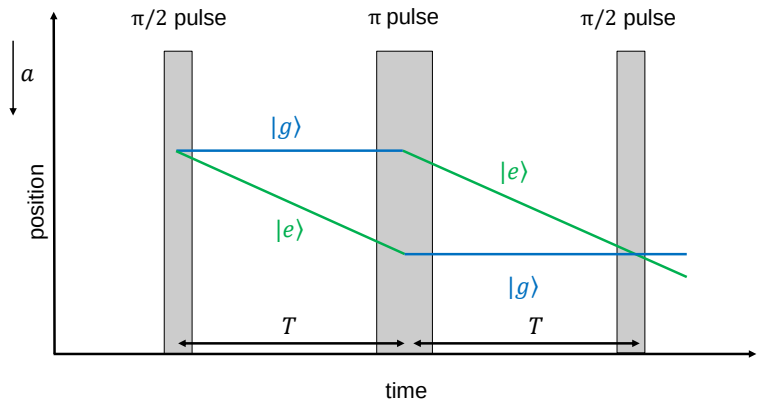


Figure 2.4: Mach-Zehnder atom interferometer, modified from (Schilling, 2019)

The phase shift $\Delta\Phi$ is given by the phase differences Φ_i between the two Raman lasers at the time of the i-th laser pulse (Lautier et al., 2014):

$$\Delta\Phi = \Phi_1 - 2\Phi_2 + \Phi_3. \tag{2.20}$$

The observable of the interferometer is the population of atoms per state. The transition probability P is derived form the measured population N_i in the two output ports of the interferometer:

$$P = \frac{N_1}{N_1 + N_2} = \frac{C}{2} cos(\Delta\Phi), \tag{2.21}$$

where C is the interferometer contrast. The presence of an acceleration a is reflected in the phase shift $\Delta\Phi$ as follows

$$\Delta\Phi = k_{eff} a T^2, \tag{2.22}$$

with $k_{eff} = |\mathbf{k}_{eff}|$ as effective wave number of the Raman pulse and T as time interval between the pulses.

Terrestrial cold atom gravimeters have already been developed for example by LNE-SYRTE (Cold Atom Gravimeter, CAG (Gillot et al., 2016)), Humboldt University of Berlin (Gravimetric Atom Interferometer, GAIN (Freier et al., 2016)) and by iXBlue, formerly Muquans (Absolute Quantum Gravimeter, AQG (Ménoret et al., 2018)) which is a commercial product. No sensors are developed for space applications yet, but experiments for space have been performed. Within the framework of the rocket experiment MAIUS-1, rocket interference experiments of Bose-Einstein condensates in free-fall have been performed (Lachmann et al., 2021). The Cold Atom Laboratory (CAL) has been installed on the International Space Station in May 2018. This experiment uses laser-cooled atoms in a microgravity environment. Bose-Einstein Condensate and Cold Atom Laboratory (BECCAL) is a future experiment for the International Space Station (Frye et al., 2021). In addition, there are initiatives to demonstrate a CAI accelerometer on board of a satellite. The development of a quantum pathfinder mission is planned within the study Cold Atom Rubidium Interferometer in Orbit for Quantum Accelerometry (CARIOQA) (Lévèque et al., 2022).

A better performance is expected for CAI sensors on board of a satellite compared to the one of terrestrial sensors. A longer free fall time due to the microgravity environment induces a higher sensitivity as it scales quadratically with the interrogation time. An advantage of an CAI accelerometer is the flat noise Power Spectral Density (PSD) for low frequencies with very good repeatability, no hard moving parts and intrinsically accurate measurement thanks to the stability of the atom transitions (Carraz et al., 2014). One of the difficulties is the low frequency sampling. Simulation studies on this concept are documented in Carraz et al. (2014), Douch et al. (2018b), Trimeche et al. (2019), Abrykosov et al. (2019) and Müller and Wu (2020). In Carraz et al. (2014) a sensitivity of $3.5\,\mathrm{mE}/\sqrt{\mathrm{Hz}}$ is estimated for CAI gradiometer ($1\,\mathrm{E} = 1 \times 10^{-9}\,\mathrm{s}^{-2}$, named after Roland von Eötvös). The sensitivity depends on several factors and its estimation for this study is described in section 3.3.2.

Combination of Electrostatic Accelerometer and Cold Atom Interferometry Accelerometer

High performance is expected for a combination of an EA with a CAI accelerometer, since the weaknesses of one sensor can be compensated by the strengths of the other. CAI has a high long-term stability and calibration is not needed as the scale factor is very well known owing to its absolute nature of measurements. Nevertheless, the low sampling rate is the main drawback. In contrast, the EA has a continuous output and has a high sensitivity in higher frequencies. Inaccuracies occur due to the bias drift and the imperfect determination of the calibration parameters.
For a hybridization, the two accelerometers should be ideally at the same point of the satellite body. This point would be the satellite center of mass for a GRACE-like mission. One option to realize a hybrid system is to place a mirror for Raman transitions on the proof mass of the EA (Carraz et al., 2014). The ground prototype, reported by Christophe et al. (2018), has a rigidly fixed mirror at the accelerometer housing. The control of the proof mass of the EA could facilitate to deal with satellite rotation during the free fall time of the atom cloud. A combination of an atom gravimeter with a mechanical accelerometer is also presented in Lautier et al. (2014).
Aside from that, the measurements of the two sensors need to be combined with an algorithm. For the real time processing a Kalman filter is convenient. In Christophe et al. (2018) a Kalman filter is used to estimate the bias of the classical accelerometer in each cycle:

$$b_i = b_{i-1} + G_b(a_{EA,i} - b_{i-1} - a_{CAI,i}), \tag{2.23}$$

where b_i is the bias of EA in the i-th cycle, $a_{EA,i}$ is measurement of the EA and $a_{CAI,i}$ is the measurement of the CAI accelerometer, G_b is the gain of the correction. The output of the EA can contrarily be used to determine the CAI fringe index (Christophe et al., 2018). In HosseiniArani et al. (2022) an extended Kalman filter is studied to combine electrostatic and CAI measurements. The electrostatic acceleration measurements are used for the prediction of the phase shift in order to solve the fringe ambiguity of the CAI measurements. The CAI measurements are then used as actual observation for the EA bias estimation.
Another filter option is to first apply a high-pass filter to the electrostatic measurements and a low-pass filter to the CAI measurements and combine the filtered measurements afterwards (Knabe et al., 2022).

2.3.3 Concepts for Orbit Design

When investigating new sensor technology concepts, it is important to quantify their impact for NGGM orbit constellations. The two GRACE satellites are nearly in the same polar orbit with a inter-satellite distance of about 200 km. The drawback of this configuration is a poor sensitivity in east-west direction which leads to striping effects in the north-south direction. There are several concepts to improve the sampling and to reduce temporal aliasing. These configuration concepts can be divided in single pair and double pair constellations. A more isotropic error pattern is expected if observations also contain cross-track or radial information on the gravity field.
Concepts for single pair constellations are for example pendulum, Cartwheel or Helix formations (Elsaka et al., 2014). In the pendulum mission the longitude of the ascending node Ω

and the mean anomaly differs for the two satellites. This leads to measurements in along-track direction and in cross-track direction. The baseline of the two satellites is oriented at the equator in cross-track direction and at the pole in along-track direction (Elsaka, 2010). For this formation, the orbit and attitude control is very challenging due to the relative motion. In the Cartwheel constellation, the two satellites fly in individual orbits and perform a 2:1 elliptical motion about their center of mass. In each orbit, measurements in along track direction and in radial direction are performed (Elsaka, 2010). Using the Helix, along-track, cross-track and radial information can be obtained. Cartwheel and Helix constellations have even higher challenges for formation control.
Furthermore, several studies investigated two pair constellations leading to the best results in the recovered gravity field (Elsaka et al., 2014; Purkhauser et al., 2020). However, the economic point of two satellite pairs being in orbit has to be considered. A promising two pair concept is the Bender design (Bender et al., 2008). This constellation exists of one inline pair in a polar orbit and another inline pair in an orbit with a lower inclination, e.g. 63°. The results of the Bender formation have a better temporal resolution and reduce the aliasing errors, but it is economically much more challenging. From the technological point of view it is feasible (Massotti et al., 2021).
MOBILE is another concept which is based on hl-SST (Pail et al., 2019). The observation of the radial component leads to a more isotropic error pattern compared to the ll-SST in along-track direction. The constellation consists of two MEO satellites with an altitude of 10 000 km and one LEO satellite with an altitude between 350 km and 400 km. The laser-based ranging instrument is on board of the LEO satellite and the MEO satellites are equipped with passive reflectors or transponders.

In Massotti et al. (2021) a joint concept called Mass change And Geosciences International Constellation (MAGIC) of ESA and National Aeronautics and Space Administration (NASA) for NGGM is evaluated. The recommended constellation for MAGIC is a Bender configuration. At the ESA Council in November 2022, the government ministers approved the NGGM initiative MAGIC with the objective to contribute to the observation of water volume in oceans, ice sheets and glaciers for a better understanding of sea level changes and the improvement of water management. In addition, NASA aims to realize a GRACE-FO successor (Flechtner et al., 2022). It can be concluded that the realization of a Bender configuration is realistic in the future with the GRACE-FO successor as polar pair and the inclined pair MAGIC.

3 Evaluation of Simulation Environment

This chapter introduces the simulation environment. The closed-loop simulation consists of the generation of observations, the estimation of the gravity field parameters and the comparison of the estimated parameters with the true parameters (cf. section 3.1). First, satellite dynamics are simulated which is briefly described in sections 3.1 and 3.2. Observations are generated based on these satellite dynamics and the reference gravity field. In the next step, noise time series of sensor performances, control system behavior and time-variable background models are added. Models for these noise sources are explained in the sections 3.3, 3.4 and 3.5. The estimation procedure of the gravity field model parameters is given in section 3.6.

3.1 Overview of the Simulation Environment

A closed-loop simulation is performed in order to evaluate the gravity field solutions achieved with different measurement concepts, sensors, actuators and orbit configurations. First, satellite dynamics are simulated with the software eXtended High Performance Satellite Dynamics Simulator (XHPS), which is developed by ZARM and Deutsches Zentrum für Luft- und Raumfahrt (DLR) (Wöske et al., 2016). The software runs in MATLAB/Simulink with double precision. The system of differential equations is solved by transforming it into a system of ordinary differential equations. In these simulations, the Runge-Kutta method is used for the numerical integration. The dynamics are calculated with the integrator based on the gravity field and further external as well as internal forces and torques. In the simulations, an Earth gravity field model, an ocean tide model, a solid Earth tide model, a pole tide model and models for the effects from Sun and Moon are considered. Aside from that, an attitude control system and non-gravitational accelerations are included.
The models for non-gravitational perturbations are explained in more detail in section 3.2, because the modeling is important for the analysis of novel accelerometer concepts. Beyond that, the control systems play a major role for the calculation of the satellite dynamics and further analysis. In section 3.4.1 the modeling of a drag-free control system and in section 3.4.2 the modeling of an attitude control system are explained. While models for attitude control are available in the XHPS library, a model was created for the drag-free system by the author of this thesis.
Noise time series for sensors and actuators are modeled using LISA Technology Package Data Analysis (LTPDA) which is a MATLAB toolbox for accountable and reproducible data analysis (Hewitson et al., 2009). It was developed for the data analysis of the LISA Pathfinder mission.

As different mission concepts are studied, the procedures for the recovery of the gravity field differ. In section 3.6.2, the recovery based on range accelerations and, in section 3.6.3, the recovery based on gravity gradients are addressed. The simulation procedures for these two cases are illustrated in Figure 3.1 and Figure 3.2, respectively. Noise-free observations are calculated from the satellite position and velocity data, attitude data as well as the reference gravity field model. The latter is the high-resolution model Eigen-6c4 which is inferred from combining Laser Geodynamics Satellite (LAGEOS), GRACE, GOCE and terrestrial data (Förste et al., 2014). In the next step, noise time series of different sources are added. SH coefficients are estimated and evaluated with respect to the SH coefficients of the reference gravity field. The recovery parts are carried out on the computer cluster system of the Leibniz University of Hannover, Germany.

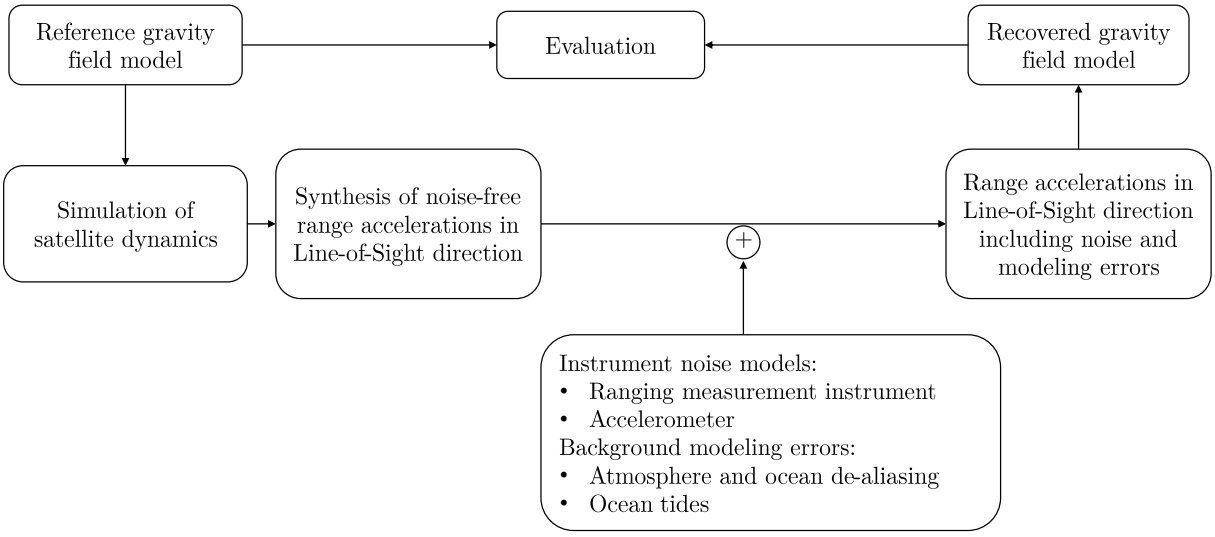


Figure 3.1: Simulation procedure for range accelerations

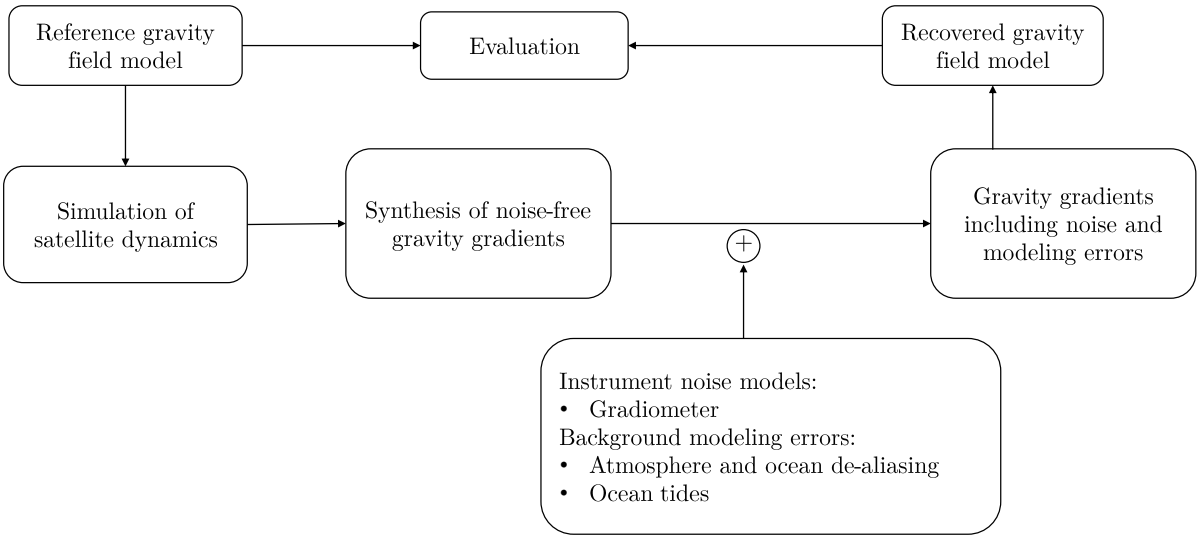
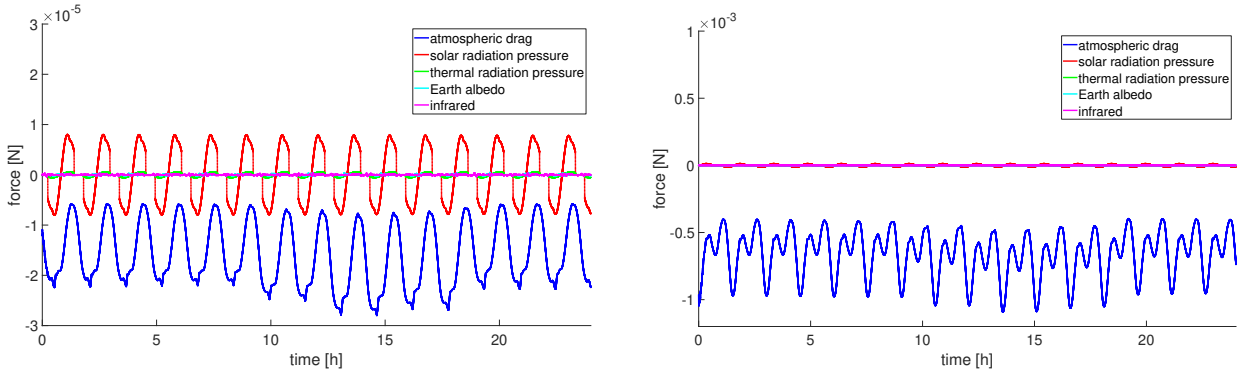


Figure 3.2: Simulation procedure for gradiometry

3.2 Modeling of Non-gravitational Forces

The modeling of non-gravitational forces acting on the satellite is an important component. The magnitude depends on the satellite orbit, especially on its altitude, as well as the shape and mass of the satellite body and the environmental conditions. The accelerometer has to be designed for the magnitude of the non-gravitational accelerations, i.e. the saturation limit of the sensor must not be exceeded. The modeling of non-gravitational forces is fundamental for the drag compensation analysis in section 4.2 and the CAI accelerometer analysis in section 4.3.
The non-gravitational forces are mainly caused by the atmospheric drag, the solar radiation pressure, the Earth albedo, infrared radiation of the Earth and thermal radiation pressure from the satellite itself. In the XHPS toolbox, models are available for these dissipative forces. The magnitude of non-gravitational forces depends on the surface area and mass of the satellite. Hence, it is necessary to model the satellite geometry. This is implemented by a detailed finite element model of the satellite. A detailed description of the used models is given in Wöske et al. (2018) and Wöske (2021). The atmospheric drag is the biggest perturbation effect for LEO satellites. The density model of the atmosphere is relevant for the atmospheric drag calculation which strongly depends on the solar activity. The density is calculated using the JB2008 atmosphere model. In addition, the thermospheric winds are computed based on the Horizontal Wind Model 1993 which are required for the calculation of the relative velocity. The drag coefficient is considered as constant. The second largest effect is the solar radiation pressure for LEO satellites and is the result of the absorption or reflection of photons from the Sun. It depends on the distance to the Sun, the Sun direction, the geometry and optical properties of the satellite surface. The Earth albedo is the radiation reflected by the Earth. Furthermore, there is thermal radiation of the Earth's surface and atmosphere. The thermal radiation pressure is a secondary effect which is caused by the thermal heating of the satellite surface due to the radiation. In Figure 3.3 the non-gravitational forces acting on the satellite for two different altitudes of 303 km and 462 km are illustrated over the time period of one day. The mass of the satellite is 600.98 kg. A surface model of a GRACE satellite body is used.



(a) $h = 462\,\text{km}$ (b) $h = 303\,\text{km}$

Figure 3.3: Non-gravitational forces of the different effects acting on a GRACE-like shaped satellite body; note the different scaling of the plots

The solar radiation pressure is more dominant for higher orbit altitudes and in the same order of magnitude as the atmospheric drag. The latter one increases strongly from 3×10^{-5} N at 467 km to 1×10^{-3} N at the lower orbit altitude of 303 km. The non-gravitational perturbations acting on the satellite can be reduced by decreasing cross-sectional satellite surface or by increasing the mass of the satellite. In fact, there is the possibility to use a drag-free system which compensates the perturbations.

3.3 Modeling of the Sensor Behavior

This section describes models for the behavior and noise of the main sensors. Some of the performance models are already validated by in orbit operation. However, CAI accelerometers have not been on board of satellite yet. Thus, their behavior models have to be estimated for space applications.
Noise time series are generated using the LTPDA toolbox (Hewitson et al., 2009). The colored noise is generated by the construction of a coloring filter through a fitting procedure to the input model and applying it to white noise. The input model is a one-sided PSD model. The Amplitude Spectral Density (ASD) is the square root of the PSD and is used in the following as it simplifies the interpretation of the graphs.

3.3.1 Classical Electrostatic Accelerometer

The determination of the sensor accuracy in space is not trivial as the several disturbing effects affect the measurements (Gruber et al., 2014a). The GOCE mission was a special case, where the performances could be verified thanks to the existence of several accelerometers on board of the satellite. EAs suffer from their drift in the low frequencies which is shown in the ASD model by the increasing slope with decreasing frequency. The assumption of a $1/f^2$ behavior in low frequencies may be more realistic than a $1/f$ behavior. A big advantage of the EA behavior is the continuous measurement readout. The noise of the GRACE and GRACE-FO accelerometer is simulated using the model according to Darbeheshti et al. (2017) and Kim (2000) :

$$n_{ACC,GRACE-FO}(f) = 10^{-10}\sqrt{1 + \frac{0.005\,\mathrm{Hz}}{f}}\ \ \mathrm{m/s^2/\sqrt{Hz}}. \tag{3.1}$$

The noise of the GOCE accelerometer is modeled using (Touboul et al., 2016; Marque et al., 2010)

$$n_{ACC,GOCE}(f) = 2\ 10^{-12}\sqrt{\left(\frac{0.001\,\mathrm{Hz}}{f}\right)^2 + 1 + \left(\frac{f}{0.1\,\mathrm{Hz}}\right)^4}\ \ \mathrm{m/s^2/\sqrt{Hz}}. \tag{3.2}$$

These models are illustrated in Figure 3.4. Additionally, the Logarithmic frequency resolution axis Amplitude Spectral Density (LASD) of the generated noise time series is plotted. The LASD is a modified version of Welch's method. The LASD method includes an estimation of the optimal frequency resolution for each Fourier frequency on a logarithmic frequency axis (Tröbs & Heinzel, 2006).

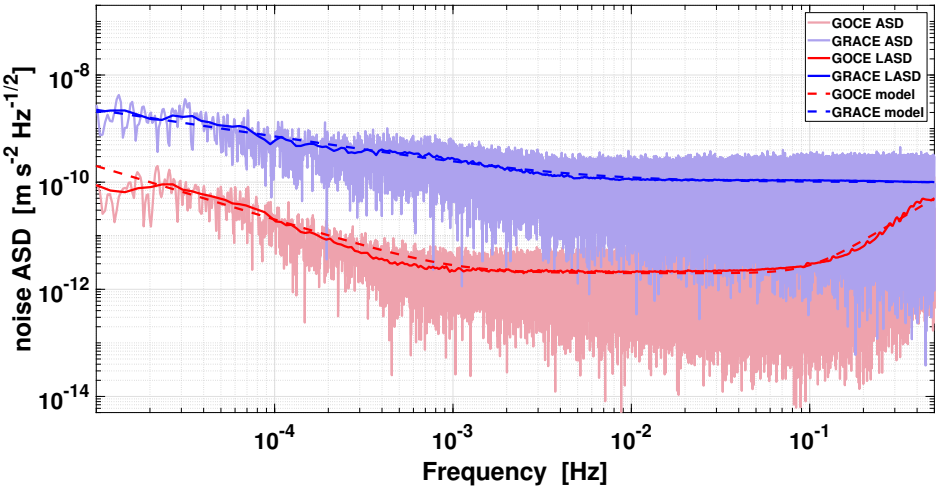


Figure 3.4: Noise performance models of the GOCE and the GRACE-FO accelerometer

3.3.2 Cold Atom Interferometry Accelerometer

In an atom interferometer, cold atoms are in free fall and operate as test mass. Laser pulses in a time interval T are used to split and recombine the atomic wave functions into different momentum states according to the superposition principle (Pereira dos Santos & Landragin, 2007; Schilling et al., 2012). The output phase Φ can be obtained by measuring the relative atomic populations in the output states after recombination. The acceleration a_k during cycle k is obtained from the measured phase Φ_k with the evolution time T as

$$a_k = \frac{\Phi_k}{k_{eff} T^2}, \tag{3.3}$$

where $k_{eff} = |\boldsymbol{k}_{eff}|$ is the norm of the effective wave vector of the laser light used to transfer momentum to the atoms (Kasevich & Chu, 1991). In this study, the duration of one interferometer measurement cycle T_c is assumed with 12 s. It consists of the preparation time T_p, the interferometer duration $2T$ and the detection time T_d:

$$T_c = T_p + 2T + T_d. \tag{3.4}$$

As the sensitivity of the accelerometer to the acceleration varies during one measurement cycle, the transfer function must be taken into account. The phase of the interferometer Φ_k at the k-th cycle is given by (Knabe et al., 2022)

$$\Phi_k = k_{eff} \int_{kT_c}^{(k+1)T_c} g_{a,k}(t) a(t) dt. \tag{3.5}$$

The response function $g_{a,k}$ (cf. Figure 3.5) is given by

$$g_{a,k}(t) = 0 \qquad \text{for } kT_c < t < kT_c + T_p, \tag{3.6}$$
$$g_{a,k}(t) = t - (kT_c + T_p) \qquad \text{for } kT_c + T_p < t < kT_c + T_p + T, \tag{3.7}$$
$$g_{a,k}(t) = kT_c + T_p + 2T - t \qquad \text{for } kT_c + T_p + T < t < kT_c + T_p + 2T, \tag{3.8}$$
$$g_{a,k}(t) = 0 \qquad \text{for } kT_c + T_p + 2T < t < (k+1)T_c. \tag{3.9}$$

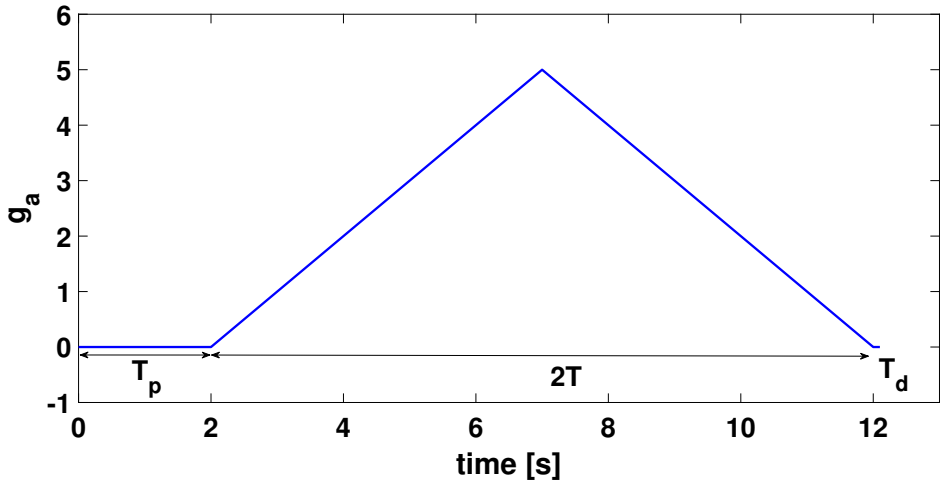


Figure 3.5: Response in the time domain of the transfer function for the phase shift to acceleration conversion

Parameters based on state-of-the-art accelerometers on ground are used to estimate the performance. The assumed number of interfering atoms is $N = 10^6$ and the contrast is $C = 0.8$. The momentum transfer, depending on laser wavelength λ, is $k_{eff} = 4\pi\lambda \approx 1.6\times10^7\,\mathrm{m}^{-1}$ for a two photon Raman transition using rubidium atoms. Microgravity in space is expected to allow for a dramatic increase of the free fall interferometer interrogation time T, which would greatly improve the performances of a CAI. A measurement time of $T = 5\,\mathrm{s}$ and a preparation time of 2 s are introduced for the following calculations. The detection time is neglected as it is only a few tens of ms.
The quantum projection limited phase noise is given by (Knabe et al., 2022)

$$\sigma_\Phi = \sqrt{\frac{T_c}{C^2 N}} = 4.2\,\mathrm{mrad}/\sqrt{\mathrm{Hz}}. \tag{3.10}$$

The sensitivity function of a 3 pulse atom interferometer is

$$H(f) = 16\frac{(2k_{eff})^2}{(2\pi f)^4}\sin^4(2\pi f T/2). \tag{3.11}$$

In order to take into account fluctuations of systematic effects, a $1/f$ flicker floor noise of $\sigma_f = 0.1\,\mathrm{mrad}$ is imposed. The acceleration PSD can then be expressed as (cf. Figure 3.6)

$$S_a^2(f) = (2\sigma_\Phi^2 + 2\ \ln(2)\sigma_f^2/f)/H(f). \tag{3.12}$$

This model is used in the following to estimate the performances of a CAI accelerometer in a satellite.
The sensitivity function $H(f)$ shows an increasing slope in the frequencies higher than 0.083 Hz, as the interferometer cycle time is 12 s. The function $H(f)$ becomes zero for certain values. Therefore, the noise ASD is additionally estimated with another method for higher frequencies. Noise time series are filtered in the time domain using the response function of an atom interferometer. The result is given in Figure 3.7.

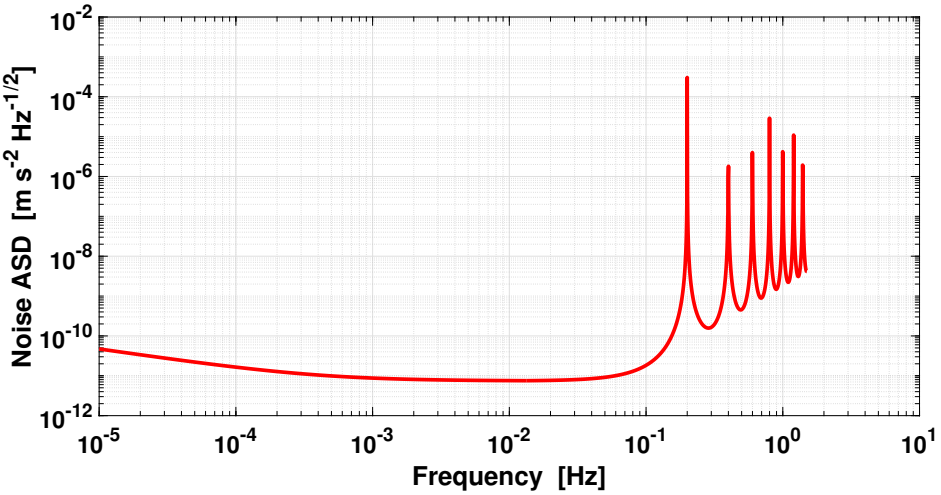


Figure 3.6: Anticipated ASD of a space CAI accelerometer noise

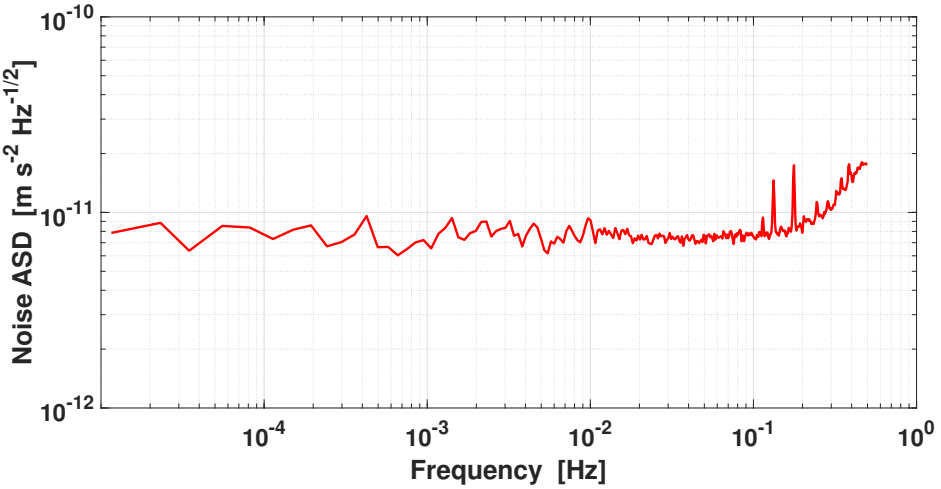


Figure 3.7: Anticipated ASD of a space CAI accelerometer noise filtered with the response function in the time domain

Combination of measurements of an electrostatic accelerometer and an atom interferometer

Measurements of the two sensors, the EA and the CAI accelerometer, need to be combined. This hybridization has to consider the quality of the different measurements. CAI measurements are more accurate in lower frequency bands. In contrast, the electrostatic measurements are performing better in higher frequencies. A benefiting combination can be achieved by low-pass and high-pass filtering. The combination is illustrated in Figure 3.8. Another approach for the combination is a Kalman filter (HosseiniArani et al., 2022).

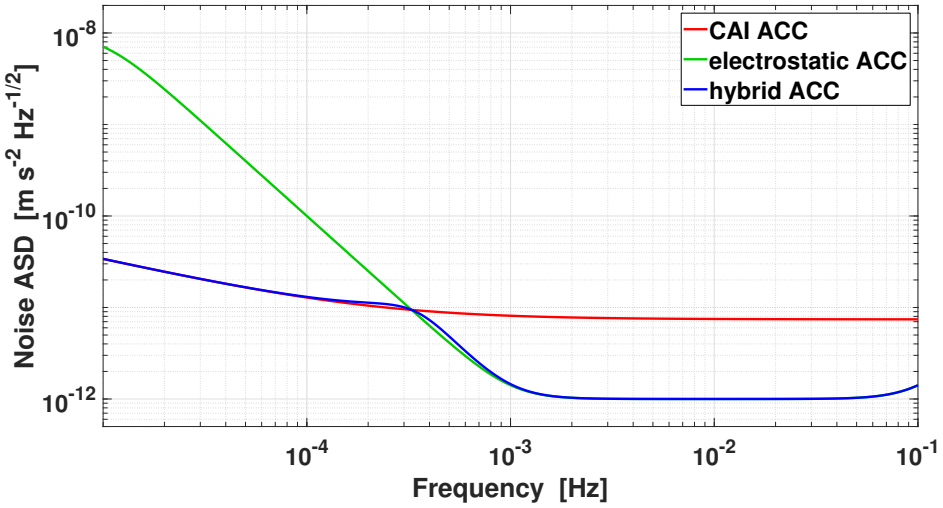


Figure 3.8: Model of a hybrid accelerometer

3.3.3 Ranging Measurement Instruments

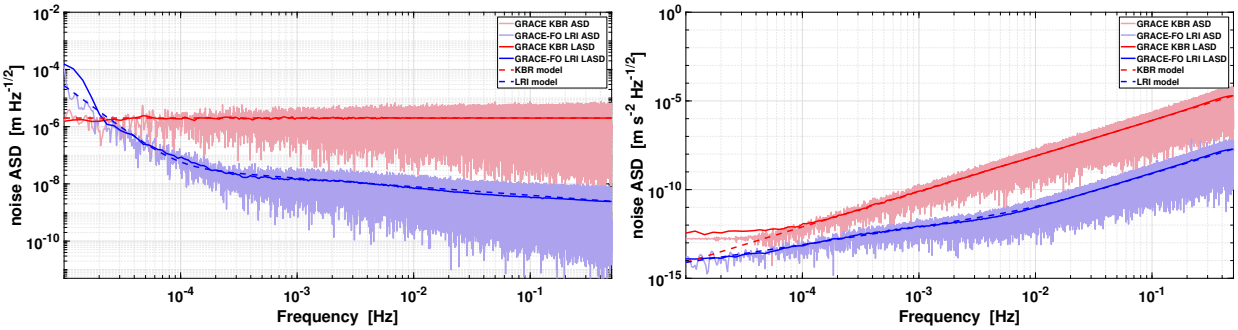
Range measurements between two satellites in the low-low satellite-to-satellite mode are simulated for two different instruments: KBR and LRI. The KBR instrument is on board of GRACE and GRACE-FO. Its noise is modeled using (Frommknecht et al., 2006)

$$n_{KBR,GRACE} = 2\,\mu\mathrm{m}/\sqrt{\mathrm{Hz}}. \tag{3.13}$$

The LRI instrument is currently demonstrated on GRACE-FO. The first approximation of the instrument performance by Abich et al. (2019) is used as noise model:

$$n_{LRI,GRACE-FO}(f) = 2 \times 10^{-9} f^{-0.003} \left(\frac{3 \times 10^{-7}}{f}\right)^3 \ \mathrm{m}/\sqrt{\mathrm{Hz}}. \tag{3.14}$$

The noise models of the two instruments with the ASD and the LASD of the generated noise time series are presented in Figure 3.9. Figure 3.9 (a) shows the noise of the ranging measurements and Figure 3.9 (b) the noise in terms of accelerations which is obtained by the multiplication by the factor $(2\pi f)^2$ and used in the simulation process.



(a) Ranging measurement noise

(b) Ranging noise converted to accelerations

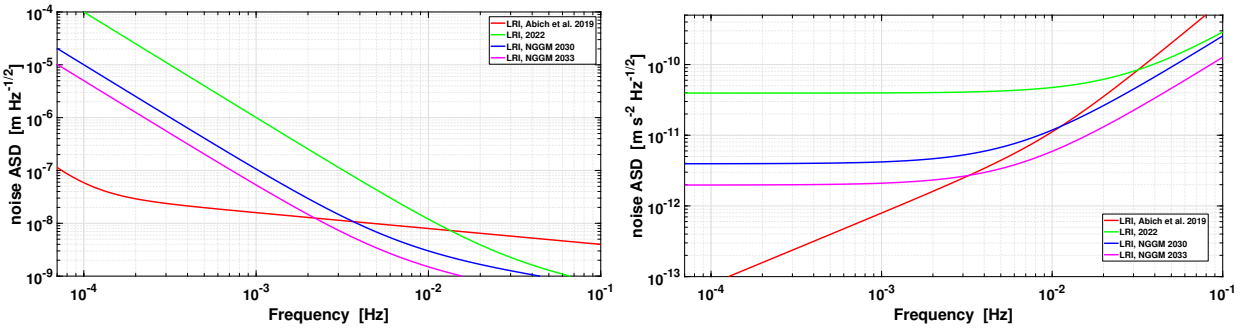
Figure 3.9: Noise performance models of the KBR instrument and the LRI instrument

In Figure 3.10 a new model for the LRI performance in GRACE-FO with the state of knowledge from 2022 and expected improvements for NGGM in 2030 and after 2033 are given (V. Müller, personal communication, October 2022). The corresponding ASD models are denoted in the equations (3.15), (3.16) and (3.17), respectively. The noise models depend on the inter-satellite distance L which is assumed with 200 km in Figure 3.10.

$$n_{LRI,GRACE-FO} = \frac{L \times 1 \times 10^{-15}}{\sqrt{f}} + \frac{1 \times 10^{-12}}{f^2} \ \mathrm{m}/\sqrt{\mathrm{Hz}} \tag{3.15}$$

$$n_{LRI,NGGM2030} = \frac{L \times 1 \times 10^{-15}}{\sqrt{f}} + \frac{1 \times 10^{-13}}{f^2} \ \mathrm{m}/\sqrt{\mathrm{Hz}} \tag{3.16}$$

$$n_{LRI,NGGM2033} = \frac{L \times 5 \times 10^{-16}}{\sqrt{f}} + \frac{5 \times 10^{-14}}{f^2} \ \mathrm{m}/\sqrt{\mathrm{Hz}} \tag{3.17}$$



(a) Ranging measurement noise

(b) Ranging measurement noise converted to accelerations

Figure 3.10: Different noise performance models of the LRI instrument and expectations for the future

3.4 Modeling of Control System Behavior

3.4.1 Drag-free Control

Drag compensation prevents orbit decay and saturation of accelerometers. Drag compensation is also called drag-free control in this thesis. The mission GOCE was the first gravity satellite mission with a drag-free control system, which was based on disturbance rejection. These disturbances are non-gravitational accelerations acting on the satellite. In this section, the GOCE drag-free control system and its model in the simulation environment is described. Furthermore, NGGM drag-free control is addressed.
The components of a control system are sensors and actuators. The actuator of the GOCE drag-free system is an ion propulsion assembly (Romanazzo et al., 2011). The drag control systems needs to be optimized for the specific satellite mission. One crucial factor is the orbit altitude. The magnitude of the non-gravitational accelerations in along-track direction

changes significantly with the orbit altitude. The atmospheric density depends on the solar activity. The control system has to cope with different solar activities and thus with different atmospheric drag magnitudes.
Hence, the simulated system performance strongly depends on sensor and actuator models. The sensor is in this case the accelerometer model, described in section 3.3.1. The flowchart (Figure 3.11) gives an overview of the modeled drag-free control system.

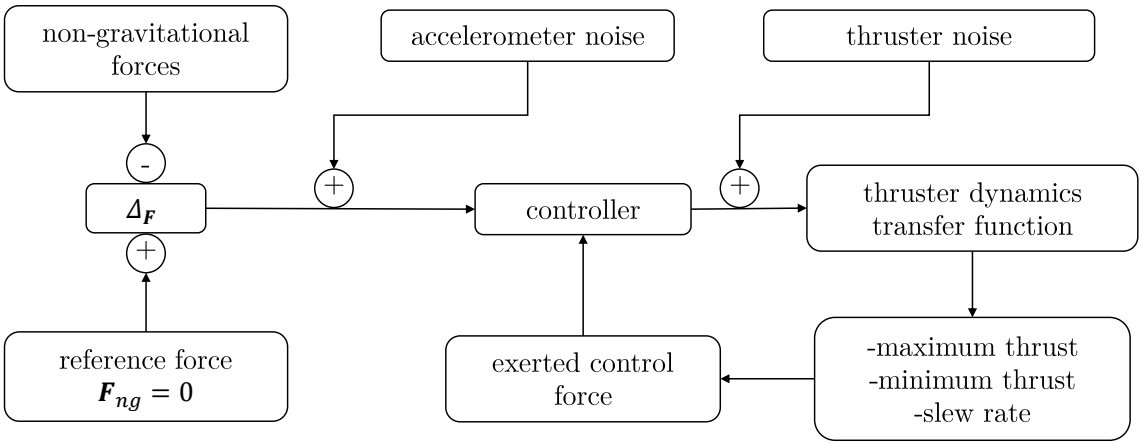


Figure 3.11: Flowchart of the drag-free control system

In Canuto et al. (2018) the thruster behavior is described by a transfer function. The control force, which is actuated by the thruster, is given by

$$F_{thr}(f) = \frac{e^{-f\delta_t}}{f^2 + 2\zeta_t\omega_t f + \omega_t^2}(F_{ref}(f) + n_{thr}(f)), \tag{3.18}$$

where the parameters of the transfer function are the natural frequency ω_t, the damping ratio ζ_t and the delay δ_t. Additionally, the control force depends on the thruster noise n_{thr} and the reference force F_{ref}. The parameters of the GOCE mission are specified in Canuto et al. (2018) and given in Table 3.1.
The thruster noise depends on the force which the thruster executes. The GOCE thruster noise is between $1\,\mu N/\sqrt{Hz}$ and $10\,\mu N/\sqrt{Hz}$ (Allasio et al., 2010). The thruster noise is simulated using a model for the PSD (Canuto et al., 2010):

$$n_{thr}^2 = \left(\left(\frac{0.005}{f}\right)^2 + 1\right)(10^{-6})^2 \ \ N^2\,Hz^{-1} \tag{3.19}$$

and is illustrated in Figure 3.12. Besides, the maximum and minimum thrust and the possible rate of change have to be considered. The thruster of the GOCE mission had a maximum thrust level of 21 mN, a minimum thrust level of 0.6 mN and a possible change rate of $2.5\,mN\,s^{-1}$ (Romanazzo et al., 2011). These instrument restrictions are included as constraints of the model.

Table 3.1: Transfer function parameters of the thrusters of the GOCE mission

delay δ_t	natural frequency ω_t	damping ratio ζ_t
0.1 s	18 rad s^{-1}	1

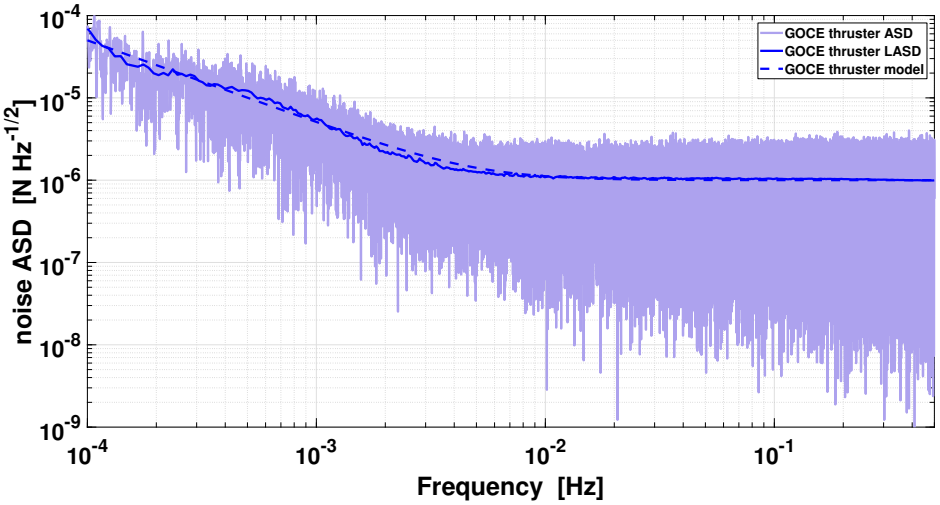


Figure 3.12: ASD of thruster noise

In literature, there are two widely-used approaches for a drag-free control system: the H_∞ methodology and simple Proportional-Integral-Derivative (PID) strategies (Canuto & Andreis, 2003). A PID controller, which is included in the model of this thesis, consists of an proportional, an integral and a derivative part. This type of controller is robust in the performance. The combination of the three different time behaviors produces the controller output $c(t)$:

$$c(t) = K_p e(t) + K_i \int e(t)dt + K_d \frac{de}{dt}, \tag{3.20}$$

where K_p is the proportional gain, K_i is the integral gain, K_d is the derivative gain, e is the difference between the desired and the actual output. The error signal is defined as the difference between the reference and the actual signal and acts as the input of the controller, which computes the derivative and the integral of the error signal with respect to time.

In Massotti et al. (2020) alternative drag compensation concepts are discussed. One promising technology is the use of two different thruster types: Drag Control Thruster and Fine Control Thruster. Ion thrusters of these types already approved their flight heritage in the GOCE mission, but the GOCE thrusters are designed for an altitude of 250 km. Lower thruster ranges are required as for future satellite missions higher altitudes are intended. Candidates for the Fine Control Thruster already exist. Miniaturized Gridded Ion Engines of Radio-Frequency type (mini-RIT) have been tested and demonstrated thrust capabilities in the range between 50 µN to 500 µN and 10 µN to 100 µN (Massotti et al., 2013). In Reissner et al. (2014) the performance of Field Emission Electric Propulsion (FEEP) thruster technology is characterized. Haagmans et al. (2020) define the required thruster range for

future satellite missions from 50 µN to 2 mN. This wide thrust range is needed because of the variability of the thermosphere neutral density within one solar cycle by a factor of ten. One option to ensure the energy supply are deployable solar arrays (Haagmans et al., 2020).

Table 3.2: Characterization of the two thruster types

Thruster type	Thrust range	MBW	Utilization
Drag Control Thruster	50 µN to 6 mN (10 mN for orbit operations)	1 mHz to 100 mHz	drag compensation and orbit maintenance
Fine Control Thruster	50 µN to 1 mN	1 mHz to 100 mHz	cross-track and radial drag compensation and 3-axis torques for angular drag control

3.4.2 Attitude Control

The attitude determination and control must be taken into account in the study of future satellite mission. The experience of previous satellite mission is an appropriate assumption for simulation studies. The requirements depend on the mission design. In case of a ll-SST mission, like GRACE and GRACE-FO, the pointing between the two satellites is important due to the range measurements. The requirements for the attitude control are less stringent for missions with only one satellite like GOCE.

The attitude control system of GOCE worked uniquely with magnetic torquers. This is reflected in the attitude errors as they show the periodicity imposed by the magnetic field and the orbit period (Steiger et al., 2014). The aerodynamic forces constitute an important element for attitude control. The controllability is limited because the magnetic torquers can not produce a torque along the direction of the Earth's magnetic field. Therefore, only the pitch axis can be controlled permanently. A controllability with a time horizon of half an orbit is guaranteed for the roll and yaw axes (Romanazzo et al., 2011). The attitude error in pitch direction is below 10 mrad. The two other directions show an error up to 100 mrad (Sechi et al., 2011). Furthermore, attitude control is required to minimize the command force of the drag-free system. This is done by keeping the small front of the satellite perpendicular to the flight direction. This minimizes the effective area and consequently the fuel consumption.
Additionally to the magnetic torquers, cold gas thruster are used as actuators in GRACE and GRACE-FO. The GRACE-FO mission has an attitude error of a few mrad which is sufficient for the microwave ranging system due to its wide beam and receive field of view. Laser interferometry requires 100 µrad pointing accuracy which is achieved by internal pointing control using a movable mirror in the instrument.

Different attitude control systems are implemented in the XHPS software. One possibility is the quaternion feedback control law. The controller aims driving ω to zero and $\delta_{\mathbf{q}}$ to

the identity quaternion (Markley & Crassidis, 2014). The control torque $\mathbf{L}$ is given by

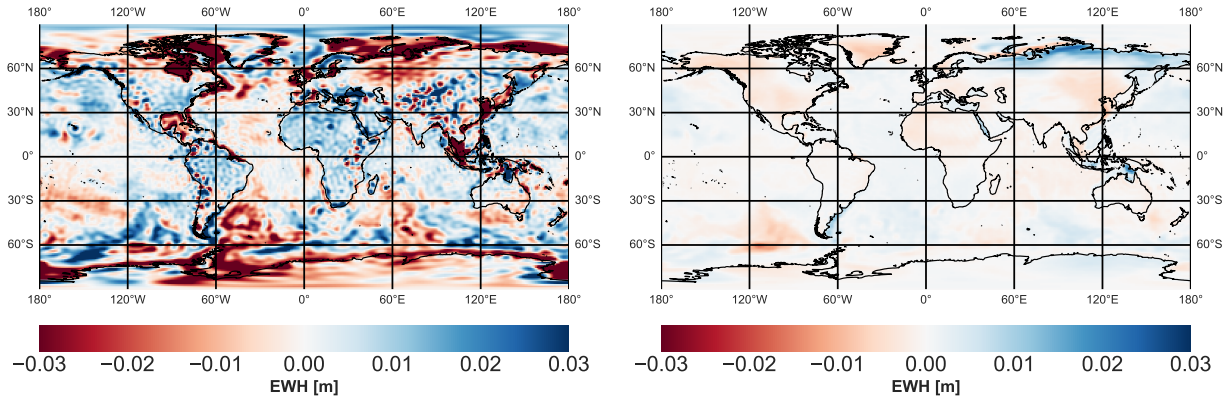
$$\mathbf{L} = -k_p \delta_{\mathbf{q}} - k_d \omega, \tag{3.21}$$

where k_p and k_d are the positive control gains. The difference between the target and actual quaternion is $\delta_{\mathbf{q}}$. The target quaternion can be defined, as an example, in such a way that the satellite points in the direction of the velocity vector. This leads to a minimum effective area for the atmospheric drag which minimizes the non-gravitational accelerations due to atmospheric drag. Using this method results in a short computation time but the behavior of the actuators and sensor is not considered.
A reference attitude has to be given to the attitude control system (cf. appendix A.2). In the case of GOCE, the x-axis should point in flight direction, which is the direction of the velocity vector, the z-axis in nadir direction and the y-axis is perpendicular to these.
The reference attitude for GRACE and GRACE-FO reads as follows: the x-axis has to point in the direction of the other satellite and the z-axis has to point in the nadir direction (cf. appendix A.2). The detailed attitude simulation of GRACE is composed of two steps. The first step is a precomputation with ideal attitude control. In the second step, one satellite is controlled with respect to the precomputed position of the other one considering an attitude control system model.
The attitude control model for GRACE-FO is implemented in XHPS using a Kalman filter. The star camera noise model of Kim (2000) is used which is 9×10^{-6} rad for the roll direction and 5×10^{-5} rad for the pitch and the yaw directions. The controller limits for the activation of the thrusters are 2.5 mrad for the roll axis and 0.25 mrad for pitch and yaw axis as the latter ones have to be controlled more accurately.

3.5 Time-variable Background Modeling Errors

The time-variable background modeling is out of the scope of this work. However, the error due to time-variable background modeling is one limiting factor in the gravity field recovery. Variations of water masses in the soil and sub-surface aquifers and continental ice-sheets are quantified with the monthly gravity field solutions. In contrast, mass redistribution in atmosphere and ocean are characterized by much higher frequencies (Dobslaw et al., 2016). Consequently, these time-variable atmosphere and ocean modeling errors need to be considered. Models for Atmosphere and Ocean De-aliasing (AOD) and ocean-tide errors are included. The differences between various products or some percentage of a product are considered as model errors.
The product Atmosphere and Ocean De-Aliasing Level-1B (AOD1B) provides a priori information about temporal variations in the Earth's gravity field caused by global mass variability in atmosphere and ocean (Dobslaw et al., 2017). In the simulation, the time-averaged AOD1B product (GAC) is used which is the monthly average of the coefficients representing the combined mass anomalies of atmosphere and ocean. Releases 5 (RL5) and 6 (RL6) are considered. In Figure 3.13, the difference between the AOD models RL5 and RL6 as well as 10 % of RL6 are represented in the space domain as an example of the month April 2006. The Figure shows that the considered AOD modeling errors range up to 3 cm in terms of EWH. The difference between the models results in a larger error than 10 % of RL6.

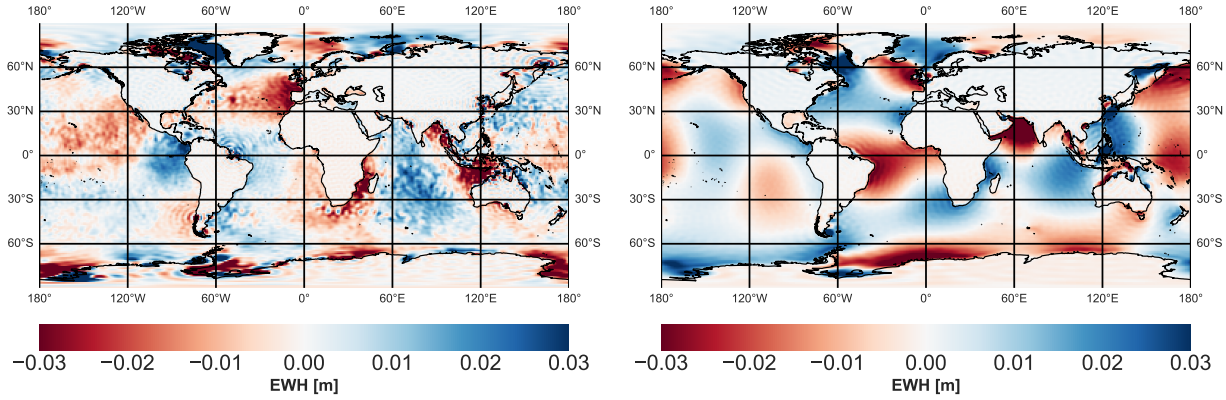
In Dobslaw et al. (2016) another approximation of errors at large spatial scales representing global numerical atmosphere and ocean models is discussed. The AOD model errors are mainly caused by the underlying geophysical models (Dobslaw et al., 2016). The atmosphere and ocean error model (AOerr) is based on the analysis of pressure anomaly data from four atmospheric and oceanic models. The AOerr product is represented in SH coefficients up degree and order 180 with a sampling interval of 6 hours. The AOerr variability is stated with 5 hPa, which is equivalent to a change of 5 cm in water height.



(a) Difference between RL5 and RL6

(b) 10 % of RL6

Figure 3.13: Models for AOD error for April 2006



(a) Difference between EOT11a and FES2014b

(b) 10 % of FES2014b

Figure 3.14: Models for ocean-tide error for April 2006

The ocean tide models are based on the analysis of satellite altimetry data and hydrodynamic models. The products EOT11a (Savcenko & Bosch, 2012) and FES2014b (Carrère et al., 2016; Lyard et al., 2021) are used in this study. Data sets and routines from Mayer-Gürr et al. (2012) and Mayer-Gürr et al. (2021) are used for representation of the ocean tide models in spherical harmonic coefficients. The scaling of monthly averages or the differences of monthly averages between EOT11a and FES2014b are considered. The spatial plot of the

difference between the two products and 10 % scaling of FES2014b is given in Figure 3.14 for April 2006. The ocean-tide modeling errors are in the same order of magnitude as the AOD modeling errors.
The corresponding range acceleration noise time series are calculated based on the SH coefficients representing AOD and ocean-tide errors and the satellite orbit data. In Figure 3.15, the ASD of the different error assumptions for AOD and ocean tides in terms of range accelerations are plotted. Hence, it can be recognized that the modeling errors in frequencies important for the gravity field recovery are of significant order of magnitude.

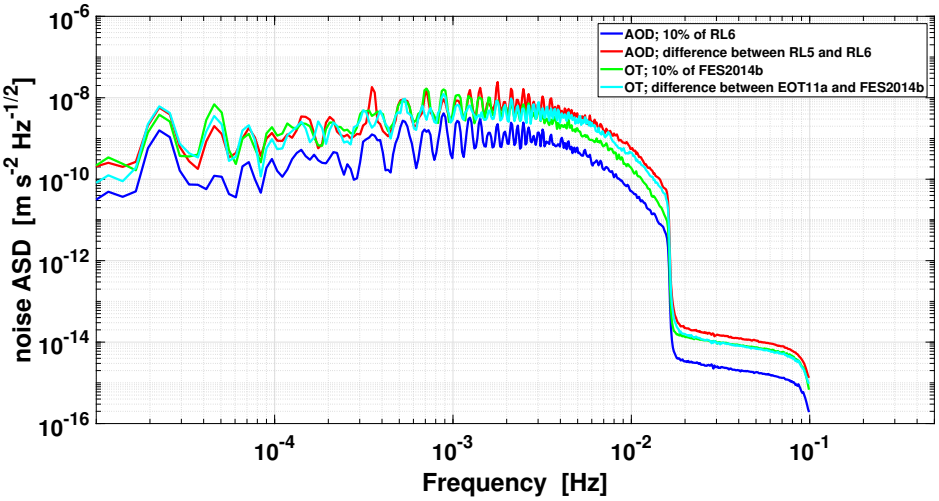


Figure 3.15: ASD of different assumptions for AOD error and ocean-tide error

3.6 Gravity Field Recovery

Global gravity field models are recovered from the synthesized noisy observations. The central unknown parameters are the spherical harmonic coefficients of the gravity field model. The coefficient differences between reference and estimated gravity field give valuable insights. This chapter includes, on the one hand, the recovery of the gravity field solution from range accelerations (section 3.6.2) and, on the other hand, the gravity field recovery from gradiometry measurements (section 3.6.3). Both are calculated with a least-squares adjustment according to the Gauss-Markov model. Therefore, a rough overview of the procedure is given in section 3.6.1. In section 3.6.4, the method to estimate a combined solution from range accelerations and gradients is presented.

3.6.1 Least-squares Adjustment

The spherical harmonic coefficients S_{nm} and C_{nm} are estimated with a least-squares adjustment. The reference gravity field model is Eigen-6c4 (Förste et al., 2014). The basic formulation of the Gauss-Markov model is:

$$\boldsymbol{l} + \boldsymbol{v} = \boldsymbol{A}\boldsymbol{x}, \tag{3.22}$$

where $\boldsymbol{l}$ is the observation vector with the dimension of $s \times 1$ and $\boldsymbol{v}$ is the observation error vector with dimension $s \times 1$, $\boldsymbol{x}$ is vector of unknown parameters with dimension $u \times 1$ and $\boldsymbol{A}$ is the design matrix with dimension $s \times u$. The estimated parameters $\hat{\boldsymbol{x}}$ are derived by

$$\hat{\boldsymbol{x}} = (\boldsymbol{A}^T \boldsymbol{P} \boldsymbol{A})^{-1} \boldsymbol{A}^T \boldsymbol{P} \boldsymbol{l}. \tag{3.23}$$

The term $\boldsymbol{A}^T \boldsymbol{P} \boldsymbol{A}$ is the normal equation matrix $\boldsymbol{N}$. The right-hand side vector $\boldsymbol{w}$ is $\boldsymbol{A}^T \boldsymbol{P} \boldsymbol{l}$. The matrix $\boldsymbol{P}$ is the weighting matrix which is obtained from the stochastic model:

$$\boldsymbol{\Sigma}_{ll} = \sigma_0^2 \boldsymbol{Q}_{ll} = \sigma_0^2 \boldsymbol{P}^{-1}. \tag{3.24}$$

The least-squares adjustment is initially based on the assumption of white noise. However, the observations contain colored noise and so an adequate error model is needed. Therefore, the variance-covariance matrix $\boldsymbol{\Sigma}_{ll}$ is used to down-weight and de-correlate the observations. It is assembled from the post-fit residuals of the whole observation period. The auto-covariance vector $\boldsymbol{r}$ of the observations is calculated from the post-fit residuals. The biased estimation of the auto-covariance r_i using the post-fit residuals v_n is given by

$$r_i = \frac{1}{N} \sum_{n=0}^{N-1-|i|} v_n v_{n+1} \tag{3.25}$$

which is recommended by Koch et al. (2010). The variance-covariance matrix is built using the auto-covariance vector:

$$\boldsymbol{\Sigma}_{ll} = \begin{bmatrix} r_0 & r_1 & r_2 & \cdots & r_{N-1} \\ r_1 & r_0 & r_1 & \cdots & r_{N-2} \\ r_2 & r_1 & r_0 & \cdots & r_{N-3} \\ \vdots & \vdots & \vdots & \ddots & \vdots \\ r_{N-1} & r_{N-2} & r_{N-3} & \cdots & r_0 \end{bmatrix} \tag{3.26}$$

which results in the symmetric, positive definite Toeplitz matrix. The Toeplitz matrix can be decomposed by Cholesky approach. The obtained triangular matrix is finally used for de-correlating the design matrix and the observation vector. The triangular matrix is called de-correlation filter (Wu, 2016).

The adjusted residuals $\hat{\boldsymbol{v}}$ can be calculated after the parameter estimation:

$$\hat{\boldsymbol{v}} = \boldsymbol{A} \hat{\boldsymbol{x}} - \boldsymbol{l}, \tag{3.27}$$

The empirical variance of the unit weight follows with:

$$\hat{\sigma}_0^2 = \frac{\hat{\boldsymbol{v}}^T \boldsymbol{P} \hat{\boldsymbol{v}}}{s - u}. \tag{3.28}$$

In practice, the empirical variance of the unit weight $\hat{\sigma}_0^2$ is actually estimated according to Koch (1999) using

$$\hat{\sigma}_0^2 = \frac{\boldsymbol{l}^T \boldsymbol{P} \boldsymbol{l} - \boldsymbol{w}^T \hat{\boldsymbol{x}}}{s - u}. \tag{3.29}$$

in order to avoid recomputation of the design matrix A after the adjustment. The variance-covariance matrix of the estimated coefficients

$$\boldsymbol{\Sigma}_{\hat{\boldsymbol{x}}\hat{\boldsymbol{x}}} = \hat{\sigma}_0^2 \boldsymbol{N}^{-1} \tag{3.30}$$

includes information about the formal errors.

The practical recovery consists of the following steps:

- assembly of the normal matrix $\boldsymbol{N}$ with weighting matrix $\boldsymbol{P}$ as unit matrix,
- inversion of the normal matrix to derive the SH coefficients,
- computation of the residuals $\hat{\boldsymbol{v}}$,
- computation of the variance-covariance matrix $\boldsymbol{\Sigma}_{ll}$ using the residuals,
- assembly of the normal matrix $\boldsymbol{N}$ using the variance-covariance matrix $\boldsymbol{\Sigma}_{ll}$
- inversion of the normal matrix to derive the final SH coefficients and formal errors.

For large data sets, parallel computing is applied for the assembly of the normal matrix in order to reduce the calculation time. This is applied for gravity field recovery with maximum degree and order of 200. The observations are divided into segments and the design matrix $\boldsymbol{A}$ is partitioned in blocks. As a result, the normal matrix $\boldsymbol{N}$ and the matrix $\boldsymbol{w}$ are separately assembled for each segment and afterwards summed up to obtain the complete matrices. The Math Kernel Library is used and the computations are carried out on the cluster system at the Leibniz University of Hanover, Germany.

In the following sections, the assembly of the functional models for range accelerations and gradiometry is described.

3.6.2 Range Accelerations

Several approaches exist for the recovery of the gravity field model from ll-SST observations such as the classical variational approach (Reigber, 1989), the energy balance approach (Jekeli, 1999) or the acceleration approach (Liu, 2008). The acceleration approach links the range accelerations to the gradient of the gravity potential (Weigelt, 2017) and is applied here. It was first tested by Reubelt (2009) for hl-SST.

The range accelerations in LOS direction $\ddot{\rho}$ are:

$$\ddot{\rho} = \ddot{\boldsymbol{r}}_{AB}\, \boldsymbol{e}_{AB} + \dot{\boldsymbol{r}}_{AB}\, \dot{\boldsymbol{e}}_{AB}, \tag{3.31}$$

where $\ddot{\boldsymbol{r}}_{AB} = \ddot{\boldsymbol{r}}_B - \ddot{\boldsymbol{r}}_A$ is the difference of the gradient of the Earth's gravitational potential at the positions of the two satellites A and B. Thus, it provides the link to the gravity field: $\ddot{\boldsymbol{r}}_{AB} = \nabla V_B - \nabla V_A$. The variable $\boldsymbol{e}_{AB}$ is the unit vector of the LOS and $\dot{\boldsymbol{e}}_{AB}$ is its time derivative. The term $\dot{\boldsymbol{r}}_{AB} = \dot{\boldsymbol{r}}_B - \dot{\boldsymbol{r}}_A$ is the velocity difference between satellites A and B. The second term $\dot{\boldsymbol{r}}_{AB}\, \dot{\boldsymbol{e}}_{AB}$ is neglected in this study, because no acceleration measurements

are needed for its estimation and the focus is set on the benefit of novel accelerometers. However, the precision of the relative velocity vector limits the solution as it is only measured by GNSS with 0.1 mm/s accuracy (Weigelt, 2017).

The functional model is written as

$$\begin{aligned}\ddot{\rho} &= (\nabla V_B - \nabla V_A)\boldsymbol{e}_{AB} \\ &= (g_{B,x} - g_{A,x})e_x + (g_{B,y} - g_{A,y})e_y + (g_{B,z} - g_{A,z})e_z \\ &= \sum_{n=2}^{N}\sum_{m=0}^{N} \boldsymbol{A}_{\hat{\boldsymbol{x}}_{nm}}\hat{\boldsymbol{x}}_{nm},\end{aligned} \tag{3.32}$$

with the parameter vector elements

$$\hat{\boldsymbol{x}}_{nm} = \{\bar{C}_{nm}, \bar{S}_{nm}\} \tag{3.33}$$

and the design matrix elements

$$\boldsymbol{A}_{\hat{\boldsymbol{x}}_{nm}} = \left(\frac{\partial g_{B,x}}{\partial \hat{\boldsymbol{x}}_{nm}} - \frac{\partial g_{A,x}}{\partial \hat{\boldsymbol{x}}_{nm}}\right) e_x + \left(\frac{\partial g_{B,y}}{\partial \hat{\boldsymbol{x}}_{nm}} - \frac{\partial g_{A,y}}{\partial \hat{\boldsymbol{x}}_{nm}}\right) e_y + \left(\frac{\partial g_{B,z}}{\partial \hat{\boldsymbol{x}}_{nm}} - \frac{\partial g_{A,z}}{\partial \hat{\boldsymbol{x}}_{nm}}\right) e_z. \tag{3.34}$$

In order to validate the de-correlation filter, the results without and with variance-covariance matrix are represented in Figure 3.17 and Figure 3.16. The formal errors and the true errors, which are the coefficients differences between reference and recovered gravity field, are displayed. The iterative results of degree RMS of the geoid height are given in Figure 3.16. The solution converges after two iterations and cumulative geoid error decreases by 0.08 mm. The solutions of iteration 1 (orange line) and iteration 2 (green line) do not differ significantly. Hence, all following simulations in this thesis will be performed with one iteration only. In addition to that, this saves valuable computation time on the cluster system.

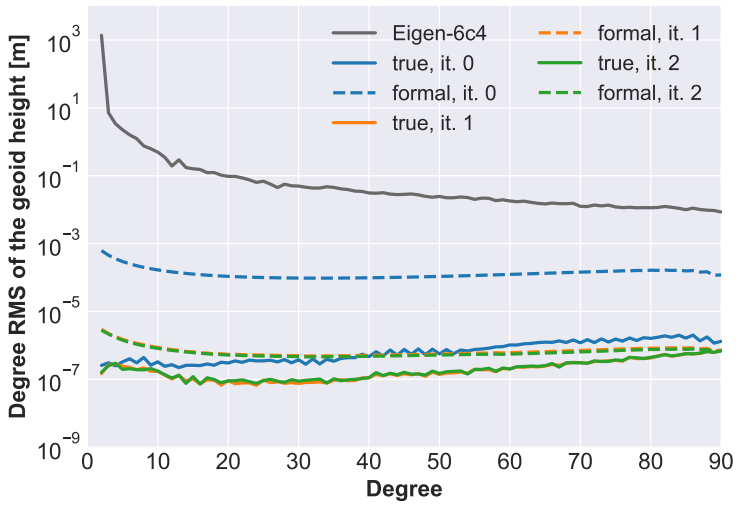
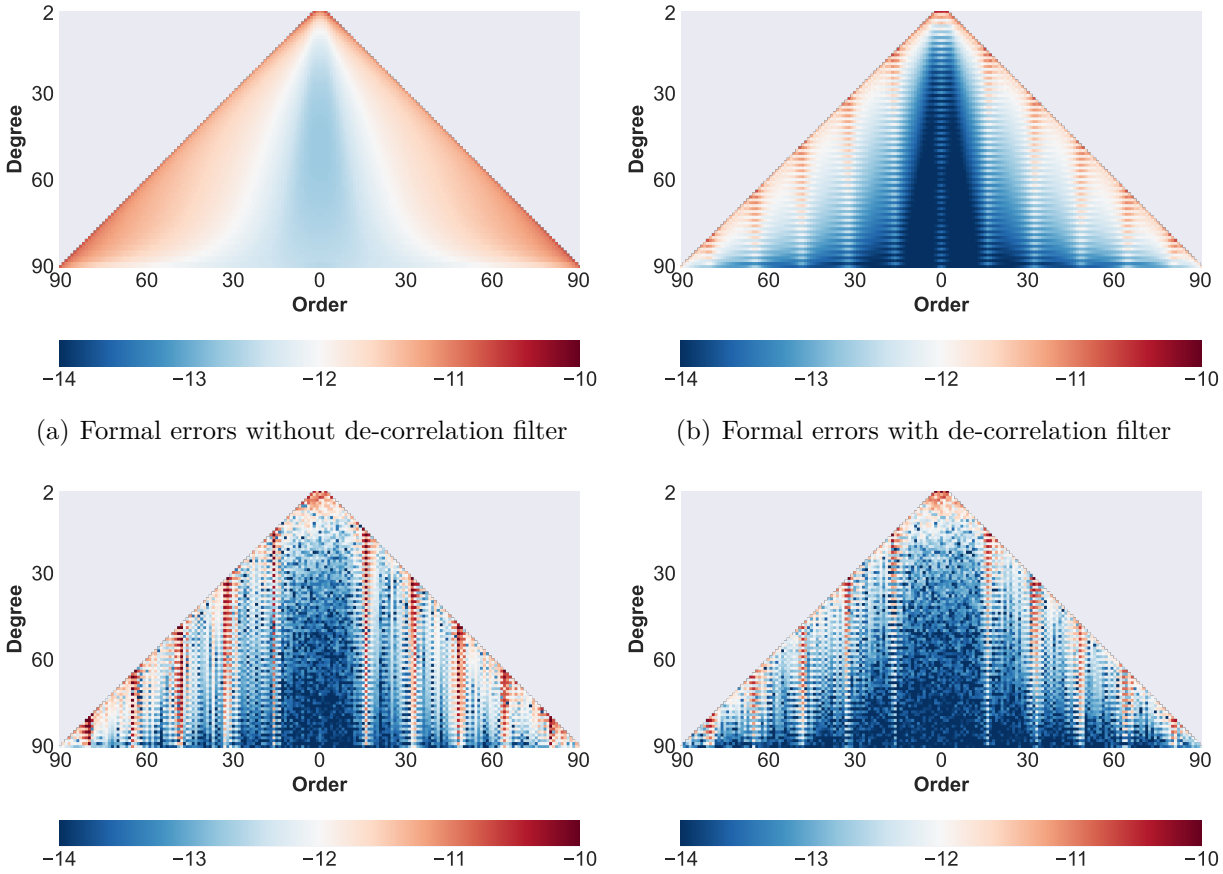


Figure 3.16: Degree RMS of the coefficient differences between recovered gravity and reference gravity and formal errors for iteration results; parameters: altitude of 246 km, hybrid accelerometer, KBR noise

Figure 3.17 shows the results for each coefficient as pyramid representation on a logarithm scale. The reduction of the true errors and the striping effects is illustrated. After applying the de-correlation filter, the formal errors are consistent with the true errors.



(a) Formal errors without de-correlation filter

(b) Formal errors with de-correlation filter

(c) True errors without de-correlation filter

(d) True errors with de-correlation filter

Figure 3.17: Evaluation of the de-correlation filter by coefficient differences between recovered and reference gravity field as pyramid representation (logarithm scale); parameters: altitude of 246 km, EA noise at the level of $1 \times 10^{-10}\,\mathrm{m/s^2}$, LRI noise

3.6.3 Gradiometry

The principle of gradiometry is the measurement of the second derivative of the gravitational potential. The main instrument is the gradiometer which consists of several accelerometers in a specific configuration. The measurements are acceleration differences along a short baseline. The GOCE gradiometer is composed of six accelerometers which are arranged pairwise with a baseline length of 0.5 m. One pair forms one gradiometer arm. All three gradiometer arms are orthogonal to each other. The observed gradient tensor $\boldsymbol{\Gamma}$ contains the gravity gradient tensor $\boldsymbol{V}$, the centrifugal part $\boldsymbol{\Omega\Omega}$ and the Euler part $\dot{\boldsymbol{\Omega}}$ (Rummel, 1986):

$$\boldsymbol{\Gamma} = \boldsymbol{V} + \boldsymbol{\Omega\Omega} + \dot{\boldsymbol{\Omega}}, \tag{3.35}$$

with

$$\boldsymbol{V} = \begin{bmatrix} V_{xx} & V_{xy} & V_{xz} \\ V_{xy} & V_{yy} & V_{yz} \\ V_{xz} & V_{yz} & V_{zz} \end{bmatrix}, \; \boldsymbol{\Omega} = \begin{bmatrix} 0 & -\omega_z & \omega_y \\ \omega_z & 0 & -\omega_x \\ -\omega_y & \omega_x & 0 \end{bmatrix}, \; \dot{\boldsymbol{\Omega}} = \begin{bmatrix} 0 & -\dot{\omega}_z & \dot{\omega}_y \\ \dot{\omega}_z & 0 & -\dot{\omega}_x \\ -\dot{\omega}_y & \dot{\omega}_x & 0 \end{bmatrix}. \tag{3.36}$$

Differential mode ($\boldsymbol{a}_{dm,ij}$) and common mode ($\boldsymbol{a}_{cm,ij}$) accelerations are calculated from the acceleration measurements:

$$\boldsymbol{a}_{dm,ij} = \frac{1}{2}(\boldsymbol{a}_i - \boldsymbol{a}_j), \qquad \boldsymbol{a}_{cm,ij} = \frac{1}{2}(\boldsymbol{a}_i + \boldsymbol{a}_j), \tag{3.37}$$

where i and j are the accelerometer indices of one pair. The diagonal gravity gradient components are obtained by the measured accelerations differences and angular velocities:

$$V_{xx} = -2\frac{a_{dm,14,x}}{L_x} - \omega_y^2 - \omega_z^2 \tag{3.38}$$

$$V_{yy} = -2\frac{a_{dm,25,y}}{L_y} - \omega_x^2 - \omega_z^2, \tag{3.39}$$

$$V_{zz} = -2\frac{a_{dm,36,z}}{L_z} - \omega_x^2 - \omega_y^2. \tag{3.40}$$

For the recovery of the gravity field coefficients a direct, time-wise approach is applied. The coefficients are estimated in an adjustment including a stochastic model which is described in section 3.6.1. The required observations for the recovery are the gravity gradients, the attitude quaternions and the satellite positions. The gravity gradients are the second-order derivatives of the gravitational potential along the axes $k, l \in \{x, y, z\}$ in the Gradiometer Reference Frame (GRF):

$$V_{kl} = \frac{\partial^2 V}{\partial k \partial l}. \tag{3.41}$$

The functional model is given by

$$V_{kl} = V_{kl}^0 + \sum_{n=2}^{N} \sum_{m=0}^{N} \boldsymbol{A}_{\hat{x}_{nm}} \hat{\boldsymbol{x}}_{nm}, \tag{3.42}$$

with the initial gradients V_{kl}^0 computed from the normal gravity field model, the parameter vector elements

$$\hat{\boldsymbol{x}}_{nm} = \{\bar{C}_{nm}, \bar{S}_{nm}\} \tag{3.43}$$

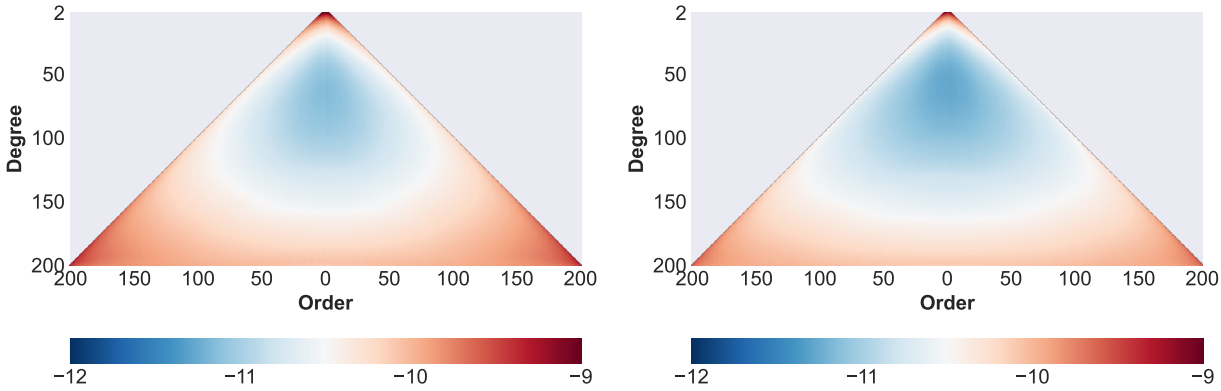
and the design matrix elements

$$\boldsymbol{A}_{\hat{\boldsymbol{x}}_{nm}} = \boldsymbol{R}_{LNORF}^{GRF} \frac{\partial V_{kl}^{LNORF}}{\partial \hat{\boldsymbol{x}}_{nm}} (\boldsymbol{R}_{LNORF}^{GRF})^T. \tag{3.44}$$

The gradients are measured in GRF. Consequently, the base functions are transformed from Local North-Oriented Reference Frame (LNORF) to GRF using the rotation matrix

$\boldsymbol{R}^{GRF}_{LNORF}$. For the partial derivatives and further details the reader is referred to Wu (2016). The definition of the reference frames is given in appendix A.1.

The stochastic model is validated for the gradiometry case. The two-dimensional, formal errors and the coefficient differences are shown in Figure 3.18 before and after applying the de-correlation filter. The formal errors and the true errors are consistent. The true errors are reduced when applying the de-correlation filter. The one-dimensional errors are illustrated in Figure 3.19 as degree RMS of the geoid height. Figure 3.19 shows the improvement after the first iteration. This is also reflected in the cumulative geoid error which is reduced by 2.93 cm.



(a) Formal errors without de-correlation filter

(b) Formal errors with de-correlation filter

(c) True errors without de-correlation filter

(d) True errors with de-correlation filter

Figure 3.18: Evaluation of the de-correlation filter by coefficient differences between recovered and reference gravity field as pyramid representation (logarithm scale); parameters: gradiometry component V_{yy}, altitude of 246 km, EA noise at a level of $2 \times 10^{-12}\,\mathrm{m/s^2}$, $L_y = 0.5\,\mathrm{m}$

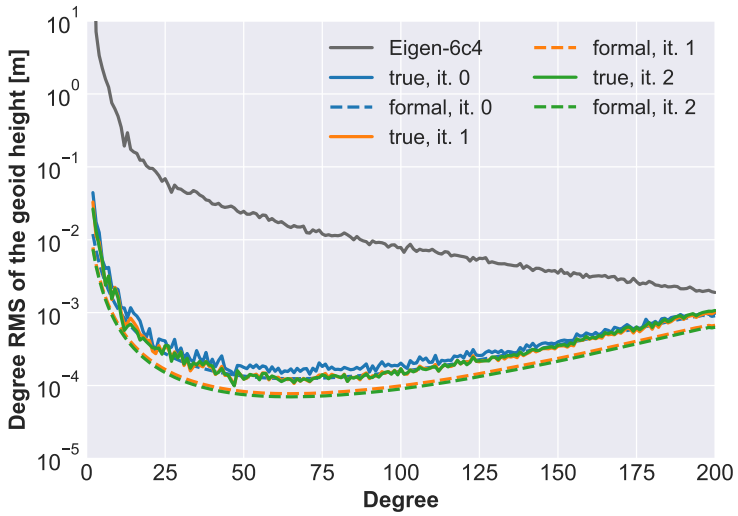


Figure 3.19: Degree RMS of the coefficient differences between recovered gravity and reference gravity and formal errors for iteration results; parameters: gradiometry component V_{yy}, altitude of 246 km, electrostatic accelerometer noise at a level $2 \times 10^{-12}\,\mathrm{m/s^2}$, $L_y = 0.5\,\mathrm{m}$

3.6.4 Combination of Range Accelerations and Gravity Gradients

The observation groups are combined by the summation of the normal equation system. The corresponding elements of the left-hand side and the right-hand side of the normal equations systems are added and weighting factors are applied. The variance component estimation for combining different groups of observations is described in Koch and Kusche (2001). In this study the posterior variances of the individual adjustments are used. Cross-track gravity gradients V_{yy} and range acceleration from ll-SST are combined as follows:

$$\hat{\boldsymbol{x}} = \left(\frac{1}{\sigma^2_{ll-SST}} \boldsymbol{N}_{ll-SST} + \frac{1}{\sigma^2_{Vyy}} \boldsymbol{N}_{Vyy} \right)^{-1} \left(\frac{1}{\sigma^2_{ll-SST}} \boldsymbol{w}_{ll-SST} + \frac{1}{\sigma^2_{Vyy}} \boldsymbol{w}_{Vyy} \right), \tag{3.45}$$

where σ^2_{ll-SST} and σ^2_{Vyy} are the variance components. The posterior variances of the individual analysis are used as initial values. The variance components are estimated iteratively according to Koch and Kusche (2001). In Figure 3.20 the degree RMS of the coefficient differences of iterative computations are given for two examples. It is shown that the posterior variances of the individual solutions are already good estimates of the variance components (cf. combination, iteration 0 in Figure 3.20). The initial variance components are 0.8063 for the cross-track gradient solution and 0.7145 for the ll-SST solution. The variance component estimation results are 0.9718 and 0.7777 in the first iteration. The estimation converges after two iterations with the variance components of 0.9767 and 0.7684. However, the recovered gravity field coefficients are only affected slightly by the iteration process. Thus, in Figure 3.20 the difference between iteration 0 and iteration 1 is marginally noticeable. However, the cumulative error is reduced from an error of 1.83 cm with the initial variance components to 1.80 cm. The cumulative geoid error of the single ll-SST solution is 3.68 cm and 8.05 cm of the cross-track gradiometry solution.

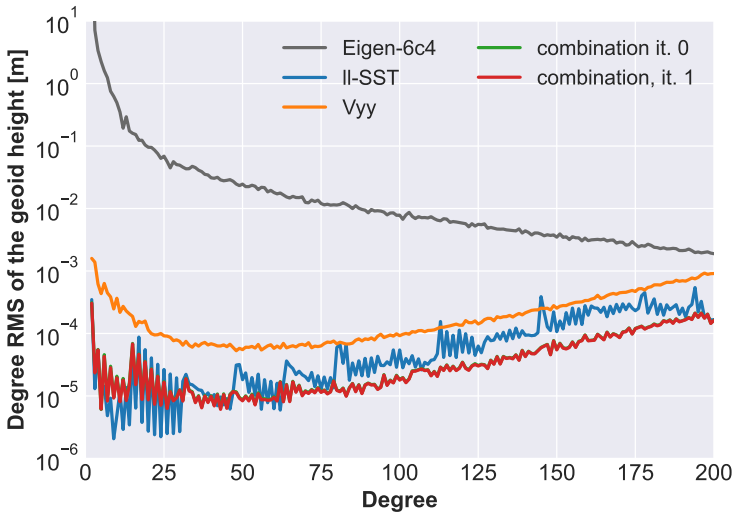


Figure 3.20: Degree RMS of the coefficient differences between recovered and reference gravity field for the iterative variance component estimation

3.7 Summary

Chapter 3 includes the description of different simulation environment elements:

- simulation of satellite dynamics,
- modeling of sensor behavior,
- modeling of control system behavior,
- modeling of further noise sources,
- gravity field recovery from synthesized measurements.

Non-gravitational accelerations are modeled using the XHPS toolbox. Models for atmospheric drag, solar radiation pressure, Earth albedo, infrared and thermal radiation pressure as well as the surface model and mass of the satellite are considered. Attitude control system behavior models from XHPS are used to ensure that the effective area is realistic. In addition to the models available in XHPS, the author of this thesis modeled a the drag compensation system behavior. The drag compensation system is an important component for the accelerometer performance analysis.
The accelerometer noise is modeled based on PSD models, i.e. derived from in-orbit performances of GOCE, GRACE and GRACE-FO accelerometers. The PSD of CAI accelerometer is estimated based on ground experiments and performance expectations for the microgravity environment in space. Furthermore, the transfer function of an atomic interferometer is implemented. The combination of electrostatic and CAI measurement is carried out by low-pass and high-pass filtering. State-of-the-art ranging measurement instruments behaviors are modeled for ll-SST scenarios. Time-variable background modeling is the major challenge concerning gravity field recovery. Hence, error assumptions due to temporal variation in

atmosphere and ocean and ocean tides are included.
SH coefficients are estimated within a least-squares adjustment. The adjustment procedure is explained for two cases: using ll-SST observation and using gradiometry measurements. Moreover, the parameter estimation for the combination these two measurement concepts is given.

4 Impact of New Measurement Concepts on Gravity Field Recovery

The modeled sensor behaviors, control system behaviors and mission concepts presented in chapter 3 have to be evaluated in terms of their relevance for the measurement of the Earth's gravitational field. The impact of different accelerometer types on the gravity field solution is studied for ll-SST missions (section 4.4) and gradiometry missions (section 4.5). These studies are performed under the assumption that satellites are equipped with a drag compensation system. The advantages, disadvantages and other aspects of a drag compensation system are examined separately in section 4.2. Section 4.3 provides an analysis concerning the CAI accelerometer. It considers the variation of the signal within an interferometer cycle, which is an important component. In section 4.6, a new mission concept is studied which addresses the addition of a cross-track gradiometer to a ll-SST mission.

4.1 Selection of Simulation Scenarios

In previous sections, individual components have been investigated. In this section, the interaction between these components is analyzed. A meaningful analysis is only achieved when instruments and satellite orbits are considered together. Therefore, several parameters of sensors, actuators and orbits are varied. In Figure 4.1, the interaction between some central components is illustrated. Considered components are the attitude control system, the drag-free control system, the accelerometer and orbit parameters. Sensors and actuators of an attitude control system are described in the sections 2.2.2 and 3.4.2. In this work, state-of-the-art attitude control system models are used. On the one hand, the attitude control system is required for the measurements of the KBR system and the LRI system. On the other hand, the attitude control system can help to reduce the effective area of the spacecraft on which the atmospheric drag acts. The smaller the front area in flight direction of the satellite, the more reduced is the force due the atmospheric drag. Moreover, the rotation of the satellite also affects the performance of the CAI accelerometer. The rotation leads to an additional phase shift and can also cause a contrast loss of the interferometer (cf. section 4.5). The parameters of the drag-free control system strongly depend on the satellite orbit and the accelerometer.

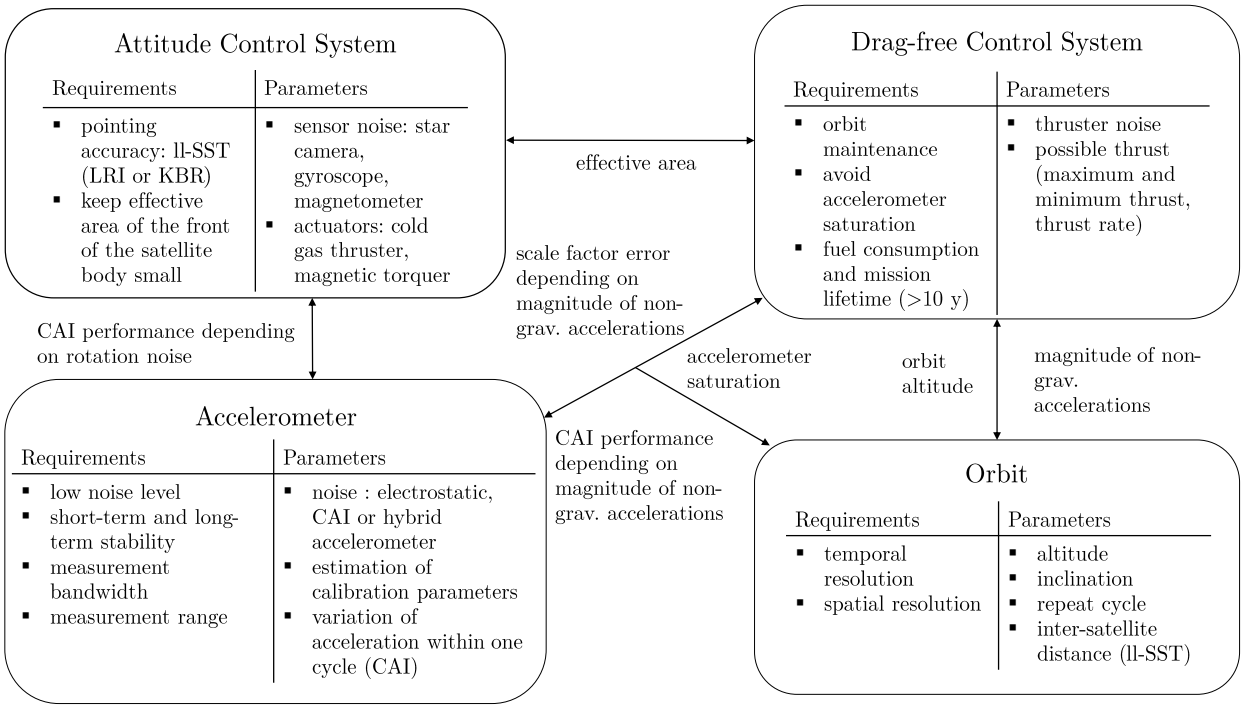


Figure 4.1: Interaction between components of a satellite gravity mission

Low orbits lead to higher non-gravitational forces acting on the satellite. The thruster parameters have to be adapted to the needed control force. Aside from that, a lower altitude leads to a higher propellant consumption which is a key factor for the mission lifetime. The interaction between the drag-free system and the accelerometer has several aspects. The drag-free system can avoid saturation of the accelerometer. The magnitude of the non-gravitational accelerations is also critical for the accelerometer performance, for example the error due to the scale factor and the variation within one CAI cycle.

From the described relations, it can be concluded that the orbit altitude has a large influence on the accelerometer, the drag-free system and also on the gravity field solution. Therefore, several orbit altitudes of approximately 462 km, 363 km, 303 km and 246 km are tested. Obtaining a repeat orbit is taken into account in the orbit design, which results in the given orbit altitudes. In order to recover monthly gravity field solutions, all selected orbits have a repeat period of 29 days. An inclination of 89.9° is chosen which leads to a small polar gap. The selected orbit scenarios are given in Table 4.1.
The orbit data is simulated using the XHPS software, which is briefly introduced in section 3.1. Initial positions and velocities for the orbit integration are calculated from the Keplerian elements given in Table 4.1. The eccentricity is set to 0.001, the right ascension of the ascending node Ω and the argument of the perigee ω are set to zero. The mean anomaly M is chosen for the two satellites such that the distance between them is approximately 200 km. The satellites have to point to each other which is defined by the initial attitude information (cf. appendix A.2). A stepsize of 5 s is used for the synthesis of the observations and the recovery of the gravity field solutions.

Table 4.1: Orbit parameters of selected scenarios

	Altitude	Inclination	Repeat period	Number of orbital revolutions to repeat
Orbit 1	462.015 km	89.9°	29 days	443
Orbit 2	362.751 km	89.9°	29 days	453
Orbit 3	303.662 km	89.9°	29 days	459
Orbit 4	246.041 km	89.9°	29 days	465

4.2 Drag Compensation Analysis

On the one hand, drag-free systems enable orbit maintenance, on the other hand, accelerometer saturation is prevented. Whether drag compensation is needed to avoid accelerometer saturation, it is discussed in section 4.2.3 for several orbit altitudes. Another aspect is the possible reduction of the error contribution due to accelerometer imperfections by a drag-free system. This aspect is evaluated for ll-SST and gradiometry missions. The propellant consumption of the drag compensation limits the mission lifetime which is also briefly addressed.

4.2.1 Drag Compensation Requirements due to Accelerometer Imperfections for ll-SST Missions

The requirement for drag compensation depends on the knowledge of the scale factor and the noise level of the accelerometer. In a simplified scenario the measured acceleration a_{meas} consists of the true acceleration a_{true}, the scale factor s_{true} and the noise of the accelerometer n_{acc} according to:

$$a_{meas} = s_{true}\, a_{true} + n_{acc}. \tag{4.1}$$

The scale factor is estimated with a calibration method and the measurement is corrected with the estimated scale factor s_{est}:

$$a_{est} = \frac{s_{true}\, a_{true} + n_{acc}}{s_{est}}. \tag{4.2}$$

The residual error due to imperfect calibration is given by

$$v_{est-true} = a_{est} - a_{true}, \tag{4.3}$$

$$v_{est-true} = \frac{s_{true}\, a_{true} + n_{acc}}{s_{est}} - a_{true}, \tag{4.4}$$

$$v_{est-true} = \frac{s_{true} - s_{est}}{s_{est}} a_{true} + \frac{n_{acc}}{s_{est}}. \tag{4.5}$$

The objective is to achieve that the error influence due to the imperfect determination of the scale factor is lower than the accelerometer noise:

$$\frac{s_{true} - s_{est}}{s_{est}} a_{true} < \frac{n_{acc}}{s_{est}}. \tag{4.6}$$

Consequently, a requirement on the maximum acceleration signal is defined by

$$a_{true} < \frac{n_{acc}}{s_{true} - s_{est}}. \tag{4.7}$$

Adding a tolerance factor of 1/2 gives the final definition of the maximum allowed acceleration signal

$$a_{true} < \frac{1}{2}\frac{n_{acc}}{s_{true} - s_{est}}, \tag{4.8}$$

where $s_{true} - s_{est}$ is the difference between the estimated and the true scale factor and defined as the scale factor knowledge s_{know}. The ASD of the required drag compensation is estimated according to Gruber et al. (2014a) with

$$ASD(f) < \frac{1}{2}\frac{ASD_{n_{acc,x}}(f)}{s_{know}}, \tag{4.9}$$

where $\frac{1}{2}$ is a tolerance factor, s_{know} is the scale factor knowledge and $ASD_{n_{acc,x}}$ is accelerometer noise in terms of ASD for the x-axis. The scale factor is estimated to 1 % accuracy for the previous missions. This knowledge is assumed to be significantly more accurate for future gravity missions. In Gruber et al. (2014a) s_{know} is assumed with 0.2 %. In Abrykosov et al. (2019) an accuracy of the scale factor of 10^{-5} is assumed for a hybrid accelerometer, where the classical accelerometer is calibrated by the CAI measurements. The scale factor of the CAI is very well known with an uncertainty of 1×10^{-9} or even better. In fact, it is expected that a calibration of the EA using the measurements of a CAI can also achieve an accuracy of 1×10^{-9} for the estimation of the scale factor of the electrostatic one.
The requirement depends on the accelerometer noise, as the degradation by the scale factor uncertainty has to be lower than the noise. An example can be found in Figure 4.2.

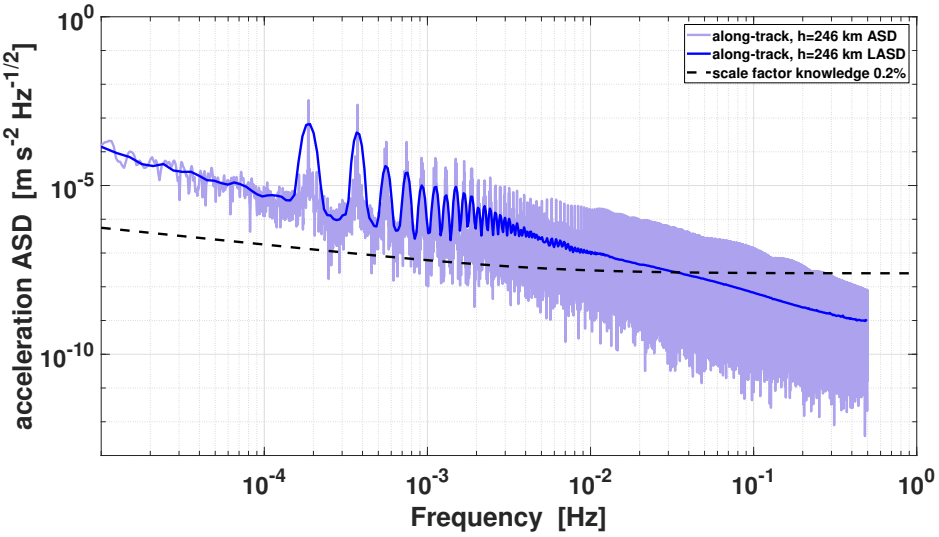


Figure 4.2: ASD of the non-gravitational acceleration signal in along-track direction for the altitude of 246 km (blue lines) and the requirement is based on scale factor knowledge of 0.2 % (dotted line)

The ASD is estimated with two different methods: the Welch's method and the modified one. The results of the Welch's method is abbreviated with ASD and the results of the modified logarithmic Welch's method with LASD. The blue curves are ASD and LASD of the acceleration signal due to non-gravitational forces. The dotted line represents the assumption for the maximum allowed acceleration signal which is calculated with equation (4.9). Consequently, the requirement is not achieved because the blue curve lies above the dotted line.
In the Figures of this section, the sensitive axes of the GRACE accelerometer are chosen for the requirement calculation. Figures 4.3 and 4.4 show the ASD of the non-gravitational acceleration signal in along-track direction for altitudes of 246 km, 303 km, 363 km and 462 km. In the Figures 4.5 and 4.6, it is presented for the cross-track component and in the Figures 4.7 and 4.8 for the radial component. The results of two different time epochs are considered in order to represent the maximum and minimum of the solar cycle and consequently the maximum and minimum of the non-gravitational acceleration signal.
The ASD or LASD of non-gravitational acceleration signal (colored lines) must be below the requirement (dotted lines). In along-track direction, the acceleration has the largest magnitude due to the atmospheric drag. Both assumptions for scale factor knowledge of an EA are not achieved. This applies to all orbit scenarios of different altitudes and over the full relevant frequency range. Consequently, the scale factor is not estimated accurately enough when only having one EA for along-track measurements. The EA measurements are degraded by the inaccurately determined scale factor to such an extent that this error accounts for a larger contribution than the accelerometer noise. Either the scale factor estimations have to be improved or the magnitudes of the non-gravitational signal have to be reduced in order to prevent the degradation.

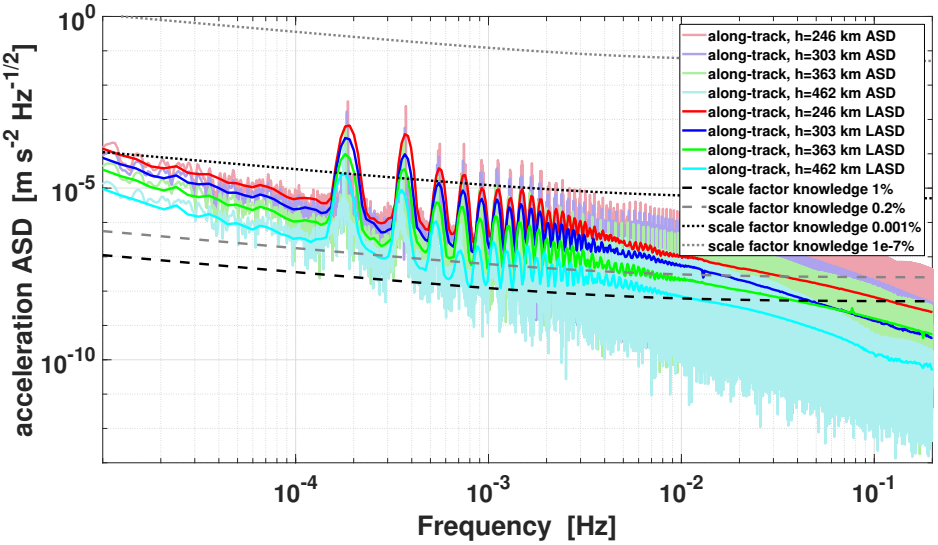


Figure 4.3: ASD of the non-gravitational acceleration signal in along-track direction for different altitudes (colored lines) and the requirement with different assumptions for the scale factor knowledge (dotted lines), July 2000 representing solar cycle maximum

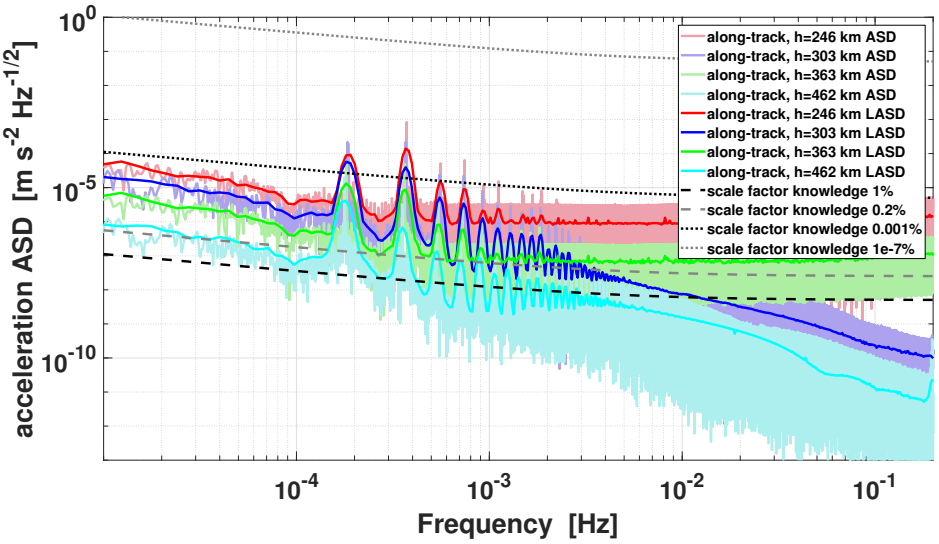


Figure 4.4: ASD of the non-gravitational acceleration signal in along-track direction for different altitudes (colored lines) and the requirement with different assumptions for the scale factor knowledge (dotted lines), January 2006 representing solar cycle minimum

The cross-track component holds the same conclusion as the along-track component. Although the magnitude is lower overall for all altitude scenarios, a scale factor knowledge of 1 % and 0.2 % is not sufficient.

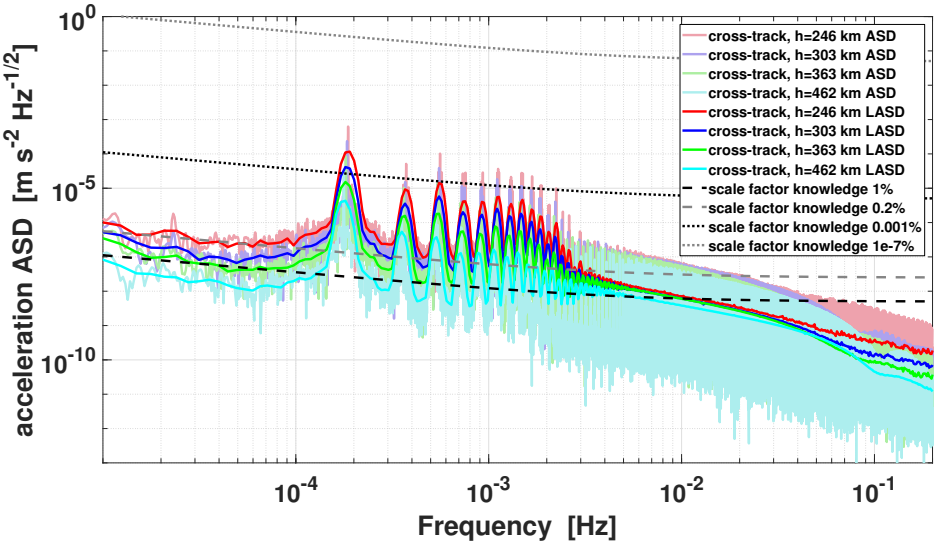


Figure 4.5: ASD of the non-gravitational acceleration signal in cross-track direction for different altitudes (colored lines) and the requirement with different assumptions for the scale factor knowledge (dotted lines), July 2000 representing solar cycle maximum

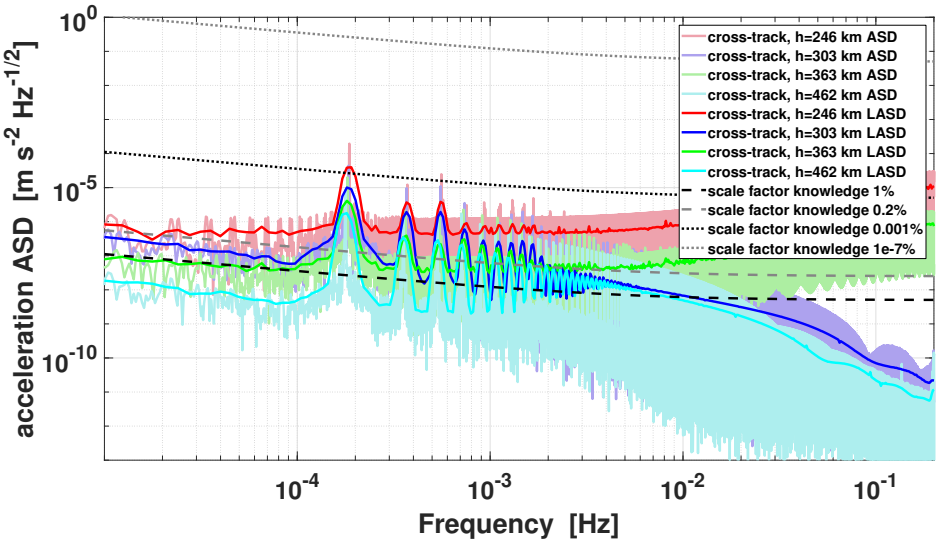


Figure 4.6: ASD of the non-gravitational acceleration signal in cross-track direction for different altitudes (colored lines) and the requirement with different assumptions for the scale factor knowledge (dotted lines), January 2006 representing solar cycle minimum

The radial component shows an even lower ASD of non-gravitational accelerations. Furthermore, the ASD curves of the four altitudes are more similar than those of the other two directions. The atmospheric drag, which decreases with increasing altitude, acts mainly in the along-track and the cross-track direction. Nevertheless, the scale factor estimation for an EA is not accurate enough. The stated conclusions are valid for both periods of different solar activities, for the period July 2000 as well as for January 2006.

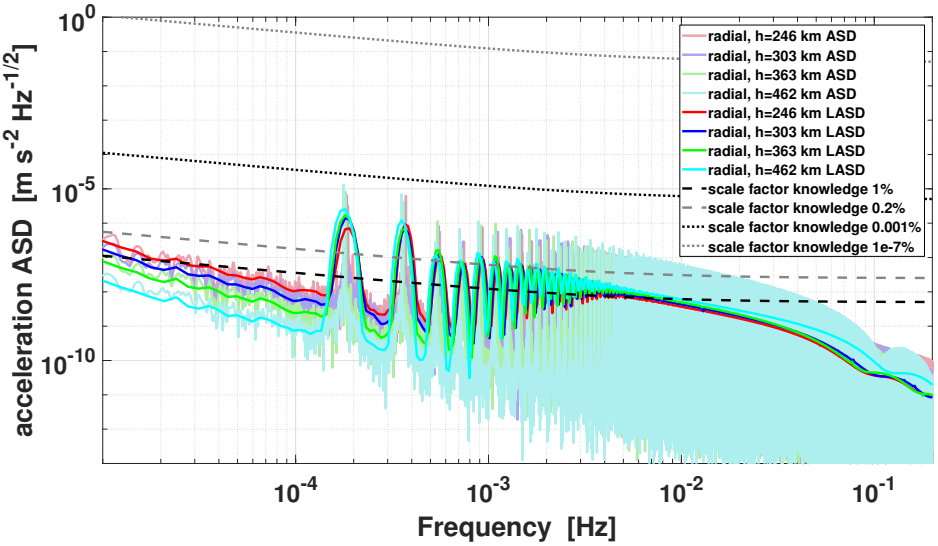


Figure 4.7: ASD of the non-gravitational acceleration signal in radial direction for different altitudes (colored lines) and the requirement with different assumptions for the scale factor knowledge (dotted lines), July 2000 representing solar cycle maximum

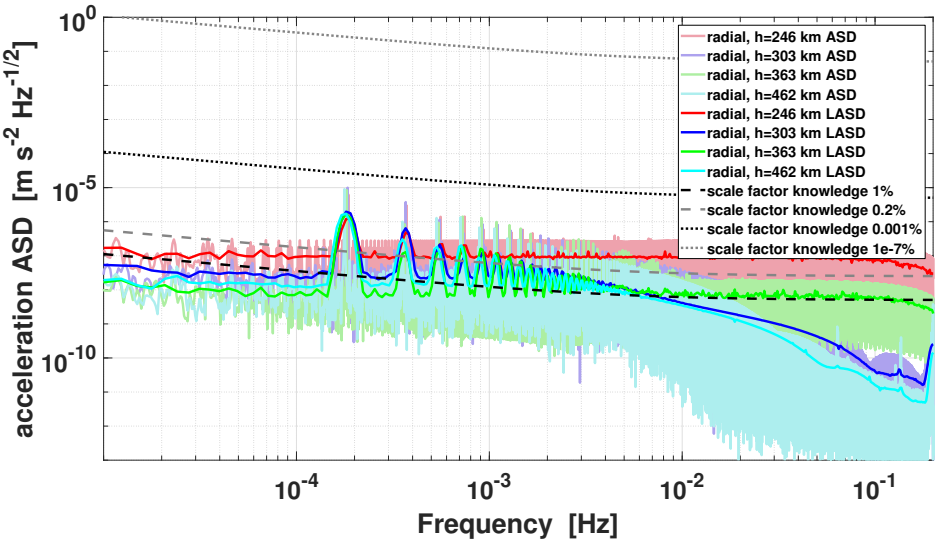


Figure 4.8: ASD of the non-gravitational acceleration signal in radial direction for different altitudes (colored lines) and the requirement with different assumptions for the scale factor knowledge (dotted lines), January 2006 representing solar cycle minimum

The requirement is easily fulfilled for all altitudes and directions when a scale factor knowledge of 1×10^{-9} is assumed, which is feasible for a CAI accelerometer. In along-track direction, the requirement curve is almost three orders of magnitude above the highest peaks of the acceleration signal. In cross-track direction, it is four orders of magnitude and in radial direction even five. This shows that a degradation due to the scale factor in CAI measurements does not occur.
With an assumption of 1×10^{-5}, there are still some peaks above the requirement curve in along-track direction for the two lower altitudes. The requirement is achievable with altitudes of 303 km, 363 km and 462 km for the cross-track component. However, a scale factor knowledge of 1×10^{-5} would be sufficient in radial direction even for a low altitude of 246 km.

4.2.2 Drag Compensation Requirements for Gradiometry due to Accelerometer Imperfections

The measured gradient tensor $\hat{V}$ is degraded by several noise sources. As an example, the measured component $\hat{V}_{xx}$ includes the following errors (linear approximation) in addition to the gravitational gradient V_{xx} (Douch et al., 2018a; Douch et al., 2018b):

$$\hat{V}_{xx} = V_{xx} + n_{xx} - 2\omega_y n_{\omega y} - 2\omega_z n_{\omega z} - 2d\Theta_z V_{xy} + 2d\Theta_y V_{xz} + \nabla V_{xx} dr + err_{de-aliasing} + \beta \frac{a_{i,x} + a_{j,x}}{L}, \tag{4.10}$$

where n_{xx} is the gradiometer noise, $-2\omega_y n_{\omega y} - 2\omega_z n_{\omega z}$ is the error due to the correction of the centrifugal terms, $2d\Theta_z V_{xy} + 2d\Theta_y V_{xz}$ error due to the attitude determination, $\nabla V_{xx} dr$ the error due to the satellite position, $err_{de-aliasing}$ is the de-aliasing error, $\beta \frac{a_{i,x}+a_{j,x}}{L}$ is the error due to the non-zero common-mode rejection.
The contribution of the common mode is caused by accelerometer imperfections, e.g. if the

scale factors of pairs of accelerometers are not exactly equalized. Stummer et al. (2012) and Stummer (2012) show that the measured gravity gradient V_{yy} of GOCE is degraded by the non-perfect common mode rejection as the y-component is affected by strong cross-winds. In this section, the focus is on this noise contribution only. The true gradient $\Gamma_{true,xx}$ is given by acceleration differences of the gradiometer pair ij divided by the baseline length L

$$\Gamma_{true,xx} = \frac{a_{true,i,x} - a_{true,j,x}}{L}. \tag{4.11}$$

In a simplified scenario, which only considers the scale factors, the estimated gradient $\Gamma_{est,xx}$ is written as

$$\Gamma_{est,xx} = \frac{\frac{s_{true,i,x}a_{true,i,x}}{s_{est,i,x}} - \frac{s_{true,j,x}a_{true,j,x}}{s_{est,j,x}}}{L}, \tag{4.12}$$

$$\Gamma_{est,xx} = \frac{\frac{s_{true,i,x}}{s_{est,i,x}} + \frac{s_{true,j,x}}{s_{est,j,x}}}{2}\left(\frac{a_{true,i,x} - a_{true,j,x}}{L}\right) + \frac{\frac{s_{true,i,x}}{s_{est,i,x}} - \frac{s_{true,j,x}}{s_{est,j,x}}}{2}\left(\frac{a_{true,i,x} + a_{true,j,x}}{L}\right) \tag{4.13}$$

$$= \alpha\left(\frac{a_{true,i,x} - a_{true,j,x}}{L}\right) + \beta\left(\frac{a_{true,i,x} + a_{true,j,x}}{L}\right), \tag{4.14}$$

with the true measurements $a_{true,i,x}$ and $a_{true,j,x}$ of two accelerometers having the indices i and j, the common mode gain β, the differential mode gain α, the baseline length L, the true scale factor s_{true} and the estimated scale factor s_{est}. The Common Mode Rejection Ratio (CMRR) is the ratio of the common mode gain β to the differential mode gain α:

$$CMRR = log_{10}\left(\frac{\alpha}{\beta}\right). \tag{4.15}$$

It indicates how much the gradient is degraded by the common mode signal. In an ideal case, α is 1 and β is nearly zero. The aim is to keep the term $\beta\left(\frac{a_i+a_j}{L}\right)$ as small as possible. Thus, the objective is that this item is lower than the gradiometer noise n_{gradio}:

$$\frac{\frac{s_{true,i,x}}{s_{est,i,x}} - \frac{s_{true,j,x}}{s_{est,j,x}}}{2}\frac{a_{true,i,x} + a_{true,j,x}}{L} < n_{gradio}. \tag{4.16}$$

The accelerometers are arranged around the origin of the GRF which is located in the center of mass of the satellite. Consequently, the common mode acceleration reflects the sum of the non-gravitational forces acting on the satellite. It follows from the above and with the assumption that the gradiometer baseline length is 1 m:

$$\frac{s_{true,i,x}}{s_{est,i,x}} - \frac{s_{true,j,x}}{s_{est,j,x}}a_{ng,x} < n_{acc}. \tag{4.17}$$

The final definition of the maximum allowed non-gravitational acceleration signal is

$$a_{ng,x} < \frac{n_{acc}}{\frac{s_{true,i,x}}{s_{est,i,x}} - \frac{s_{true,j,x}}{s_{est,j,x}}}. \tag{4.18}$$

The ASD of required drag compensation is formulated as

$$ASD(f) < \frac{ASD_{n_{acc,x}}(f)}{\frac{s_{true,i,x}}{s_{est,i,x}} - \frac{s_{true,j,x}}{s_{est,j,x}}}. \tag{4.19}$$

In order to get a realistic assumption for $\frac{s_{true,i,x}}{s_{est,i,x}} - \frac{s_{true,j,x}}{s_{est,j,x}}$, the scale factors are estimated by the calibration method of Siemes (2012), which is briefly described in section 2.2.4. The term $\frac{s_{true,i,x}}{s_{est,i,x}} - \frac{s_{true,j,x}}{s_{est,j,x}}$ varies between 3×10^{-7} and 2×10^{-5}. The calibration procedure is tested with simulated data.

The ASD of non-gravitational acceleration signal is given for along-track in Figure 4.9 and 4.10, for cross-track direction in Figure 4.11 and 4.12 and for radial direction in Figure 4.13 and 4.14. The requirements based on a scale factor difference knowledge of 3×10^{-7} and 2×10^{-5} are additionally illustrated. The accelerometer noise is modeled using the ASD model of the GOCE accelerometers.

The two scenarios with higher orbit altitudes of 462 km and 363 km show compliance with the requirement using a scale factor difference knowledge of 3×10^{-7} in along-track direction. Some peaks in the frequencies between 1×10^{-4} Hz and 1×10^{-3} Hz do not meet the requirements for the two low-altitude scenarios. This is much more evident for the results of the month which represents the solar cycle maximum. In this case, the requirement is not fully met for an altitude of 363 km. The requirement is not achieved for all orbit altitudes with a scale factor difference knowledge of 2×10^{-5}.

The magnitude of the non-gravitational acceleration ASD is again smaller for the cross-track component. To this end, a differential scale factor knowledge of 3×10^{-7} fulfills the requirement, whereat a knowledge of 2×10^{-5} does not. This holds true for all scenarios.

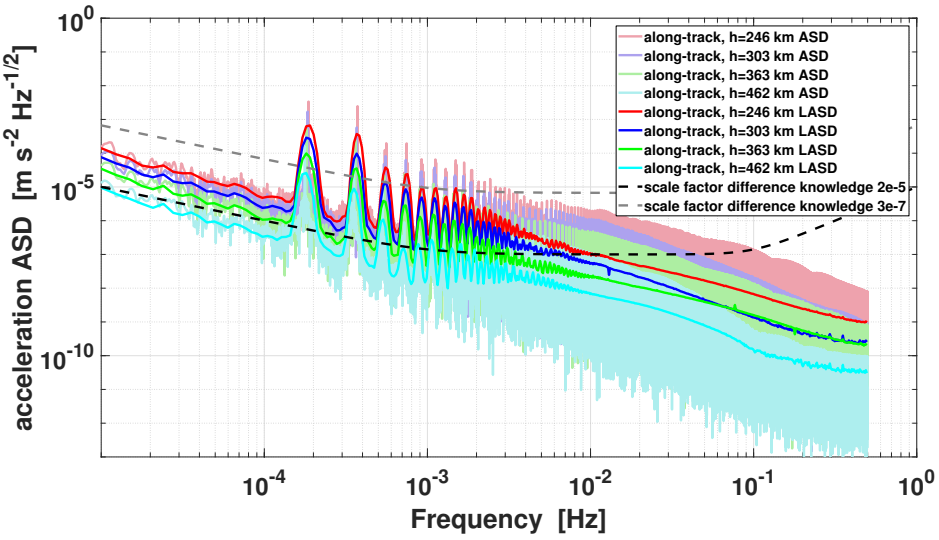


Figure 4.9: ASD of the non-gravitational acceleration signal in along-track direction for different altitudes (colored lines) and the requirement with different assumptions for differential scale factor knowledge (dotted lines), July 2000 representing solar cycle maximum

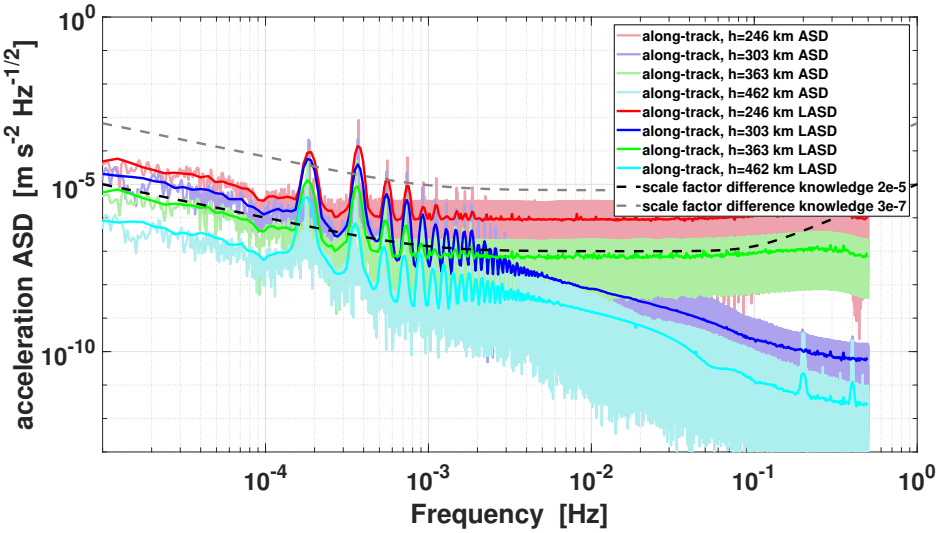


Figure 4.10: ASD of the non-gravitational acceleration signal in along-track direction for different altitudes (colored lines) and the requirement with different assumptions for differential scale factor knowledge (dotted lines), January 2006 representing solar cycle minimum

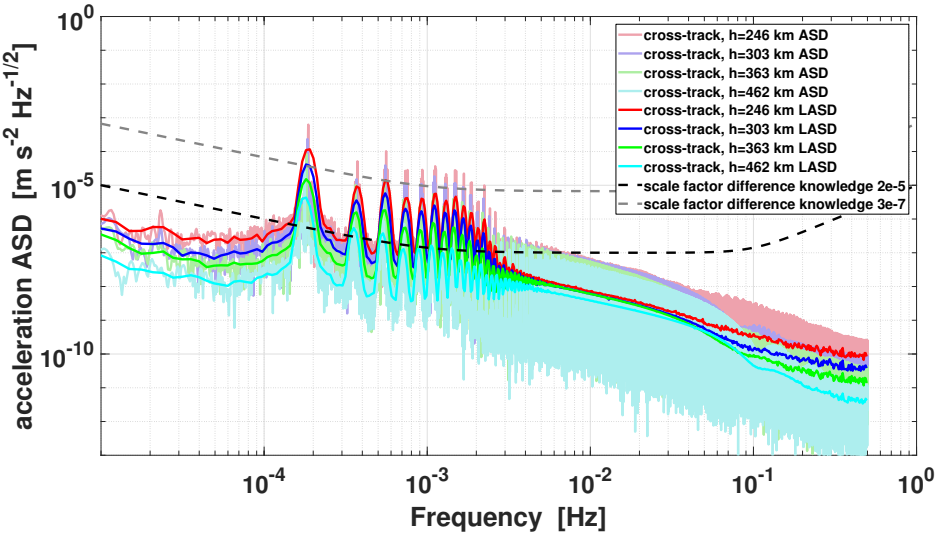


Figure 4.11: ASD of the non-gravitational acceleration signal in cross-track direction for different altitudes (colored lines) and the requirement with different assumptions for differential scale factor knowledge (dotted lines), July 2000 representing solar cycle maximum

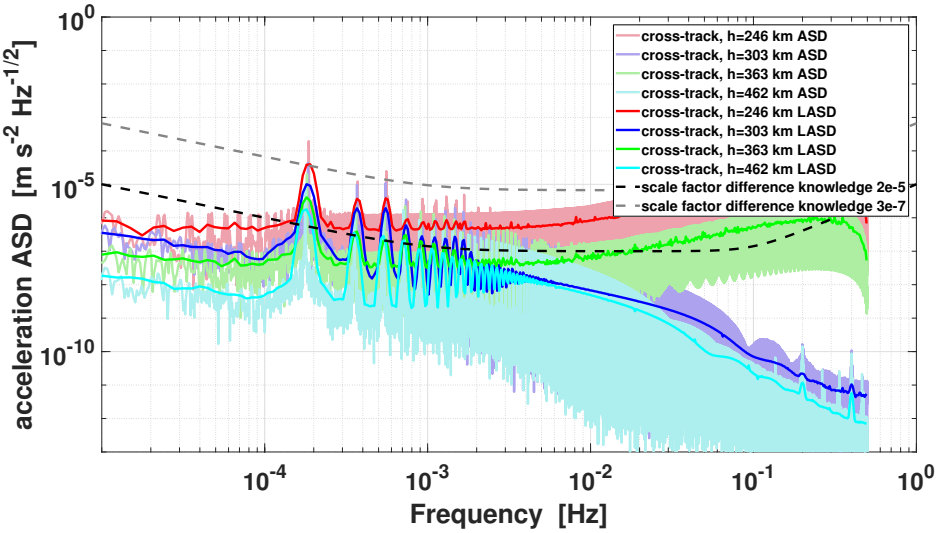


Figure 4.12: ASD of the non-gravitational acceleration signal in cross-track direction for different altitudes (colored lines) and the requirement with different assumptions for differential scale factor knowledge (dotted lines), January 2006 representing solar cycle minimum

In scenarios of the radial direction, the requirement using a scale factor difference knowledge of 3×10^{-7} is explicitly met. For a scale factor difference knowledge of 2×10^{-5}, there is only a small violation of the limit.
In conclusion, scale factors of an EA are not estimated accurately enough for the along-track direction. In cross-track direction, it depends on the altitude and whether the scale factor difference knowledge can be approximated with 2×10^{-5} or 3×10^{-7}. No large degradation due to an uncertain estimation of the scale factor is expected in radial direction.

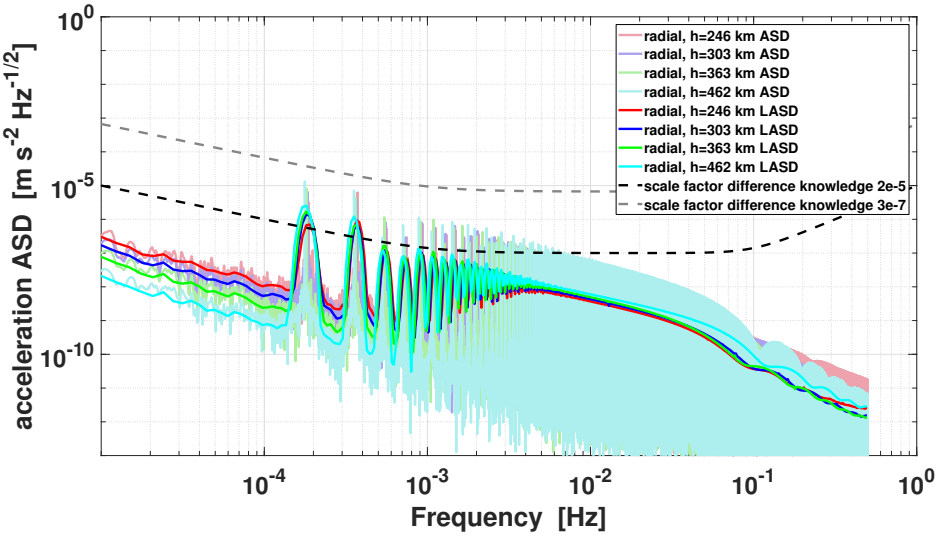


Figure 4.13: ASD of the non-gravitational acceleration signal in radial direction for different altitudes (colored lines) and the requirement with different assumptions for differential scale factor knowledge (dotted lines), July 2000 representing solar cycle maximum

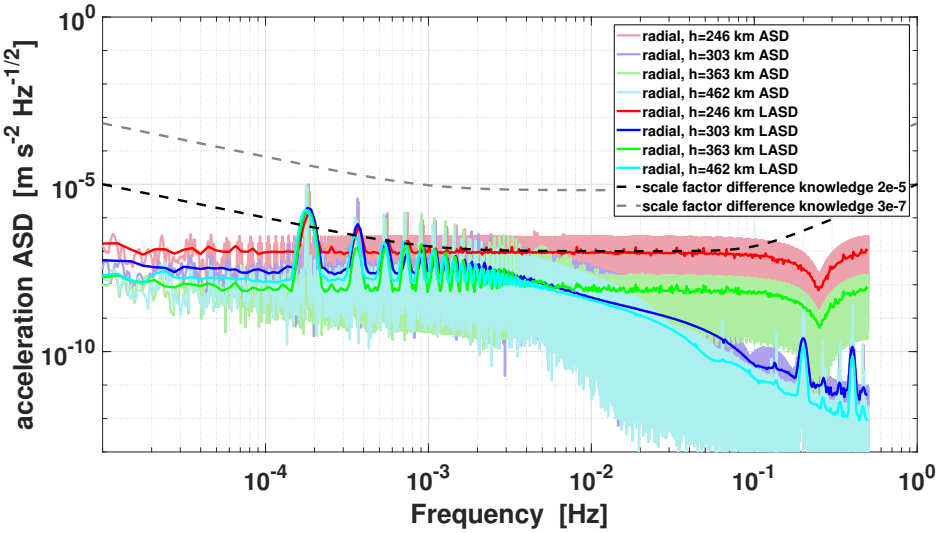


Figure 4.14: ASD of the non-gravitational acceleration signal in radial direction for different altitudes (colored lines) and the requirement with different assumptions for differential scale factor knowledge (dotted lines), January 2006 representing solar cycle minimum

In Figure 4.15, the residual non-gravitational accelerations after applying drag compensation are displayed. Two different cases for the drag-free control system are considered: one is a model of the GOCE control system and the other one is a system using fine control thrusters. The requirement with the scale factor difference knowledge of 2×10^{-5} is kept using the GOCE control parameters while the more stringent requirement is not achieved. The fine control parameters enable very small residual acceleration and both requirements are achieved. This fine controlling might be too optimistic, but it is also two orders of magnitude below the dotted curve of the scale factor difference knowledge of 3×10^{-7}. Thus, even some relaxed fine controlling would work.

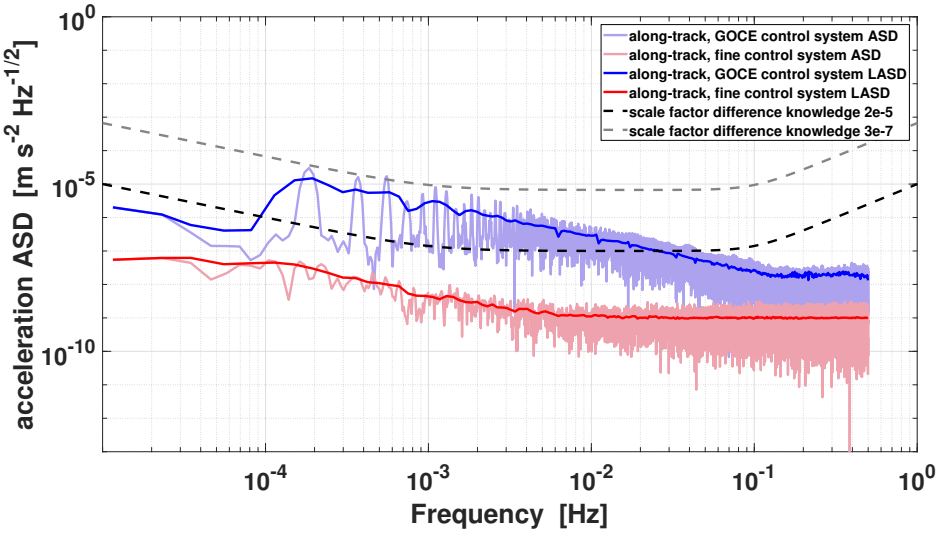
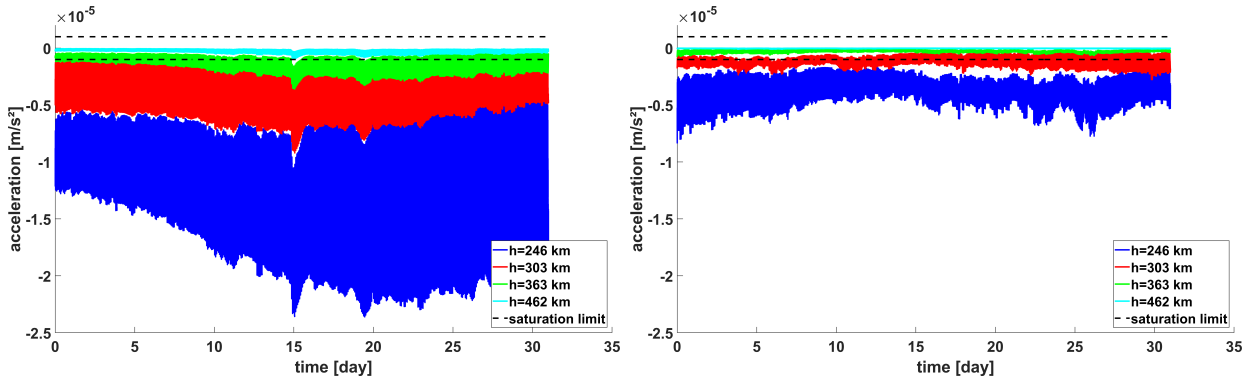


Figure 4.15: ASD of the residual non-gravitational acceleration using drag compensation (colored lines) and the requirement with different assumptions for the scale factor knowledge (dotted lines)

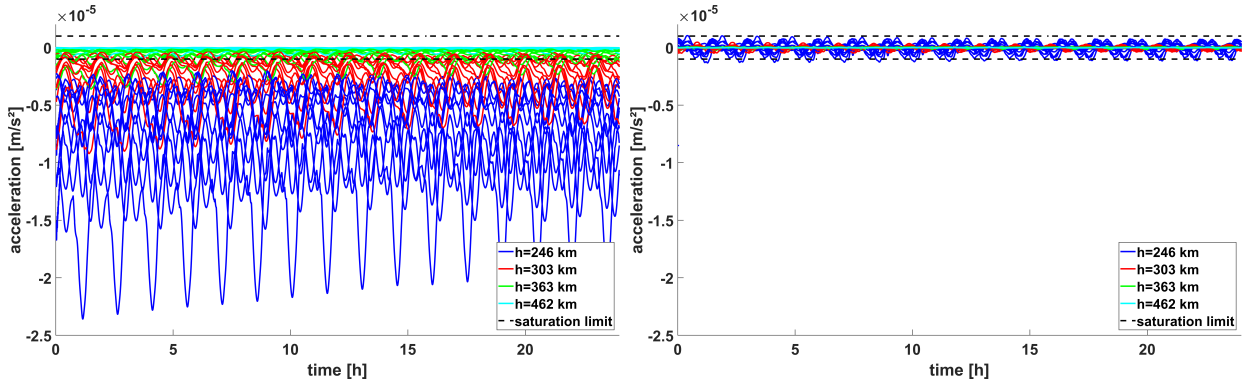
4.2.3 Saturation of the Accelerometer

The requirement for the drag compensation system also depends on the saturation limit, which is $\pm 6.5 \times 10^{-6}$ m/s^2 for GOCE accelerometers. The limit is even less stringent with $\pm 5 \times 10^{-5}$ m/s^2 for GRACE accelerometers. The saturation limit can be assumed with $\pm 1 \times 10^{-6}$ m/s^2 for future satellite gravity missions (Gruber et al., 2014a). The magnitude of the non-gravitational accelerations strongly depend on the altitude of the satellite and the solar activity. Thus, it is calculated for different orbit altitudes and for various months within a solar cycle. The satellite body model and the mass of the GRACE-FO are used for these calculations. The month July 2000 is representative for the maximum of a solar cycle and January 2006 for the minimum. The non-gravitational accelerations as well as the saturation limit are illustrated in Figure 4.16 for the two months. The enormous influence of the solar cycle on the strength of the non-gravitational accelerations is demonstrated.



(a) July 2000 representing solar cycle maximum (b) January 2006 representing solar cycle minimum

Figure 4.16: Non-gravitational accelerations in along-track direction for different orbit altitudes and saturation limit



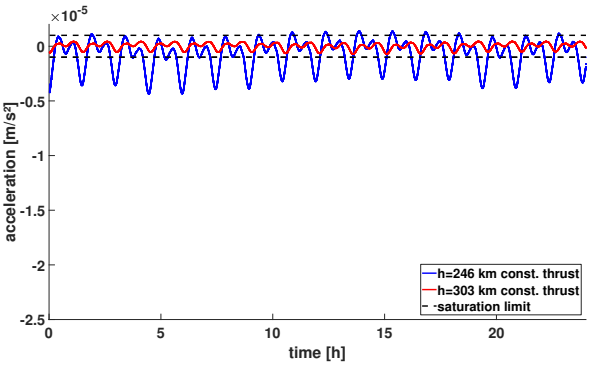
(a) Along-track direction (b) Cross-track direction

Figure 4.17: Non-gravitational accelerations in along- and cross-track direction for different orbit altitudes and saturation limit

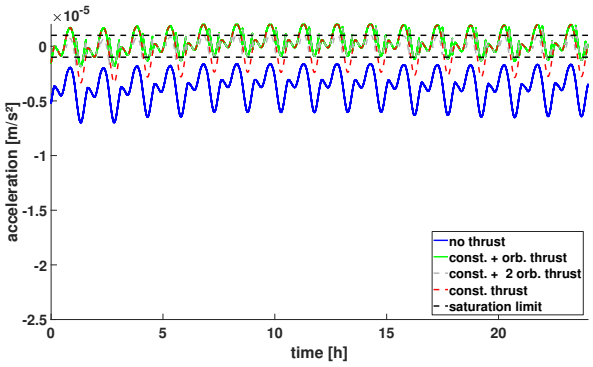
Table 4.2: Maximum absolute value of the non-gravitational acceleration signals for different altitudes and measurement directions

altitude	along-track direction	cross-track direction	radial direction
246 km	$23.36 \times 10^{-6}\,\mathrm{m/s^2}$	$13.56 \times 10^{-7}\,\mathrm{m/s^2}$	$4.37 \times 10^{-8}\,\mathrm{m/s^2}$
303 km	$9.21 \times 10^{-6}\,\mathrm{m/s^2}$	$5.21 \times 10^{-7}\,\mathrm{m/s^2}$	$2.69 \times 10^{-8}\,\mathrm{m/s^2}$
363 km	$3.60 \times 10^{-6}\,\mathrm{m/s^2}$	$2.50 \times 10^{-7}\,\mathrm{m/s^2}$	$2.53 \times 10^{-8}\,\mathrm{m/s^2}$
462 km	$1.00 \times 10^{-6}\,\mathrm{m/s^2}$	$0.73 \times 10^{-7}\,\mathrm{m/s^2}$	$4.47 \times 10^{-8}\,\mathrm{m/s^2}$

Figure 4.17 shows the limit and the non-gravitational accelerations in time domain for several days between July 2000 and December 2006. The maximum or minimum magnitude of the non-gravitational accelerations signal of all tested time epochs are given in Table 4.2 for all directions of the orbital frame. Figure 4.17 indicates that it can only be guaranteed for an altitude of 462 km to not exceed the saturation limit of $\pm 1 \times 10^{-6}\,\mathrm{m/s^2}$ in along-track direction. Given an altitude of 363 km, this can only be assured when solar activity is low. Increasing the limit to $\pm 4 \times 10^{-6}\,\mathrm{m/s^2}$ is an option for such an altitude. The saturation limit is not that critical for cross-track direction. Accelerometer saturation does not occur for radial component cases as the magnitude is in the order of $10^{-8}\,\mathrm{m/s^2}$. The saturation limit is exceeded for the altitudes of 303 km and 246 km in along-track direction which demonstrates the necessity of drag compensation for these altitudes. In order to avoid the accelerometer saturation also for lower altitudes, a constant thrust is applied (cf. Figure 4.18 (a)).



(a) Residual non-gravitational accelerations for 246 km and 303 km after applying a constant thrust



(b) Non-gravitational accelerations for 246 km for the cases: no thrust, constant thrust and constant thrust with additional thrust for each orbital revolution

Figure 4.18: Control system using constant thrust levels, calculation for January 1st, 2006

The saturation is not exceeded for an altitude of 303 km with the addition of a constant thruster force. On the contrary, further compensation would be needed for an altitude of 246 km. Thus, as shown in Figure 4.18 (b), additional thrusts are applied per orbit revolution. In a first scenario, the control system works with two different thrust levels per orbital revolution (2.2 mN, 3.1 mN). In a second scenario the control system works with three different thrust levels per revolution (1.6 mN, 2.2 mN, 3.1 mN). In the latter one, the limit is almost achieved, but not completely due the long-term variation of the non-gravitational

force acting on the satellite. A constant thrust or three different thrust levels per orbit revolution would minimize the performance and construction requirements for the drag control system.
It has to be noted, $\pm 1 \times 10^{-6}$ m/s^2 is a severe saturation limit. Already a limit of $\pm 6.5 \times 10^{-6}$ m/s^2 is not exceeded without compensation for the altitudes of 303 km, 363 km and 462 km and with a constant thrust for the altitude of 246 km. However, the maximum measurement range of an accelerometer is highly related to the accelerometer sensitivity. The smaller the measurement range is, the higher is the sensitivity. This fact reinforces the need of drag compensation for low orbit altitudes of 246 km and 303 km.

4.2.4 Propellant Consumption

The mission lifetime is mainly limited through the propellant consumption. The propellant consumption per second of the drag-free system can be roughly estimated by

$$dm/ds = \frac{F}{I_{sp}\ g_0}, \tag{4.20}$$

where F is the non-gravitational forces acting on the satellite, I_{sp} is the specific impulse and g_0 is the standard acceleration due to gravity (Gruber et al., 2014a). The actuator of the drag-free system is an ion propulsion system, where the specific impulse is 2000 s. The specific impulse of cold gas thrusters, needed for orbit maneuvers, can be assumed with 60 s. The propellant consumption is estimated for the ion propulsion system for one month and then extrapolated for a mission duration of 10 years. An extra margin of 20 % is added according to Gruber et al. (2014a). The GOCE mission carried 40 kg Xenon on board, sufficient for 56 months. However, it was a longer mission lifetime than planned by reason of the large margin in the propellant budget for the ion propulsion system which was enabled by low solar activity. The atmospheric density is a critical parameter and is strongly influenced by the solar activity and the orbit altitude. Thus, the calculations are performed for several time spans: July 2000, March 2003, June 2005, January 2006 and December 2006. This covers the minimum and maximum of a solar cycle as well as other examples in between. The propellant consumption is plotted as a function of altitude in Figure 4.19. The red crosses represent the calculated consumption values. The dashed lines are the fitted curves for the calculations of the same time span. The solid blue line is the fitted curve using all data points.
The average consumption for a mission with 10 years of lifetime and an orbit altitude of 246 km is estimated with 80 kg. The results coincide with the consumption of the GOCE mission of 40 kg for approximately 5 years. However, the estimation is possibly on the optimistic side as GOCE started at the minimum of a solar cycle. Reasons for this might be further consumption needed for calibration procedures and due to the lower orbit phase at the mission end. Figure 4.19 shows that the consumption increases exponentially with decreasing altitude. If the orbit is maintained by a constant thrust, the required propellant is reduced only very slightly, as the highest disturbance is at zero frequency, i.e. a constant. An increase of the orbit altitude from 246 km to 303 km reduces the average propellant consumption significantly from 8.2 kg/yr to 2.5 kg/yr.

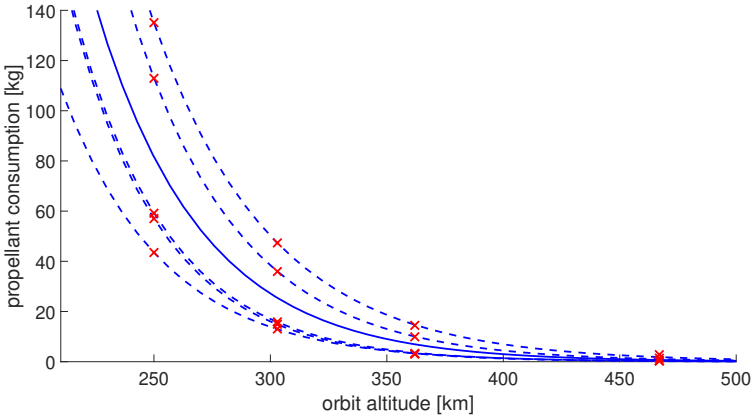


Figure 4.19: Propellant consumption of the ion thrusters for a mission duration of 10 years

4.3 Cold Atom Interferometry Accelerometer Analysis

The simulated non-gravitational accelerations are analyzed concerning their variation in an interferometer cycle in this section. In this study part, only accelerations in along-track direction are included, because non-gravitational accelerations have the largest impact on LEO satellites in this direction and consequently the maximum effect is expected. In this section, only a single satellite is investigated since the findings apply for any satellite. An attitude control system with a nadir pointing mode is included in the calculation of non-gravitational accelerations. Misalignment errors and errors due to the non-orthogonality of the accelerometer frame axes are not considered. Degradation induced by the cross-track and nadir axes would appear when the true alignment differs from the target alignment. Simulations with satellite altitudes of 462 km and 303 km are performed. The mass of the satellite is assumed to be equal to 600.98 kg which is the mass of GRACE-FO at the start of the mission. A detailed surface model of a GRACE-FO satellite body is used. The mass and shape of the satellite and the altitude of 462 km are the parameters of the GRACE-FO mission, allowing a realistic comparison to the results of the mission. Moreover, a lower altitude of 303 km is chosen, which would lead to a higher sensitivity to the gravity field signal at the cost of higher non-gravitational accelerations and thus, it is interesting for future gravity missions. In order to get a continuous signal for the computation of ϕ_k in equation (3.5), the acceleration time series is approximated with an interpolation polynomial. The Newton polynomial interpolation is applied for each cycle separately. The best agreement is achieved with a quadratic polynomial.

The variation between the minimum acceleration and the maximum acceleration within one cycle is calculated for the orbit scenarios with different altitudes. The variation for January 1st, 2006 is given in Figure 4.20. The variation in 12 s is in the order of 10^{-9} m/s^2 for an altitude of 462 km and 10^{-8} m/s^2 for an altitude of 303 km. The transfer function of an atomic interferometer is used to investigate the effect of this variation in one cycle. The output of the atom interferometer is compared to the true acceleration value at $t = 7$ s of each cycle, i.e. the middle time of the interferometer. In Figure 4.21 the ASD of this difference and the ASD of the variation in one cycle are shown. The estimated error of the acceleration measurements is at the level of 3×10^{-11} m/s^2 for an altitude of 462 km and 2×10^{-10} m/s^2 for an altitude of 303 km.

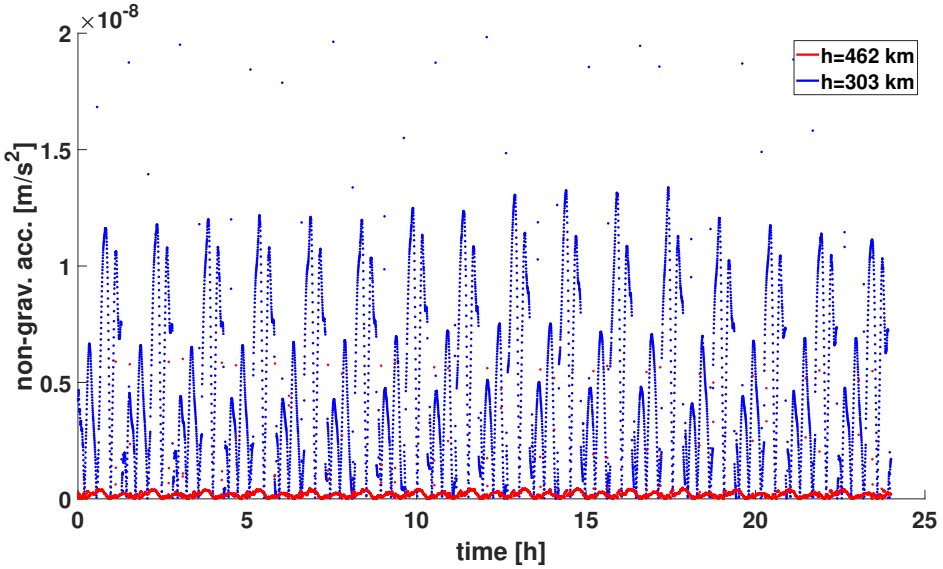


Figure 4.20: Variation of non-gravitational accelerations within one interferometer cycle for two different altitudes: 462 km (red) and 303 km (blue) for January 1st, 2006

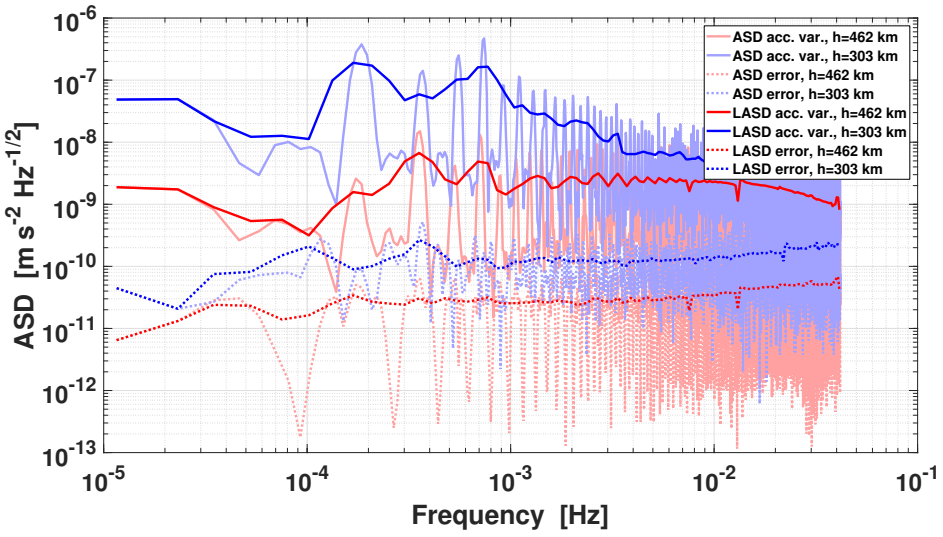
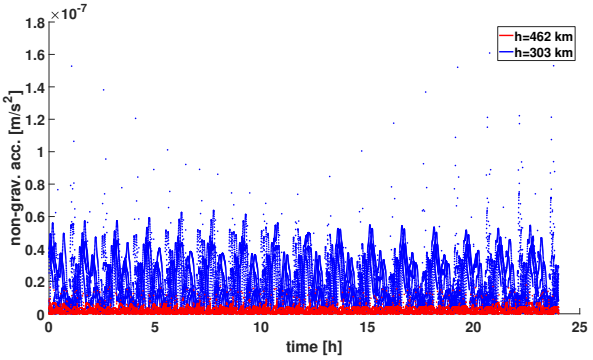


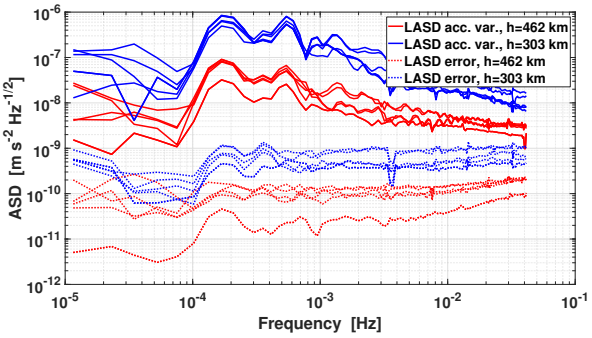
Figure 4.21: ASD of the variation of non-gravitational accelerations within one interferometer cycle (acc. var. - solid lines) and corresponding error contribution to the CAI measurements (error - dotted lines) for two different altitudes: 462 km and 303 km for January 1st, 2006

The results given in Figure 4.21 are only exemplary for one day (January 1st, 2006). Therefore, various calculations for different time epochs are shown in Figure 4.22. The maximum variation of non-gravitational accelerations is in the order of $1.7 \times 10^{-7}\,\mathrm{m/s^2}$ for the altitude of 303 km (cf. Figure 4.22 (a)). The variation remains below $5 \times 10^{-8}\,\mathrm{m/s^2}$ in most cases. The corresponding error contribution is given in Figure 4.22 (b) and shows a similar result for the various cases. The ASD of the error contribution varies between $1 \times 10^{-10}\,\mathrm{m/s^2/\sqrt{Hz}}$ and $1 \times 10^{-9}\,\mathrm{m/s^2/\sqrt{Hz}}$. The error contributions of the scenarios with an altitude of 462 km

are at a lower level between $1 \times 10^{-11}\,\mathrm{m/s^2/\sqrt{Hz}}$ and $2 \times 10^{-10}\,\mathrm{m/s^2/\sqrt{Hz}}$. The reason for this less impact is the lower variation of the non-gravitational accelerations, which is below $2 \times 10^{-8}\,\mathrm{m/s^2}$ and, in most cases, even at the level of $1 \times 10^{-9}\,\mathrm{m/s^2}$.



(a) Variation of non-gravitational accelerations within one interferometer cycle for two different altitudes: 462 km (red) and 303 km (blue)



(b) ASD of the variation of non-gravitational accelerations within one interferometer cycle (acc. var. - solid liens) and corresponding error contribution to the CAI measurements (error - dotted lines) for two different altitudes: 462 km and 303 km

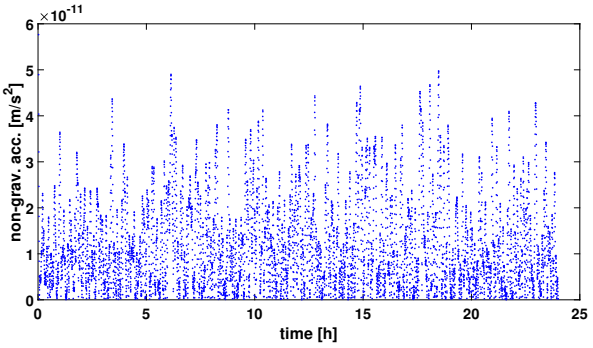
Figure 4.22: Acceleration variation and its error estimation for various time epochs

In conclusion, the error due to the acceleration variation in one interferometer cycle varies between $1 \times 10^{-11}\,\mathrm{m/s^2/\sqrt{Hz}}$ and $1 \times 10^{-9}\,\mathrm{m/s^2/\sqrt{Hz}}$, depending on the altitude and solar cycle. This error contribution is significant, compared to the acceleration noise (cf. section 3.3.2). Therefore, temporal filtering of the non-gravitational accelerations, due to the interferometer response function, has to be taken into account.

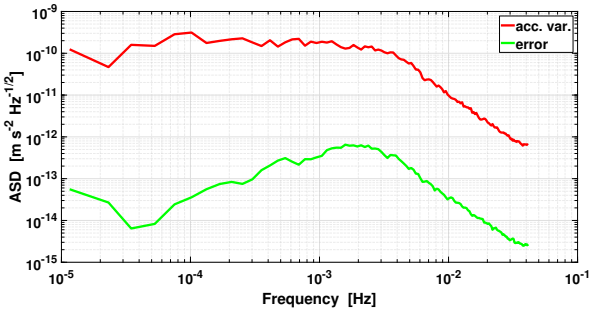
Beyond that, the impact of using a drag compensation system is studied. The thruster model of GOCE is used. As it is impossible to find a good fitting polynomial for the time series including thruster noise, a filter is applied first. Here, a second order Butterworth filter with cutoff frequencies of $1 \times 10^{-6}\,\mathrm{Hz}$ and $5 \times 10^{-3}\,\mathrm{Hz}$ is used. The variation of accelerations within one interferometer cycle is shown in Figure 4.23 (a) and its ASD in Figure 4.23 (b). The estimated error contribution due to the residual variation of non-gravitational accelerations is now below the noise of an atomic interferometer and hence acceptable (Figure 4.23 (b)).

Another option is a cycle time reduction. However, a decrease of the cycle length would reduce the sensitivity of the atom interferometer in addition to a smaller variation of the accelerations in one cycle. Thus, several cycle lengths are tested in order to find the best compromise of these two complementary arguments. The sensitivity of the atom interferometer is calculated according to the equations (3.10), (3.11) and (3.12). The considered parameter values are given in section 3.3.2. The estimated error contributions and the estimated sensitivities of the atom interferometer are plotted in Figure 4.24 for cycle lengths of 6 s, 8 s, 10 s and 12 s. Figure 4.24 (a) shows the results for an altitude of 303 km. For a cycle time of 12 s, the error due to the acceleration variation is dominating in all frequencies. The best scenario is achieved for a cycle time of 8 s. The error estimations for an altitude of

462 km are given in Figure 4.24 (b). In this case, the error due to the acceleration variations is lower and consequently the best compromise is achieved with a longer cycle time. A CAI measurement cycle time of 10 s or 12 s is the best solution.

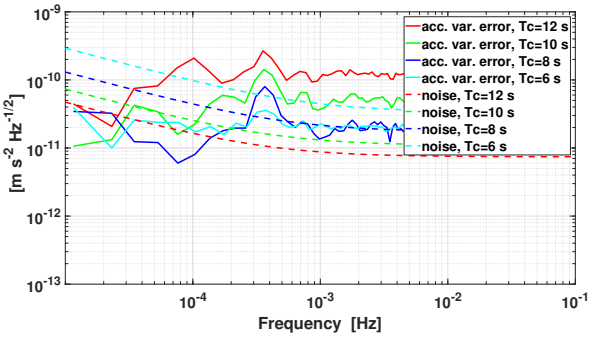


(a) Residual variation of non-gravitational accelerations within one interferometer cycle under drag-free control

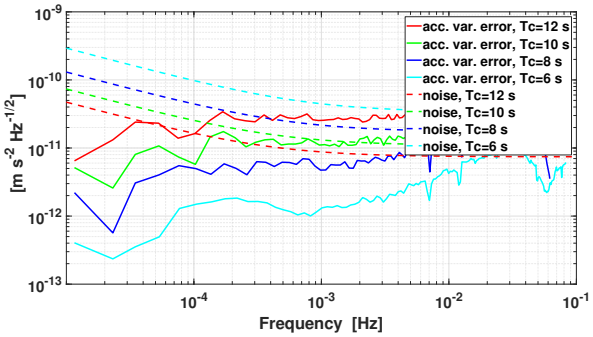


(b) ASD of the residual variation of non-gravitational accelerations within one interferometer cycle and corresponding error contribution under drag-free control

Figure 4.23: Acceleration variation and its error estimation under drag compensation; orbit altitude of 303 km



(a) Altitude of 303 km



(b) Altitude of 462 km

Figure 4.24: Error contribution due to acceleration variation and sensitivity of the atom interferometer

In summary, the acceleration variation in one interferometer cycle has to be taken into account because it can have a critical impact on the performance of the CAI accelerometer. A balance between the cycle time length and sensitivity has to be found. Drag compensation is a good option to reduce the impact of this acceleration variation.

4.4 Gravity Field Solutions using Different Accelerometer Types for ll-SST Missions

In this section, recovered gravity field solutions of ll-SST missions are presented using several sensor behavior models and orbit scenarios. The ASD of considered noise sources are shown in Figure 4.25. The errors due to AOD and ocean tides are the dominating ones in the frequencies between 3×10^{-4} Hz and 5×10^{-3} Hz. In Figure 4.25, the considered noise for AOD is 10 % of the AOD1B product RL 6 and for the ocean tides it is 10 % of the FES2014b product. On the instrument side in the low frequencies, the EA noise is the limiting factor. How strong the accelerometer noise and in which frequency range it is dominant, depends on the type of accelerometer and also on the ranging measurement instrument.

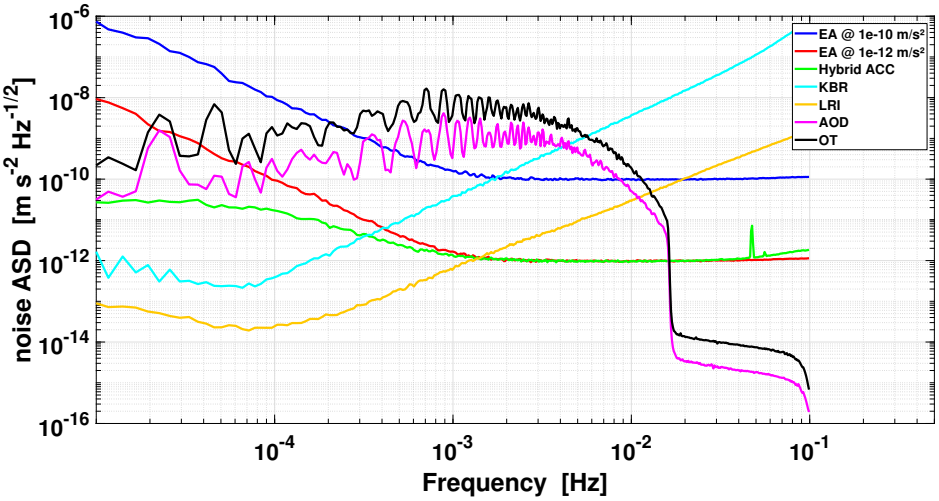
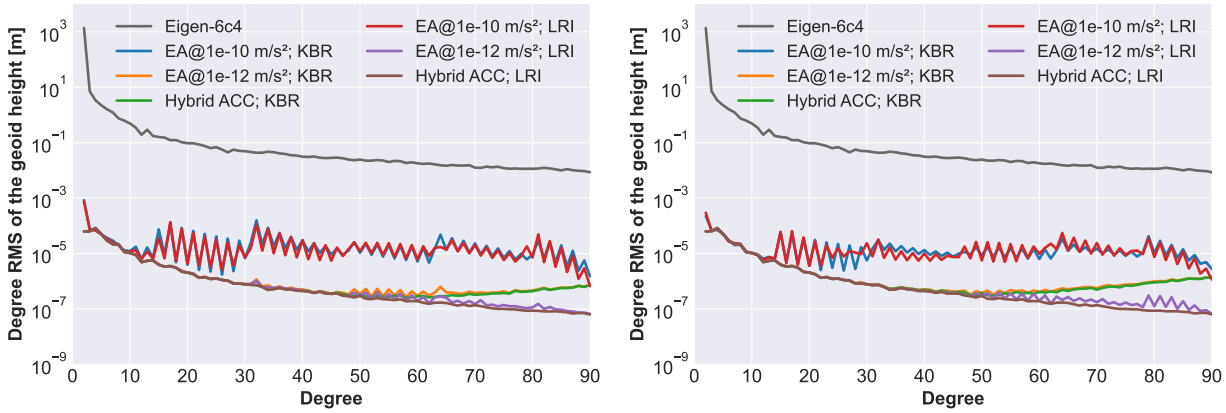


Figure 4.25: ASD of considered noise sources

In the following, results using different EA models and the hybrid accelerometer model of Figure 3.8 are discussed. Furthermore, the solutions are calculated with KBR noise and LRI noise. For the derivation and a detailed description of these noise models, the reader is referred to section 3.3. As discussed in sections 4.1, 4.2 and 4.3, the magnitude of the non-gravitational acceleration signal is important for the accelerometer performance. A higher orbit altitude leads to small non-gravitational accelerations which is beneficial. In contrast, the gravitational signal attenuates with the distance to the Earth. Thus, several orbit altitude are tested: 462 km, 363 km, 303 km and 246 km (cf. Table 4.1). All scenarios in this section are simulated with the assumption that the satellite is equipped with a drag-free system. Consequently, no additional errors due to the scale factor knowledge or the variation of acceleration within one interferometer cycle are considered.

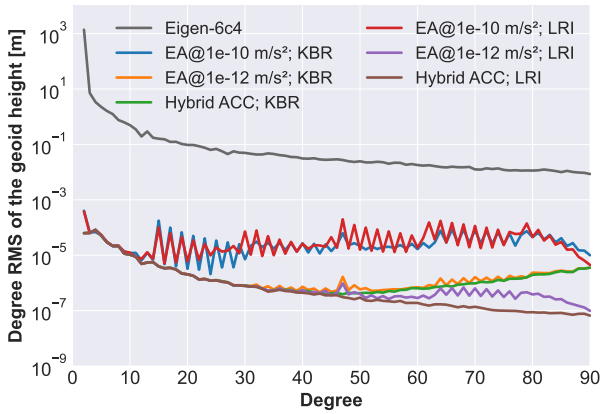
Differences between the reference gravity field model and the recovered gravity field model are calculated in order to evaluate the simulation results applying different types of accelerometers. These coefficient differences are shown, as they represent the true errors. The formal errors are not shown, but the agreement with the true errors is shown in section 3.6. The evaluation is carried out in the spectral and the space domain. The calculations of these

error representations are given in the equations (2.6) to (2.14). Figure 4.26 gives an overview of the gravity field solutions using different input parameters. The results are represented in terms of degree RMS of the geoid height. It has to be noted that the observations are synthesized using the gravity field coefficients up to degree and order 90 only. This results in a decrease of the degree RMS at higher degrees in some scenarios. Applying the same maximum degree in synthesis and recovery allows a fair comparison of the various scenarios, because the omission error and the aliasing from high-frequency signal to low-frequency signal is not included in the results.

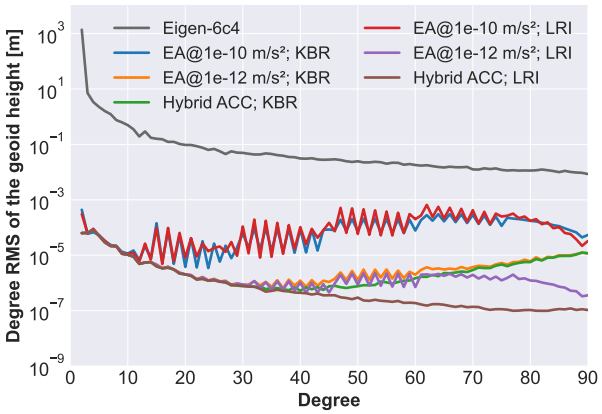


(a) h=246 km

(b) h=303 km



(c) h=363 km



(d) h=462 km

Figure 4.26: Degree RMS of the coefficient differences for different accelerometer noise models, ranging noise models for the altitudes of (a) 246 km, (b) 303 km, (c) 363 km and (d) 462 km including AOD and ocean-tide error

It is evident from Figure 4.26 that up to degree 10, there is no significant difference between the solutions of all scenarios. This is caused by the dominance of the AOD and ocean-tide errors in these low order coefficients. At degrees higher than 10, the solution using an EA with a noise level of $1 \times 10^{-10}\,\mathrm{m/s^2}$ in the frequencies from $2 \times 10^{-3}\,\mathrm{Hz}$ to $1 \times 10^{-1}\,\mathrm{Hz}$ (cf. blue and red curves) is considerably worse than the ones with a noise level of $1 \times 10^{-12}\,\mathrm{m/s^2}$ in the mentioned frequencies. Hence, it can be concluded that the accelerometer with noise

level of $1 \times 10^{-10}\,\mathrm{m/s^2}$ is the limiting instrument. This is confirmed by the fact that the noise for the distance measurement has hardly any influence on the results. The results with LRI noise (red curve) and KBR noise (blue curve) are very similar for this accelerometer performance for all orbit scenarios.
The improvement is large, when using an EA with a noise level of $1 \times 10^{-12}\,\mathrm{m/s^2}$ in the frequencies from $2 \times 10^{-3}\,\mathrm{Hz}$ to $1 \times 10^{-1}\,\mathrm{Hz}$ instead. The results for the EA with a noise level at $1 \times 10^{-12}\,\mathrm{m/s^2}$ and for the hybrid accelerometer (combination EA with $1 \times 10^{-12}\,\mathrm{m/s^2}$ noise in MBW and CAI with $1 \times 10^{-11}\,\mathrm{m/s^2}$ noise in all frequencies) are the same up to degree 30 for the altitudes of 363 km and 462 km and up to degree 40 for the altitude of 246 km and 303 km. The reason for this is the degradation due to the AOD and ocean-tide errors in these frequencies. In higher degrees, the solutions with LRI noise perform better compared to KBR noise. This impact is stronger for the two higher altitudes. It can be noticed that gravity field solutions with a hybrid accelerometer are smoother than the solutions with the electrostatic one, but they are at the same error level when introducing KBR noise. This behavior also holds true with LRI noise for the altitudes of 246 km and 303 km. For scenarios with higher altitudes, the ranging measurement noise has a higher influence in the degrees from 50 to 90.
Time-variable background model errors are introduced by a scaling of the models, 10 % of AOD1B product RL 6 and 10 % of the FES2014b product, in the simulations shown in Figure 4.26. Another option is to take the difference between different models into account. In Figure 4.27 the gravity solutions with these two options for the background modeling errors are compared.
When using the EA with a noise level of $1 \times 10^{-10}\,\mathrm{m/s^2}$, the choice of error assumption for background modeling does not matter. The cases with better performing accelerometers show that the error with RL5-RL6 for AOD and EOT11a-FES2014b is higher than 10 % of the products. Consequently, the degradation by AOD and ocean tides is slightly larger.

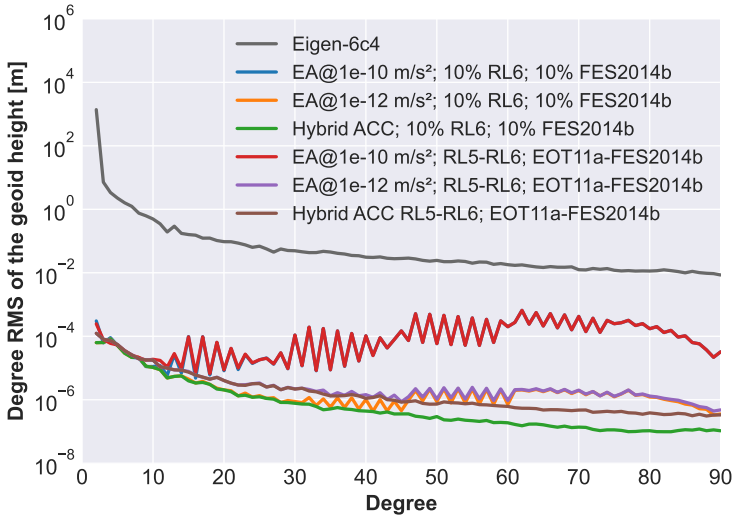
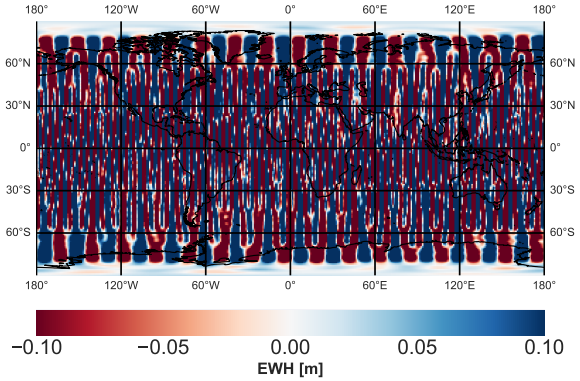


Figure 4.27: Degree RMS of the coefficient differences for different accelerometer noise models with an LRI noise model for the altitude of 462 km including different error assumptions for AOD and ocean-tide error

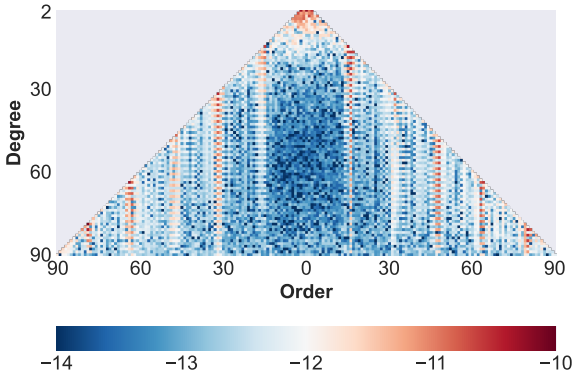
In order to evaluate the differences between the simulation scenarios more accurately, the

pyramid representation of the coefficient differences and the results in the space domain are given. As the selection of the very low altitude of 246 km is critical due to the short mission lifetime, only results for the altitudes of 303 km (Figures 4.28 and 4.29) and for 462 km (Figures 4.30 and 4.31) are shown in this section. The latter ones are representative for the orbits of GRACE and GRACE-FO. The results for further scenarios of Figure 4.26 are given in the Appendix A.3: Figures A.5 and A.6 for the orbit altitude of 246 km and Figures A.7 and A.8 for 363 km. Figure 4.28 shows that the gravity field solution is largely degraded by the accelerometer with noise level of $1 \times 10^{-10}\,\mathrm{m/s^2}$. The solution is covered with striping effects up to 1 m in north-south direction in space and at specific orders in the pyramid representation (the color bar of the plots is limited to ± 0.1 m for a better comparison of different scenarios). These effects are largely reduced in the simulation scenario with an EA with a higher sensitivity of $1 \times 10^{-12}\,\mathrm{m/s^2}$, but stripes are still visible with a magnitude of maximum 0.1 m. The solution is only marginally improved when using a hybrid accelerometer. Introducing LRI noise instead of KBR noise improves the two latter solutions significantly (cf. Figure 4.29). While there are still artifacts in the electrostatic solution, they vanish by the addition of a CAI accelerometer. The coefficient differences are mainly caused by AOD and ocean-tide errors.
The simulation results with an altitude of 462 km are generally worse, this is valid for all instrument scenarios. The striping effects increase especially for the scenario with KBR noise and EA noise at a level of $1 \times 10^{-10}\,\mathrm{m/s^2}$ (Figure 4.30). The sectorial coefficients and coefficients in higher degrees and orders are less accurate and striping effects at specific orders are stronger. The use of an accelerometer with a higher sensitivity helps a lot to improve the solution. The addition of CAI gives a small enhancement. In terms of EWH, the error is up to 0.8 m. The addition of a CAI accelerometer to an EA gives more obvious improvements when using LRI noise (cf. Figure 4.31). The striping effects in north-south direction of 0.15 m and the degradation at specific orders of the coefficients are largely reduced. It can be stated, that the instrument performance has a higher influence on the quality of the gravity field solution when the orbit altitude is higher.

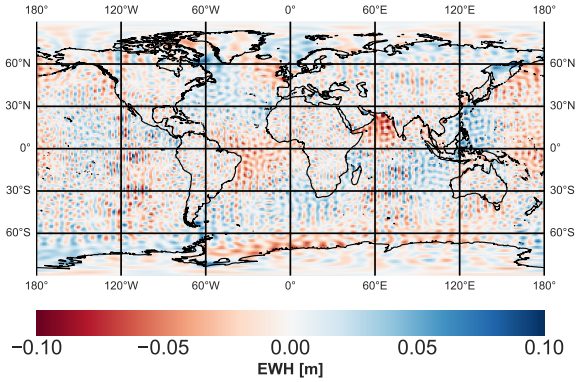
In space domain, north-south striping effects are characteristic for GRACE solutions due to the the sampling and flight direction of the polar in-line pair. Therefore, they are typically filtered out in order to reduce noise and systematic errors. A common method is a spatial averaging filter, where the neighboring points over a particular region are averaged and weighted (Jekeli, 1981; Wahr et al., 1998). Localized noise can be attenuated by averaging. However, in the filtering process not only noise but also gravity signal information is suppressed. The systematic errors increase strongly with SH degree (Klees et al., 2008).
The result with the EA shows large striping effects at orders $m = 16 \times k, k \in \mathbb{N}$. These specific orders correspond to the orbit frequency and multiples of it. This reveals, that the CAI accelerometer counteracts the problem with orbit resonances and striping effects owing to its low noise in low frequencies. It can be concluded that the bias drift of the EA in low frequencies causes degradation in the orbital resonance order 16 and its integer multiples. However, this problem can also be solved by filtering, because frequencies below 1.8×10^{-4} Hz imply no gravity field signal. In McGirr et al. (2022), an improvement of GRACE gravity solutions is achieved by applying a high-pass filter to the accelerometer data and removing the low-frequency components below 4.5×10^{-5} Hz.



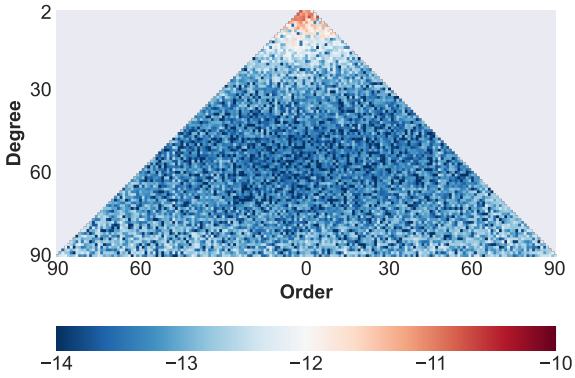
(a) EA with $1 \times 10^{-10}\,\mathrm{m/s^2}$ noise in MBW



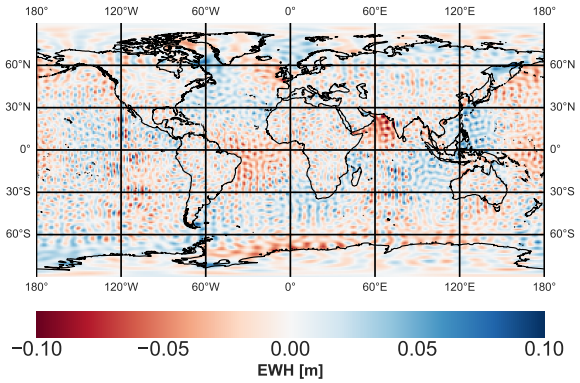
(b) EA with $1 \times 10^{-10}\,\mathrm{m/s^2}$ noise in MBW



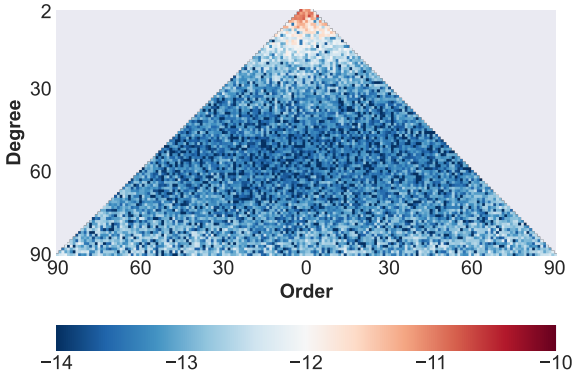
(c) EA with $1 \times 10^{-12}\,\mathrm{m/s^2}$ noise in MBW



(d) EA with $1 \times 10^{-12}\,\mathrm{m/s^2}$ noise in MBW

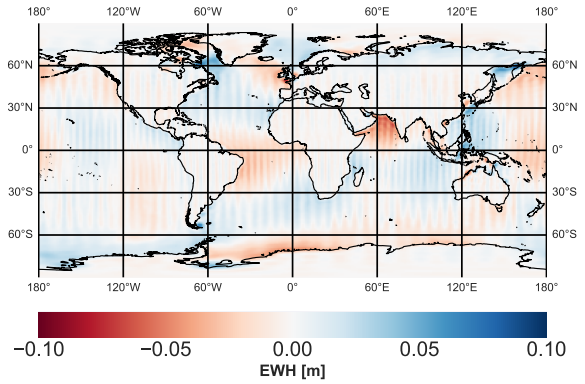


(e) Hybrid accelerometer (EA with $1 \times 10^{-12}\,\mathrm{m/s^2}$ noise in MBW and CAI with $1 \times 10^{-11}\,\mathrm{m/s^2}$ noise)

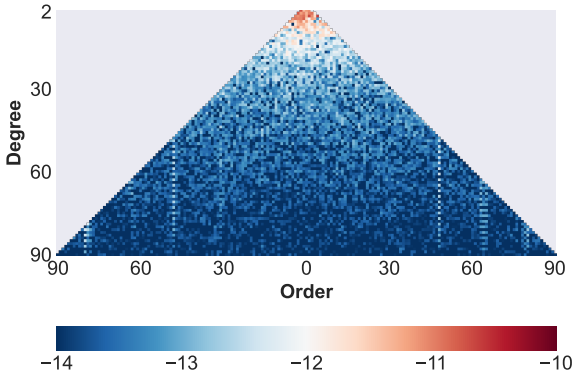


(f) Hybrid accelerometer (EA with $1 \times 10^{-12}\,\mathrm{m/s^2}$ noise in MBW and CAI with $1 \times 10^{-11}\,\mathrm{m/s^2}$ noise)

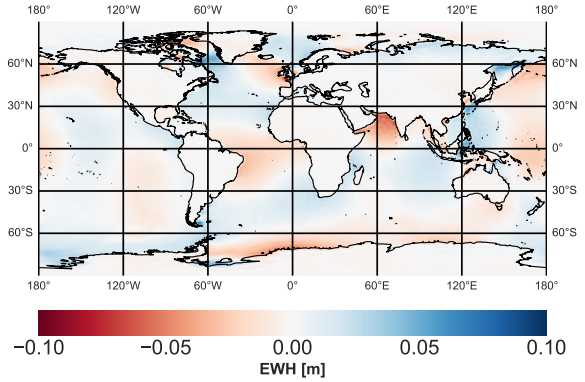
Figure 4.28: Coefficient differences between recovered and reference gravity field: spatial representation in terms of EWH and pyramid representation (logarithm scale); parameters: h=303 km, KBR measurement noise and different accelerometer noise models



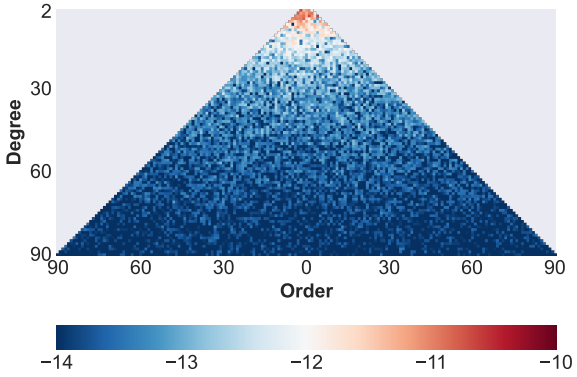
(a) EA with $1 \times 10^{-12}\,\mathrm{m/s^2}$ noise in MBW



(b) EA with $1 \times 10^{-12}\,\mathrm{m/s^2}$ noise in MBW



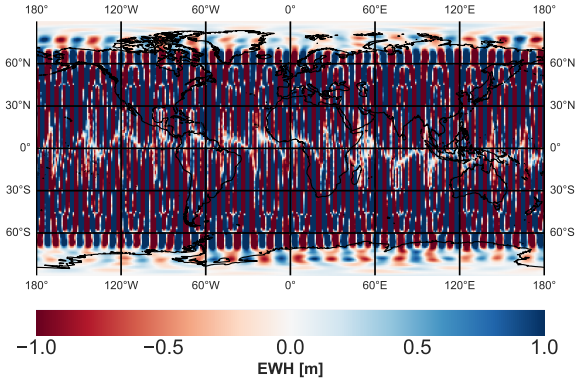
(c) Hybrid accelerometer (EA with $1 \times 10^{-12}\,\mathrm{m/s^2}$ noise in MBW and CAI with $1 \times 10^{-11}\,\mathrm{m/s^2}$ noise)



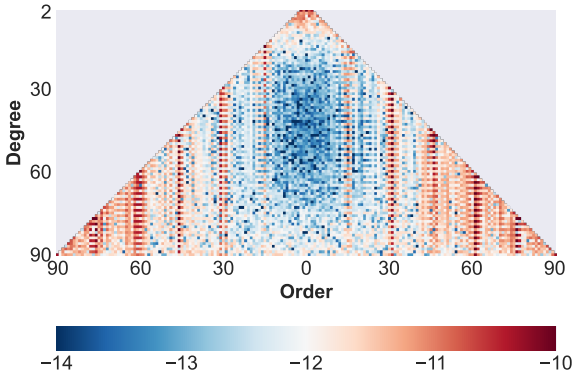
(d) Hybrid accelerometer (EA with $1 \times 10^{-12}\,\mathrm{m/s^2}$ noise in MBW and CAI with $1 \times 10^{-11}\,\mathrm{m/s^2}$ noise)

Figure 4.29: Coefficient differences between recovered and reference gravity field: spatial representation in terms of EWH and pyramid representation (logarithm scale); parameters: h=303 km, LRI measurement noise and different accelerometer noise models

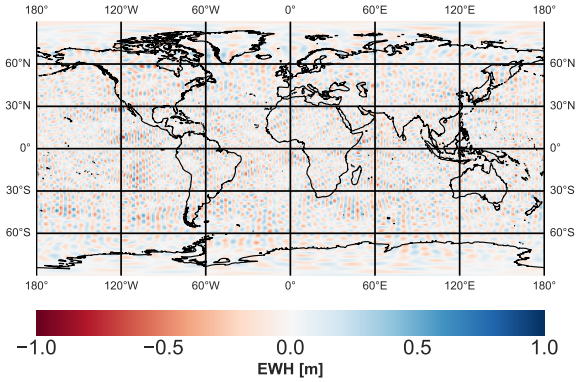
The evaluation of the true errors in the spatial domain confirms a great improvement of the recovered gravity field for the simulation with a hybrid accelerometer. The errors expressed as EWH are two orders of magnitude lower when using the hybrid sensor. The dominant factors are AOD and ocean-tide errors. This can be observed by comparing the coefficient differences to the input noise representing AOD and ocean tide de-aliasing (cf. Figure 3.13 and Figure 3.14).



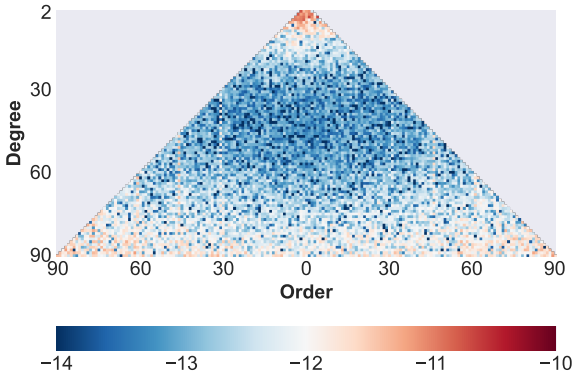
(a) EA with $1 \times 10^{-10}\,\mathrm{m/s^2}$ noise in MBW



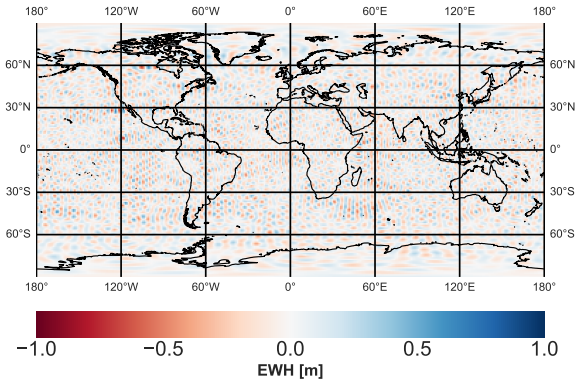
(b) EA with $1 \times 10^{-10}\,\mathrm{m/s^2}$ noise in MBW



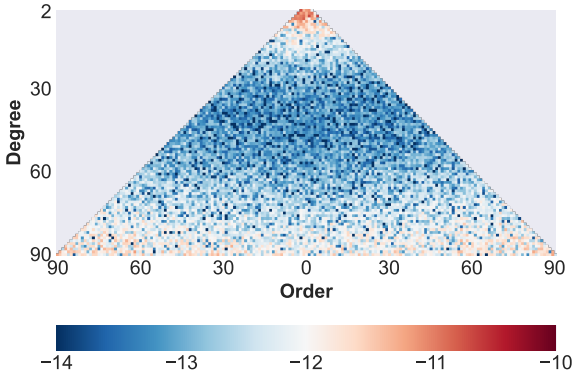
(c) EA with $1 \times 10^{-12}\,\mathrm{m/s^2}$ noise in MBW



(d) EA with $1 \times 10^{-12}\,\mathrm{m/s^2}$ noise in MBW

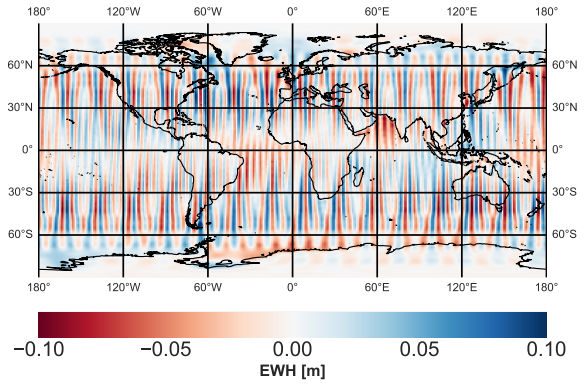


(e) Hybrid accelerometer (EA with $1 \times 10^{-12}\,\mathrm{m/s^2}$ noise in MBW and CAI with $1 \times 10^{-11}\,\mathrm{m/s^2}$ noise)

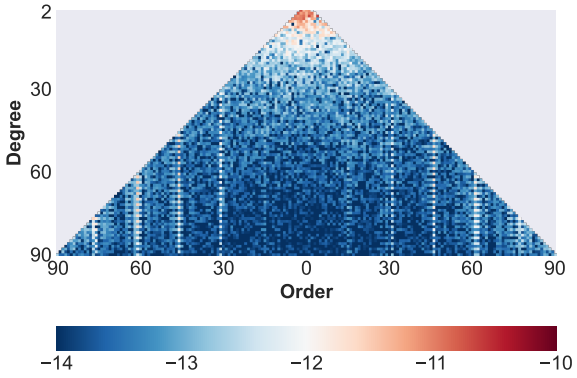


(f) Hybrid accelerometer (EA with $1 \times 10^{-12}\,\mathrm{m/s^2}$ noise in MBW and CAI with $1 \times 10^{-11}\,\mathrm{m/s^2}$ noise)

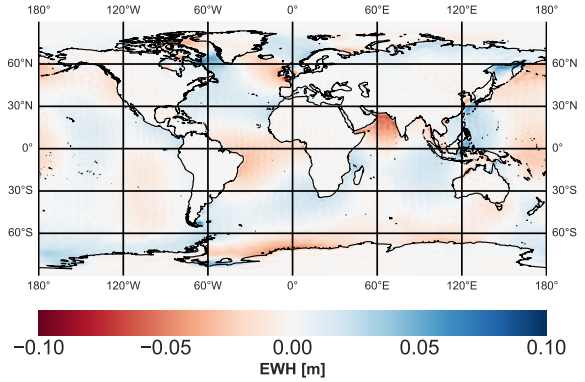
Figure 4.30: Coefficient differences between recovered and reference gravity field: spatial representation in terms of EWH and pyramid representation (logarithm scale); parameters: h=462 km, KBR measurement noise and different accelerometer noise models



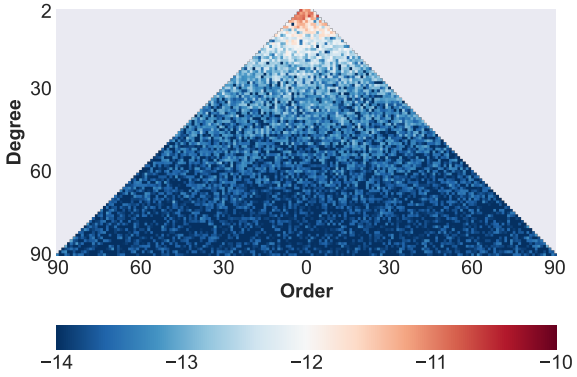
(a) EA with $1 \times 10^{-12}\,\mathrm{m/s^2}$ noise in MBW



(b) EA with $1 \times 10^{-12}\,\mathrm{m/s^2}$ noise in MBW



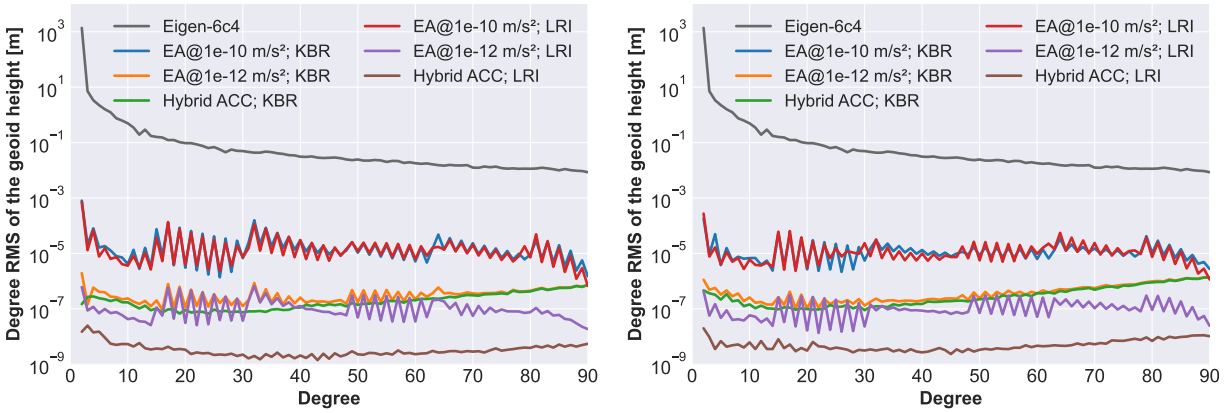
(c) Hybrid accelerometer (EA with $1 \times 10^{-12}\,\mathrm{m/s^2}$ noise in MBW and CAI with $1 \times 10^{-11}\,\mathrm{m/s^2}$ noise)



(d) Hybrid accelerometer (EA with $1 \times 10^{-12}\,\mathrm{m/s^2}$ noise in MBW and CAI with $1 \times 10^{-11}\,\mathrm{m/s^2}$ noise)

Figure 4.31: Coefficient differences between recovered and reference gravity field: spatial representation in terms of EWH and pyramid representation (logarithm scale); parameters: h=462 km, LRI measurement noise and different accelerometer noise models

As limiting factors are clearly AOD and ocean-tide errors, closed-loop simulations are performed additionally without these error sources. Accordingly, the following test scenarios include only influences of the instruments. This is performed to demonstrate more clearly the potential for improvements by enhancing the accelerometers. The degree RMS of the geoid height for several simulation scenarios are given in Figure 4.32. First, it can be seen that the influence of the instrument performance on the gravity field solution is now stronger. The lower the orbit altitude, the smaller is the degree RMS. For simulation scenarios with an EA at $1 \times 10^{-10}\,\mathrm{m/s^2}$ in MBW, the ranging instrument noise has no significant impact at altitudes of 246 km, 303 km and 363 km. In contrast, for the highest altitude of 462 km, the solution is improved by using LRI noise. The solution with only an EA (noise level $1 \times 10^{-12}\,\mathrm{m/s^2}$ in MBW) and one with the combination with CAI (noise level of $1 \times 10^{-11}\,\mathrm{m/s^2}$ in all frequencies, cf. Figure 3.8) are almost at the same level with KBR noise for the ranging measurements. The combination with CAI eliminates the zigzag behavior and the error curve is slightly lower up to degree 80. When using LRI noise, the difference between electrostatic and hybrid accelerometers becomes much more apparent.



(a) h=246 km

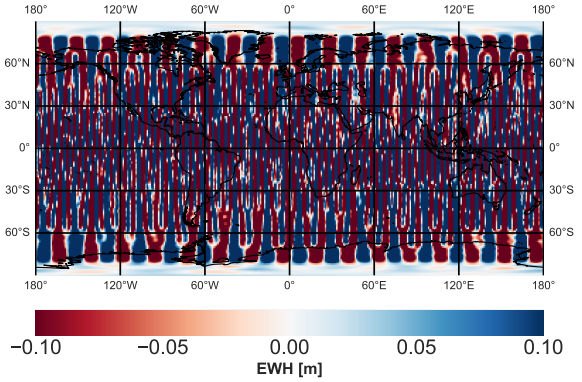
(b) h=303 km

(c) h=363 km

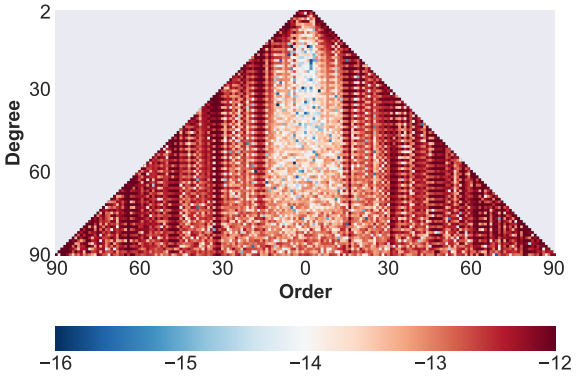
(d) h=462 km

Figure 4.32: Degree RMS of the coefficient differences for different accelerometer noise models and ranging noise models for altitudes of (a) 246 km, (b) 303 km, (c) 363 km and (d) 462 km for the instrument-only scenarios

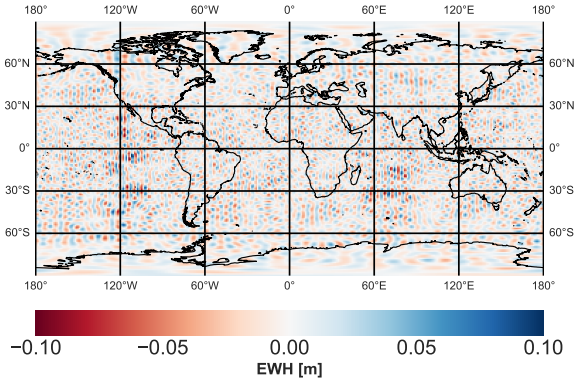
The detailed results are discussed for the altitudes of 303 km (cf. Figure 4.33 and 4.34) and 462 km (cf. Figure 4.35 and 4.36) only. It should be noted that the pyramid plots for instrument-only cases have a different scaling than the plots before. The two-dimensional error and the error in the spatial domain for all scenarios are shown in the appendix (Figures A.1, A.2, A.3 and A.4). The improvement by the utilization of the hybrid accelerometer is significantly visible. The striping effects at specific orders are almost eliminated by adding a CAI accelerometer for the orbit altitude of 303 km with KBR noise. The EWH calculated from the coefficient differences have a magnitude of 1 m for the case with KBR noise and EA noise at $1 \times 10^{-10}\,\mathrm{m/s^2}$. The result with an EA at $1 \times 10^{-12}\,\mathrm{m/s^2}$ is more accurate and the EWH is ± 0.1 m. Striping effects at some orders are still visible for the two-dimensional error representation, but they are almost eliminated by using a hybrid accelerometer instead.



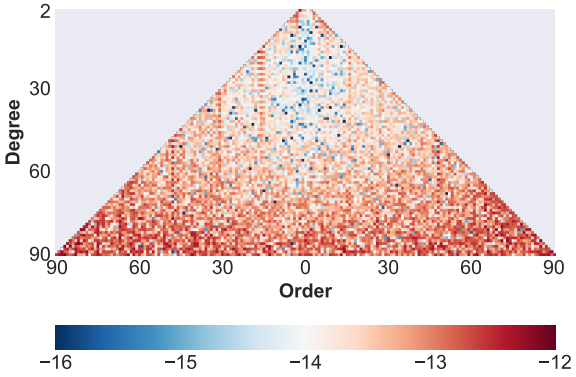
(a) EA with $1 \times 10^{-10}\,\mathrm{m/s^2}$ noise in MBW



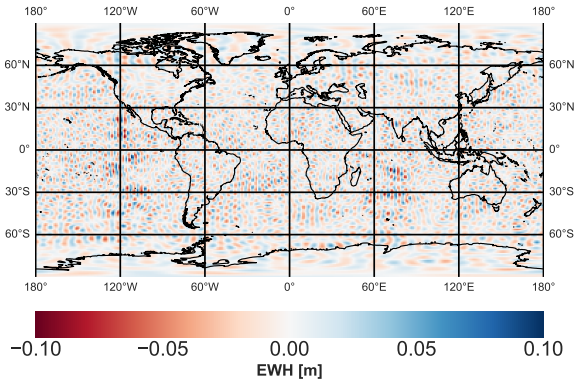
(b) EA with $1 \times 10^{-10}\,\mathrm{m/s^2}$ noise in MBW



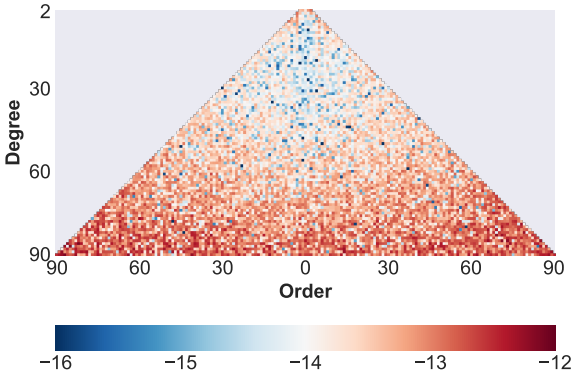
(c) EA with $1 \times 10^{-12}\,\mathrm{m/s^2}$ noise in MBW



(d) EA with $1 \times 10^{-12}\,\mathrm{m/s^2}$ noise in MBW

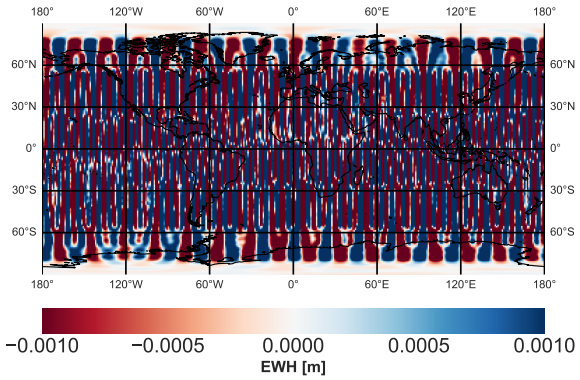


(e) Hybrid accelerometer (EA with $1 \times 10^{-12}\,\mathrm{m/s^2}$ noise in MBW and CAI with $1 \times 10^{-11}\,\mathrm{m/s^2}$ noise)

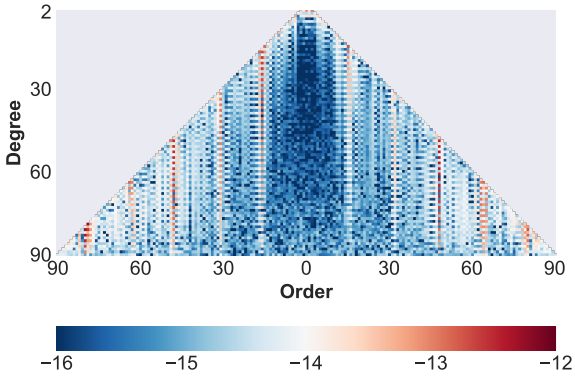


(f) Hybrid accelerometer (EA with $1 \times 10^{-12}\,\mathrm{m/s^2}$ noise in MBW and CAI with $1 \times 10^{-11}\,\mathrm{m/s^2}$ noise)

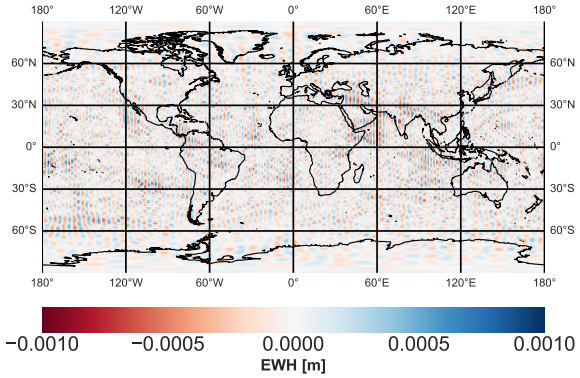
Figure 4.33: Coefficient differences between recovered and reference gravity field: spatial representation in terms of EWH and pyramid representation (logarithm scale); parameters: h=303 km, only instrument noise, KBR measurement noise and different accelerometer noise models



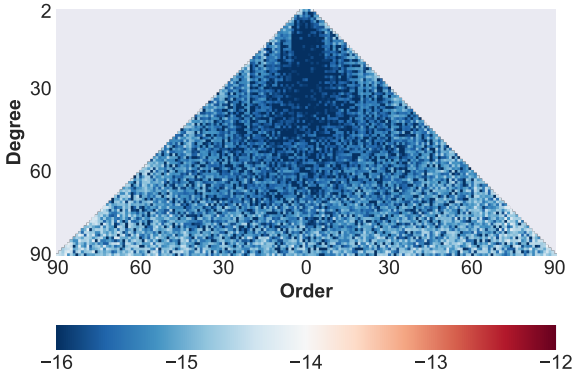
(a) EA with $1 \times 10^{-12}\,\mathrm{m/s^2}$ noise in MBW



(b) EA with $1 \times 10^{-12}\,\mathrm{m/s^2}$ noise in MBW



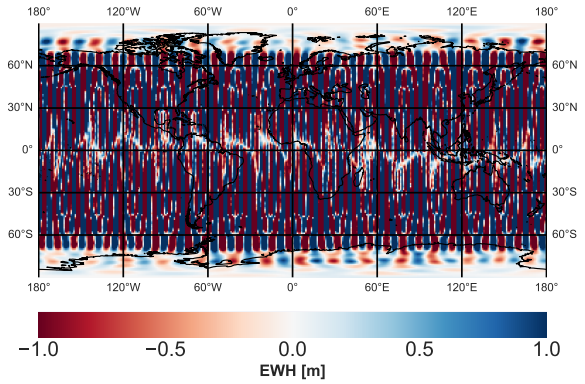
(c) Hybrid accelerometer (EA with $1 \times 10^{-12}\,\mathrm{m/s^2}$ noise in MBW and CAI with $1 \times 10^{-11}\,\mathrm{m/s^2}$ noise)



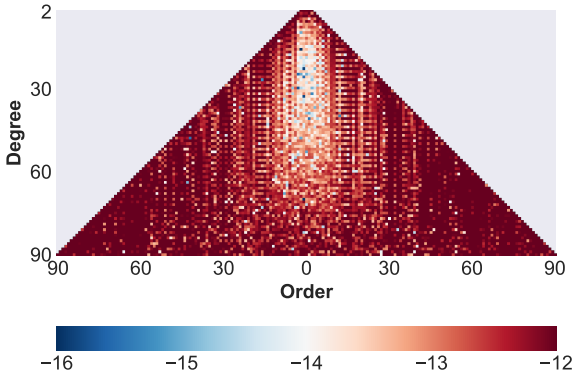
(d) Hybrid accelerometer (EA with $1 \times 10^{-12}\,\mathrm{m/s^2}$ noise in MBW and CAI with $1 \times 10^{-11}\,\mathrm{m/s^2}$ noise)

Figure 4.34: Coefficient differences between recovered and reference gravity field: spatial representation in terms of EWH and pyramid representation (logarithm scale); parameters: h=303 km, only instrument noise, LRI measurement noise and different accelerometer noise models

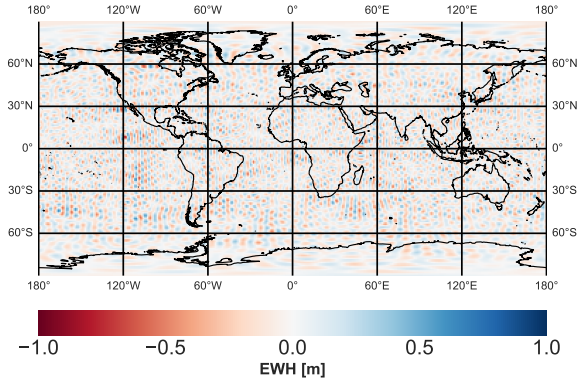
When using LRI instead of KBR noise, a similar behavior is visible. In this case, the error in EWH is reduced to ±0.8 mm when using a hybrid accelerometer. The EWH varies between ±10 mm with only an EA (with a noise level of $1 \times 10^{-12}\,\mathrm{m/s^2}$).
For an altitude of 462 km, similar improvements are achieved caused by the chosen accelerometer. In total, the outcome is worse due to the attenuation of the gravity signal with higher altitude. The scenario with LRI and hybrid accelerometer noise induces an EWH error of ±5 mm. With the performance of an EA, the error in the space domain is ±125 mm. Thus, the addition of CAI enables an improvement by the factor of 25 in terms of EWH.



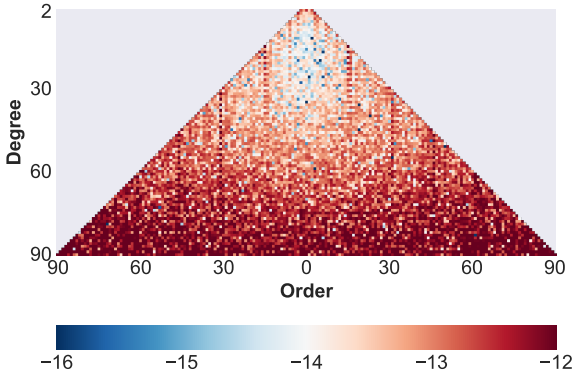
(a) EA with $1 \times 10^{-10}\,\mathrm{m/s^2}$ noise in MBW



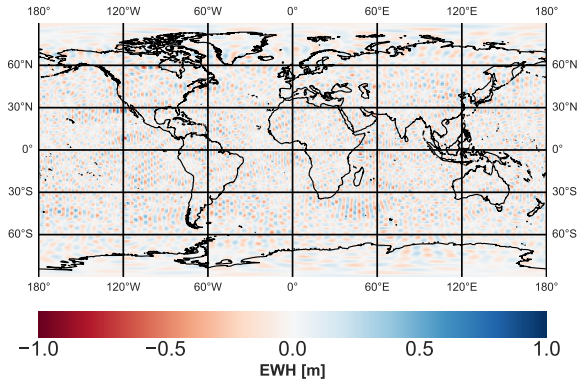
(b) EA with $1 \times 10^{-10}\,\mathrm{m/s^2}$ noise in MBW



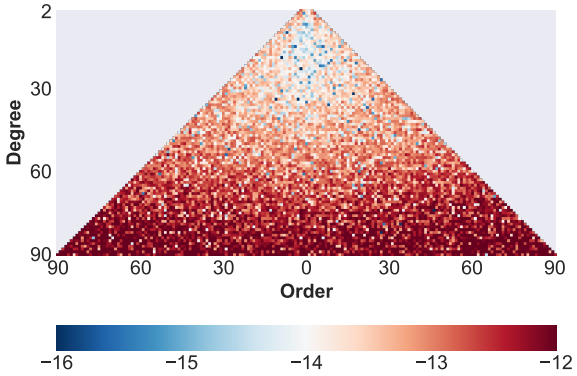
(c) EA with $1 \times 10^{-12}\,\mathrm{m/s^2}$ noise in MBW



(d) EA with $1 \times 10^{-12}\,\mathrm{m/s^2}$ noise in MBW

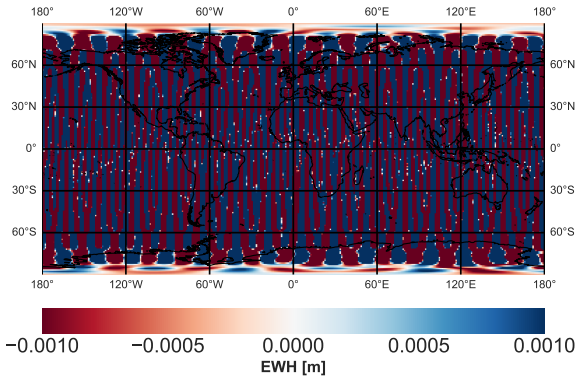


(e) Hybrid accelerometer (EA with $1 \times 10^{-12}\,\mathrm{m/s^2}$ noise in MBW and CAI with $1 \times 10^{-11}\,\mathrm{m/s^2}$ noise)

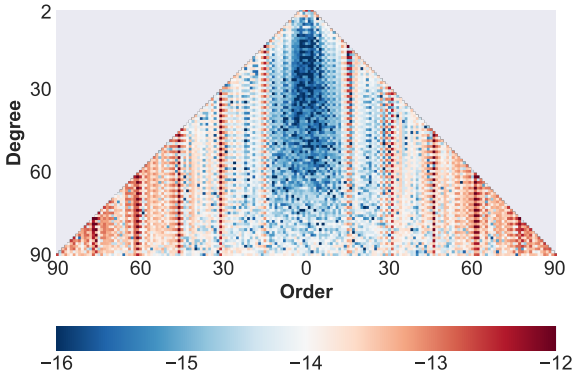


(f) Hybrid accelerometer (EA with $1 \times 10^{-12}\,\mathrm{m/s^2}$ noise in MBW and CAI with $1 \times 10^{-11}\,\mathrm{m/s^2}$ noise)

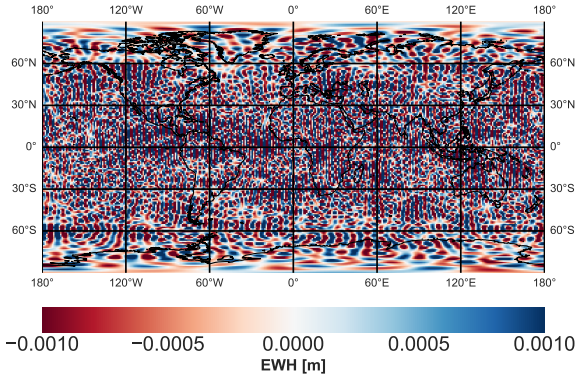
Figure 4.35: Coefficient differences between recovered and reference gravity field: spatial representation in terms of EWH and pyramid representation (logarithm scale); parameters: h=462 km, only instrument noise, KBR measurement noise and different accelerometer noise models



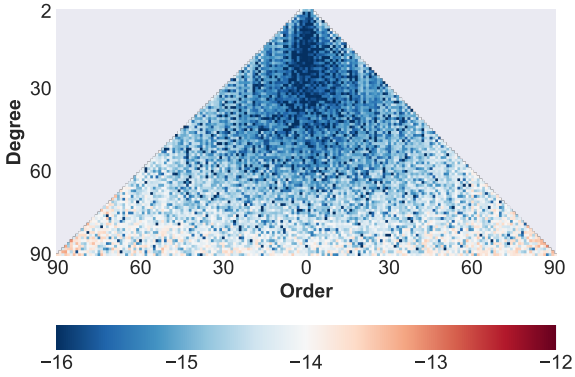
(a) EA with $1 \times 10^{-12}\,\mathrm{m/s^2}$ noise in MBW



(b) EA with $1 \times 10^{-12}\,\mathrm{m/s^2}$ noise in MBW



(c) Hybrid accelerometer (EA with $1 \times 10^{-12}\,\mathrm{m/s^2}$ noise in MBW and CAI with $1 \times 10^{-11}\,\mathrm{m/s^2}$ noise)



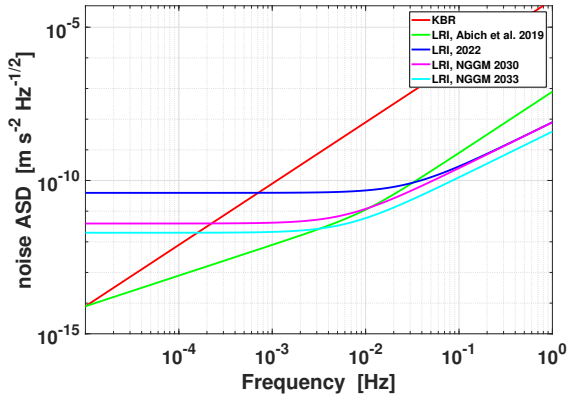
(d) Hybrid accelerometer (EA with $1 \times 10^{-12}\,\mathrm{m/s^2}$ noise in MBW and CAI with $1 \times 10^{-11}\,\mathrm{m/s^2}$ noise)

Figure 4.36: Coefficient differences between recovered and reference gravity field: spatial representation in terms of EWH and pyramid representation (logarithm scale); parameters: h=462 km, only instrument noise, LRI measurement noise and variation of accelerometer noise

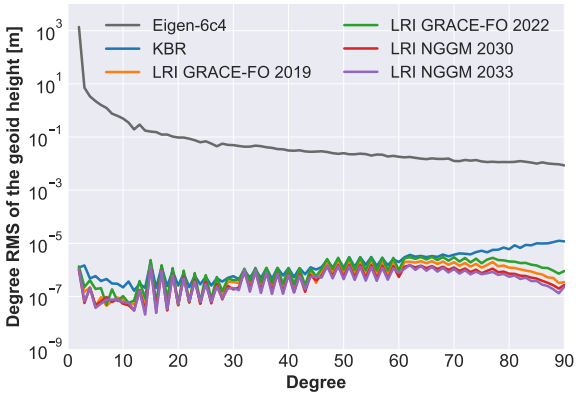
Cumulative geoid errors up to degree and order 90 are given in Table 4.3 for instrument-only scenarios. Structures of coefficients with maximum degree of 90 correspond approximately to a spatial resolution of 220 km. Cumulative geoid errors increase significantly with increasing orbit altitude. An improvement by including LRI noise instead of KBR is not verified in all scenarios, but a benefit is obtained for instrument-only scenarios with a hybrid accelerometer. In these cases, the geoid error is reduced by a factor of 100. However, the included LRI noise model is at the state of knowledge of Abich et al. (2019). The model is slightly too optimistic according to the state of knowledge in 2022. The different LRI noise models (cf. section 3.3.3) and the resulting degree RMS of the coefficient differences are illustrated in Figure 4.37. These results correspond to an orbit altitude of 462 km. The difference between solutions using the LRI model 2019 and the NGGM models is not significant when a hybrid accelerometer or an electrostatic one with noise level of $1 \times 10^{-12}\,\mathrm{m/s^2}$ is used. The simulations including the LRI noise model of 2022 result in higher coefficient differences. The biggest effect is noticed for the instrument-only scenario with a hybrid accelerometer. The scenarios including background modeling errors show that the gravity field solutions with KBR noise and LRI noise (model 2022) do not differ significantly.

Table 4.3: Cumulative geoid error up to degree and order 90; observations of one month with sampling frequency of 0.2 Hz; instrument-only scenarios

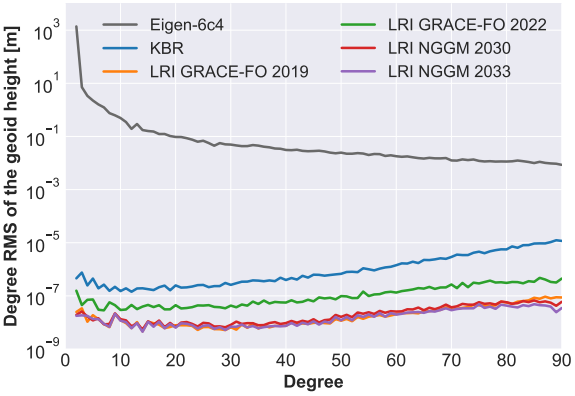
		Cumulative geoid error [mm] at altitude of			
Ranging	Accelerometer	246 km	303 km	363 km	462 km
KBR	EA, $1 \times 10^{-10}\,\mathrm{m/s^2}$	3.04	1.47	3.81	14.03
	EA, $1 \times 10^{-12}\,\mathrm{m/s^2}$	0.04	0.06	0.14	0.48
	Hybrid	0.03	0.06	0.13	0.44
LRI	EA, $1 \times 10^{-10}\,\mathrm{m/s^2}$	2.69	1.71	5.99	135.45
	EA, $1 \times 10^{-12}\,\mathrm{m/s^2}$	0.01	0.01	0.03	0.12
	Hybrid	$\ll$0.01	$\ll$0.01	$\ll$0.01	$\ll$0.01



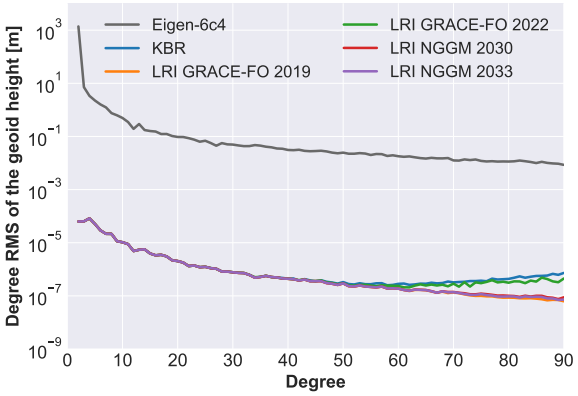
(a) Noise models for ranging instruments



(b) EA at a noise level of $1 \times 10^{-12}\,\mathrm{m/s^2}$



(c) Hybrid accelerometer



(d) Hybrid accelerometer including AOD and ocean-tide errors

Figure 4.37: Degree RMS of the coefficient differences between recovered and reference gravity field solutions with various LRI noise models for an orbit altitude of 462 km

The cumulative geoid errors of the scenarios including AOD and ocean-tide errors are given in Table 4.4. The cumulative error of the best solution is 0.42 mm. A significant degradation due to the orbit altitude is only found when the EA noise is at a level of $1 \times 10^{-10}\,\mathrm{m/s^2}$. The solutions with an EA noise level of $1 \times 10^{-12}\,\mathrm{m/s^2}$ show approximately the same cumulative geoid error for all altitudes due to the dominance of the background modeling errors. This illustrates the need to improve the models of AOD and ocean tides. The improvement by the addition of a CAI accelerometer to an EA is not significant, here. The largest improvement of 0.03 mm is achieved for the scenarios with an altitude of 462 km.

Table 4.4: Cumulative geoid error up to degree and order 90; observations of one month with sampling frequency of 0.2 Hz; scenarios including AOD and ocean-tide error

		Cumulative geoid error [mm] at altitude of			
Ranging	Accelerometer	246 km	303 km	363 km	462 km
KBR	EA, $1 \times 10^{-10}\,\mathrm{m/s^2}$	3.10	1.53	3.85	14.04
	EA, $1 \times 10^{-12}\,\mathrm{m/s^2}$	0.42	0.42	0.44	0.64
	Hybrid	0.42	0.42	0.44	0.61
LRI	EA, $1 \times 10^{-10}\,\mathrm{m/s^2}$	2.76	1.77	6.01	22.02
	EA, $1 \times 10^{-12}\,\mathrm{m/s^2}$	0.42	0.42	0.42	0.44
	Hybrid	0.42	0.42	0.42	0.42

4.5 Gravity Field Solutions using Different Accelerometer Types for Gradiometry Missions

In addition to the studied ll-SST scenarios, gravity field solutions of gradiometry missions are analyzed. The focus is on the impact of the accelerometer performances on the gravity field solution. When only additive noise for the accelerometers is considered, the measured gravity gradient $V_{\hat{y}\hat{y}}$ is given by (Douch et al., 2018b)

$$V_{\hat{y}\hat{y}} = \frac{(a_{1,y} + n_{1,y}) - (a_{2,y} + n_{2,y})}{L_y}, \tag{4.21}$$

where $a_{1,y}$ is the true acceleration of the accelerometer with index 1 and $n_{1,y}$ is its noise. The notation is analog for the second accelerometer with index 2. L_y is the distance between the two accelerometers. The gradiometer noise is then calculated from the two accelerometer noises and the baseline length:

$$n_{V_{yy}} = \frac{n_{1,y} - n_{2,y}}{L_y}, \tag{4.22}$$

where $n_{1,y}$ and $n_{2,y}$ are uncorrelated.
In this study, only a gradiometer in cross-track direction is considered. The reason for this is the critical rotation rate in along-track or nadir direction when using CAI accelerometers. According to Douch et al. (2018b), the maximum rotation rate in cross-track direction is

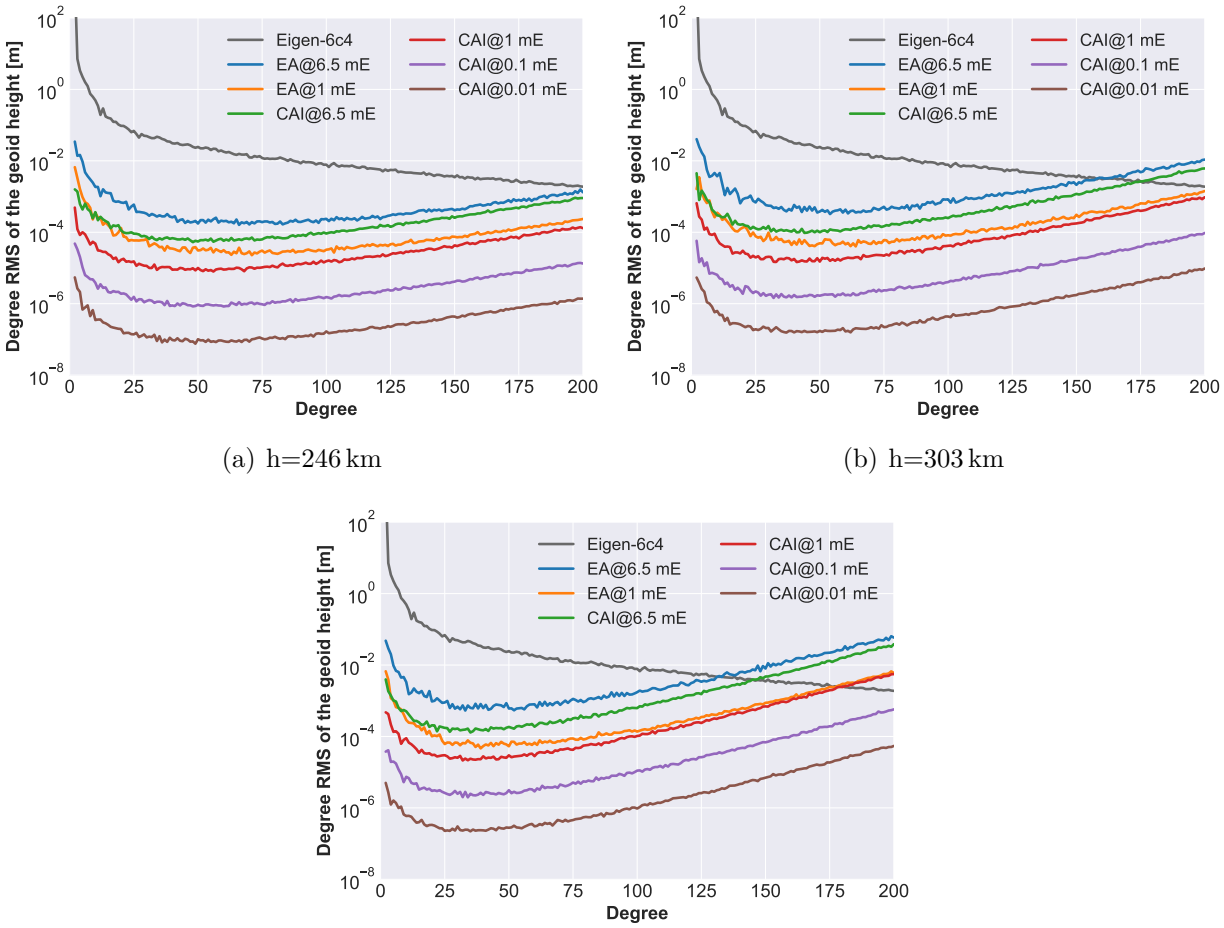
approximately 1 µrad/s. In contrast, in along-track and nadir direction the rotation rate would be 1 mrad/s. The two trajectories of the two atom clouds would not converge after the third laser pulse and consequently the contrast is reduced (Douch et al., 2018b). A second aspect is the rotation induced phase shift Φ_{rot}:

$$\Phi_{rot} = 2(k_{eff} \times v)\Omega T^2, \tag{4.23}$$

with the norm of the effective wave vector k_{eff}, the norm of the forward drift velocity v, the interferometer time T and the rotation rate Ω. In Meister et al. (2022) the rotation in along-track direction of the CAI reference mirror is evaluated as a significant degradation. One option to reduce this effect is the integration of a counter rotation of the mirror. Rotation compensation is also considered in the studies of Trimeche et al. (2019) and Migliaccio et al. (2019). The requirement for the maximum rotation rate is approximately 1 µrad/s for both aspects which is achieved for the cross-track axis in nadir pointing mode.

In Figure 4.38 the coefficient differences between recovered and reference gravity field are depicted for altitudes of 246 km, 303 km and 363 km in terms of degree RMS of the geoid height. Gradiometry develops its full strength in high degree coefficients, for which a low orbital altitude is necessary. Hence, the orbit altitude of 467 km is not investigated in this section. A GOCE-like scenario is tested with the accelerometer model given in equation (3.2) and a baseline length of 0.5 m which corresponds to a gradiometer noise at the level of 6.5 mE. Furthermore, an Electrostatic Gradiometer (EG) with lower noise level of 1 mE in the MBW, but the same increasing slope behavior in low and high frequencies, is evaluated. Beyond that, several CAI gradiometer noise models, which are characterized by white noise, are investigated: 6.5 mE, 1 mE, 0.1 mE and 0.01 mE.
The CAI gradiometer sensitivity strongly depends on the interrogation time of the interferometer. In order to achieve such high sensitivities of 1 mE or below it, interrogation times of several seconds are required. However, a low sampling rate would degrade the gravity field solution. An option to prevent this would be to have several atom clouds interrogating simultaneously as given in Trimeche et al. (2019). An interrogation time of tens of seconds would ensure a sensitivity of $1 \times 10^{-12}\,\mathrm{m/s^2}$ (Abend et al., 2023). Thus, a gradiometer sensitivity of 1 mE is possible with a measurement cycle time of 30 s.

Figure 4.38 clearly shows the result of the attenuation of the gravitational signal with increasing altitude. All coefficient differences in the scenarios with altitude of 246 km are below the static gravity field signal up to degree 200. The intersection of static gravity field signal and coefficient differences is at degree 130 for the altitude of 363 km using an EG noise level of 6.5 mE. When comparing the simulations including white noise of the CAI and the colored noise of the EG, the improvement by the flat noise curve is larger in low degree coefficients. However, an improvement is achieved in all coefficients up to degree 200. It can be concluded that CAI gradiometer characterized by white noise significantly improve the gravity field solution compared to EG with the same noise level in the MBW.



(a) h=246 km

(b) h=303 km

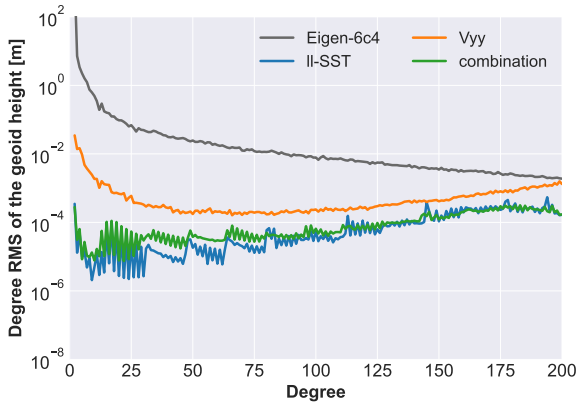
(c) h=363 km

Figure 4.38: Degree RMS of the coefficient differences between recovered and reference gravity field solutions of the cross-track component for different gradiometer noise models

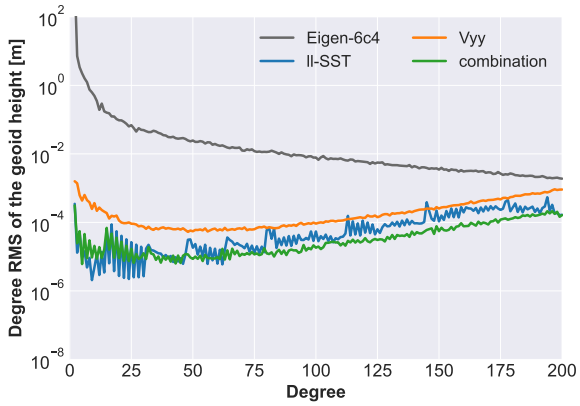
4.6 Combined Gravity Field Solutions from ll-SST and Cross-track Gradiometry

The addition of a cross-track gradiometer to one of the satellites of a ll-SST mission seems promising as this provides supplemental observations in east-west direction. Solutions of ll-SST are characterized by their striping effects in north-south direction. Implementing the gradiometer in cross-track direction instead of along-track or radial direction has further advantages concerning the rotation rates as addressed in section 4.5.
In this section, different instrument sensitivities and behaviors are studied for the mission concept. Combinations of gravity field solutions of section 4.4 and section 4.5 are investigated with maximum degree and order of 200. The solutions are combined at normal equation level, the theory is described in section 3.6.4. The reciprocal values of the posterior variances of the individual solutions are used as initial weighting factors. The posterior variances of all scenarios vary between 0.70 and 1.17. The variance components are estimated iteratively as given in section 3.6.4 and Koch and Kusche (2001). The concept is investigated for

the orbit altitudes of 246 km, 303 km and 363 km, and only instrument noise models for ranging measurement instruments, accelerometers and gradiometers have been considered. The spatial representation plots are given in terms of EWH as in section 4.4. The EWH in this section are also calculated from the coefficient differences up to degree and order 90 to allow a better comparison to the ones of section 4.4.
First, results using the orbit data with an altitude of 246 km are investigated. Further results for orbit altitudes of 303 km and 363 km are given in the appendix A.4. Different sensor behavior models are introduced for the ranging measurement instrument, for the accelerometer in the center of mass for each satellite used for the ll-SST solution and for the two accelerometers forming the cross-track gradiometer. Figures 4.39 and 4.40 show combinations of a gradiometer with a GRACE-like scenario. However, the addition of an electrostatic cross-track gradiometer with a noise level of 6.5 mE in the MBW does not improve the solution of a classical GRACE scenario (cf. Figure 4.39 (a) and Figure A.10 in the appendix). It can be noted that at some degrees the combination solution performs worse than the ll-SST solution. The stochastic modeling of the individual solutions has to be improved in order to achieve a better combination solution. In contrast, there is an improvement using a CAI cross-track gradiometer with a white noise level of 6.5 mE (cf. Figure 4.39 (b) and Figure A.11). The enhancement is significant in coefficient degrees and orders higher than 50.



(a) cross-track component V_{yy}: EG noise at a level of 6.5 mE in MBW

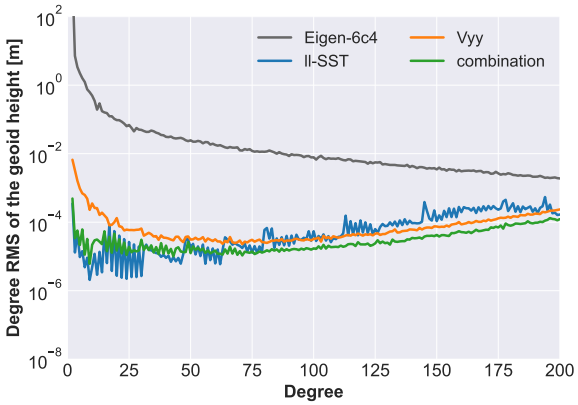


(b) cross-track component V_{yy}: CAI gradiometer noise at a level of 6.5 mE in all frequencies

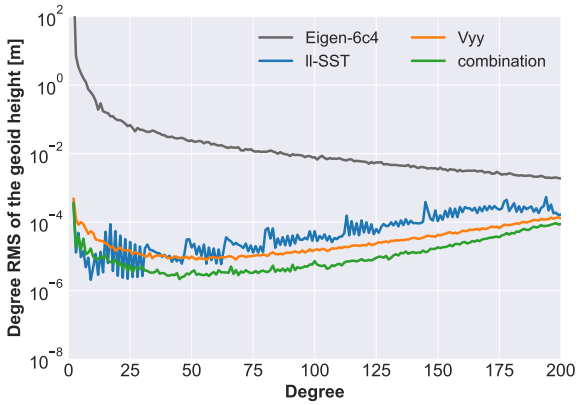
Figure 4.39: Degree RMS of the coefficient differences between recovered and reference gravity field using KBR noise and EA noise at a level of $1 \times 10^{-10}\,\mathrm{m/s^2}$ for ll-SST and different gradiometer noise levels for the cross-track gradiometer, altitude of 246 km

An electrostatic cross-track gradiometer with a noise of 1 mE in the MBW improves the gravity field solution. Especially the SH coefficients of degrees higher than 75 are improved (Figure 4.40 (a)). The two-dimensional error plots in Figure 4.43 reveal the improvement in more detail. The striping effects at orders $m = 16 \times k, k \in \mathbb{N}$ in the ll-SST-only solution are largely reduced. Additionally, the strong degradation in the sectorial coefficients in the ll-SST solution is decreased. The plots in the spatial domain show a reduction of the known striping effect in north-south direction. Adding a cross-track gradiometer with a noise level of 6.5 mE or 1 mE at all frequencies improves the gravity field solution of a classical

GRACE-like scenario in a similar way. These scenarios show that a better EG performance of at least 1 mE in the MBW is needed in order to benefit from it. In contrast, there is already a benefit with a noise of 6.5 mE for the CAI gradiometer, which is characterized by white noise. Representations of the two-dimensional errors and the errors in the spatial domain are given in the appendix A.4 for further scenarios.

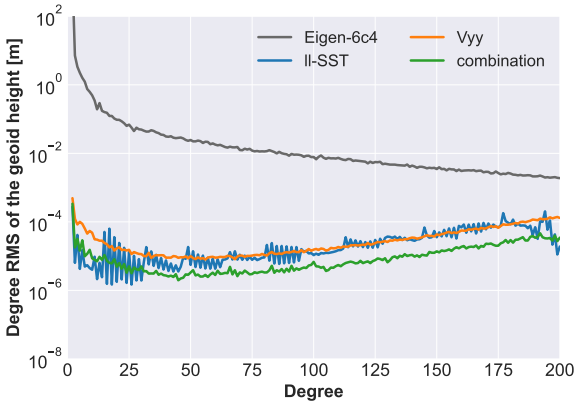


(a) cross-track component V_{yy}: EG noise at a level of 1 mE in MBW

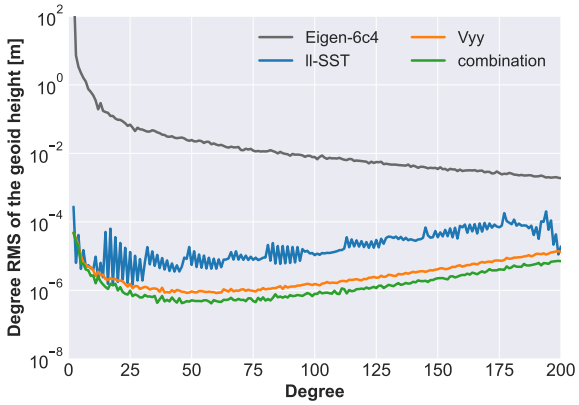


(b) cross-track component V_{yy}: CAI gradiometer noise at a level of 1 mE in all frequencies

Figure 4.40: Degree RMS of the coefficient differences between recovered and reference gravity field using KBR noise and EA noise at a level of $1 \times 10^{-10}\,\mathrm{m/s^2}$ for ll-SST and different gradiometer noise levels for the cross-track gradiometer, altitude of 246 km



(a) cross-track component V_{yy}: CAI gradiometer noise at a level of 1 mE in all frequencies

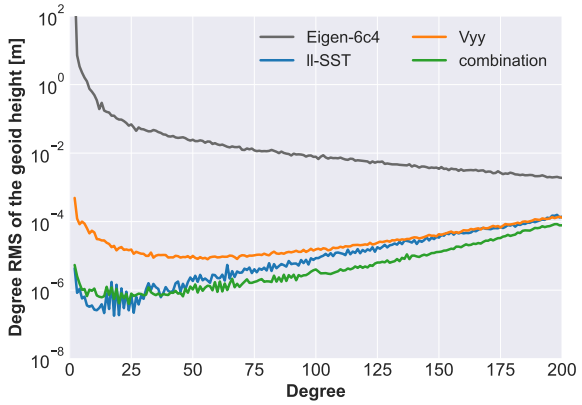


(b) cross-track component V_{yy}: CAI gradiometer noise at a level of 0.1 mE in all frequencies

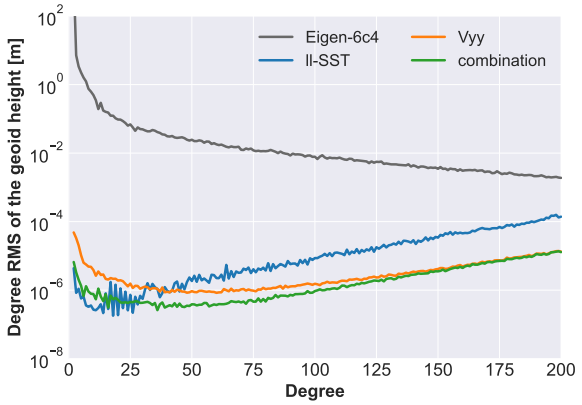
Figure 4.41: Degree RMS of the coefficient differences between recovered and reference gravity field using LRI noise and EA noise at a level of $1 \times 10^{-10}\,\mathrm{m/s^2}$ for ll-SST and different gradiometer noise levels for the cross-track gradiometer, altitude of 246 km

An even higher sensitivity of a cross-track gradiometer is needed for combinations with a GRACE-FO-like mission, which is simulated with LRI noise and an EA with a noise level of

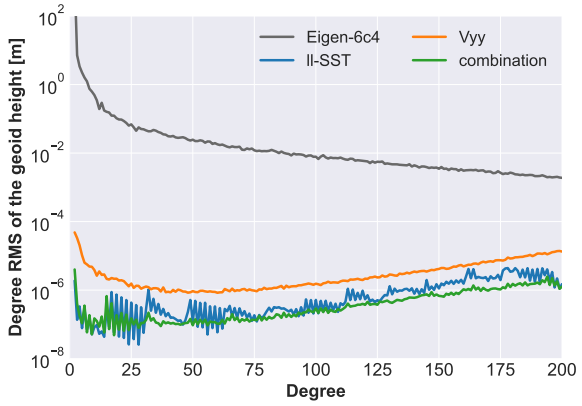
$1 \times 10^{-10}\,\mathrm{m/s^2}$. The combinations with gradiometers with noise levels of 1 mE and 0.1 mE show great improvements in high degree and order coefficients and concerning striping effects (cf. Figure 4.41 (a), Figure 4.41 (b) and Figure 4.44).
As next scenarios, combinations of a ll-SST mission using an EA noise level of $1 \times 10^{-12}\,\mathrm{m/s^2}$ and a cross-track gradiometer with sensitivities of 1 mE, 0.1 mE and 0.01 mE are shown in Figure 4.42. The sensitivities of 1 mE and 0.1 mE are suitable when KBR noise is used. The error curve of the ll-SST solution with KBR noise and the curve of gradiometry solution with 0.1 mE intersect approximately at degree 40. Consequently, a combination of the two individual solutions is meaningful. The coefficients in the degrees below 40 benefit from the ll-SST solution and the coefficients above 40 from the gradiometry solution (cf. Figure 4.42 (b)). The combinations with 1 mE and 0.1 mE are illustrated with the pyramid representation and in the space domain, cf. Figure 4.45, Figure 4.46 and Figure 4.47.



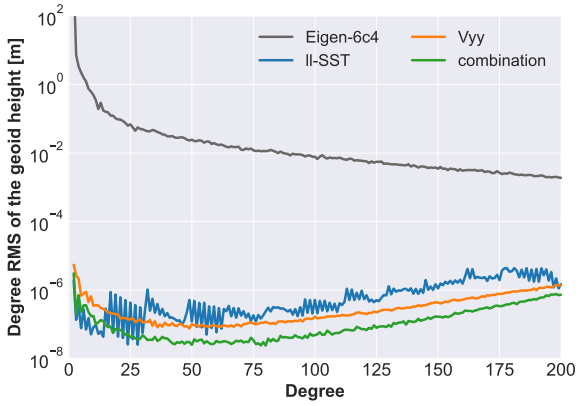
(a) ll-SST: KBR noise and EA noise at a level of $1 \times 10^{-12}\,\mathrm{m/s^2}$, cross-track component V_{yy}: CAI gradiometer noise at a level of 1 mE



(b) ll-SST: KBR noise and EA noise at a level of $1 \times 10^{-12}\,\mathrm{m/s^2}$, cross-track component V_{yy}: CAI gradiometer noise at a level of 0.1 mE

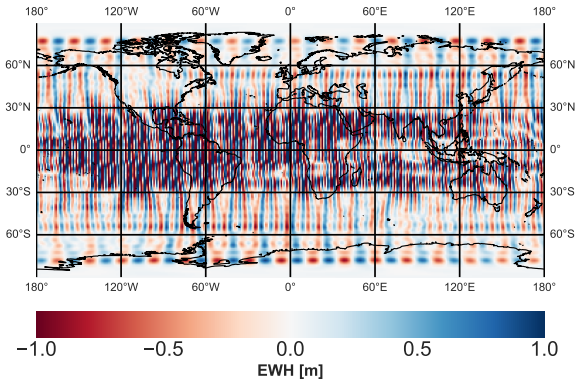


(c) ll-SST: LRI noise and EA noise at a level of $1 \times 10^{-12}\,\mathrm{m/s^2}$, cross-track component V_{yy}: CAI gradiometer noise at a level of 0.1 mE

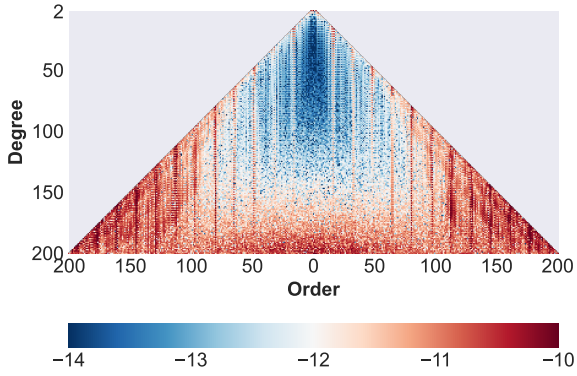


(d) ll-SST: LRI noise and EA noise at a level of $1 \times 10^{-12}\,\mathrm{m/s^2}$, cross-track component V_{yy}: CAI gradiometer noise at a level of 0.01 mE

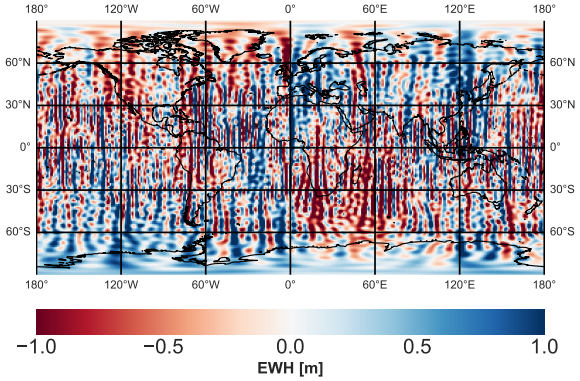
Figure 4.42: Degree RMS of the coefficient differences between recovered and reference gravity field using and EA noise at a level of $1 \times 10^{-12}\,\mathrm{m/s^2}$ for ll-SST and different gradiometer noise levels for the cross-track gradiometer, altitude of 246 km



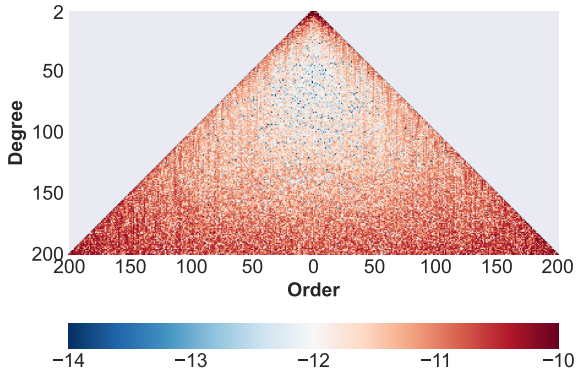
(a) ll-SST: KBR noise and EA at a noise level of $1 \times 10^{-10}\,\mathrm{m/s^2}$ in MBW



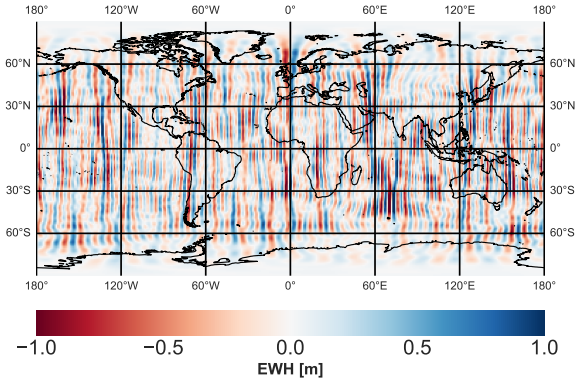
(b) ll-SST: KBR noise and EA at a noise level of $1 \times 10^{-10}\,\mathrm{m/s^2}$ in MBW



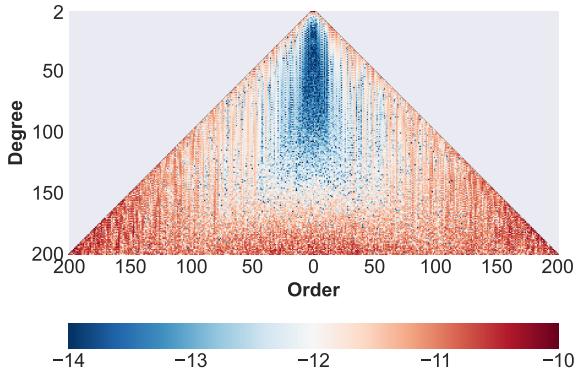
(c) Cross-track component V_{yy}: EG at a noise level of 1 mE in MBW



(d) Cross-track component V_{yy}: EG at a noise level of 1 mE in MBW

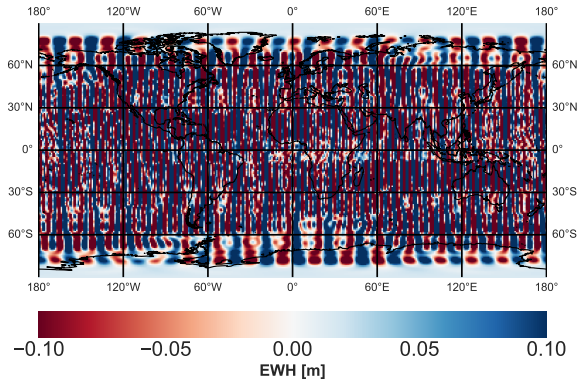


(e) Combination of ll-SST and cross-track gradiometry

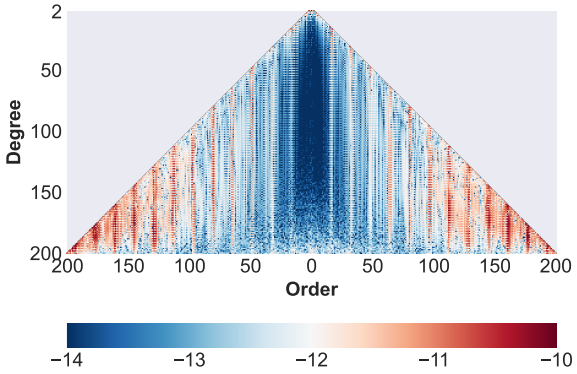


(f) Combination of ll-SST and cross-track gradiometry

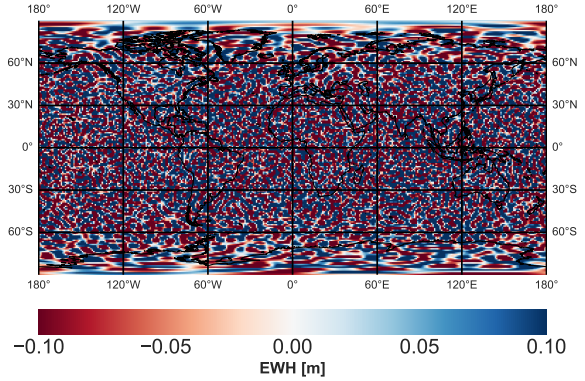
Figure 4.43: Coefficient differences between recovered and reference gravity field: spatial representation in terms of EWH and pyramid representation (logarithm scale), instrument-only scenario: h=246 km, ll-SST: KBR noise and EA at a noise level of $1 \times 10^{-10}\,\mathrm{m/s^2}$, cross-track component V_{yy}: EG at a noise level of 1 mE



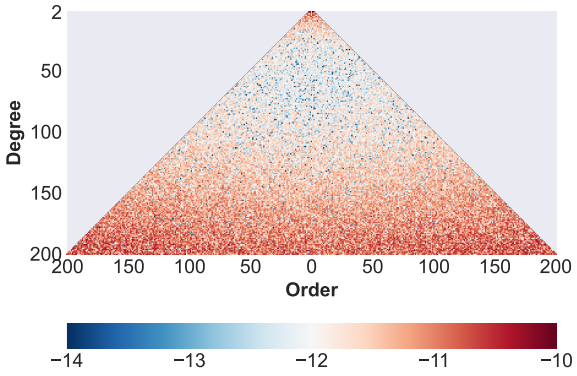
(a) ll-SST: LRI noise and EA at a noise level of $1 \times 10^{-10}\,\mathrm{m/s^2}$ in MBW



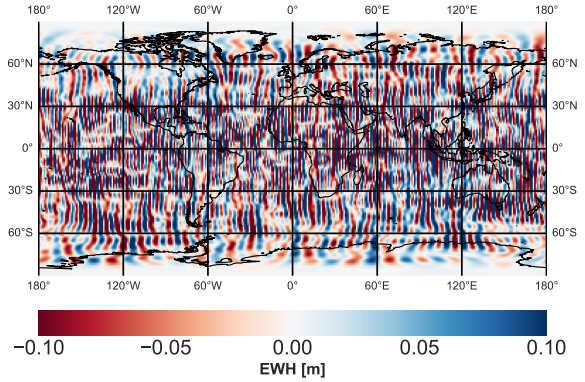
(b) ll-SST: LRI noise and EA at a noise level of $1 \times 10^{-10}\,\mathrm{m/s^2}$ in MBW



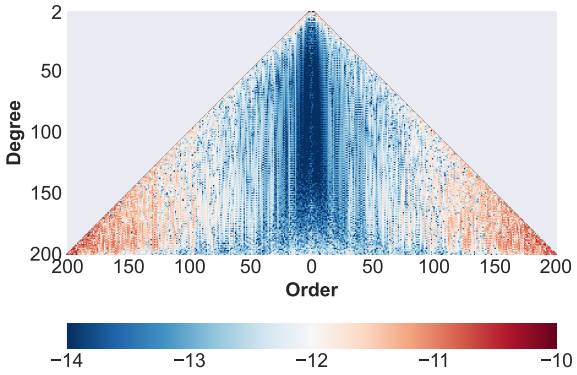
(c) Cross-track component V_{yy}: CAI gradiometer at a noise level of 1 mE



(d) Cross-track component V_{yy}: CAI gradiometer at a noise level of 1 mE

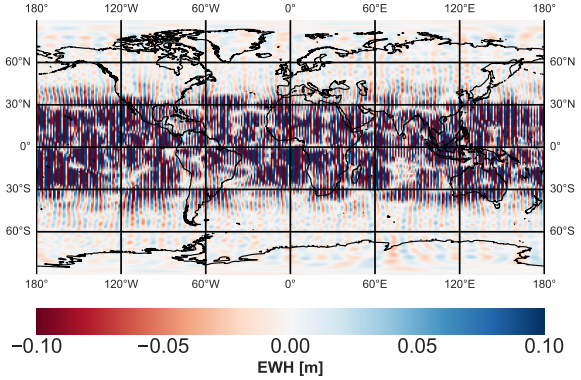


(e) Combination of ll-SST and cross-track gradiometry

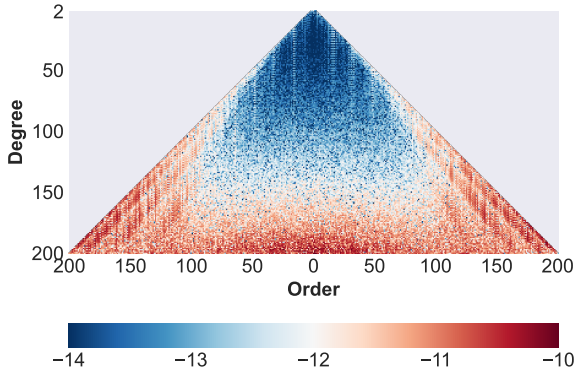


(f) Combination of ll-SST and cross-track gradiometry

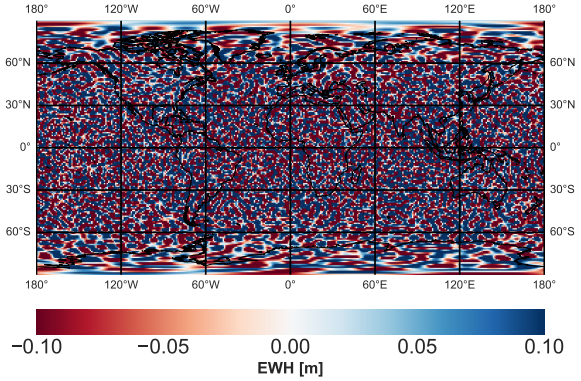
Figure 4.44: Coefficient differences between recovered and reference gravity field: spatial representation in terms of EWH and pyramid representation (logarithm scale), instrument-only scenario: h=246 km, ll-SST: LRI noise and EA at a noise level of $1 \times 10^{-10}\,\mathrm{m/s^2}$, cross-track component V_{yy}: CAI gradiometer at a noise level of 1 mE



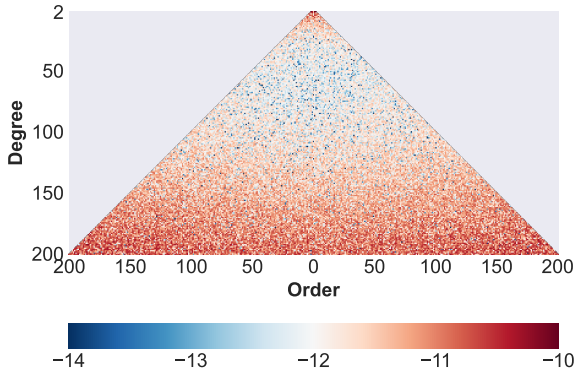
(a) ll-SST: KBR noise and EA at a noise level of $1 \times 10^{-12}\,\mathrm{m/s^2}$ in MBW



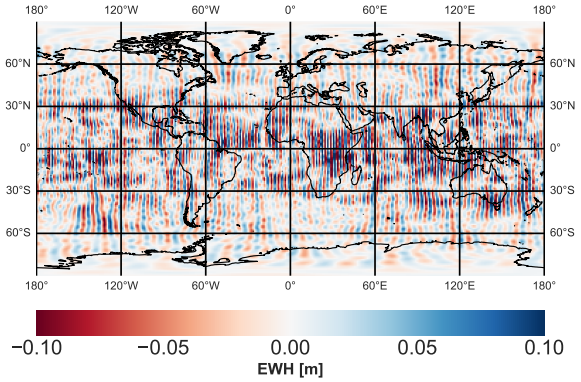
(b) ll-SST: KBR noise and EA at a noise level of $1 \times 10^{-12}\,\mathrm{m/s^2}$ in MBW



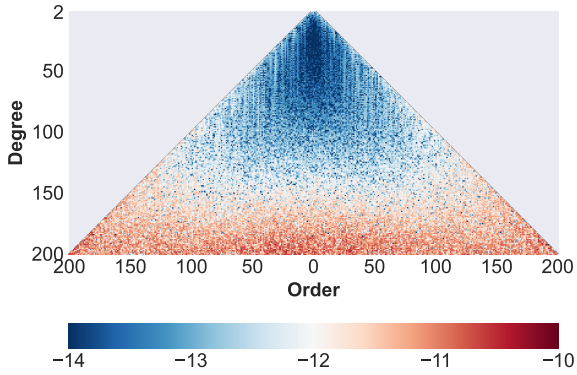
(c) Cross-track component V_{yy}: CAI gradiometer at a noise level of 1 mE



(d) Cross-track component V_{yy}: CAI gradiometer at a noise level of 1 mE

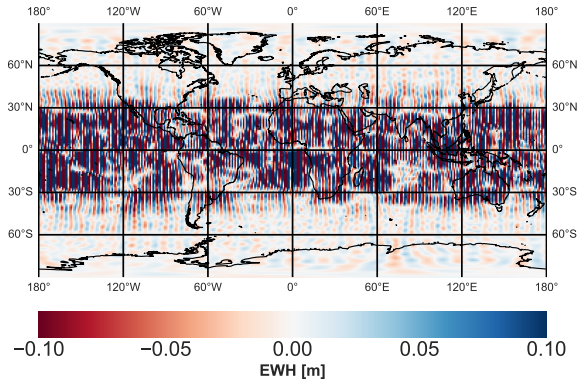


(e) Combination of ll-SST and cross-track gradiometry

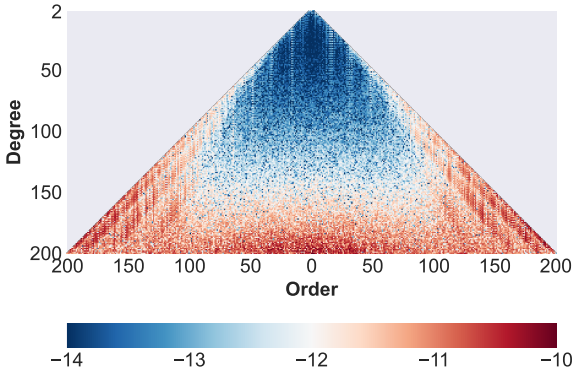


(f) Combination of ll-SST and cross-track gradiometry

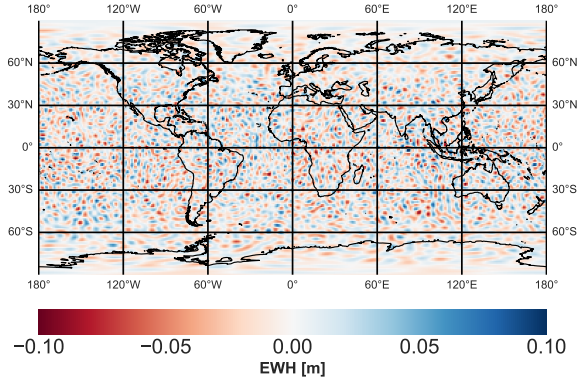
Figure 4.45: Coefficient differences between recovered and reference gravity field: spatial representation in terms of EWH and pyramid representation (logarithm scale), instrument-only scenario: h=246 km, ll-SST: KBR noise and EA at a noise level of $1 \times 10^{-12}\,\mathrm{m/s^2}$, cross-track component V_{yy}: CAI gradiometer at a noise level of 1 mE



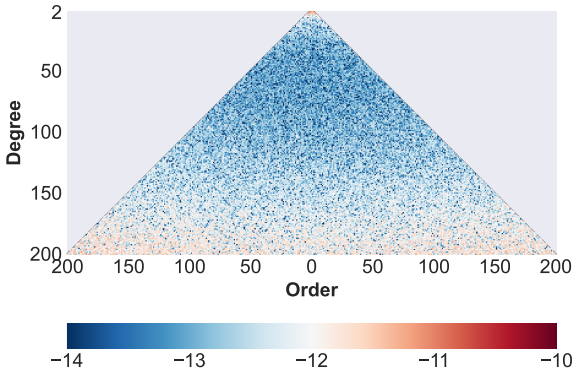
(a) ll-SST: KBR noise and EA at a noise level of $1 \times 10^{-12}\,\mathrm{m/s^2}$ in MBW



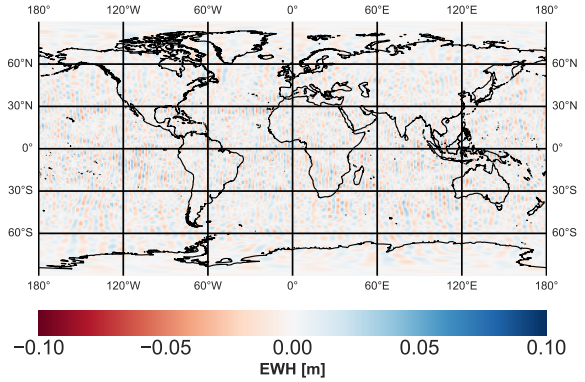
(b) ll-SST: KBR noise and EA at a noise level of $1 \times 10^{-12}\,\mathrm{m/s^2}$ in MBW



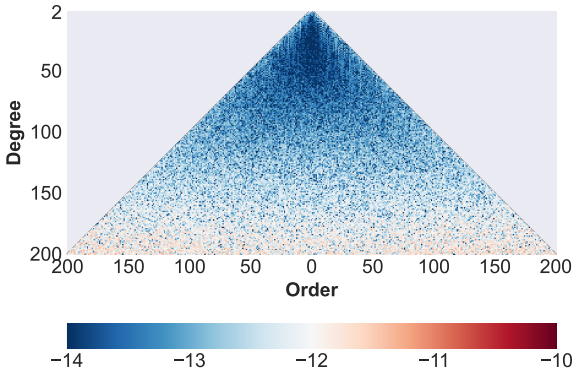
(c) Cross-track component V_{yy}: CAI gradiometer at a noise level of 0.1 mE



(d) Cross-track component V_{yy}: CAI gradiometer at a noise level of 0.1 mE

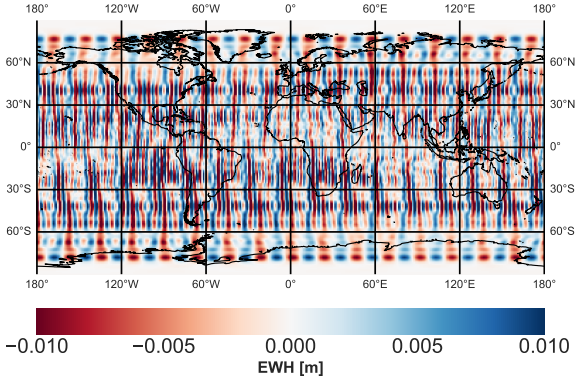


(e) Combination of ll-SST and cross-track gradiometry

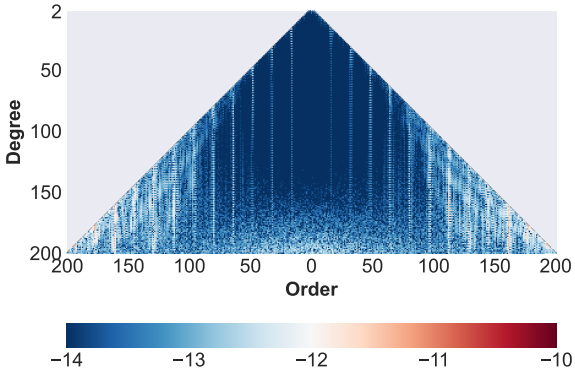


(f) Combination of ll-SST and cross-track gradiometry

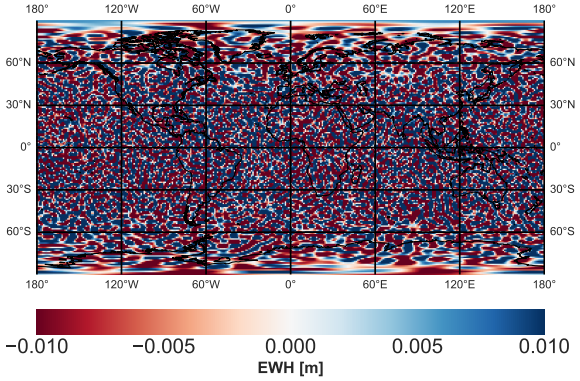
Figure 4.46: Coefficient differences between recovered and reference gravity field: spatial representation in terms of EWH and pyramid representation (logarithm scale), instrument-only scenario: h=246 km, ll-SST: KBR noise and EA at a noise level of $1 \times 10^{-12}\,\mathrm{m/s^2}$, cross-track component V_{yy}: CAI gradiometer at a noise level of 0.1 mE



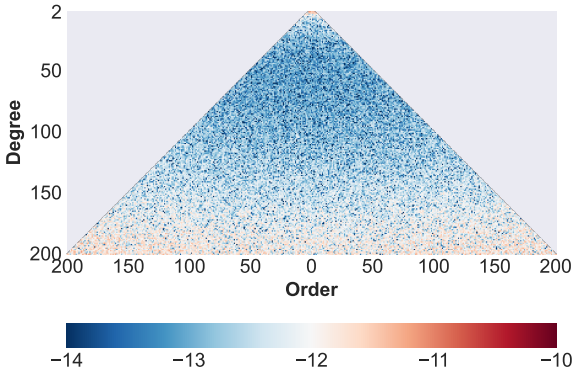
(a) ll-SST: LRI noise and EA at a noise level of $1 \times 10^{-12}\,\mathrm{m/s^2}$ in MBW



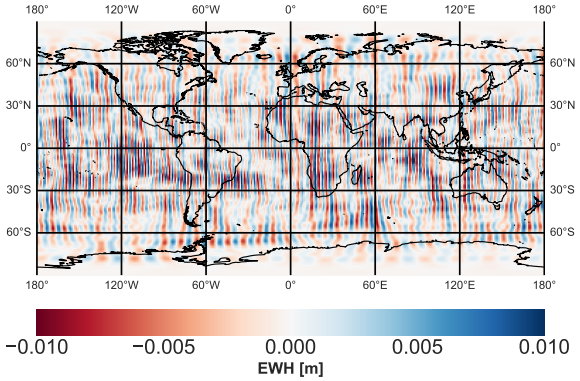
(b) ll-SST: LRI noise and EA at a noise level of $1 \times 10^{-12}\,\mathrm{m/s^2}$ in MBW



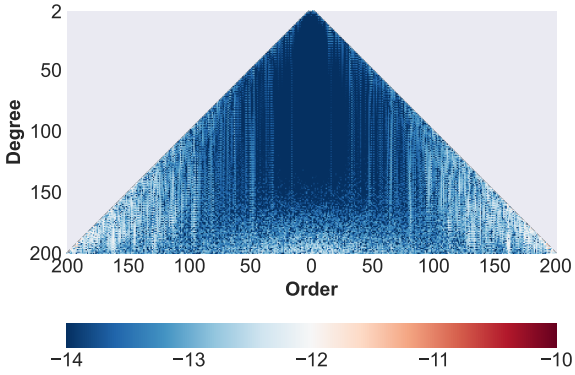
(c) Cross-track component V_{yy}: CAI gradiometer at a noise level of 0.1 mE



(d) Cross-track component V_{yy}: CAI gradiometer at a noise level of 0.1 mE



(e) Combination of ll-SST and cross-track gradiometry



(f) Combination of ll-SST and cross-track gradiometry

Figure 4.47: Coefficient differences between recovered and reference gravity field: spatial representation in terms of EWH and pyramid representation (logarithm scale), instrument-only scenario: h=246 km, ll-SST: LRI noise and EA at a noise level of $1 \times 10^{-12}\,\mathrm{m/s^2}$, cross-track component V_{yy}: CAI gradiometer at a noise level of 0.1 mE

The presented results emphasize the gravity field solution enhancement by the combination of the two measurement concepts. However, long interrogation times are required in order

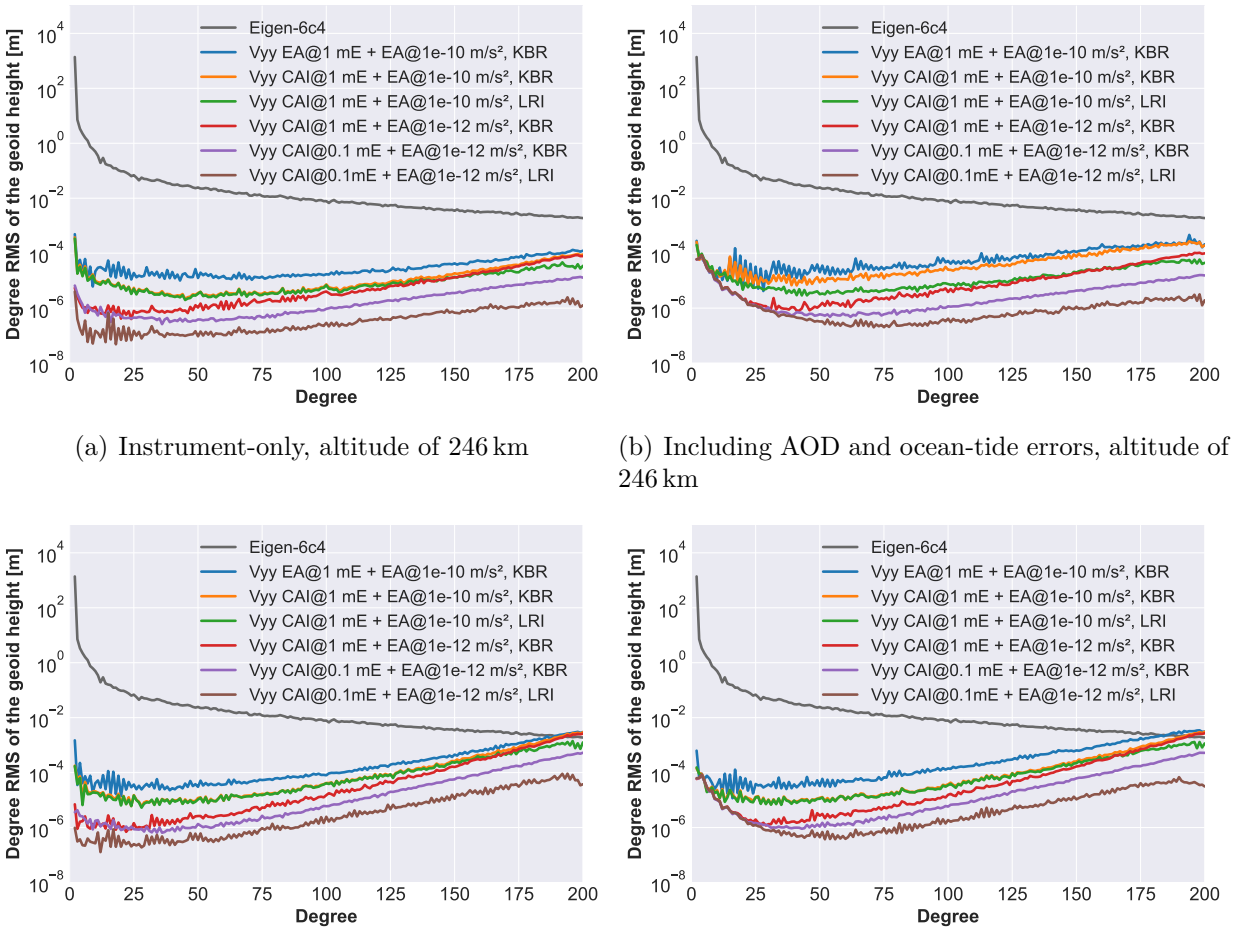
to achieve these high sensitivities of the gradiometer. It is expected, that this aspect affects the high-frequency part of the recovered gravity field model. This effect is not considered in the closed-loop simulation. A combination of an electrostatic and a CAI accelerometer would solve this problem, since the high-frequency parts are measured by the electrostatic one. A deconvolution filter is one option to achieve an optimal estimate of the signal in case of a CAI-only sensor (Migliaccio et al., 2019).
The cumulative geoid errors up to degree and order 200 are given in Table 4.5 for selected scenarios. They are calculated using the true coefficient differences between reference and recovered gravity field. The maximum coefficient degree and order of 200 correspond approximately to a spatial resolution of 100 km. The required performance for science and user needs is stated with a monthly geoid error of 0.1 mm in Pail et al. (2015) and 1 mm in Gruber et al. (2014a) for a spatial resolution of 150 km.

Table 4.5: Cumulative geoid error up to degree and order 200; observations of one month with sampling frequency of 0.2 Hz; instrument-only scenarios

ll-SST		V_{yy}		Cumulative geoid error [cm] at altitude of		
Ranging	EA noise [m/s^2]	ACC	Noise [mE]	246 km	303 km	363 km
		EA	6.5	16.71	85.12	435.74
		EA	1	2.79	10.74	44.46
		CAI	6.5	8.05	47.16	254.85
		CAI	1	1.24	7.41	38.77
		CAI	0.1	0.12	0.72	3.93
KBR	1×10^{-10}			3.68	17.39	65.69
	1×10^{-12}			1.18	5.64	21.52
LRI	1×10^{-10}			1.13	8.20	27.41
	1×10^{-12}			0.04	0.13	0.68
KBR	1×10^{-10}	EA	6.5	3.31	14.47	73.40
	1×10^{-10}	CAI	6.5	1.83	10.05	51.34
	1×10^{-10}	EA	1	1.16	5.25	22.68
	1×10^{-10}	CAI	1	0.73	3.70	19.54
	1×10^{-12}	CAI	1	0.65	3.23	17.13
	1×10^{-12}	CAI	0.1	0.11	0.66	3.63
LRI	1×10^{-10}	EA	1	0.78	3.82	13.19
	1×10^{-10}	CAI	1	0.38	1.92	10.07
	1×10^{-12}	CAI	0.1	0.02	0.10	0.61

A degradation by an increasing orbit altitude is confirmed for all scenarios and mission concepts. A geoid error below 1 cm for 100 km can only be guaranteed for cross-track gradiometry with a CAI gradiometer at a noise level of 0.1 mE and a low altitude of 246 km or 303 km. An accelerometer noise level of 1×10^{-12} m/s^2 and LRI noise for ll-SST is required in order to achieve an error lower than 1 cm. The addition of a cross-track gradiometer

reduces the cumulative geoid error in all given scenarios, except the addition of an EG with 6.5 mE in the MBW for an altitude of 363 km. Geoid errors smaller than 1 cm can also be achieved with low altitude and low accelerometer noise levels. The combination of ll-SST and cross-track gradiometry is additionally simulated including AOD and ocean-tide errors. The degree RMS for several instrument noise scenarios are given for the altitudes 246 km and 363 km in Figure 4.48, it is given in the appendix in Figure A.9 for an altitude of 303 km. There, the instrument-only scenarios as well as the ones including background modeling errors are given. In all scenarios, 10 % of the AOD product RL6 and 10 % of the ocean tide product FES2014b are assumed as modeling errors. The individual solutions as well as the combined ones are given in the Figures 4.49 and 4.50 in the spatial and the pyramid representation for two examples.



(a) Instrument-only, altitude of 246 km

(b) Including AOD and ocean-tide errors, altitude of 246 km

(c) Instrument-only, altitude of 363 km

(d) Including AOD and ocean-tide errors, altitude of 363 km

Figure 4.48: Degree RMS of the coefficient differences between recovered and reference gravity field for combinations of ll-SST and cross-track gradiometry, instrument-only and and scenarios including AOD and ocean-tide errors for different sensor combinations, altitudes of 246 km and 363 km

The degradation by the background modeling errors is visible in the low degree coefficients. The improvement by the addition of a cross-track gradiometer is similar to the instrument-

only scenarios. The lower the sensor noise, the more the gravity field solution is affected by AOD and ocean-tide errors. The cumulative geoid errors of selected combination scenarios are provided in Table 4.6.

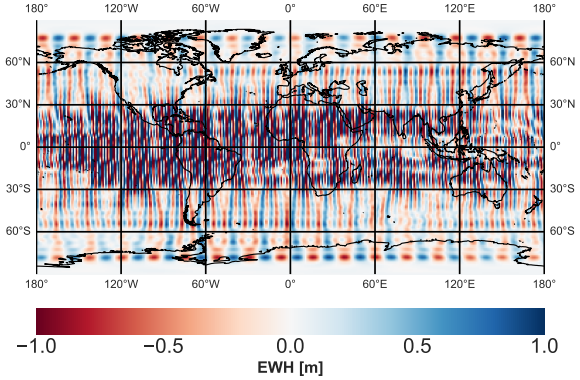
Table 4.6: Cumulative geoid error up to degree and order 200; observations of one month with sampling frequency of 0.2 Hz; scenarios including AOD and ocean-tide errors

ll-SST		V_{yy}		Cumulative geoid error [cm] at altitude of		
Ranging	EA noise [m/s^2]	ACC	Noise [mE]	246 km	303 km	363 km
KBR	1×10^{-10}	EA	1	2.91	5.16	28.63
	1×10^{-10}	CAI	1	2.35	3.89	19.75
	1×10^{-12}	CAI	1	0.81	3.31	17.32
	1×10^{-12}	CAI	0.1	0.14	0.68	3.68
LRI	1×10^{-10}	CAI	1	0.56	2.15	9.90
	1×10^{-12}	CAI	0.1	0.05	0.12	0.48

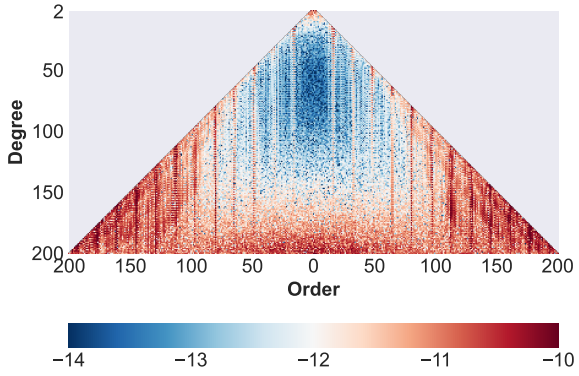
The cumulative geoid errors up to degree and order 200 and a corresponding spatial resolution of 100 km are in the worst case scenario 2.9 cm with an altitude of 246 km (cf. Table 4.6). An error at mm level is achieved for low-noise scenarios, like a cross-track gradiometer with noise of 1 mE and an accelerometer with noise of 1×10^{-12} m/s^2 in the center of mass. The cumulative geoid errors of the scenarios with an altitude of 363 km are at the cm level and dm level. In order to get a mm error, a cross-track gradiometer with white noise of 0.1 mE is required.
Furthermore, the geoid error is computed for a spatial resolution of 150 km (cf. Table 4.7). Consequently, the cumulative errors decrease to a maximum of 0.67 cm for an altitude of 246 km and 2.48 cm for 363 km. The required target performance of 0.1 mm for 150 km resolution according to Pail et al. (2015) is not achieved, but the requirement of 1 mm according to Gruber et al. (2014a) is met.

Table 4.7: Cumulative geoid error up to degree and order 133; observations of one month with sampling frequency of 0.2 Hz; scenarios including AOD and ocean-tide errors

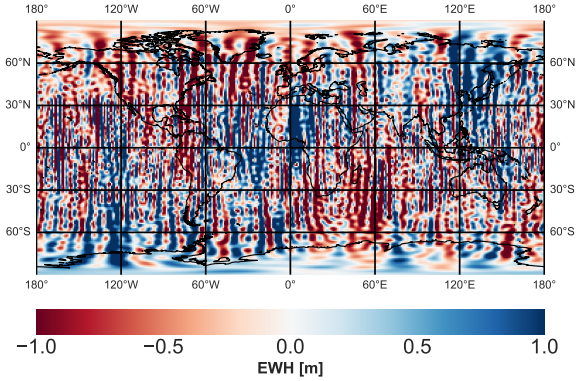
ll-SST		V_{yy}		Cumulative geoid error [cm] at altitude of		
Ranging	EA noise [m/s^2]	ACC	Noise [mE]	246 km	303 km	363 km
KBR	1×10^{-10}	EA	1	0.67	0.73	2.48
	1×10^{-10}	CAI	1	0.39	0.26	0.70
	1×10^{-12}	CAI	1	0.08	0.11	0.37
	1×10^{-12}	CAI	0.1	0.04	0.06	0.15
LRI	1×10^{-10}	CAI	1	0.12	0.24	0.65
	1×10^{-12}	CAI	0.1	0.04	0.04	0.06



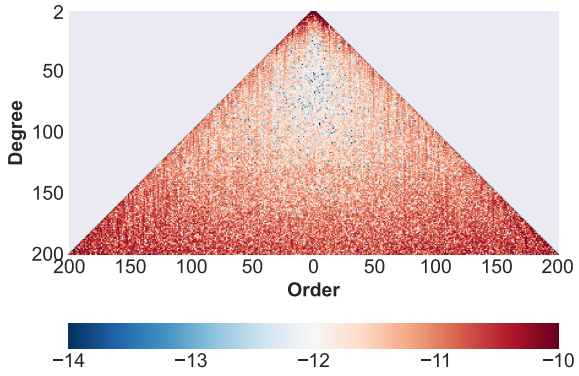
(a) ll-SST: KBR noise and EA at a noise level of $1 \times 10^{-10}\,\mathrm{m/s^2}$ in MBW



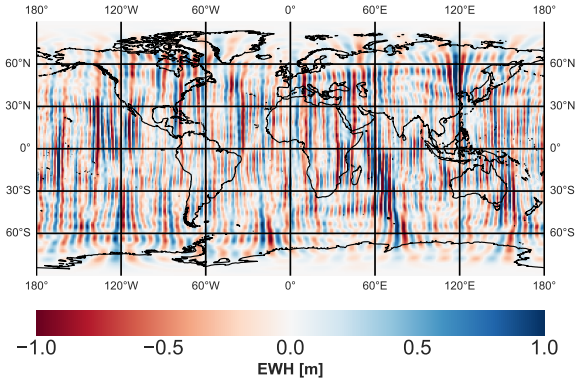
(b) ll-SST: KBR noise and EA at a noise level of $1 \times 10^{-10}\,\mathrm{m/s^2}$ in MBW



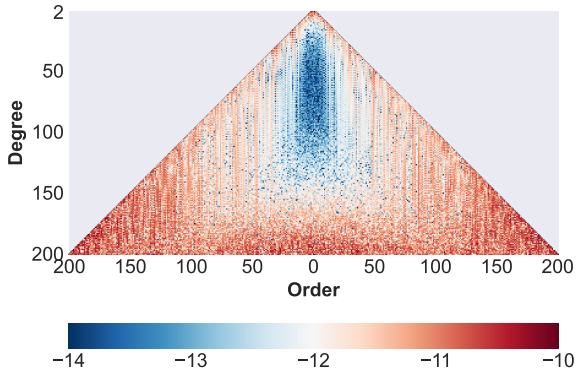
(c) Cross-track component V_{yy}: EG at a noise level of 1 mE in MBW



(d) Cross-track component V_{yy}: EG at a noise level of 1 mE in MBW

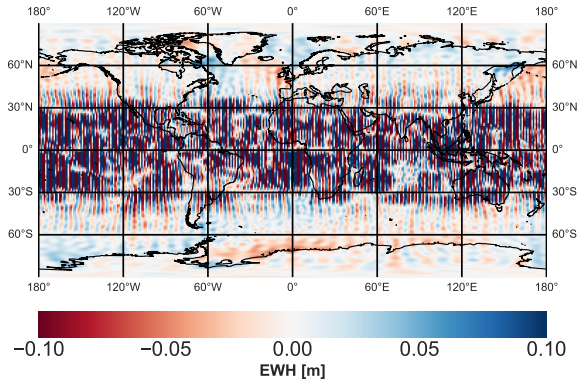


(e) Combination of ll-SST and cross-track gradiometry

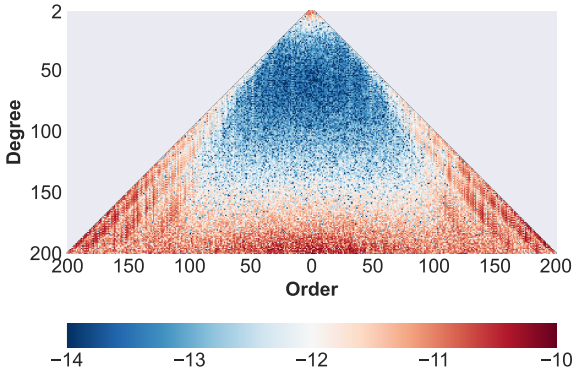


(f) Combination of ll-SST and cross-track gradiometry

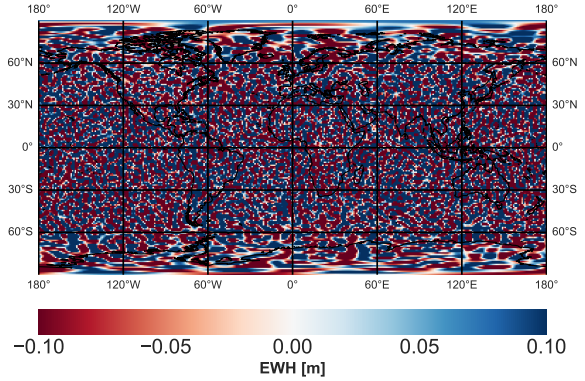
Figure 4.49: Coefficient differences between recovered and reference gravity field: spatial representation in terms of EWH and pyramid representation (logarithm scale), scenario including AOD and ocean-tide errors: h=246 km, ll-SST: KBR noise and EA at a noise level of $1 \times 10^{-10}\,\mathrm{m/s^2}$, cross-track component V_{yy}: EG at a noise level of 1 mE



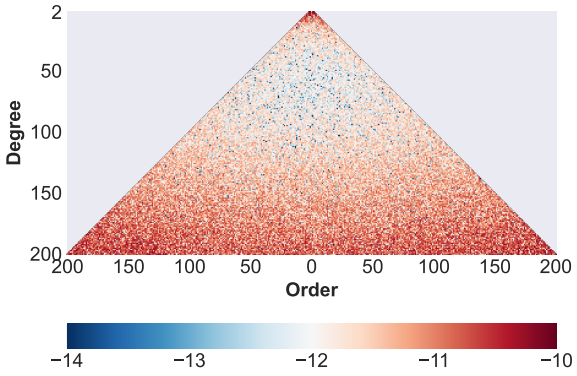
(a) ll-SST: KBR noise and EA at a noise level of $1 \times 10^{-12}\,\mathrm{m/s^2}$ in MBW



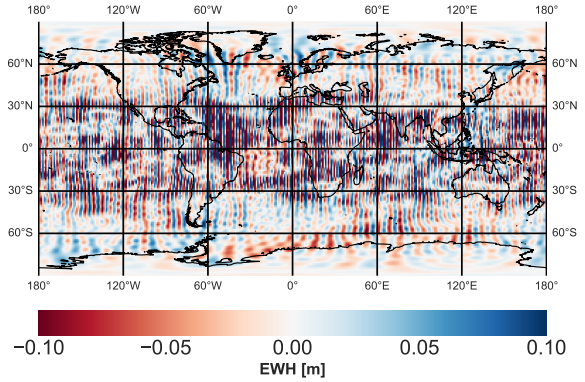
(b) ll-SST: KBR noise and EA at a noise level of $1 \times 10^{-12}\,\mathrm{m/s^2}$ in MBW



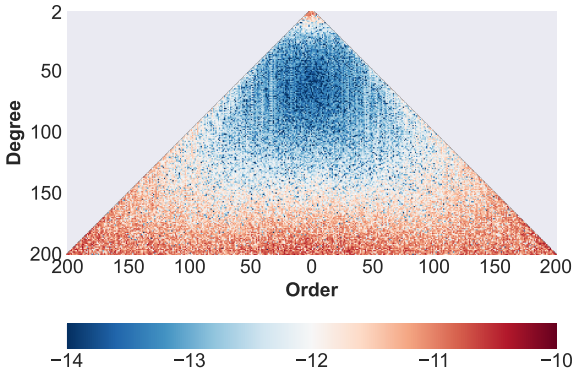
(c) Cross-track component V_{yy}: CAI gradiometer at a noise level of 1 mE



(d) Cross-track component V_{yy}: CAI gradiometer at a noise level of 1 mE



(e) Combination of ll-SST and cross-track gradiometry



(f) Combination of ll-SST and cross-track gradiometry

Figure 4.50: Coefficient differences between recovered and reference gravity field: spatial representation in terms of EWH and pyramid representation (logarithm scale), scenario including AOD and ocean-tide errors: h=246 km, ll-SST: KBR noise and EA at a noise level of $1 \times 10^{-12}\,\mathrm{m/s^2}$, cross-track component V_{yy}: CAI gradiometer at a noise level of 1 mE

4.7 Summary

The closed-loop simulation allows to quantify the impact of the sensor performance on the recovered gravity field. This research focuses on the analysis of the accelerometer performance. The benefit of a CAI accelerometer and its combination with classical EA are investigated. In addition, the combination of ll-SST and cross-track gradiometry is studied as new mission concept.

Relations between these different components of a satellite gravity mission are outlined in section 4.1. The interactions between accelerometer, drag-free control system and satellite orbit altitude are investigated. The accelerometer performance and need of a drag compensation system as well as the strength of the Earth's gravity field signal depend on the altitude. Consequently, four different orbit altitudes between 246 km and 462 km are investigated, as they are suitable for satellite gravity missions.

In section 4.2, requirements for a drag-free system are derived based on the error due to the accelerometer scale factor. Time series of non-gravitational accelerations are simulated in order to evaluate the requirements. The defined requirement is studied for a single accelerometer in the center of mass and for gradiometer measurements. The absolute scale factor is needed for ll-SST missions. The requirement using the scale factor knowledge of an EA is not achieved in all considered orbit scenarios. In contrast, with a CAI accelerometer, there is no degradation by the scale factor knowledge. The reason for this is its expected, very accurate knowledge of 1×10^{-9}. For gradiometry missions, the relative scale factor knowledge of an accelerometer pair is relevant. The non-zero common mode rejection is analyzed. The values for the differential scale factor knowledge are calculated using the GOCE calibration method with simulated data. The requirement is kept with the optimistic knowledge assumption of 3×10^{-7} and an altitude higher than 363 km. On the contrary, this is not the fact when assuming a pessimistic relative scale factor knowledge of 2×10^{-5}. A drag-free system with fine control thrusters, on the other hand, can fulfill the requirement.
Beyond that, it is shown that the saturation of the accelerometer is reached for low orbit altitudes of 246 km and 303 km in along-track direction. A constant thrust would already counteract the saturation for an orbit with 303 km altitude. However, the saturation strongly depend on the solar cycle. In spite of the advantages of a drag-free system for the accelerometer performance, the propellant consumption limits the mission duration. The propellant consumption increases with decreasing orbit altitude exponentially.

Moreover, the magnitude of the non-gravitational acceleration plays a major role for the CAI accelerometer. In order to achieve a high sensitivity, a longer measurement cycle time of a few seconds is used. However, there is an aliasing effect due to the variation of the accelerations within an interferometer cycle (cf. section 4.3). The variation of the non-gravitational accelerations in 12 s is in the order of $1 \times 10^{-9}\,\mathrm{m/s^2}$ for an altitude of 462 km and $5 \times 10^{-8}\,\mathrm{m/s^2}$ for an altitude of 303 km. The corresponding error in the accelerometer output is calculated using the transfer function of an atom interferometer. The estimated error is significant, as its maximum magnitude is, e.g., $1 \times 10^{-9}\,\mathrm{m/s^2}$ for the scenario with an altitude of 303 km and $1 \times 10^{-10}\,\mathrm{m/s^2}$ for 462 km. A reduction of this effect can be accomplished by either reducing the magnitude of non-gravitational accelerations or by reducing

the cycle time. The former could be achieved by drag compensation which is a suitable method. The decrease of the cycle time admittedly also decreases the sensitivity of the atom interferometer. Thus, the optimum between the two complementary arguments has to be found.

In section 4.4, results of the closed-loop simulation of ll-SST mission scenarios are evaluated. The coefficient differences between reference gravity field and recovered gravity field are used to assess the results with several sensor behavior models and orbit parameters. The scenarios including AOD and ocean-tide error show that the coefficient differences in low degrees are mainly caused by these two background modeling errors. Aside from that, an EA with a noise level of $1 \times 10^{-10}\,\mathrm{m/s^2}$ is the limiting instrument as the performance of the ranging measurement instruments do not affect the quality of the gravity field solution. When introducing a lower EA noise of $1 \times 10^{-12}\,\mathrm{m/s^2}$, solutions with LRI are better than the ones with KBR. The addition of a CAI accelerometer to an electrostatic one reduces the striping effects in north-south direction when LRI is used for ranging measurements. Besides, striping effects at orders $m = 16 \times k, k \in \mathbb{N}$ are reduced. This improvement is stronger for the scenarios with higher altitude. As the limiting factor is the modeling of AOD and ocean tides, instrument-only closed-loop simulations are performed as well. The benefit of the hybridization of CAI and EAs is evident in these simulations.

Outcomes on the closed-loop simulations of a gradiometry mission are also briefly presented (cf. section 4.5). The focus is on a cross-track gradiometer, since additional measurements in east-west direction are obtained and the rotation rate in cross-track direction is significantly smaller than in the other two directions.
The two mission concepts of ll-SST and cross-track gradiometry are combined in order to benefit from their complementary sensitivities in the wavelengths of the gravity field signal, which results are given in section 4.6. An electrostatic cross-track gradiometer with noise of 1 mE improves the gravity field solution of a ll-SST mission with EA noise of $1 \times 10^{-10}\,\mathrm{m/s^2}$ and KBR noise. The striping effects are reduced and coefficients of high degrees and orders are better recovered. Additionally, the combination with a CAI cross-track gradiometer, for which white noise is assumed, is studied. A gradiometer noise level of 6.5 mE is sufficient when white noise is assumed. All tested orbital altitudes of 246 km, 303 km and 363 km support this conclusion. A cross-track gradiometer with higher sensitivity is required for a ll-SST mission with an EA noise of $1 \times 10^{-12}\,\mathrm{m/s^2}$ in the MBW. A sensitivity of 1 mE or even 0.1 mE is demanded in order to benefit from the additional gradiometer. A monthly geoid error of 1 mm for a spatial resolution of 150 km can be achieved by the combination, e.g., a CAI cross-track gradiometer with white noise of 1 mE and an EA in the center of mass with a noise level of $1 \times 10^{-12}\,\mathrm{m/s^2}$ in the MBW.

5 Summary and Outlook

Satellite gravity missions are a powerful tool to measure the Earth's gravity field and its temporal variations. However, an increase of temporal and spatial resolution is demanded by the user and science community. Thus in this thesis, new concepts for future satellite missions are evaluated based on simulations.
The first part of the thesis describes the basics for determining the Earth's gravitational field with satellites including the motion of a satellite in space and the representation of the Earth's gravity field by a spherical harmonic expansion. The choice of the orbit parameters has an enormous effect on the quality of the recovered gravity field solution. Therefore, an overview of the orbit design is given. Moreover, mission concepts, sensors and control systems of state-of-the-art satellite gravity missions are introduced. Available and emerging accelerometer technologies are summarized. This includes further developments of EAs, e.g., modifications such as using a cubic test mass, free-fall tests for the calibration or optical sensing. Beyond that, the new measurement concept of cold atom interferometry, which has not been demonstrated in space yet, is described. The CAI measurements show some beneficial characteristics, e.g., long-term stability and a very well known scale factor. However, the application on board of a satellite also introduce challenges due to a lower sampling rate and the rotation of the satellite.

Simulations are performed to quantify the potential of new concepts of sensors, control systems and orbit configurations. The satellite dynamics are simulated using the XHPS software. In this work, only the modeling of non-gravitational accelerations is discussed in detail, since these accelerations are particularly important for further analyses. The modeling of the sensor behavior plays a major role and is implemented in the simulation environment using PSD models. State-of-the-art instrument behaviors, e.g., of EAs, KBR and LRI, are modeled from their known in-orbit performances. The CAI accelerometer performance is estimated based on ground experiments and expectations for space applications, which leads to an increase of the free-fall time due to the microgravity environment. Additionally, the transfer function of an atom interferometer is taken into account. A hybrid sensor consisting of an electrostatic and a CAI accelerometer combines the strengths of the two measurement principles. The combination is implemented by low-pass and high-pass filtering.
The control systems have also been included in the forward simulation to achieve a realistic simulation of the satellite dynamics. The drag-free system is important for the accelerometer performance and the orbit maintenance and is modeled according to the principle of the GOCE drag-free system. Available state-of-the-art control system models for attitude control from XHPS are used.
A closed-loop simulation is performed in order to quantify the effect on the resulting gravity field model using different sensor behavior models. One of the major drawbacks is still the

modeling of AOD and ocean tides. Their modeling is not in the scope of this study, but errors caused by these effects are considered. The SH coefficients of the gravity field model are estimated by a least-squares adjustment. The basic methodology is explained using range accelerations and gradiometry and the combination on the level of normal equations of the two observation groups is described.

Considering only the sensors, the performance of the accelerometers needs to be improved for future satellite gravity missions. The accelerometer performance is closely related to the magnitude of non-gravitational accelerations. Therefore, benefits of using a drag-free system are investigated. A detailed analysis is performed concerning the accelerometer scale factor knowledge and the connection to drag compensation. Drag compensation is required when using the scale factor knowledge of an electrostatic accelerometer, which is assumed with 0.2 % or 1 %. This outcome is valid for all studied orbit altitudes between 246 km and 462 km and for all directions in the satellite orbit frame, as the electrostatic measurements would be significantly degraded by the scale factor assuming no compensation. In contrast, the requirement is easily fulfilled without drag compensation when using the scale factor knowledge 1×10^{-7} % of a CAI accelerometer.
For gradiometry, the magnitude of the non-gravitational accelerations is important due to the non-perfect common-mode rejection. Accordingly, the differential scale factor knowledge needs to be considered. When using the more optimistic differential scale factor knowledge, the requirement is achieved for altitudes of 363 km and 462 km. A drag compensation with fine control thruster would be needed to fulfill the requirements with a more pessimistic differential scale factor knowledge.
The accelerometer saturation and the propellant consumption of a drag-free system for different altitudes are studied. The saturation limit of $\pm 1 \times 10^{-6}\,\mathrm{m/s^2}$ is exceeded for low altitudes of 246 km and 303 km. A constant thrust already avoids the saturation for a 303 km altitude test scenario. Whether the saturation limit is reached also depends on the solar cycle, where two extremes are studied.
Besides this, the magnitude of non-gravitational accelerations compromises the performance of the CAI accelerometer. The degradation by an aliasing effect due to the signal variation within an interferometer cycle of 12 s is studied. The error is estimated using the transfer function of an atom interferometer. It is significant, e.g., at the level of $2 \times 10^{-10}\,\mathrm{m/s^2}$ for an altitude of 303 km. The effect can be reduced to a non-significant magnitude by either decreasing the cycle time or by drag compensation. However, a decrease of the cycle time also decreases the sensitivity of the atom interferometer.
The performance of the improved sensors is evaluated for various ll-SST and gradiometry mission scenarios by closed-loop simulations. The SH coefficient differences between the reference gravity field model and the estimated model quantify the effect of the sensor behaviors and orbit parameters on the gravity field recovery. Monthly gravity field models are estimated. On the one hand, the ll-SST missions are evaluated with assumptions for the error effect of the background models for ocean tides and AOD. The error due to AOD and ocean-tide modeling is dominant in the low order coefficients. This demonstrates the importance of improving these models. On the other hand, instrument-only scenarios are investigated. This allows the quantification of the enhancement by instruments when the time-variable background modeling improves in the future. Scenarios including an EA with a noise level of $1 \times 10^{-10}\,\mathrm{m/s^2}$ are degraded in the SH coefficient orders higher than 12.

Thus, the solution with KBR and LRI noise are similar. An accelerometer with lower noise level of $1 \times 10^{-12}\,\mathrm{m/s^2}$ strongly improves the gravity field solution. The results with LRI noise are more accurate than the ones with KBR noise. The striping effects in north-south direction and at specific orders of the coefficients are reduced even more by adding a CAI accelerometer. The instrument noise has a larger effect on the gravity solution when the errors due to AOD and ocean tides are ignored.
The addition of a cross-track gradiometer to a ll-SST mission is investigated as a new measurement concept for gravity field missions. This concept combines the already implemented methodologies of GOCE and GRACE or GRACE-FO and exploits their strengths regarding the sensitivity with respect to the gravity field signal. The selection of the cross-track component for the gradiometer is twofold. The rotation rate in cross-track direction is significantly smaller than in the other two directions. Rotation rates in along-track and nadir direction are critical for the CAI accelerometer, because this would induce contrast loss and an additional phase shift, which cannot be de-coupled from the signal of interest. Another reason is supplemental observations in east-west direction in addition to the range measurements in north-south direction assuming a polar orbit. An electrostatic cross-track gradiometer with a noise level of 1 mE in the MBW improves the ll-SST solution with GRACE-like noise assumptions. The enhancement is most evident in coefficients with degrees higher than 75. Moreover, the striping effects are reduced. A CAI gradiometer with white noise at 6.5 mE causes a similar improvement. If the ll-SST mission is equipped with an accelerometer with a lower noise level of $1 \times 10^{-12}\,\mathrm{m/s^2}$, a lower level for the cross-track gradiometer is required in order to achieve an improvement. A CAI gradiometer with white noise of 1 mE enhances the gravity field model in the higher orders and degrees of the spherical harmonic expansion. Beyond that, the error pattern is more isotropic which is especially visible in the spatial domain. This allows to achieve a monthly cumulative geoid error of 1 mm for a spatial resolution of 150 km in the best case.

Despite the improvements gained from accelerometers, CAI, drag compensation and combination of ll-SST and gradiometry, further parts have to be investigated for future satellite gravity missions. Some aspects concerning accelerometers and drag compensation were investigated independently but might be coupled. All components have to be integrated into the closed-loop simulation for future work. Besides, the closed-loop simulation can be improved by introducing other approaches for the AOD modeling errors. The simulation results strengthen the necessity to tackle a modeling improvement of ocean tides and short-term non-tidal atmospheric and oceanic mass variation, which is the major challenge in gravity field recovery. According to Dobslaw et al. (2017), the AOD products are two times more accurate over the continents than over the oceans. Alternative ocean model configurations and modifications on parametrizations could reduce the AOD errors. Consequently, the benefit from better sensors would be significantly greater. Aside from that, the temporal aliasing effect in the gravity field solutions can be reduced by alternative satellite constellations, such as the Bender constellation. The improved sampling allows to co-estimate the short-term atmospheric and oceanic signals. This can be performed using a gravity field parametrization technique which additionally estimates low-resolution solutions for short time intervals (Daras & Pail, 2017).
The sensor behavior of a CAI accelerometer needs to be studied and modeled in more detail. One example is the effect of rotations on the measurements, which has to be considered in

the simulation of CAI measurements by modeling the rotational effect, such as contrast loss and corresponding phase shift. In principle, a 3-axis CAI accelerometer can be implemented by reproducing the setup in three orientations or by switching the light between the different axes. But the realization is challenging due to the complexity of the instrument. Furthermore, the determination of the angular velocity is critical when only the cross-track gradient is measured. Therefore, high-precision gyroscopes are required. In conclusion, CAI has a promising potential for future satellite gravity missions, which has to be investigated further.

A Appendix

A.1 Reference Frames

The following reference frames are required in the calculations of this thesis. The reader is referred to Petit and Luzum (2010) for a detailed description of the Inertial Reference Frame (IRF) and Earth-fixed Reference Frame (ERF) and transformations between them (IRF corresponds to International Celestial Reference Frame and ERF to International Terrestrial Reference System, respectively). Further details to GRF and LNORF are given in Gruber et al. (2014b).

- Inertial Reference Frame
  The IRF is fixed with respect to the distant matter of the universe. The IRF is an orthogonal, right-handed system. Its origin is at the Earth's center of mass (geocenter), the orientation is equatorial, where the z-axis is the direction of the celestial pole. The x-axis is fixed in the equatorial plane in direction to the vernal equinox.

- Earth-fixed Reference Frame
  The ERF is a spatial reference system co-rotating with the Earth in its diurnal motion in space. The ERF is an orthogonal, right-handed system. Its origin is at the geocenter, the orientation is equatorial (z-axis is the direction of the pole). The x-axis is fixed in the equatorial plane in direction to the Greenwich meridian. The angle between the x-axis of the inertial reference frame and the Greenwich meridian is the Greenwich Apparent Sideral Time (GAST).

- Gradiometer Reference Frame
  The GRF is the coordinate system in which the gravity gradients are expressed. It represents the position and orientation of the gradiometer. The origins of all one-axis gradiometer reference frames are in the same point. The reference frame axes of the accelerometers are parallel and point in the same directions.

- Local North-Oriented Reference Frame
  The LNORF is a right-handed north-west-up frame with the x-axis pointing north, the y-axis pointing west and the z-axis Up. The origin is located in the satellite center of mass. The z-axis is defined by the vector from the geocenter to the satellite center of mass and is pointing radially outward. The y-axis is parallel to the normal vector to the plane of the geocentric meridian and is pointing westward. The x-axis is parallel to the normal vector of the plane defined by y and z.

- Orbit Reference Frame
  The Orbit Reference Frame (ORF) is often used in the analysis of the results. The

along-track direction points approximately in the flight direction of the satellite. The radial direction points roughly towards the center of the Earth and the cross-track axis completes the orthogonal reference system.

A.2 Satellite Reference Attitudes for Attitude Control

The reference attitude, which depends on the formation of the satellite, is required as input for the attitude control system in addition to the measured attitude. Nadir pointing is considered for mission scenarios with only one satellite, which coincides with the ORF. The reference attitude is calculated from the position vector $\mathbf{r}_{sat}$ and the velocity vector $\mathbf{v}_{sat}$ of the satellite in the IRF:

$$\mathbf{e}_1 = \frac{\mathbf{v}_{sat}}{|\mathbf{v}_{sat}|}, \qquad \mathbf{e}_3 = \frac{-\mathbf{r}_{sat} - \mathbf{e}_1(\mathbf{e}_1 \cdot \mathbf{r}_{sat})}{|\mathbf{r}_{sat}| - \mathbf{e}_1(\mathbf{e}_1 \cdot \mathbf{r}_{sat})}, \qquad \mathbf{e}_2 = \mathbf{e}_3 \times \mathbf{e}_1, \tag{A.1}$$

where $\mathbf{e_1}$, $\mathbf{e_2}$, $\mathbf{e_3}$ are the three unit vectors.

For ll-SST the satellites have to point towards each other. The reference attitude for the first satellite is given by:

$$\mathbf{e}_{A1} = \frac{\mathbf{r}_{satB} - \mathbf{r}_{satA}}{|\mathbf{r}_{satB} - \mathbf{r}_{satA}|}, \tag{A.2}$$

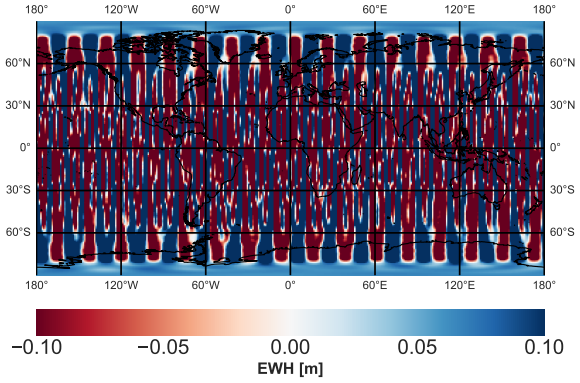
$$\mathbf{e}_{A3} = \frac{\mathbf{v}_{satB} - \mathbf{v}_{satA} - \mathbf{e}_{A1}\big((\mathbf{v}_{satB} - \mathbf{v}_{satA}) \cdot \mathbf{e}_{A1}\big)}{|\mathbf{r}_{satB} - \mathbf{r}_{satA}|}, \tag{A.3}$$

$$\mathbf{e}_{A2} = \mathbf{e}_{A3} \times \mathbf{e}_{A1}, \tag{A.4}$$

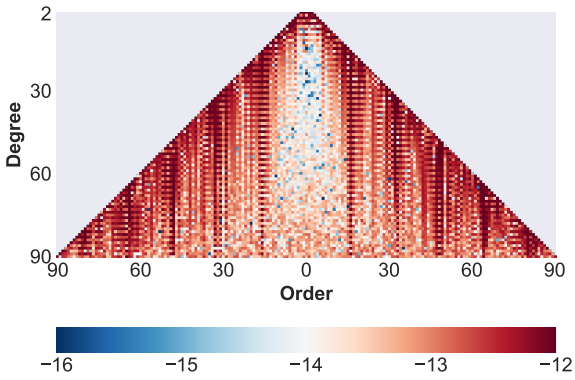
with $\mathbf{r}_{satA}$ as position vector of satellite A in IRF and $\mathbf{v}_{satA}$ as velocity vector of satellite A in IRF. The notation for satellite B is equivalent. The reference attitude of the second satellite is calculated with the same procedure. The reader is referred to Wöske (2021) for a detailed description of the attitude feedback control loop which is implemented in the XHPS software.

A.3 Simulation results - Gravity Field Solutions for ll-SST Missions

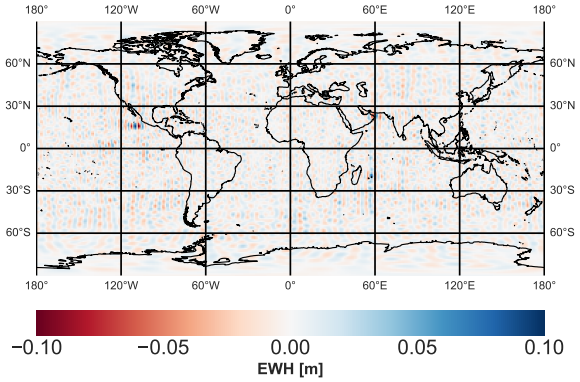
A.3.1 Instrument-only scenarios



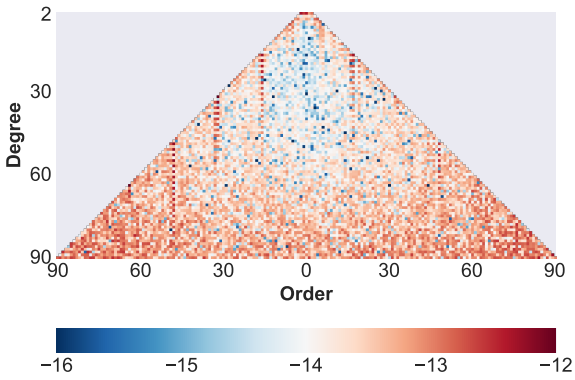
(a) EA with $1 \times 10^{-10}\,\mathrm{m/s^2}$ noise in MBW



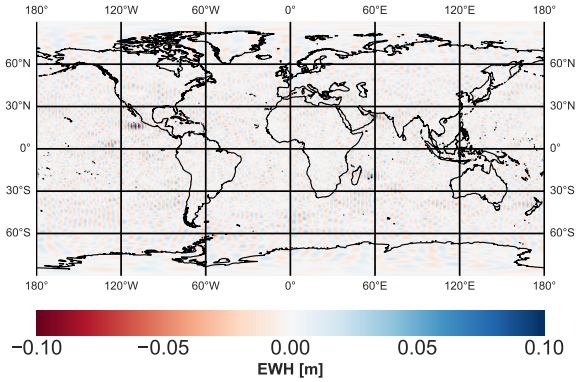
(b) EA with $1 \times 10^{-10}\,\mathrm{m/s^2}$ noise in MBW



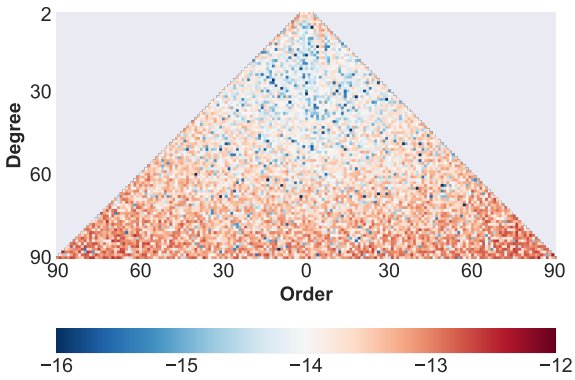
(c) EA with $1 \times 10^{-12}\,\mathrm{m/s^2}$ noise in MBW



(d) EA with $1 \times 10^{-12}\,\mathrm{m/s^2}$ noise in MBW

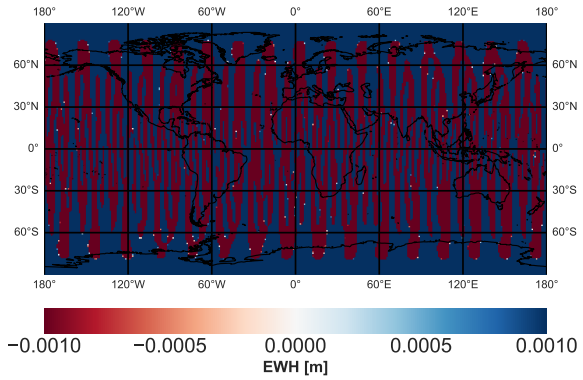


(e) Hybrid accelerometer (EA with $1 \times 10^{-12}\,\mathrm{m/s^2}$ noise in MBW and CAI with $1 \times 10^{-11}\,\mathrm{m/s^2}$ noise)

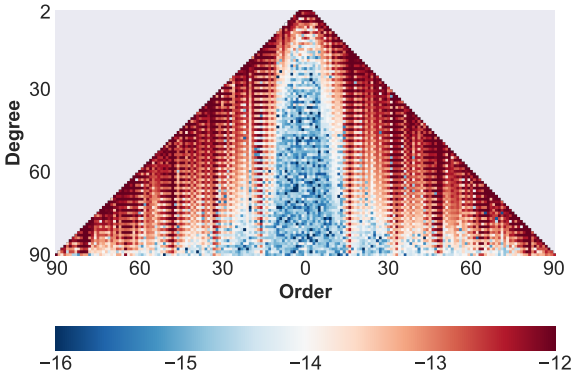


(f) Hybrid accelerometer (EA with $1 \times 10^{-12}\,\mathrm{m/s^2}$ noise in MBW and CAI with $1 \times 10^{-11}\,\mathrm{m/s^2}$ noise)

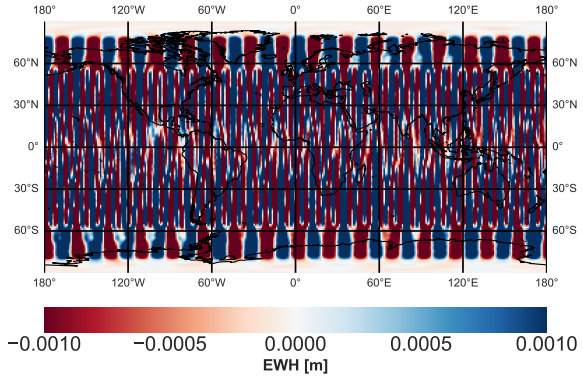
Figure A.1: Coefficient differences between recovered and reference gravity field: spatial representation in terms of EWH and pyramid representation (logarithm scale); parameters: h=246 km, only instrument noise, KBR measurement noise and different accelerometer noise models



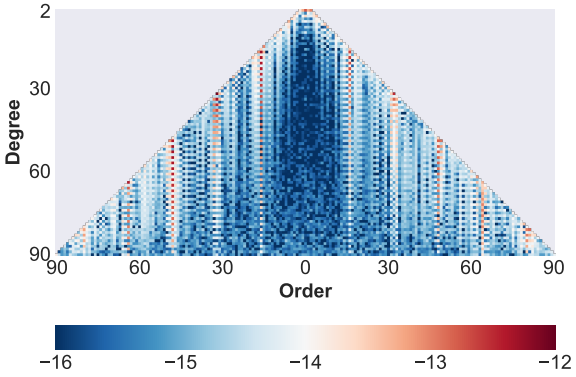
(a) EA with $1 \times 10^{-10}\,\mathrm{m/s^2}$ noise in MBW



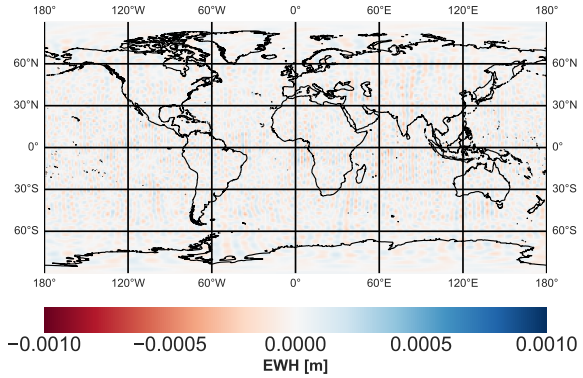
(b) EA with $1 \times 10^{-10}\,\mathrm{m/s^2}$ noise in MBW



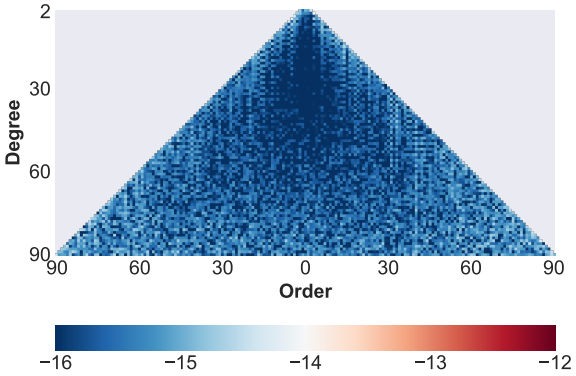
(c) EA with $1 \times 10^{-12}\,\mathrm{m/s^2}$ noise in MBW



(d) EA with $1 \times 10^{-12}\,\mathrm{m/s^2}$ noise in MBW

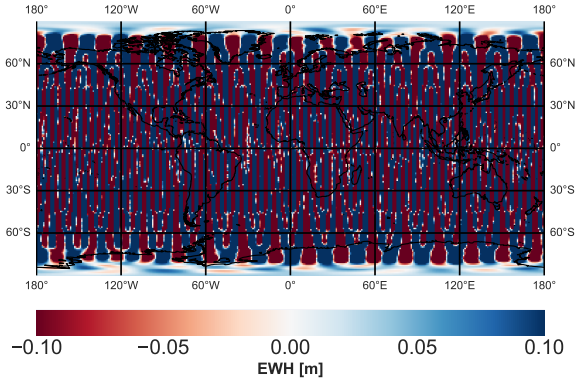


(e) Hybrid accelerometer (EA with $1 \times 10^{-12}\,\mathrm{m/s^2}$ noise in MBW and CAI with $1 \times 10^{-11}\,\mathrm{m/s^2}$ noise)

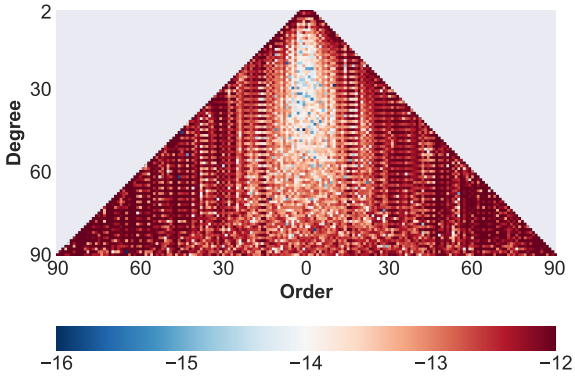


(f) Hybrid accelerometer (EA with $1 \times 10^{-12}\,\mathrm{m/s^2}$ noise in MBW and CAI with $1 \times 10^{-11}\,\mathrm{m/s^2}$ noise)

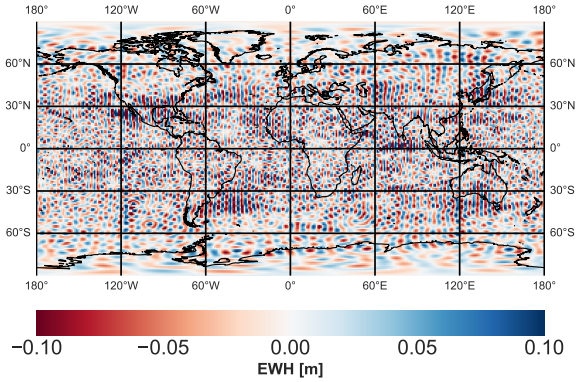
Figure A.2: Coefficient differences between recovered and reference gravity field: spatial representation in terms of EWH and pyramid representation (logarithm scale); parameters: h=246 km, only instrument noise, LRI measurement noise and different accelerometer noise models



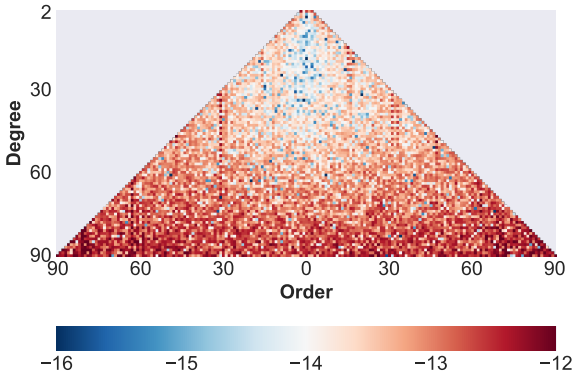
(a) EA with $1 \times 10^{-10}\,\mathrm{m/s^2}$ noise in MBW



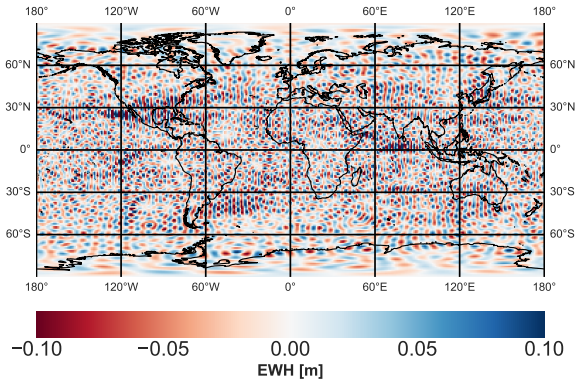
(b) EA with $1 \times 10^{-10}\,\mathrm{m/s^2}$ noise in MBW



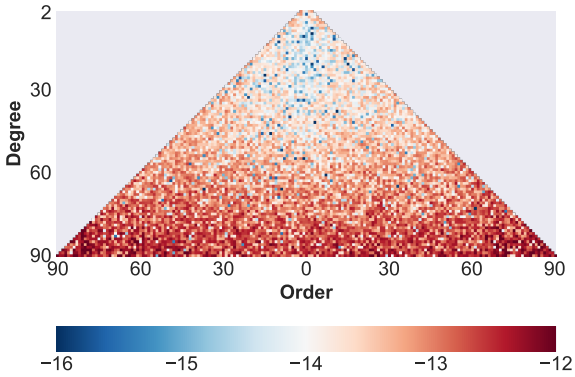
(c) EA with $1 \times 10^{-12}\,\mathrm{m/s^2}$ noise in MBW



(d) EA with $1 \times 10^{-12}\,\mathrm{m/s^2}$ noise in MBW

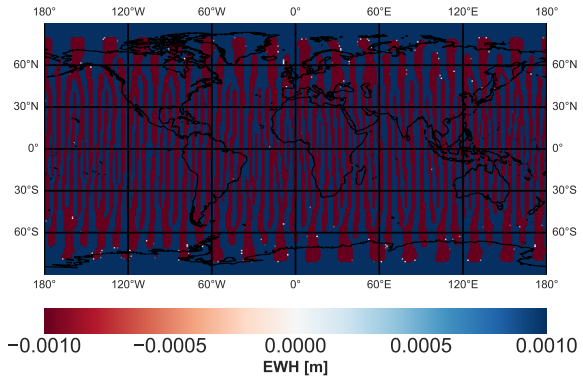


(e) Hybrid accelerometer (EA with $1 \times 10^{-12}\,\mathrm{m/s^2}$ noise in MBW and CAI with $1 \times 10^{-11}\,\mathrm{m/s^2}$ noise)

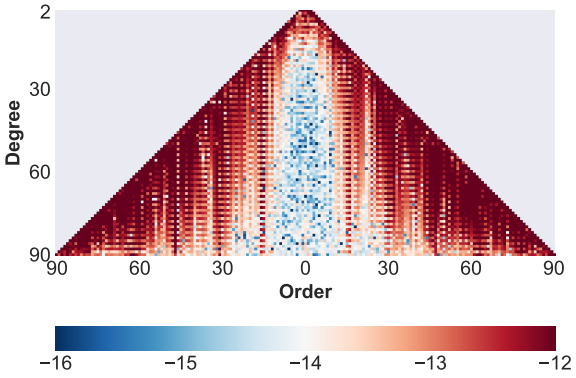


(f) Hybrid accelerometer (EA with $1 \times 10^{-12}\,\mathrm{m/s^2}$ noise in MBW and CAI with $1 \times 10^{-11}\,\mathrm{m/s^2}$ noise)

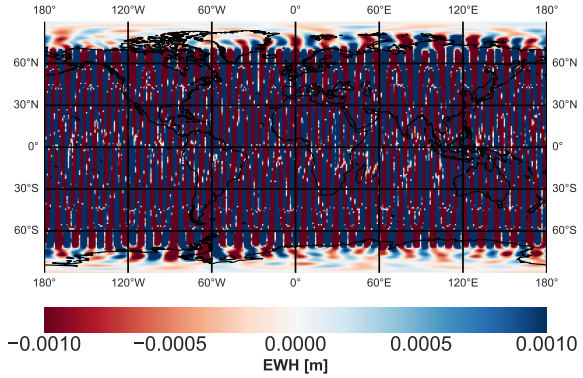
Figure A.3: Coefficient differences between recovered and reference gravity field: spatial representation in terms of EWH and pyramid representation (logarithm scale); parameters: h=363 km, only instrument noise, KBR measurement noise and different accelerometer noise models



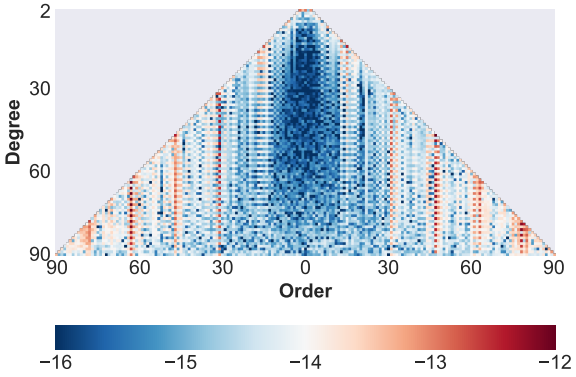
(a) EA with $1 \times 10^{-10}\,\mathrm{m/s^2}$ noise in MBW



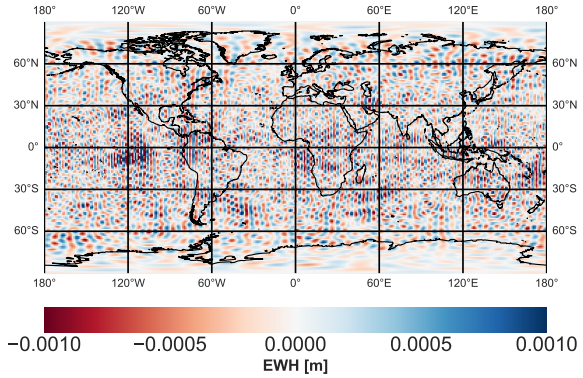
(b) EA with $1 \times 10^{-10}\,\mathrm{m/s^2}$ noise in MBW



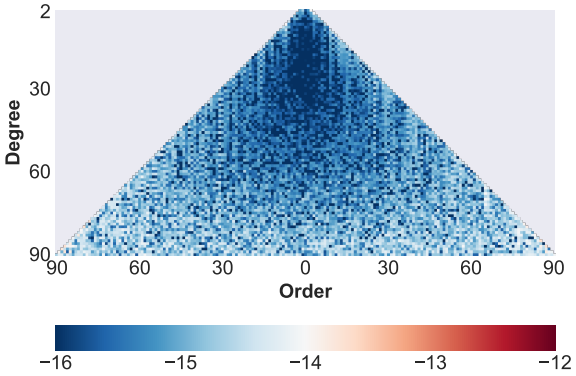
(c) EA with $1 \times 10^{-12}\,\mathrm{m/s^2}$ noise in MBW



(d) EA with $1 \times 10^{-12}\,\mathrm{m/s^2}$ noise in MBW



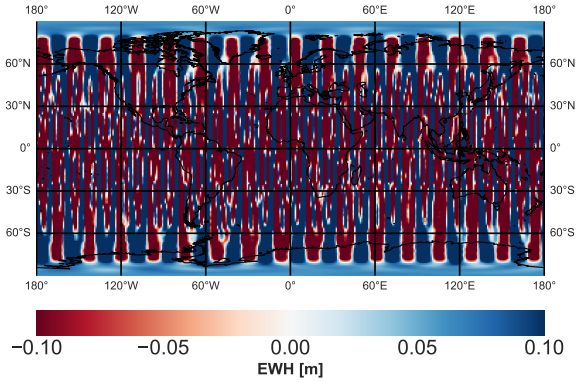
(e) Hybrid accelerometer (EA with $1 \times 10^{-12}\,\mathrm{m/s^2}$ noise in MBW and CAI with $1 \times 10^{-11}\,\mathrm{m/s^2}$ noise)



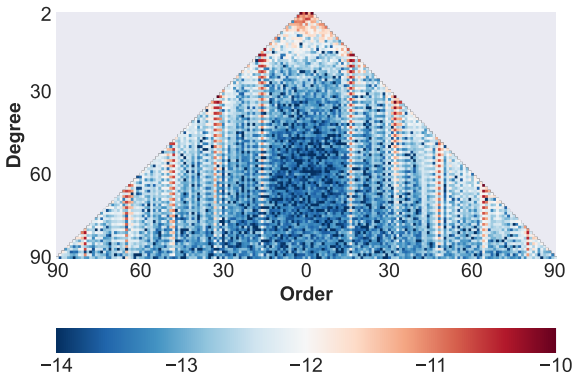
(f) Hybrid accelerometer (EA with $1 \times 10^{-12}\,\mathrm{m/s^2}$ noise in MBW and CAI with $1 \times 10^{-11}\,\mathrm{m/s^2}$ noise)

Figure A.4: Coefficient differences between recovered and reference gravity field: spatial representation in terms of EWH and pyramid representation (logarithm scale); parameters: h=363 km, only instrument noise, LRI measurement noise and variation of accelerometer noise

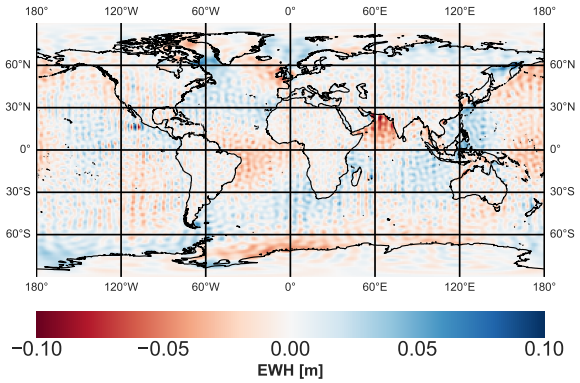
A.3.2 Scenarios including AOD and Ocean-tide Error



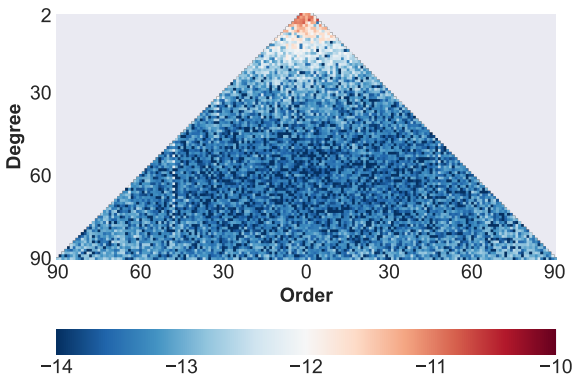
(a) EA with $1 \times 10^{-10}\,\mathrm{m/s^2}$ noise in MBW



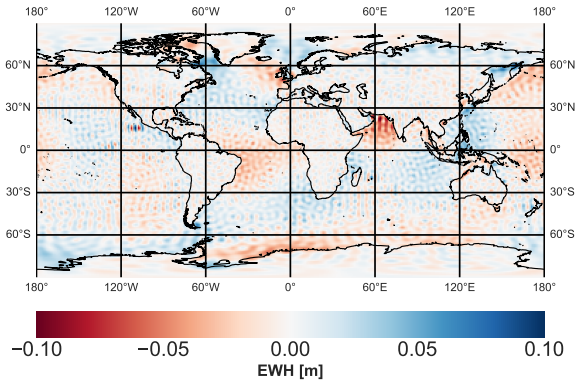
(b) EA with $1 \times 10^{-10}\,\mathrm{m/s^2}$ noise in MBW



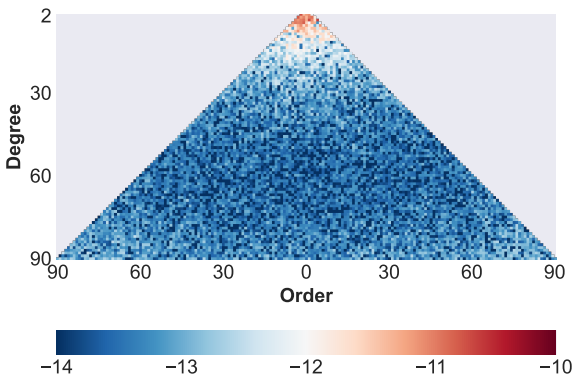
(c) EA with $1 \times 10^{-12}\,\mathrm{m/s^2}$ noise in MBW



(d) EA with $1 \times 10^{-12}\,\mathrm{m/s^2}$ noise in MBW

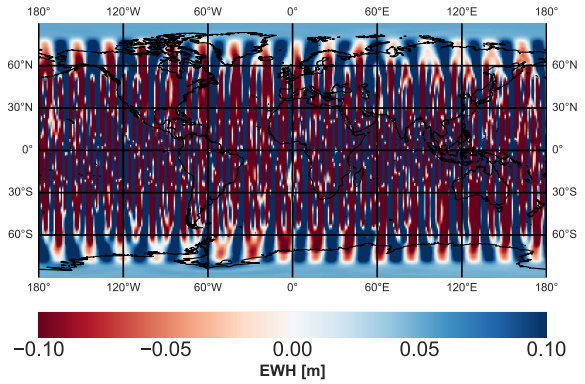


(e) Hybrid accelerometer (EA with $1 \times 10^{-12}\,\mathrm{m/s^2}$ noise in MBW and CAI with $1 \times 10^{-11}\,\mathrm{m/s^2}$ noise)

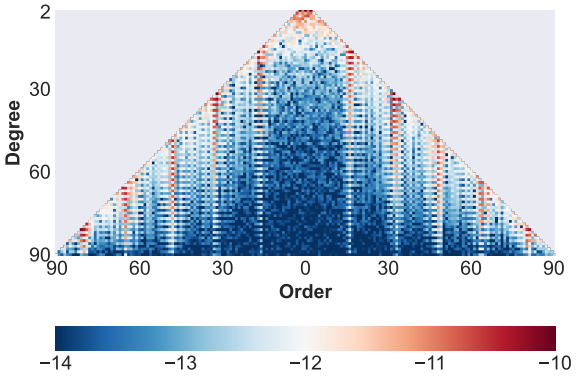


(f) Hybrid accelerometer (EA with $1 \times 10^{-12}\,\mathrm{m/s^2}$ noise in MBW and CAI with $1 \times 10^{-11}\,\mathrm{m/s^2}$ noise)

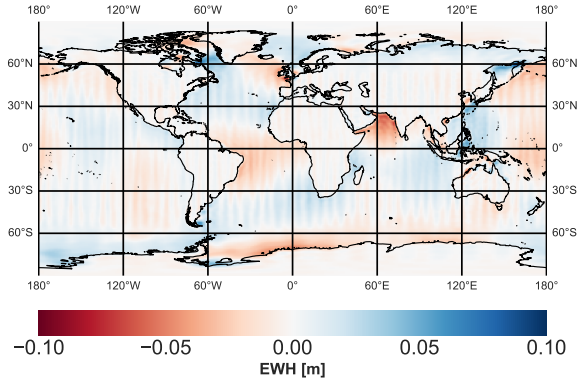
Figure A.5: Coefficient differences between recovered and reference gravity field: spatial representation in terms of EWH and pyramid representation (logarithm scale); parameters: h=246 km, KBR measurement noise and different accelerometer noise models



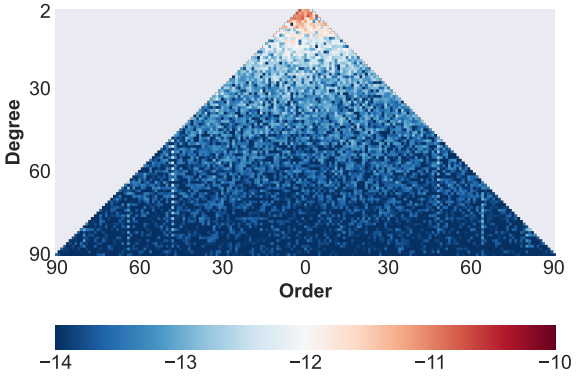
(a) EA with $1 \times 10^{-10}\,\mathrm{m/s^2}$ noise in MBW



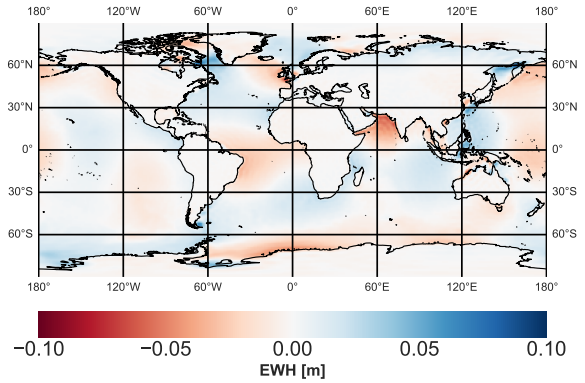
(b) EA with $1 \times 10^{-10}\,\mathrm{m/s^2}$ noise in MBW



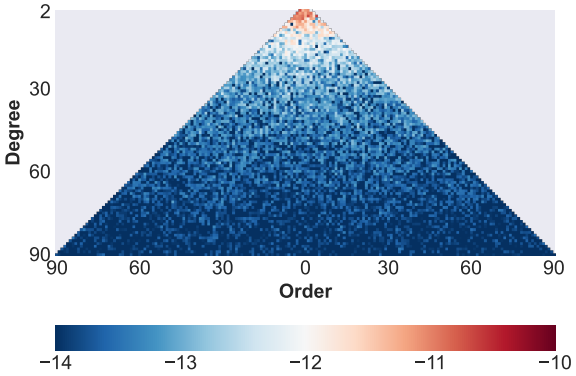
(c) EA with $1 \times 10^{-12}\,\mathrm{m/s^2}$ noise in MBW



(d) EA with $1 \times 10^{-12}\,\mathrm{m/s^2}$ noise in MBW

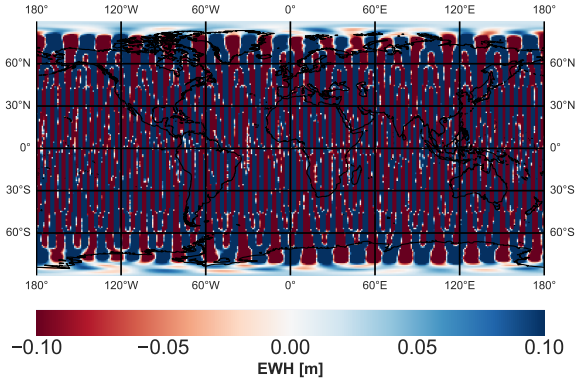


(e) Hybrid accelerometer (EA with $1 \times 10^{-12}\,\mathrm{m/s^2}$ noise in MBW and CAI with $1 \times 10^{-11}\,\mathrm{m/s^2}$ noise)

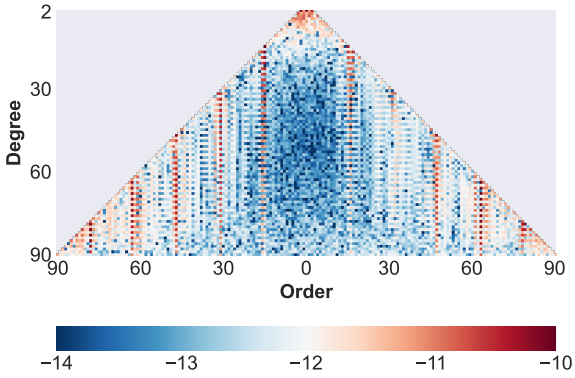


(f) Hybrid accelerometer (EA with $1 \times 10^{-12}\,\mathrm{m/s^2}$ noise in MBW and CAI with $1 \times 10^{-11}\,\mathrm{m/s^2}$ noise)

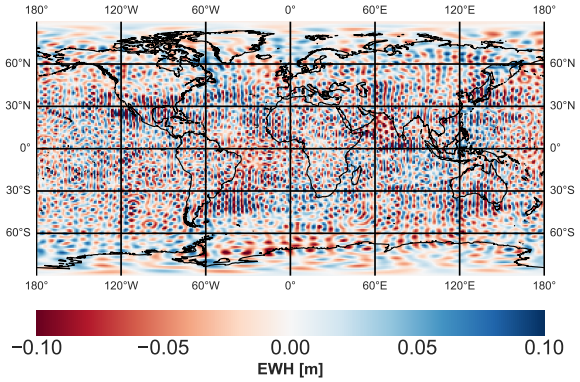
Figure A.6: Coefficient differences between recovered and reference gravity field: spatial representation in terms of EWH and pyramid representation (logarithm scale); parameters: h=246 km, LRI measurement noise and different accelerometer noise models



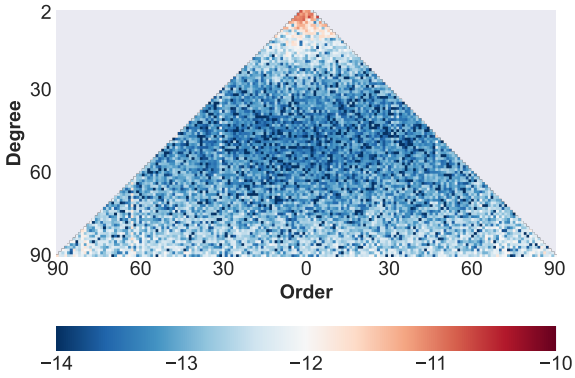
(a) EA with $1 \times 10^{-10}\,\mathrm{m/s^2}$ noise in MBW



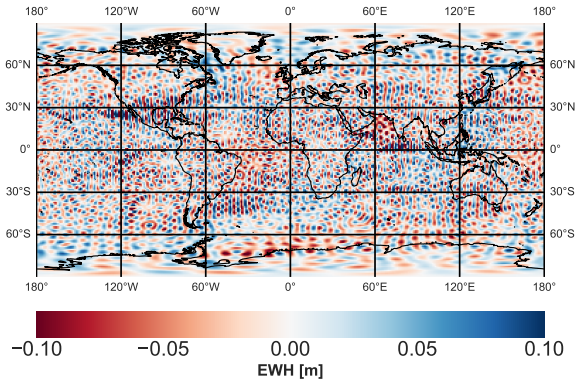
(b) EA with $1 \times 10^{-10}\,\mathrm{m/s^2}$ noise in MBW



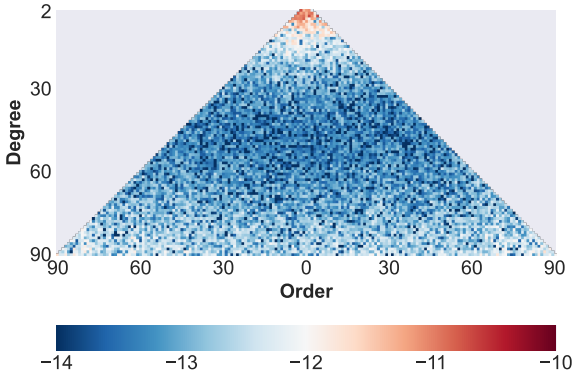
(c) EA with $1 \times 10^{-12}\,\mathrm{m/s^2}$ noise in MBW



(d) EA with $1 \times 10^{-12}\,\mathrm{m/s^2}$ noise in MBW

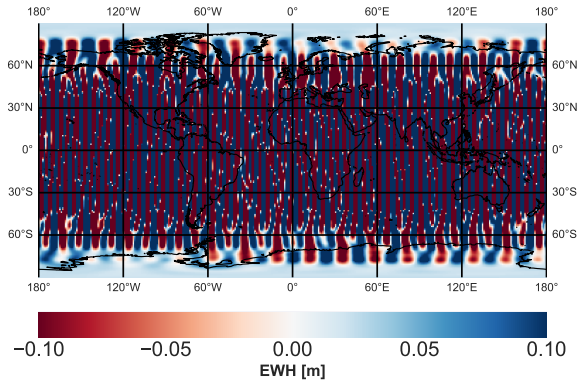


(e) Hybrid accelerometer (EA with $1 \times 10^{-12}\,\mathrm{m/s^2}$ noise in MBW and CAI with $1 \times 10^{-11}\,\mathrm{m/s^2}$ noise)

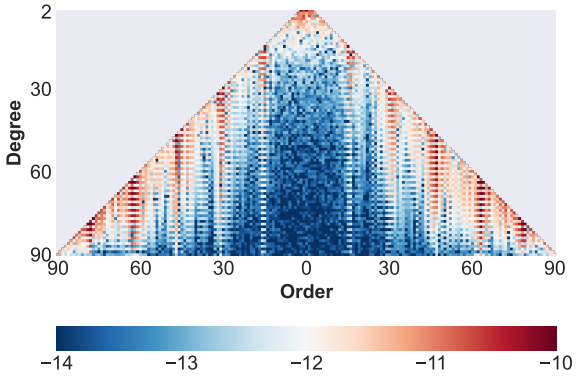


(f) Hybrid accelerometer (EA with $1 \times 10^{-12}\,\mathrm{m/s^2}$ noise in MBW and CAI with $1 \times 10^{-11}\,\mathrm{m/s^2}$ noise)

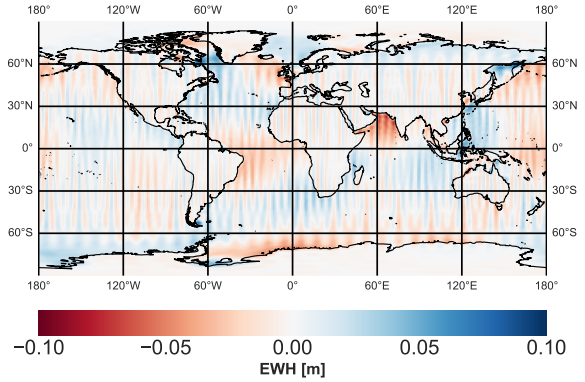
Figure A.7: Coefficient differences between recovered and reference gravity field: spatial representation in terms of EWH and pyramid representation (logarithm scale); parameters: h=363 km, KBR measurement noise and different accelerometer noise models



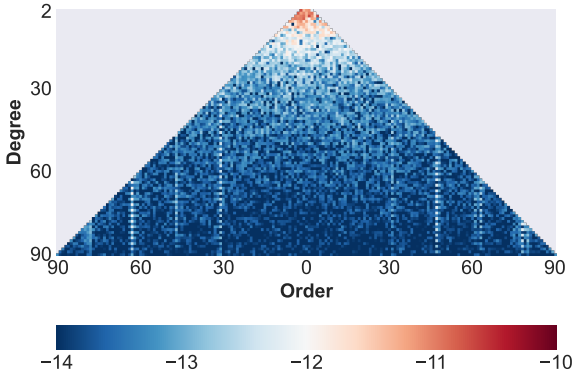
(a) EA with $1 \times 10^{-10}\,\mathrm{m/s^2}$ noise in MBW



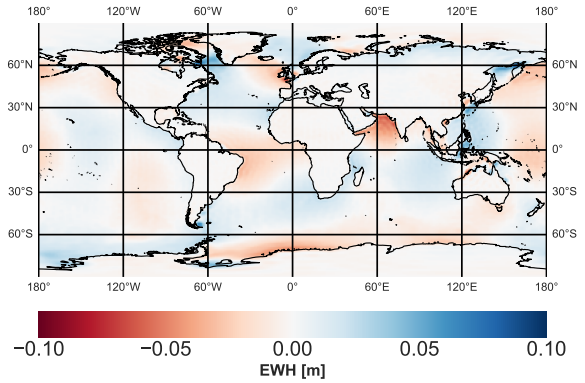
(b) EA with $1 \times 10^{-10}\,\mathrm{m/s^2}$ noise in MBW



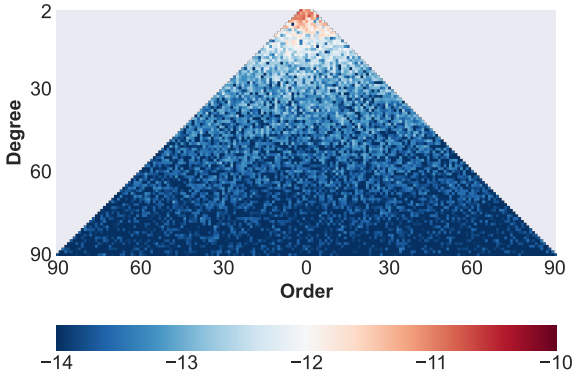
(c) EA with $1 \times 10^{-12}\,\mathrm{m/s^2}$ noise in MBW



(d) EA with $1 \times 10^{-12}\,\mathrm{m/s^2}$ noise in MBW



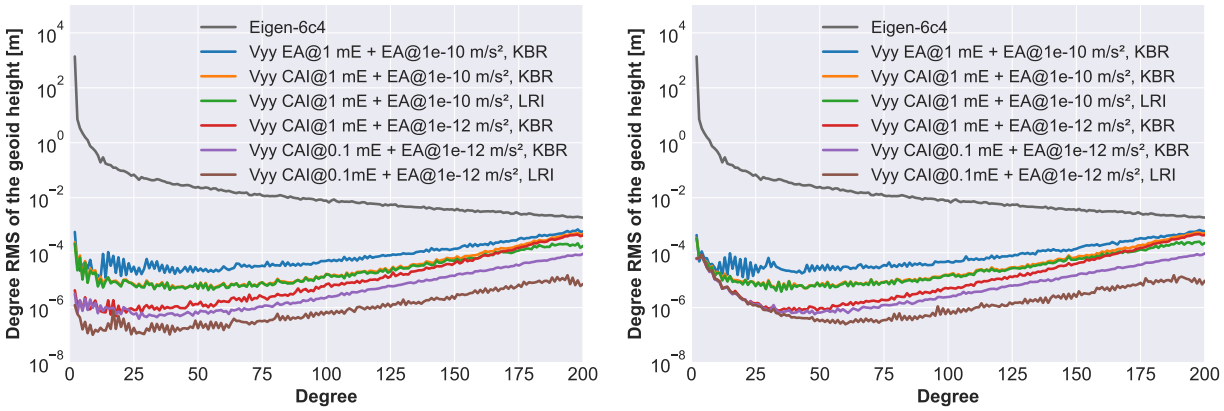
(e) Hybrid accelerometer (EA with $1 \times 10^{-12}\,\mathrm{m/s^2}$ noise in MBW and CAI with $1 \times 10^{-11}\,\mathrm{m/s^2}$ noise)



(f) Hybrid accelerometer (EA with $1 \times 10^{-12}\,\mathrm{m/s^2}$ noise in MBW and CAI with $1 \times 10^{-11}\,\mathrm{m/s^2}$ noise)

Figure A.8: Coefficient differences between recovered and reference gravity field: spatial representation in terms of EWH and pyramid representation (logarithm scale); parameters: h=363 km, LRI measurement noise and different accelerometer noise models

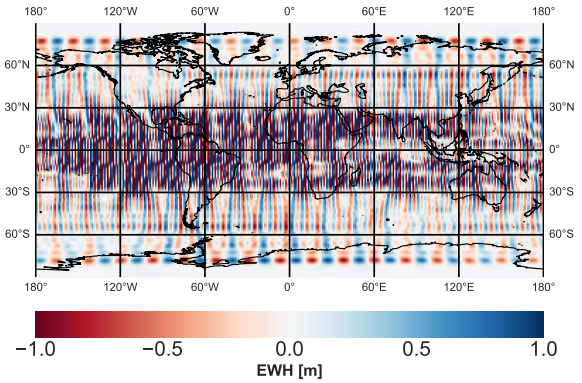
A.4 Simulation results - Combined Gravity Field Solutions from ll-SST and Cross-track Gradiometry



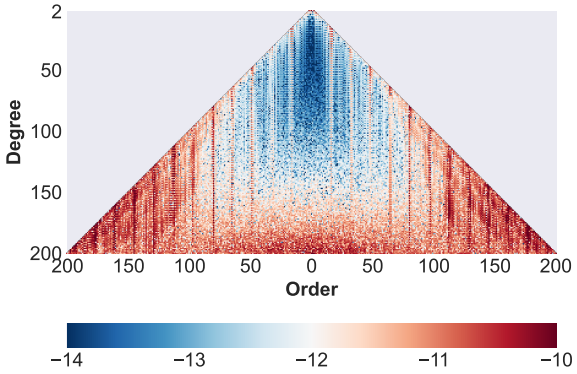
(a) Instrument-only, altitude of 303 km

(b) Including AOD and ocean-tide errors, altitude of 303 km

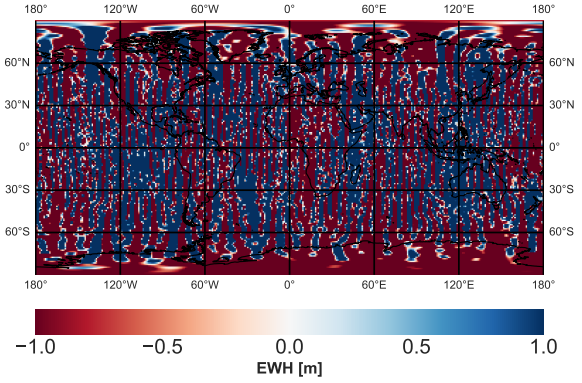
Figure A.9: Degree RMS of the coefficient differences between recovered and reference gravity field for different sensor combinations for an orbit altitude of 303 km



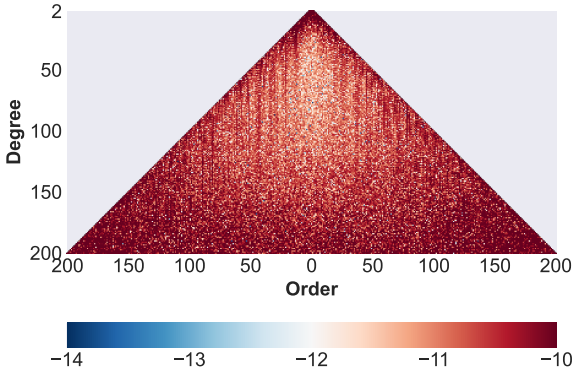
(a) ll-SST: EA at a noise level of $1 \times 10^{-10}\,\mathrm{m/s^2}$



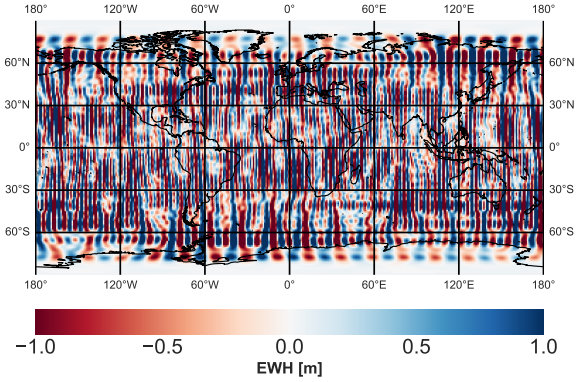
(b) ll-SST: EA at a noise level of $1 \times 10^{-10}\,\mathrm{m/s^2}$



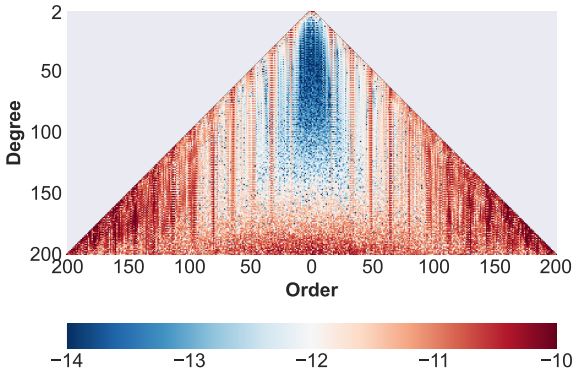
(c) Cross-track component V_{yy}: EG at a noise level of 6.5 mE



(d) Cross-track component V_{yy}: EG at a noise level of 6.5 mE

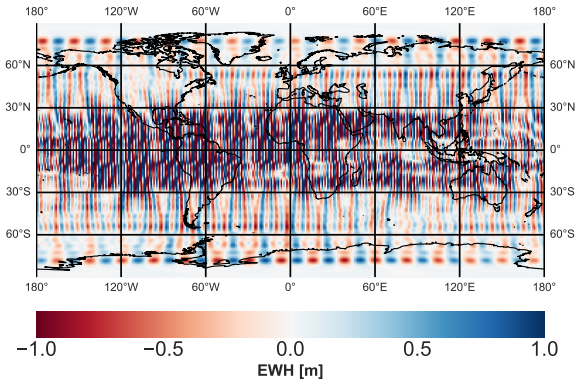


(e) Combination of ll-SST and cross-track gradiometry

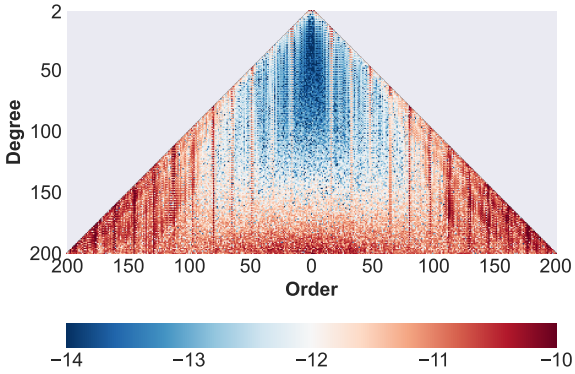


(f) Combination of ll-SST and cross-track gradiometry

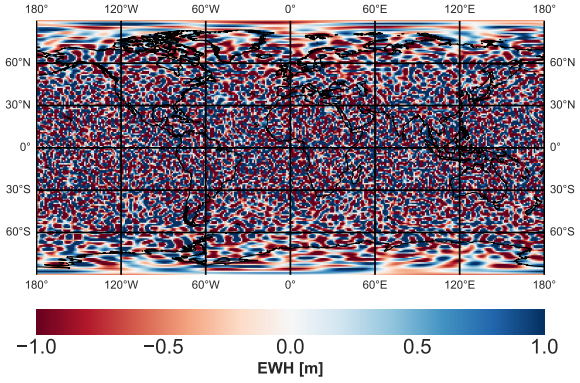
Figure A.10: Coefficient differences between recovered and reference gravity field: spatial representation in terms of EWH and pyramid representation (logarithm scale), instrument-only scenario: h=246 km, ll-SST: KBR noise and EA at a noise level of $1 \times 10^{-10}\,\mathrm{m/s^2}$, cross-track component V_{yy}: EG at a noise level of 6.5 mE



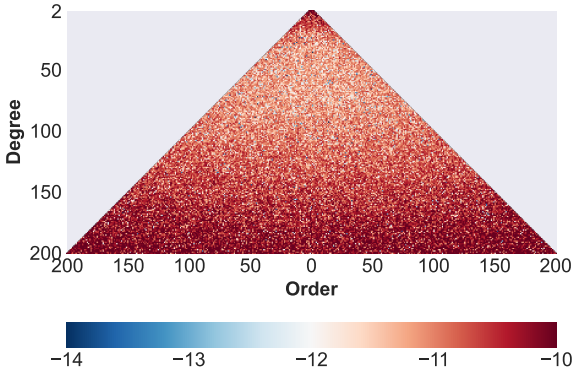
(a) ll-SST: EA at a noise level of $1 \times 10^{-10}\,\mathrm{m/s^2}$



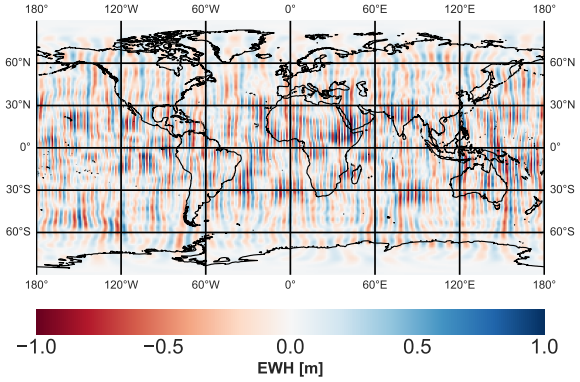
(b) ll-SST: EA at a noise level of $1 \times 10^{-10}\,\mathrm{m/s^2}$



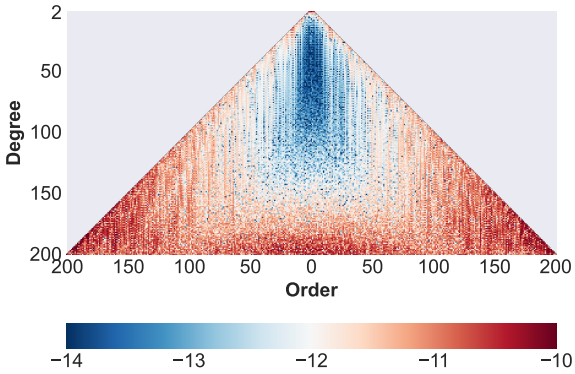
(c) Cross-track component V_{yy}: CAI gradiometer at a noise level of 6.5 mE



(d) Cross-track component V_{yy}: CAI gradiometer at a noise level of 6.5 mE

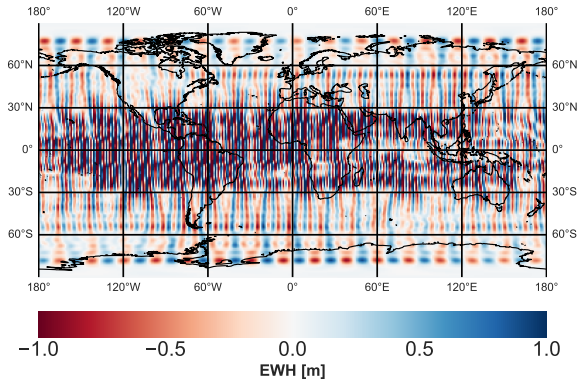


(e) Combination of ll-SST and cross-track gradiometry

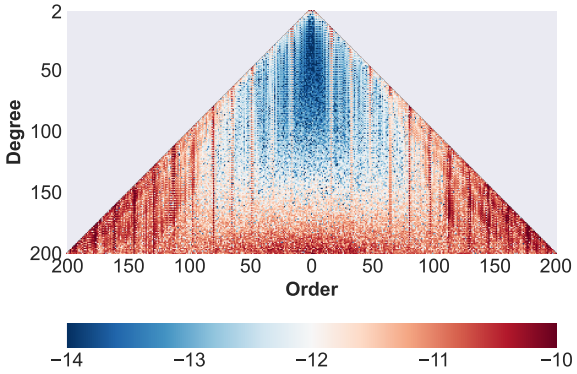


(f) Combination of ll-SST and cross-track gradiometry

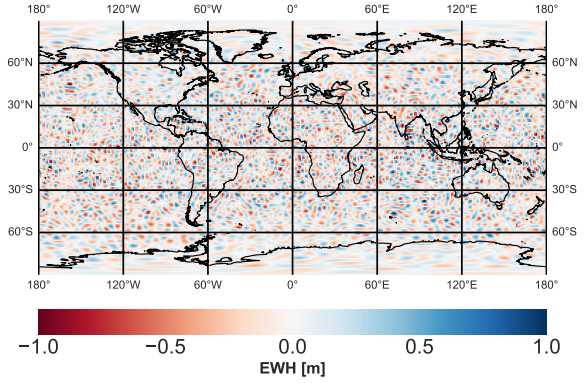
Figure A.11: Coefficient differences between recovered and reference gravity field: spatial representation in terms of EWH and pyramid representation (logarithm scale), instrument-only scenario: h=246 km, ll-SST: KBR noise and EA at a noise level of $1 \times 10^{-10}\,\mathrm{m/s^2}$, cross-track component V_{yy}: CAI gradiometer at a noise level of 6.5 mE



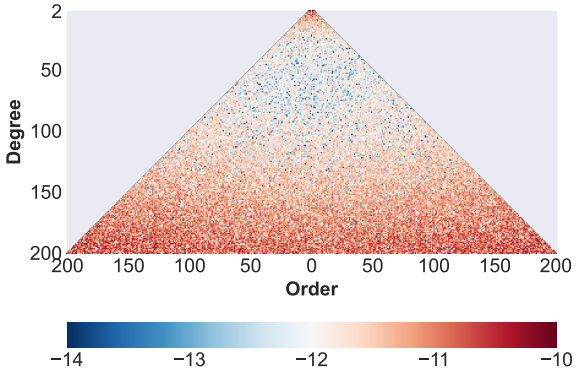
(a) ll-SST: EA at a noise level of $1 \times 10^{-10}\,\mathrm{m/s^2}$



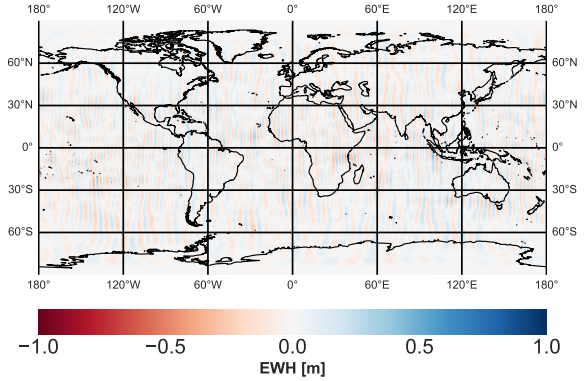
(b) ll-SST: EA at a noise level of $1 \times 10^{-10}\,\mathrm{m/s^2}$



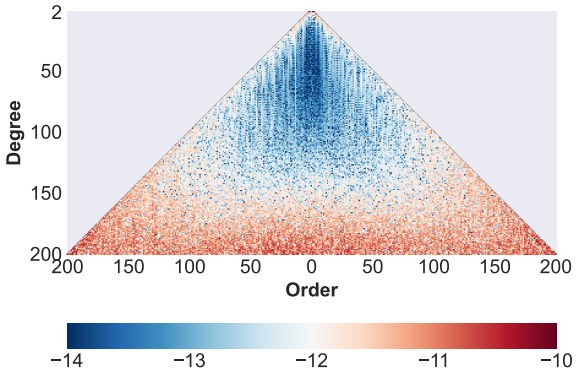
(c) Cross-track component V_{yy}: CAI gradiometer at a noise level of 1 mE



(d) Cross-track component V_{yy}: CAI gradiometer at a noise level of 1 mE

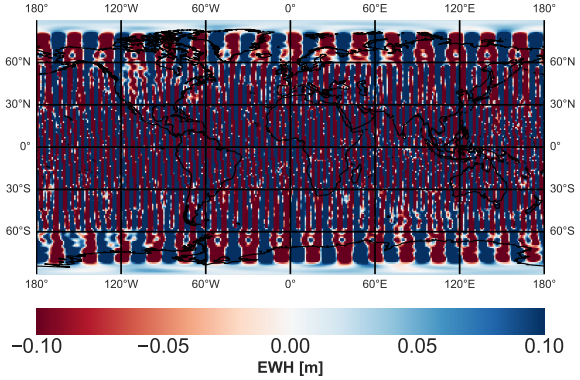


(e) Combination of ll-SST and cross-track gradiometry

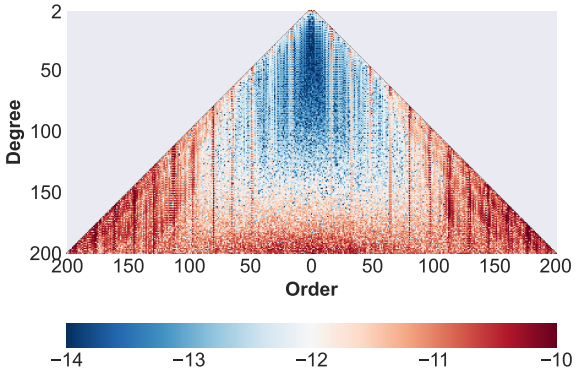


(f) Combination of ll-SST and cross-track gradiometry

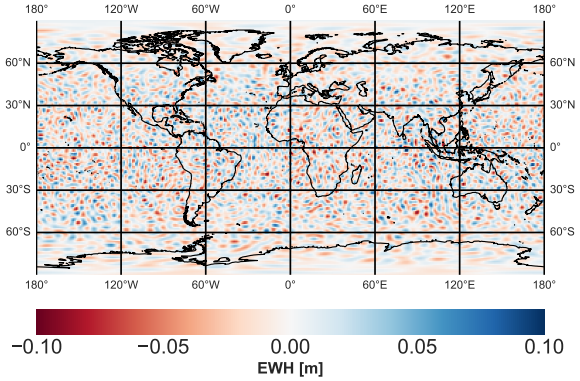
Figure A.12: Coefficient differences between recovered and reference gravity field: spatial representation in terms of EWH and pyramid representation (logarithm scale), instrument-only scenario: h=246 km, ll-SST: KBR noise and EA at a noise level of $1 \times 10^{-10}\,\mathrm{m/s^2}$, cross-track component V_{yy}: CAI gradiometer at a noise level of 1 mE



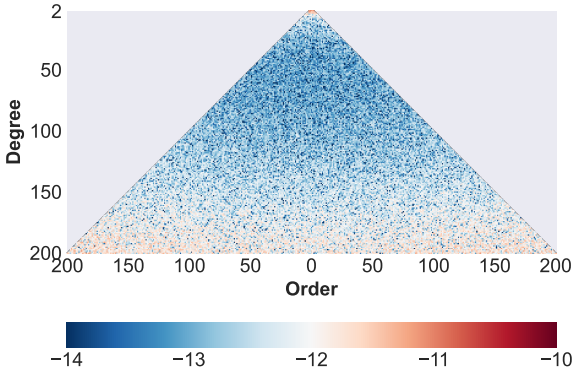
(a) ll-SST: EA at a noise level of $1 \times 10^{-10}\,\mathrm{m/s^2}$



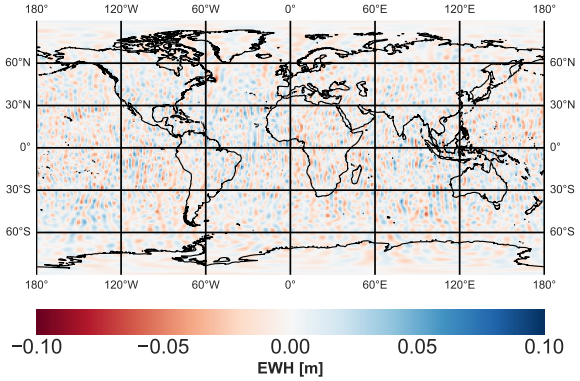
(b) ll-SST: EA at a noise level of $1 \times 10^{-10}\,\mathrm{m/s^2}$



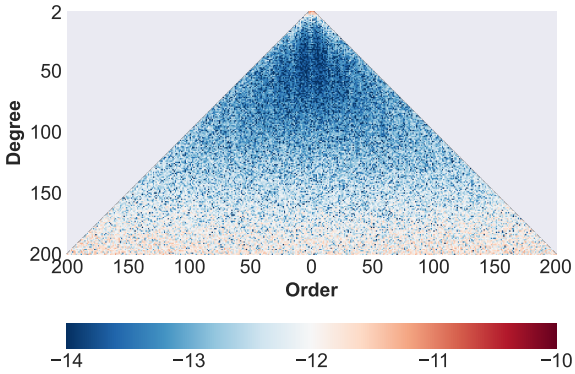
(c) Cross-track component V_{yy}: CAI gradiometer at a noise level of 0.1 mE



(d) Cross-track component V_{yy}: CAI gradiometer at a noise level of 0.1 mE

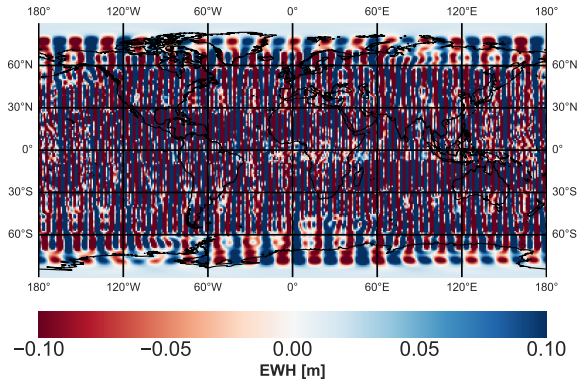


(e) Combination of ll-SST and cross-track gradiometry

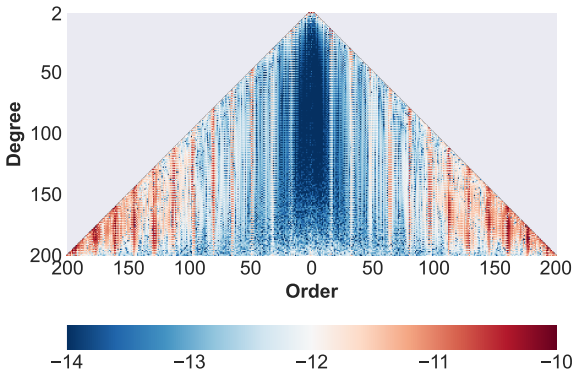


(f) Combination of ll-SST and cross-track gradiometry

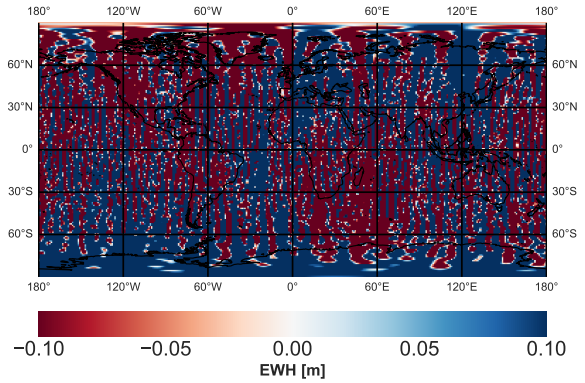
Figure A.13: Coefficient differences between recovered and reference gravity field: spatial representation in terms of EWH and pyramid representation (logarithm scale), instrument-only scenario: h=246 km, ll-SST: KBR noise and EA at a noise level of $1 \times 10^{-10}\,\mathrm{m/s^2}$, cross-track component V_{yy}: CAI gradiometer at a noise level of 0.1 mE



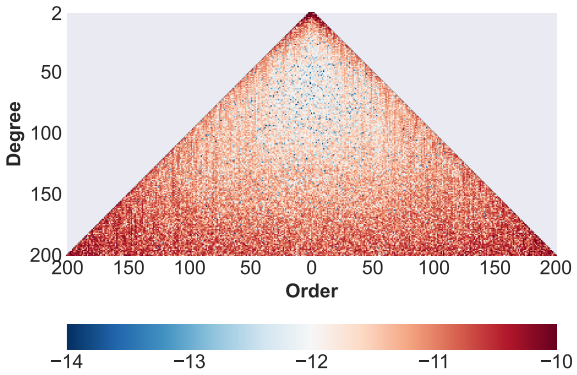
(a) ll-SST: EA at a noise level of $1 \times 10^{-10}\,\mathrm{m/s^2}$



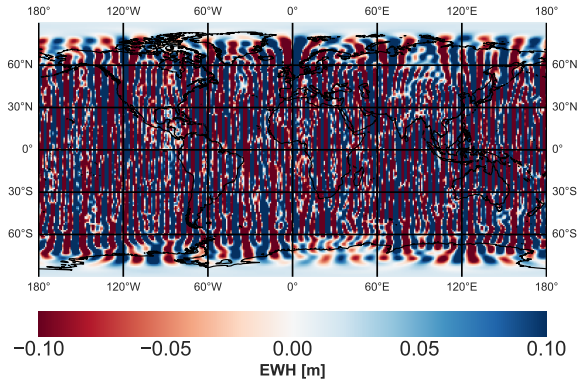
(b) ll-SST: EA at a noise level of $1 \times 10^{-10}\,\mathrm{m/s^2}$



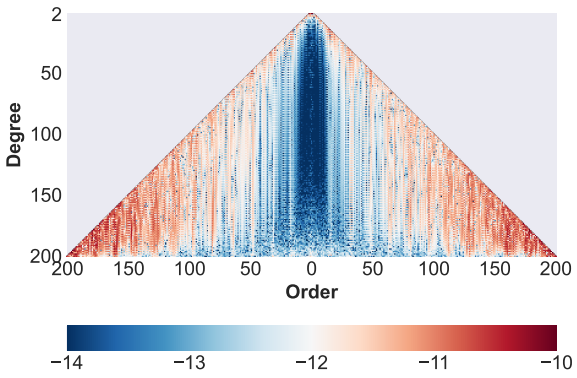
(c) Cross-track component V_{yy}: EG at a noise level of 1 mE



(d) Cross-track component V_{yy}: EG at a noise level of 1 mE

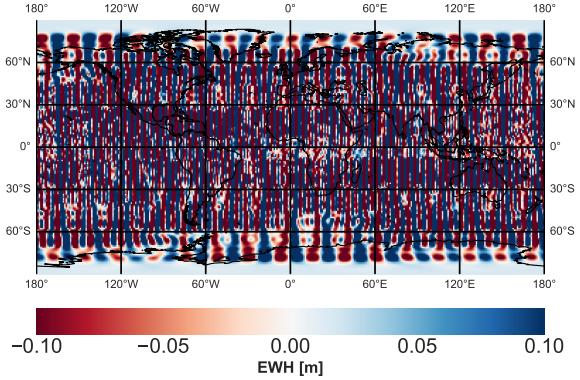


(e) Combination of ll-SST and cross-track gradiometry

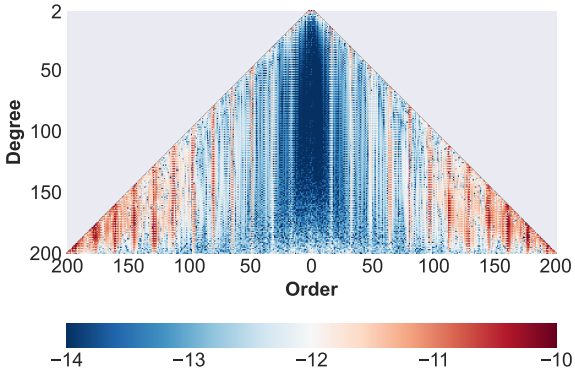


(f) Combination of ll-SST and cross-track gradiometry

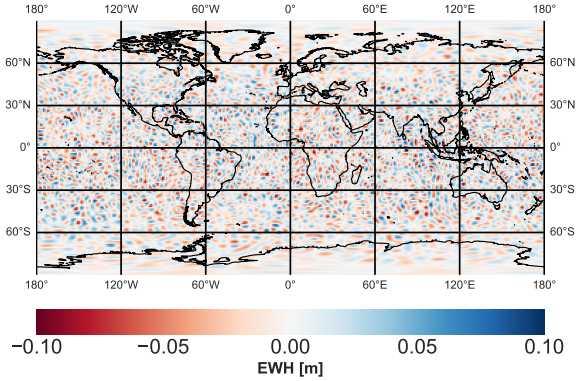
Figure A.14: Coefficient differences between recovered and reference gravity field: spatial representation in terms of EWH and pyramid representation (logarithm scale), instrument-only scenario: h=246 km, ll-SST: LRI noise and EA at a noise level of $1 \times 10^{-10}\,\mathrm{m/s^2}$, cross-track component V_{yy}: EG at a noise level of 1 mE



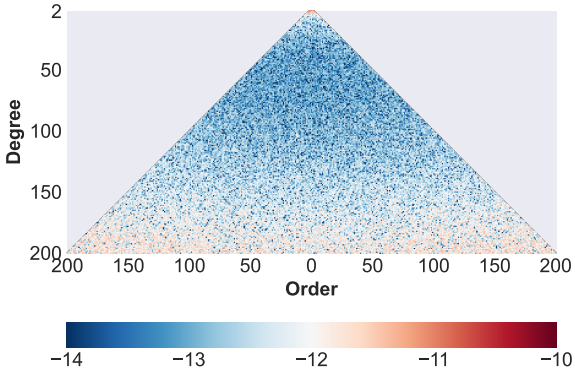
(a) ll-SST: EA at a noise level of $1 \times 10^{-10}\,\mathrm{m/s^2}$



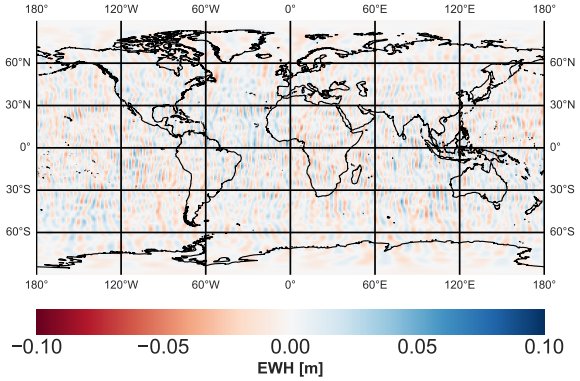
(b) ll-SST: EA at a noise level of $1 \times 10^{-10}\,\mathrm{m/s^2}$



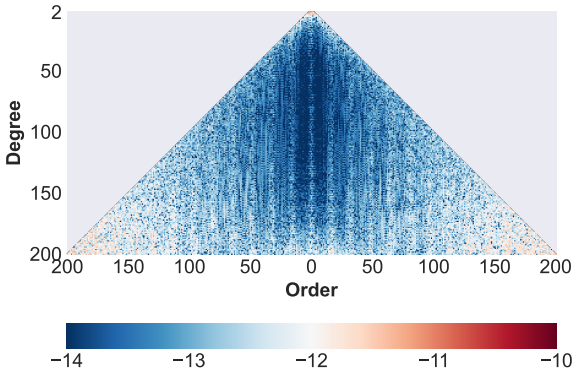
(c) Cross-track component V_{yy}: CAI gradiometer at a noise level of 0.1 mE



(d) Cross-track component V_{yy}: CAI gradiometer at a noise level of 0.1 mE

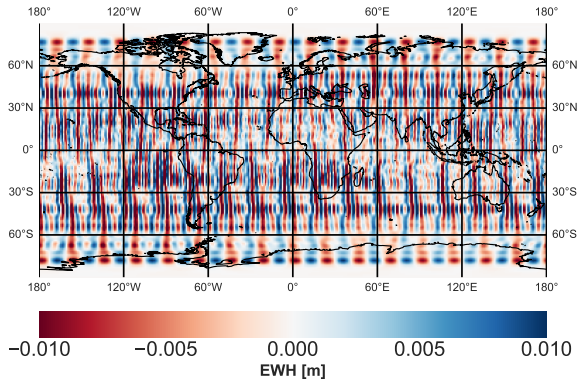


(e) Combination of ll-SST and cross-track gradiometry

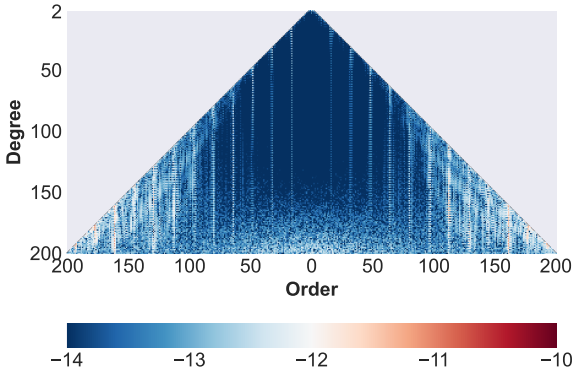


(f) Combination of ll-SST and cross-track gradiometry

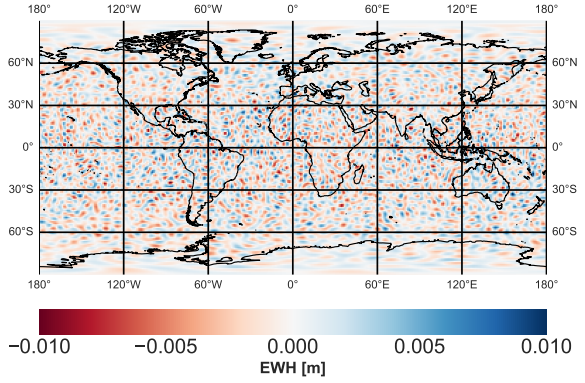
Figure A.15: Coefficient differences between recovered and reference gravity field: spatial representation in terms of EWH and pyramid representation (logarithm scale), instrument-only scenario: h=246 km, ll-SST: LRI noise and EA at a noise level of $1 \times 10^{-10}\,\mathrm{m/s^2}$, cross-track component V_{yy}: CAI gradiometer at a noise level of 0.1 mE



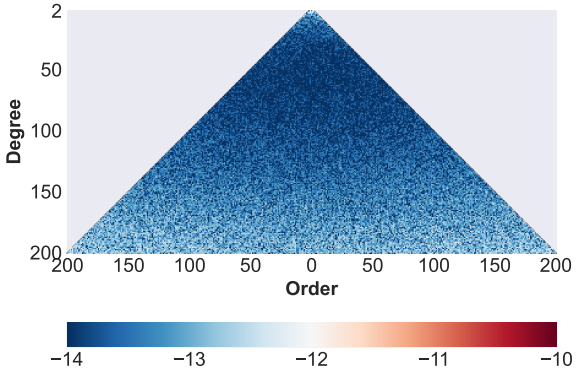
(a) ll-SST: EA at a noise level of $1 \times 10^{-12}\,\mathrm{m/s^2}$



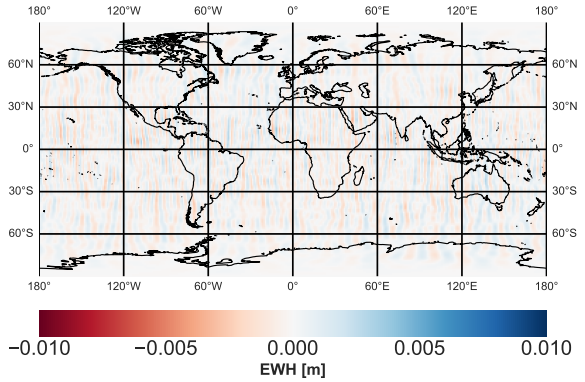
(b) ll-SST: EA at a noise level of $1 \times 10^{-12}\,\mathrm{m/s^2}$



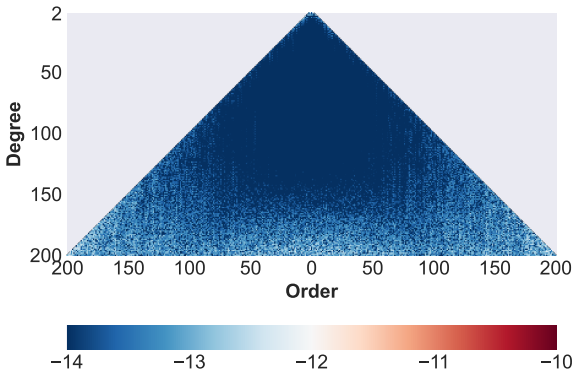
(c) Cross-track component V_{yy}: CAI gradiometer at a noise level of 0.01 mE



(d) Cross-track component V_{yy}: CAI gradiometer at a noise level of 0.01 mE

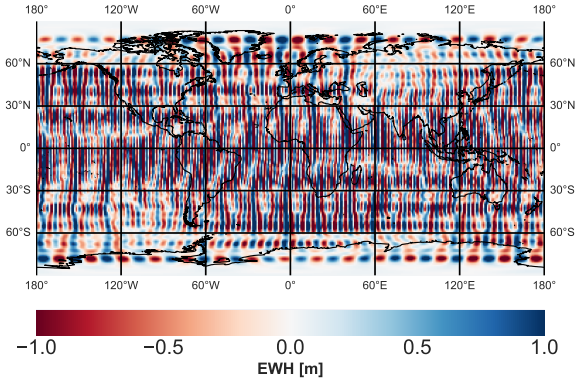


(e) Combination of ll-SST and cross-track gradiometry

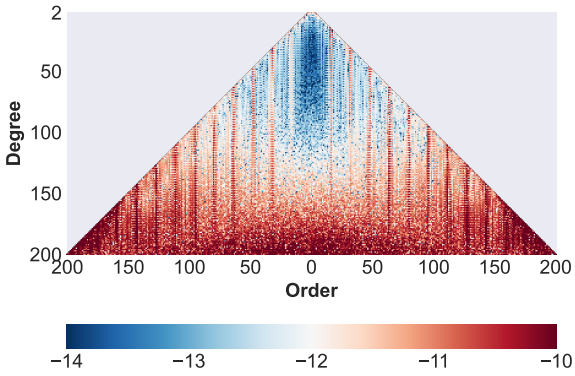


(f) Combination of ll-SST and cross-track gradiometry

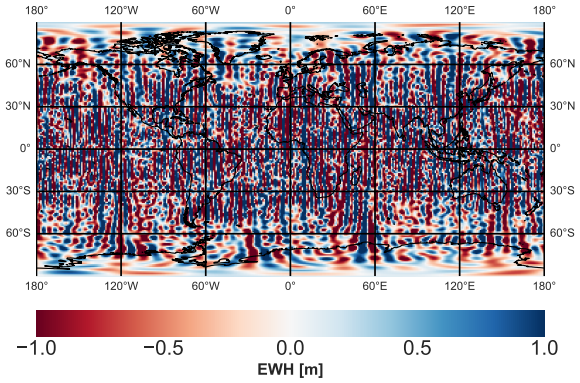
Figure A.16: Coefficient differences between recovered and reference gravity field: spatial representation in terms of EWH and pyramid representation (logarithm scale), instrument-only scenario: h=246 km, ll-SST: LRI noise and EA at a noise level of $1 \times 10^{-12}\,\mathrm{m/s^2}$, cross-track component V_{yy}: CAI gradiometer at a noise level of 0.01 mE



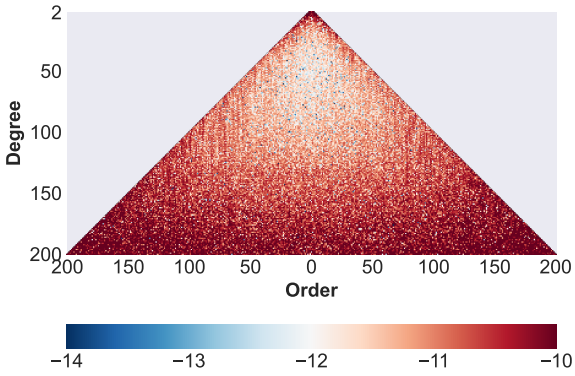
(a) ll-SST: EA at a noise level of $1 \times 10^{-10}\,\mathrm{m/s^2}$



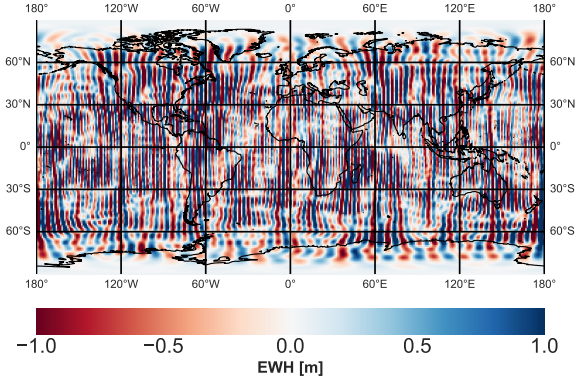
(b) ll-SST: EA at a noise level of $1 \times 10^{-10}\,\mathrm{m/s^2}$



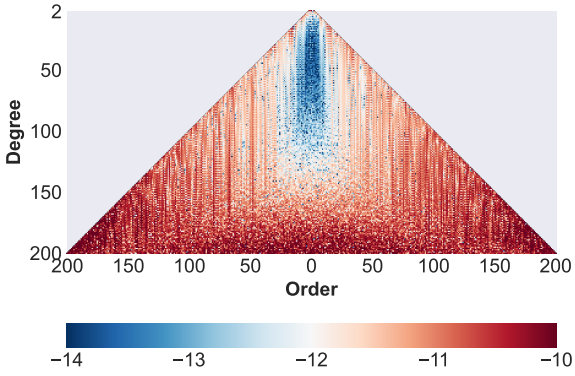
(c) Cross-track component V_{yy}: EG at a noise level of 1 mE



(d) Cross-track component V_{yy}: EG at a noise level of 1 mE

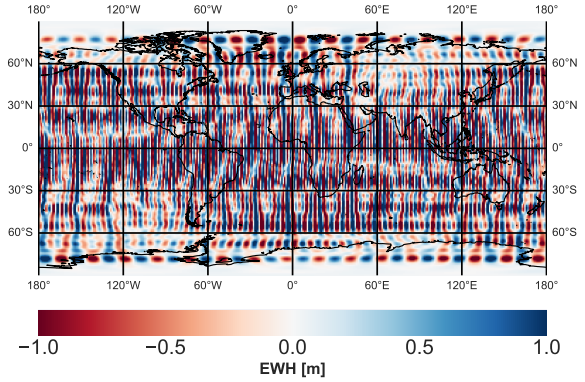


(e) Combination of ll-SST and cross-track gradiometry

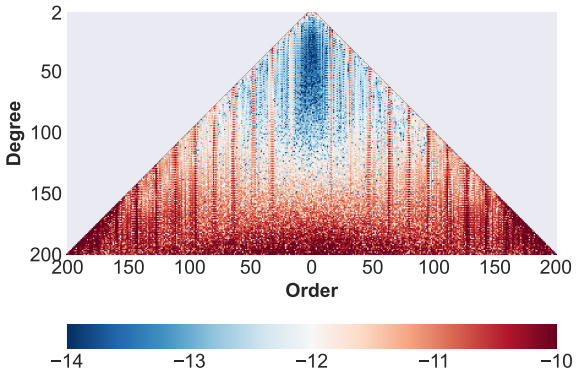


(f) Combination of ll-SST and cross-track gradiometry

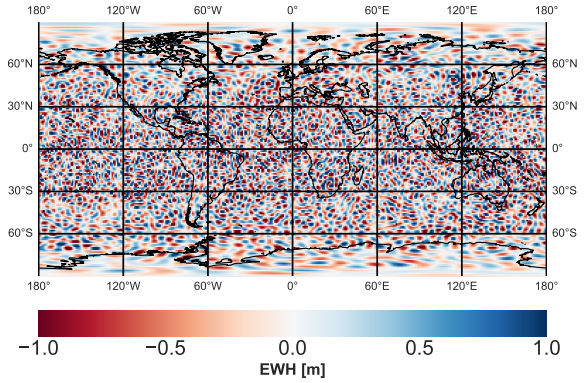
Figure A.17: Coefficient differences between recovered and reference gravity field: spatial representation in terms of EWH and pyramid representation (logarithm scale), instrument-only scenario: h=303 km, ll-SST: KBR noise and EA at a noise level of $1 \times 10^{-10}\,\mathrm{m/s^2}$, cross-track component V_{yy}: EG at a noise level of 1 mE



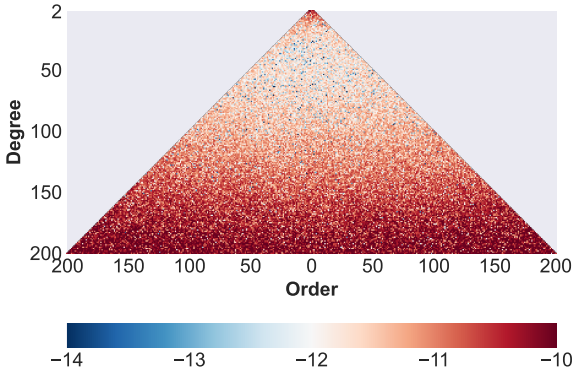
(a) ll-SST: EA at a noise level of $1 \times 10^{-10}\,\mathrm{m/s^2}$



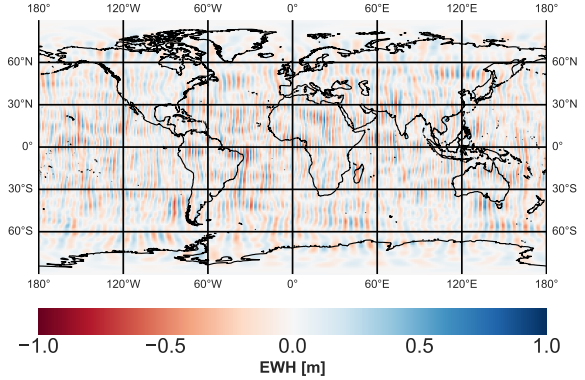
(b) ll-SST: EA at a noise level of $1 \times 10^{-10}\,\mathrm{m/s^2}$



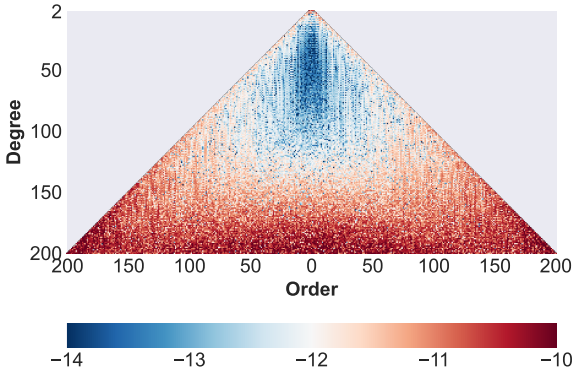
(c) Cross-track component V_{yy}: CAI gradiometer at a noise level of 1 mE



(d) Cross-track component V_{yy}: CAI gradiometer at a noise level of 1 mE

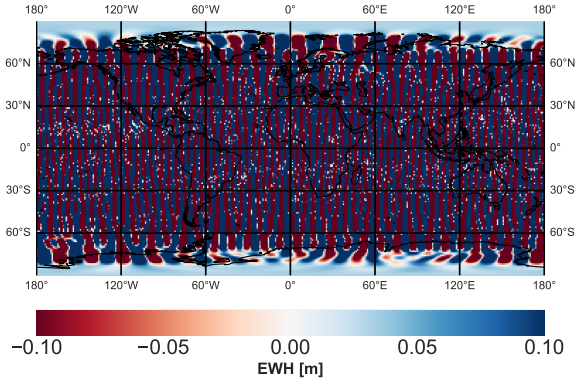


(e) Combination of ll-SST and cross-track gradiometry

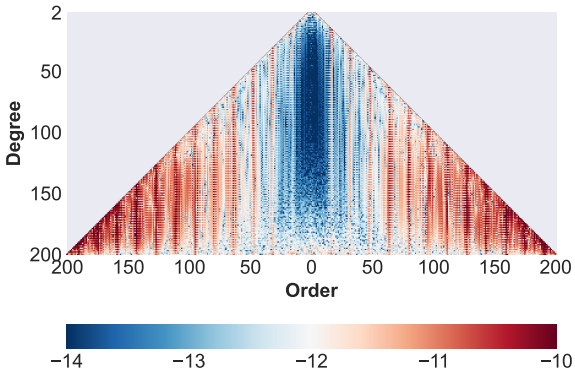


(f) Combination of ll-SST and cross-track gradiometry

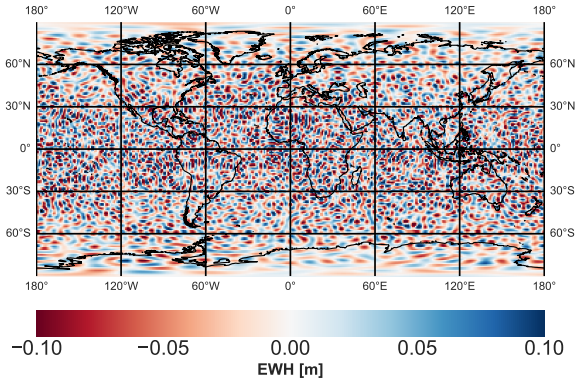
Figure A.18: Coefficient differences between recovered and reference gravity field: spatial representation in terms of EWH and pyramid representation (logarithm scale), instrument-only scenario: h=303 km, ll-SST: KBR noise and EA at a noise level of $1 \times 10^{-10}\,\mathrm{m/s^2}$, cross-track component V_{yy}: CAI gradiometer at a noise level of 1 mE



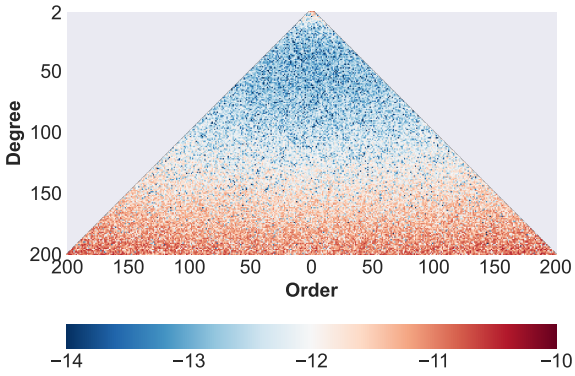
(a) ll-SST: EA at a noise level of $1 \times 10^{-10}\,\mathrm{m/s^2}$



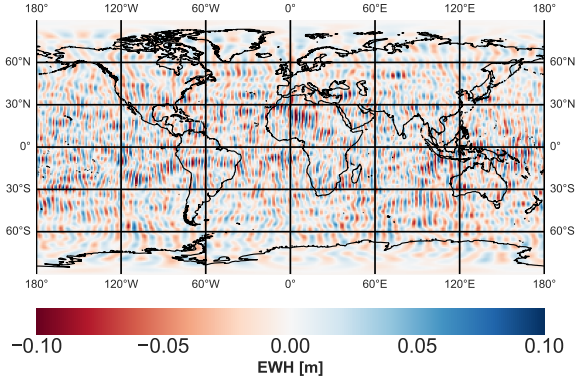
(b) ll-SST: EA at a noise level of $1 \times 10^{-10}\,\mathrm{m/s^2}$



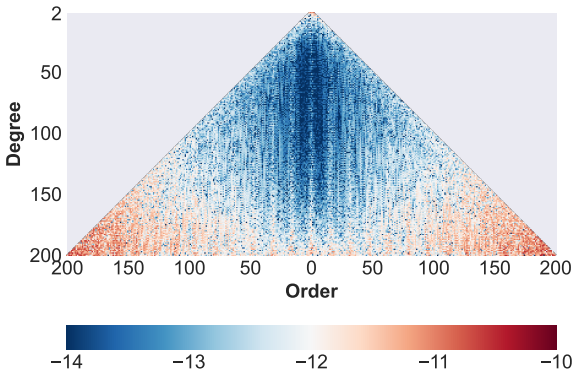
(c) Cross-track component V_{yy}: CAI gradiometer at a noise level of 0.1 mE



(d) Cross-track component V_{yy}: CAI gradiometer at a noise level of 0.1 mE

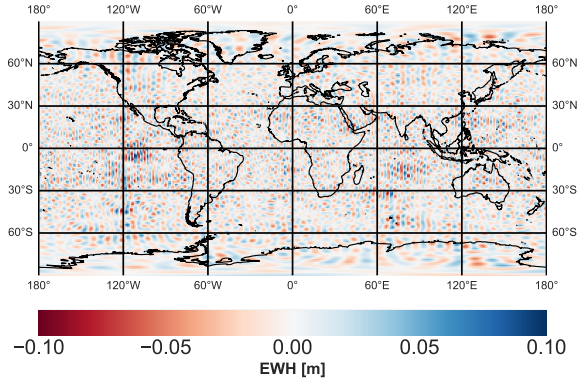


(e) Combination of ll-SST and cross-track gradiometry

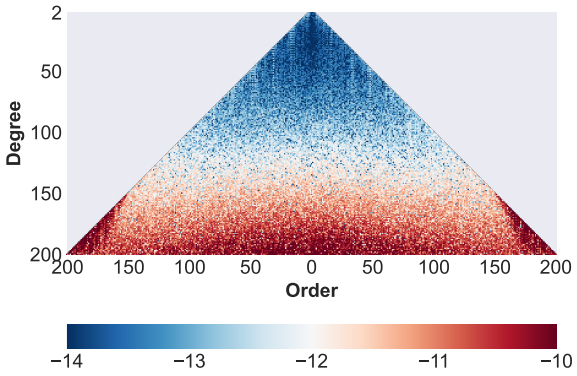


(f) Combination of ll-SST and cross-track gradiometry

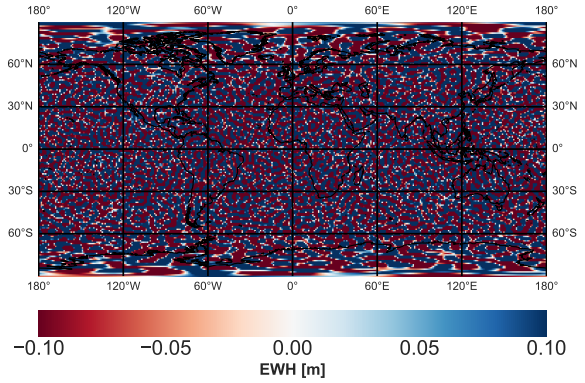
Figure A.19: Coefficient differences between recovered and reference gravity field: spatial representation in terms of EWH and pyramid representation (logarithm scale), instrument-only scenario: h=303 km, ll-SST: LRI noise and EA at a noise level of $1 \times 10^{-10}\,\mathrm{m/s^2}$, cross-track component V_{yy}: CAI gradiometer at a noise level of 0.1 mE



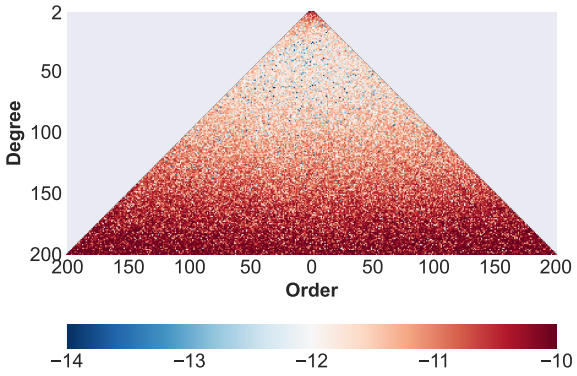
(a) ll-SST: EA at a noise level of $1 \times 10^{-12}\,\mathrm{m/s^2}$



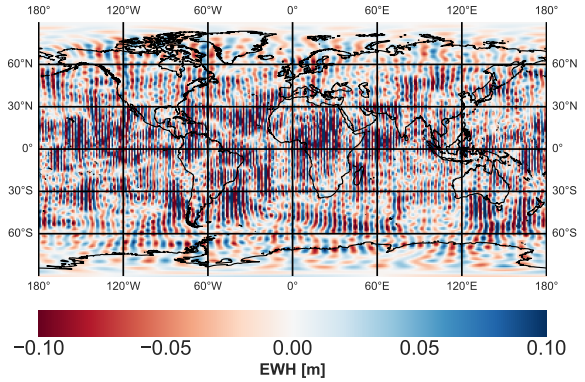
(b) ll-SST: EA at a noise level of $1 \times 10^{-12}\,\mathrm{m/s^2}$



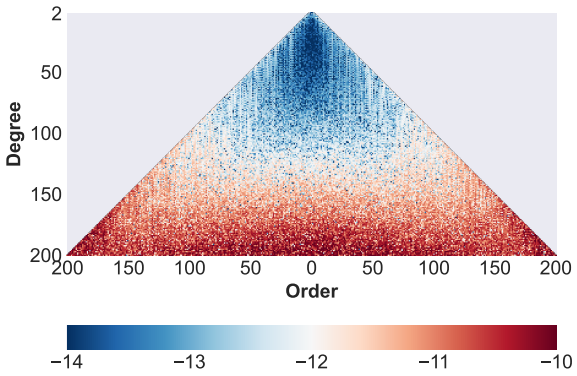
(c) Cross-track component V_{yy}: CAI gradiometer at a noise level of 1 mE



(d) Cross-track component V_{yy}: CAI gradiometer at a noise level of 1 mE

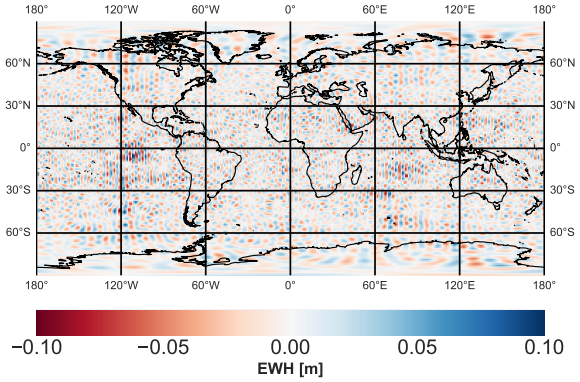


(e) Combination of ll-SST and cross-track gradiometry

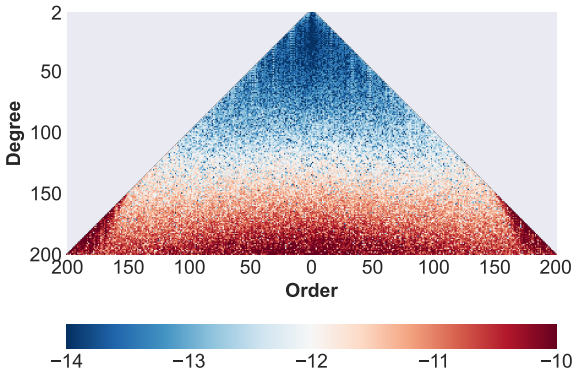


(f) Combination of ll-SST and cross-track gradiometry

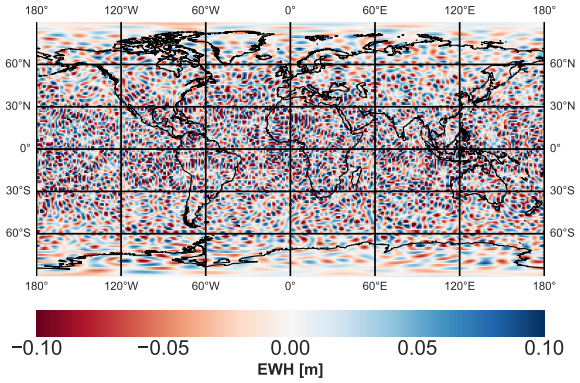
Figure A.20: Coefficient differences between recovered and reference gravity field: spatial representation in terms of EWH and pyramid representation (logarithm scale), instrument-only scenario: h=303 km, ll-SST: KBR noise and EA at a noise level of $1 \times 10^{-12}\,\mathrm{m/s^2}$, cross-track component V_{yy}: CAI gradiometer at a noise level of 1 mE



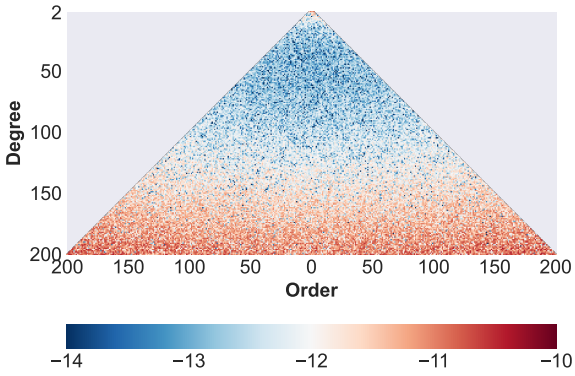
(a) ll-SST: EA at a noise level of $1 \times 10^{-12}\,\mathrm{m/s^2}$



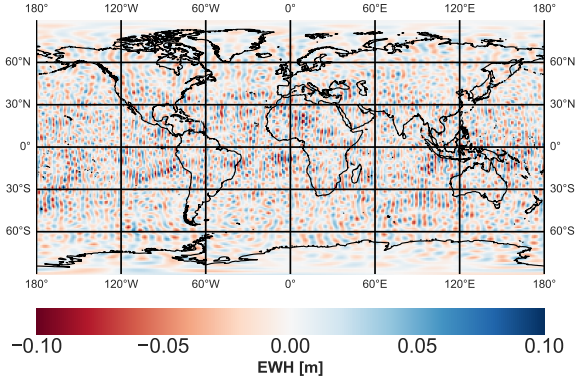
(b) ll-SST: EA at a noise level of $1 \times 10^{-12}\,\mathrm{m/s^2}$



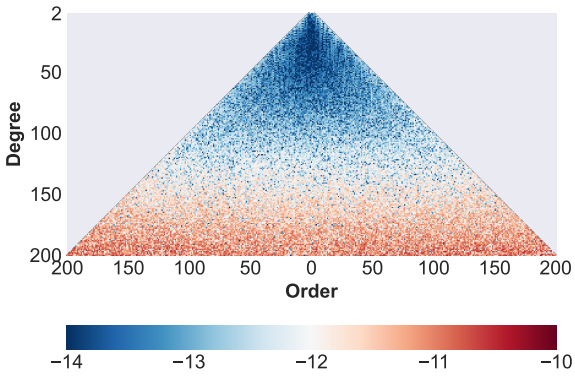
(c) Cross-track component V_{yy}: CAI gradiometer at a noise level of 0.1 mE



(d) Cross-track component V_{yy}: CAI gradiometer at a noise level of 0.1 mE

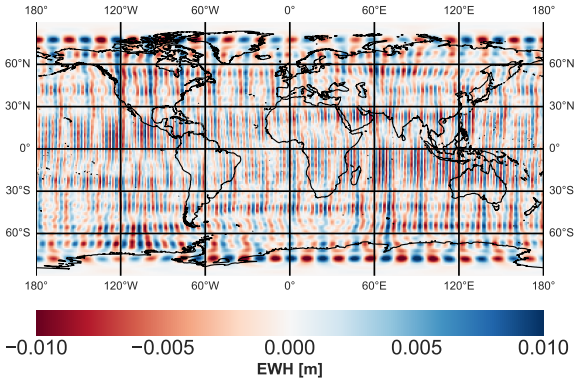


(e) Combination of ll-SST and cross-track gradiometry

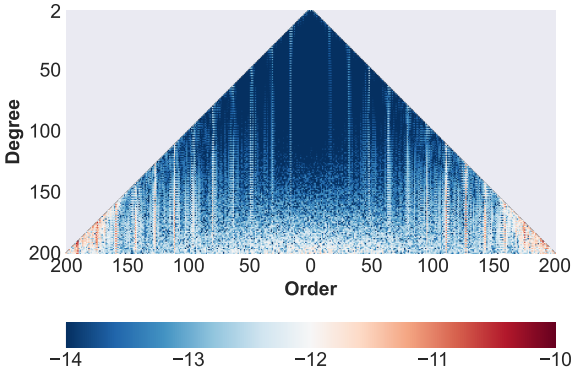


(f) Combination of ll-SST and cross-track gradiometry

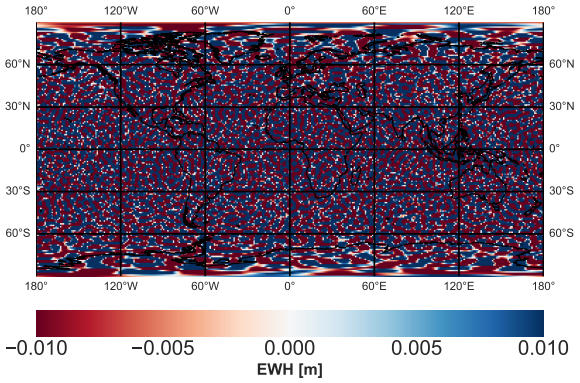
Figure A.21: Coefficient differences between recovered and reference gravity field: spatial representation in terms of EWH and pyramid representation (logarithm scale), instrument-only scenario: h=303 km, ll-SST: KBR noise and EA at a noise level of $1 \times 10^{-12}\,\mathrm{m/s^2}$, cross-track component V_{yy}: CAI gradiometer at a noise level of 0.1 mE



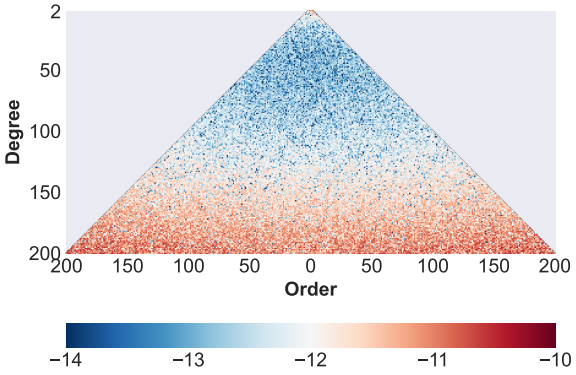
(a) ll-SST: EA at a noise level of $1 \times 10^{-12}\,\mathrm{m/s^2}$



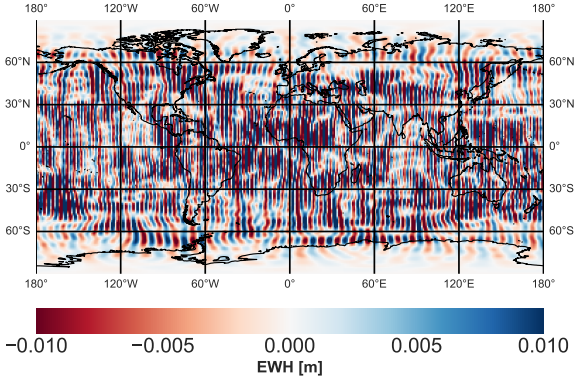
(b) ll-SST: EA at a noise level of $1 \times 10^{-12}\,\mathrm{m/s^2}$



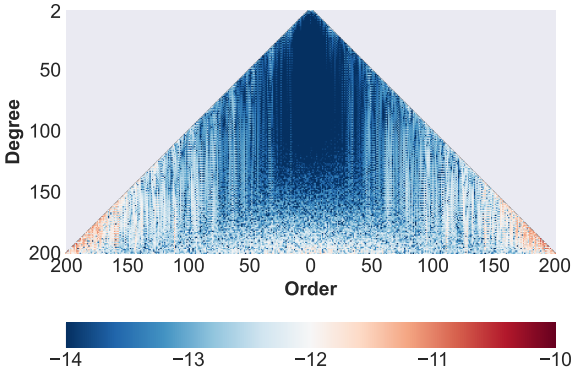
(c) Cross-track component V_{yy}: CAI gradiometer at a noise level of 0.1 mE



(d) Cross-track component V_{yy}: CAI gradiometer at a noise level of 0.1 mE

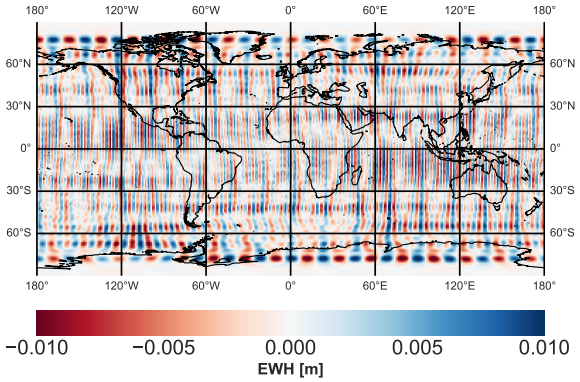


(e) Combination of ll-SST and cross-track gradiometry

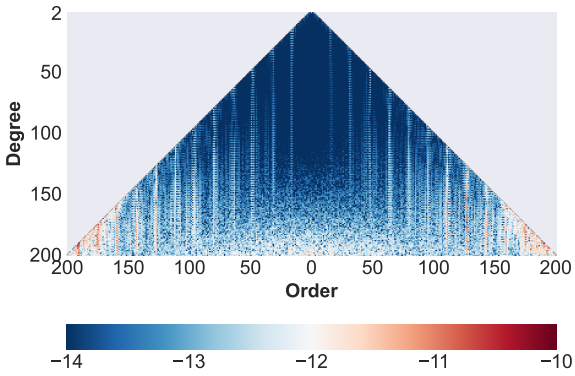


(f) Combination of ll-SST and cross-track gradiometry

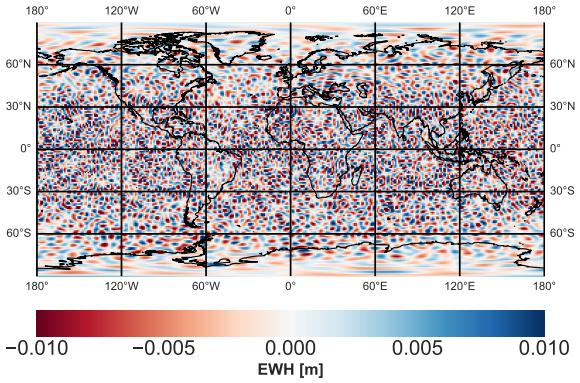
Figure A.22: Coefficient differences between recovered and reference gravity field: spatial representation in terms of EWH and pyramid representation (logarithm scale), instrument-only scenario: h=303 km, ll-SST: LRI noise and EA at a noise level of $1 \times 10^{-12}\,\mathrm{m/s^2}$, cross-track component V_{yy}: CAI gradiometer at a noise level of 0.1 mE



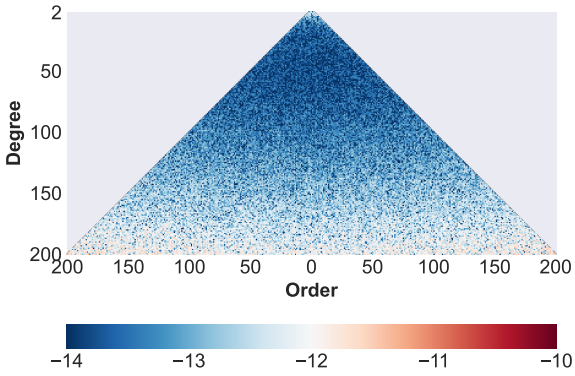
(a) ll-SST: EA at a noise level of $1 \times 10^{-12}\,\mathrm{m/s^2}$



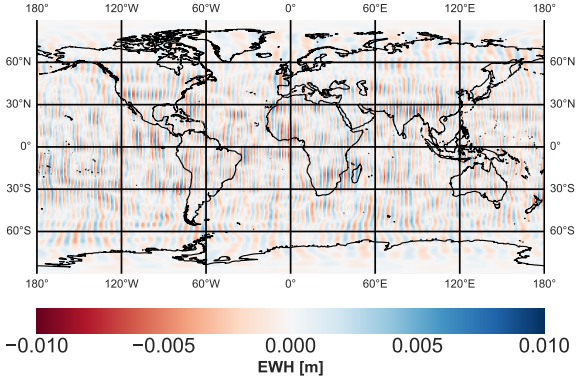
(b) ll-SST: EA at a noise level of $1 \times 10^{-12}\,\mathrm{m/s^2}$



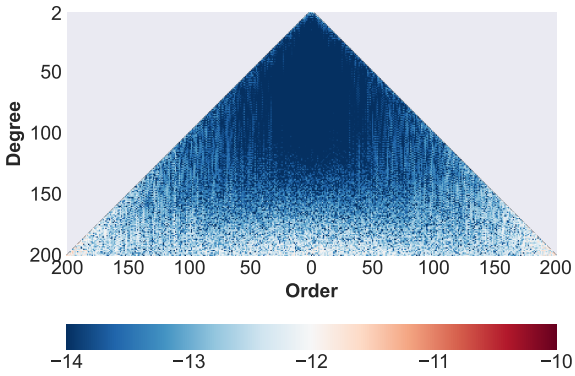
(c) Cross-track component V_{yy}: CAI gradiometer at a noise level of 0.01 mE



(d) Cross-track component V_{yy}: CAI gradiometer at a noise level of 0.01 mE

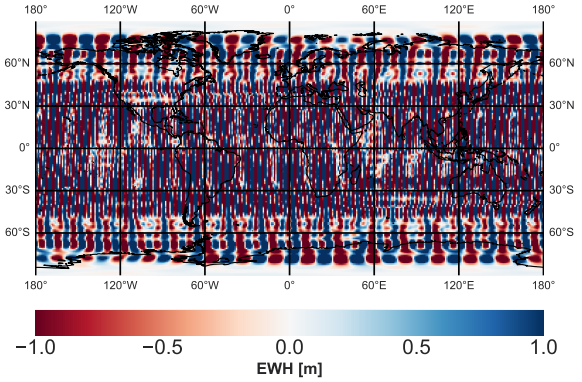


(e) Combination of ll-SST and cross-track gradiometry

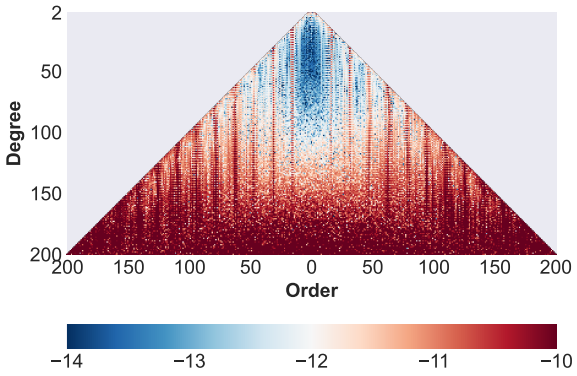


(f) Combination of ll-SST and cross-track gradiometry

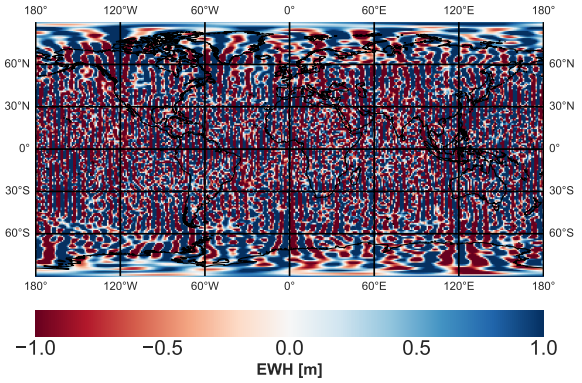
Figure A.23: Coefficient differences between recovered and reference gravity field: spatial representation in terms of EWH and pyramid representation (logarithm scale), instrument-only scenario: h=303 km, ll-SST: LRI noise and EA at a noise level of $1 \times 10^{-12}\,\mathrm{m/s^2}$, cross-track component V_{yy}: CAI gradiometer at a noise level of 0.01 mE



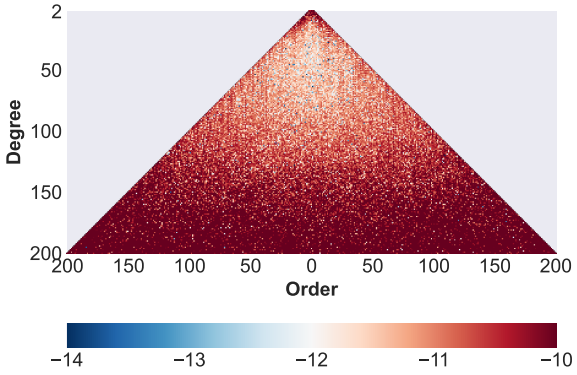
(a) ll-SST: EA at a noise level of $1 \times 10^{-10}\,\mathrm{m/s^2}$



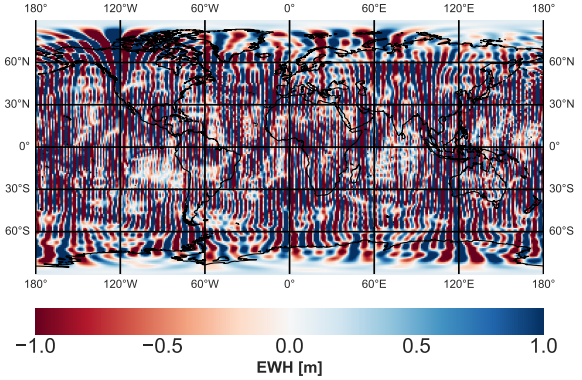
(b) ll-SST: EA at a noise level of $1 \times 10^{-10}\,\mathrm{m/s^2}$



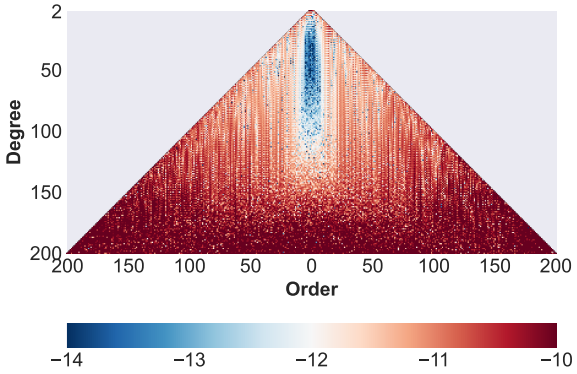
(c) Cross-track component V_{yy}: EG at a noise level of 1 mE



(d) Cross-track component V_{yy}: EG at a noise level of 1 mE

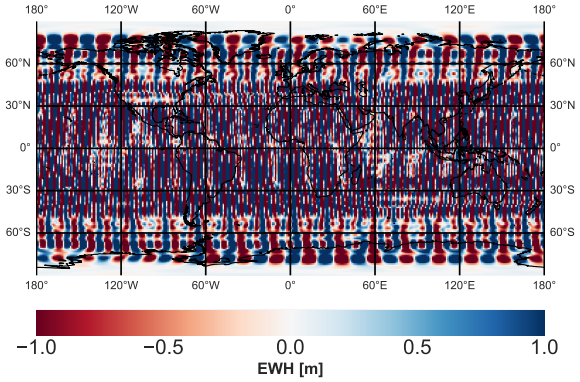


(e) Combination of ll-SST and cross-track gradiometry

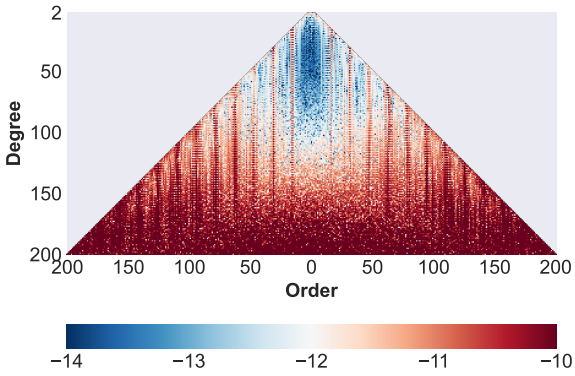


(f) Combination of ll-SST and cross-track gradiometry

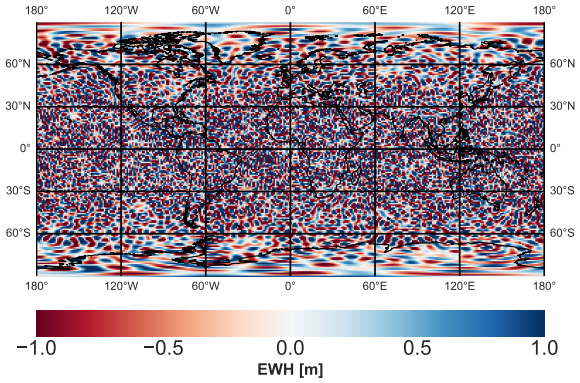
Figure A.24: Coefficient differences between recovered and reference gravity field: spatial representation in terms of EWH and pyramid representation (logarithm scale), instrument-only scenario: h=363 km, ll-SST: KBR noise and EA at a noise level of $1 \times 10^{-10}\,\mathrm{m/s^2}$, cross-track component V_{yy}: EG at a noise level of 1 mE



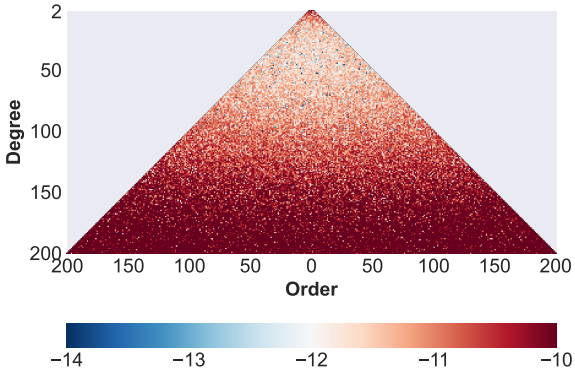
(a) ll-SST: EA at a noise level of $1 \times 10^{-10}\,\mathrm{m/s^2}$



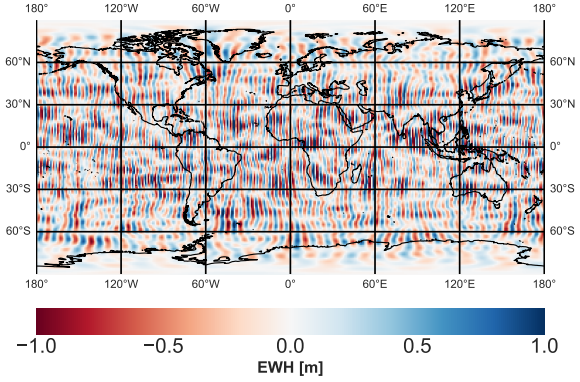
(b) ll-SST: EA at a noise level of $1 \times 10^{-10}\,\mathrm{m/s^2}$



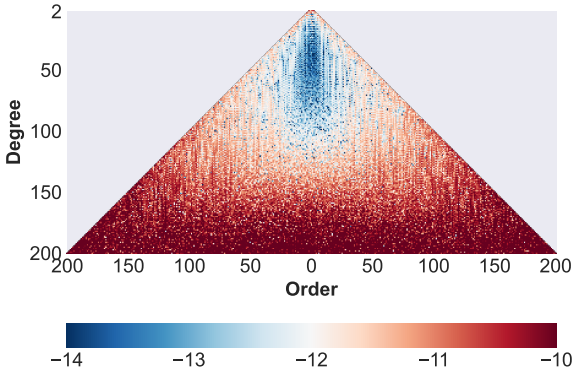
(c) Cross-track component V_{yy}: CAI gradiometer at a noise level of 1 mE



(d) Cross-track component V_{yy}: CAI gradiometer at a noise level of 1 mE

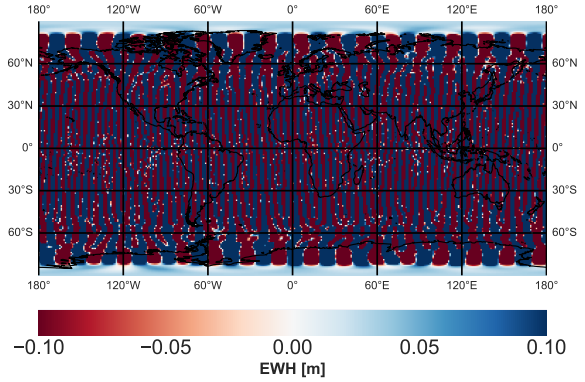


(e) Combination of ll-SST and cross-track gradiometry

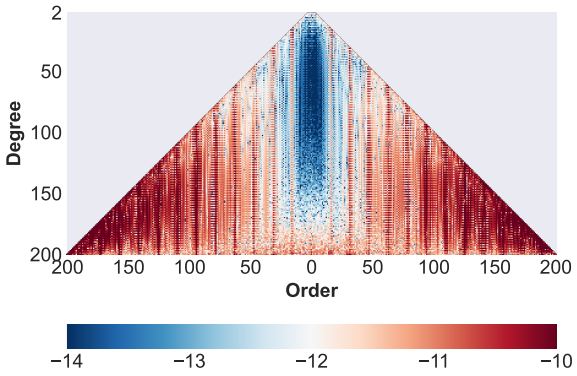


(f) Combination of ll-SST and cross-track gradiometry

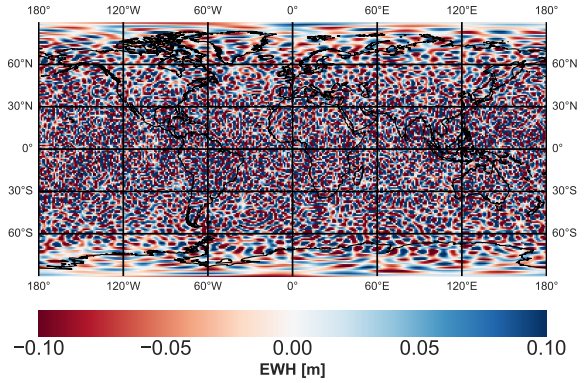
Figure A.25: Coefficient differences between recovered and reference gravity field: spatial representation in terms of EWH and pyramid representation (logarithm scale), instrument-only scenario: h=363 km, ll-SST: KBR noise and EA at a noise level of $1 \times 10^{-10}\,\mathrm{m/s^2}$, cross-track component V_{yy}: CAI gradiometer at a noise level of 1 mE



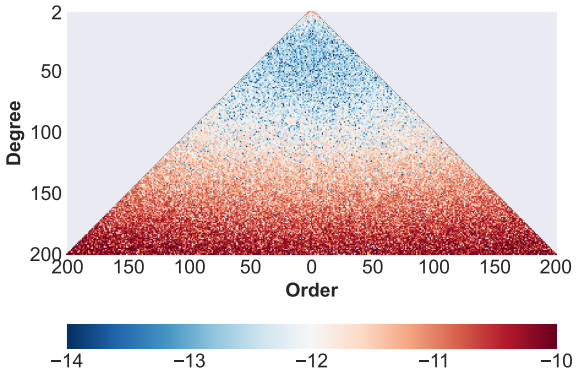
(a) ll-SST: EA at a noise level of $1 \times 10^{-10}\,\mathrm{m/s^2}$



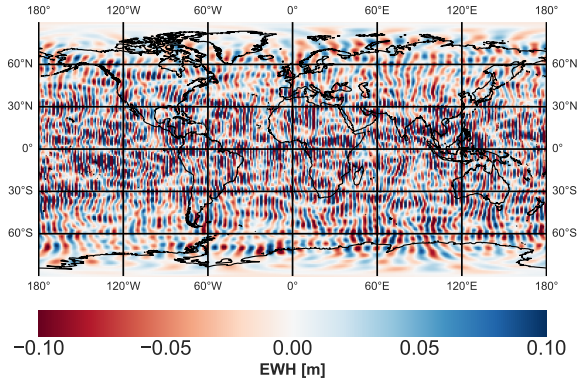
(b) ll-SST: EA at a noise level of $1 \times 10^{-10}\,\mathrm{m/s^2}$



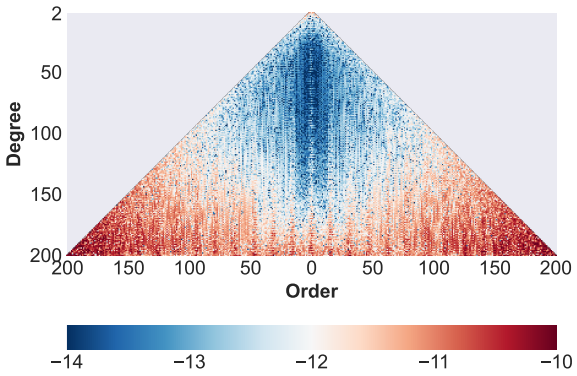
(c) Cross-track component V_{yy}: CAI gradiometer at a noise level of 0.1 mE



(d) Cross-track component V_{yy}: CAI gradiometer at a noise level of 0.1 mE

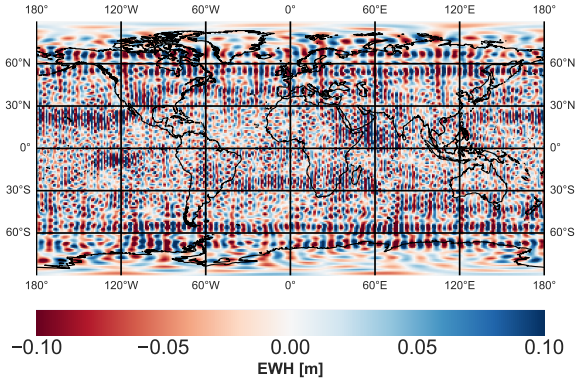


(e) Combination of ll-SST and cross-track gradiometry

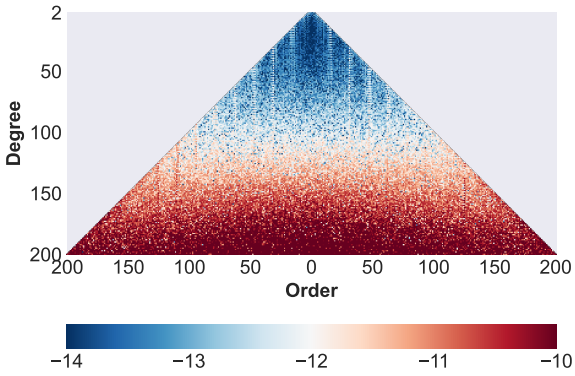


(f) Combination of ll-SST and cross-track gradiometry

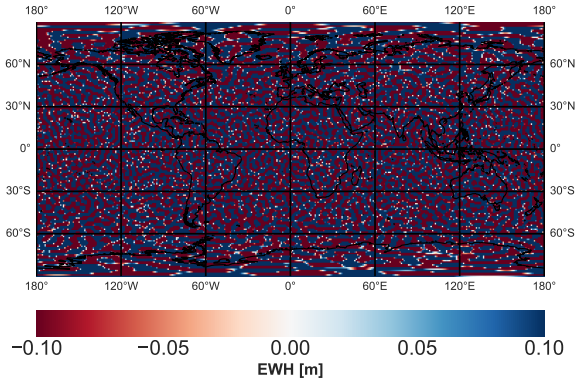
Figure A.26: Coefficient differences between recovered and reference gravity field: spatial representation in terms of EWH and pyramid representation (logarithm scale), instrument-only scenario: h=363 km, ll-SST: LRI noise and EA at a noise level of $1 \times 10^{-10}\,\mathrm{m/s^2}$, cross-track component V_{yy}: CAI gradiometer at a noise level of 0.1 mE



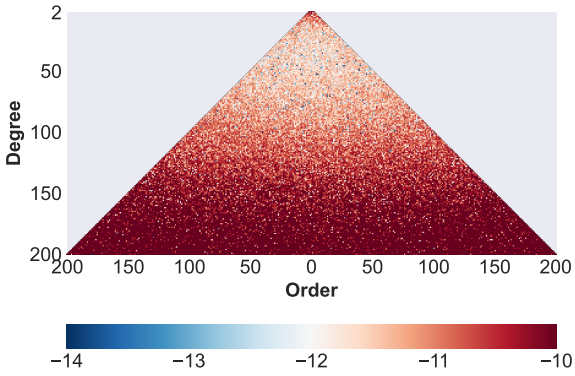
(a) ll-SST: EA at a noise level of $1 \times 10^{-12}\,\mathrm{m/s^2}$



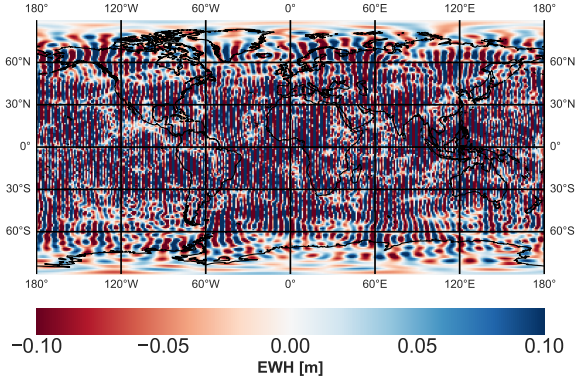
(b) ll-SST: EA at a noise level of $1 \times 10^{-12}\,\mathrm{m/s^2}$



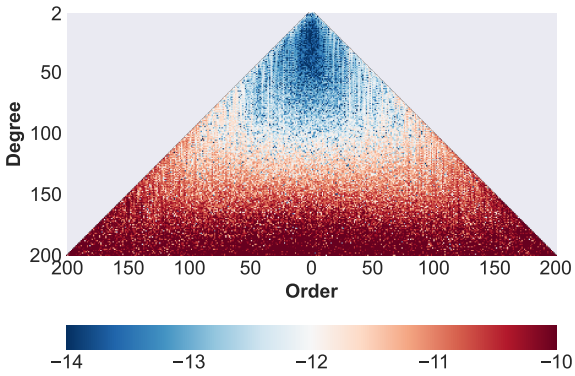
(c) Cross-track component V_{yy}: CAI gradiometer at a noise level of 1 mE



(d) Cross-track component V_{yy}: CAI gradiometer at a noise level of 1 mE

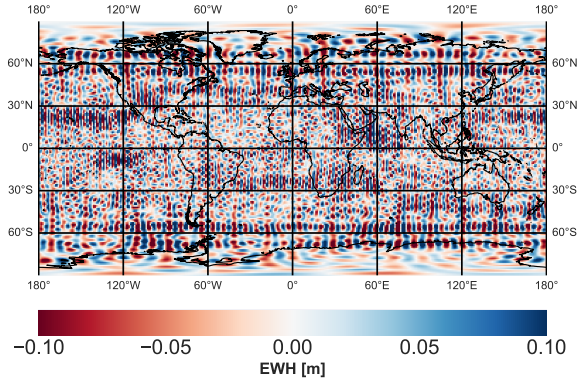


(e) Combination of ll-SST and cross-track gradiometry

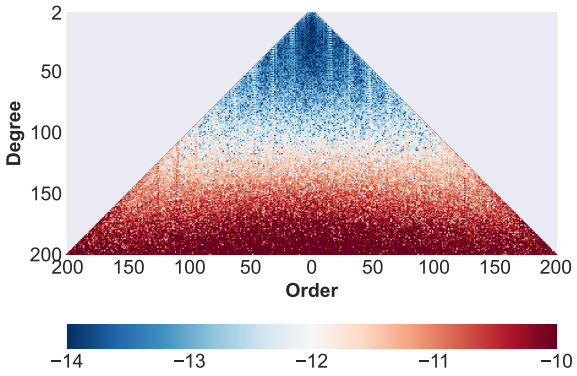


(f) Combination of ll-SST and cross-track gradiometry

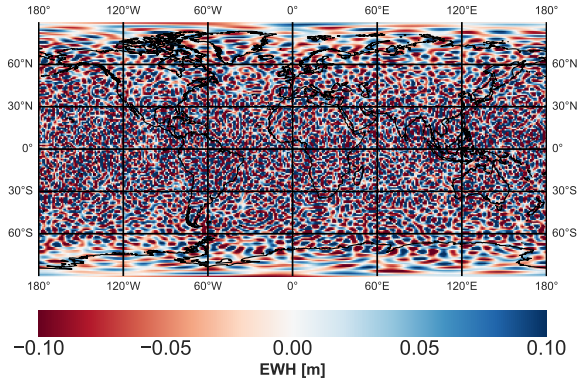
Figure A.27: Coefficient differences between recovered and reference gravity field: spatial representation in terms of EWH and pyramid representation (logarithm scale), instrument-only scenario: h=363 km, ll-SST: KBR noise and EA at a noise level of $1 \times 10^{-12}\,\mathrm{m/s^2}$, cross-track component V_{yy}: CAI gradiometer at a noise level of 1 mE



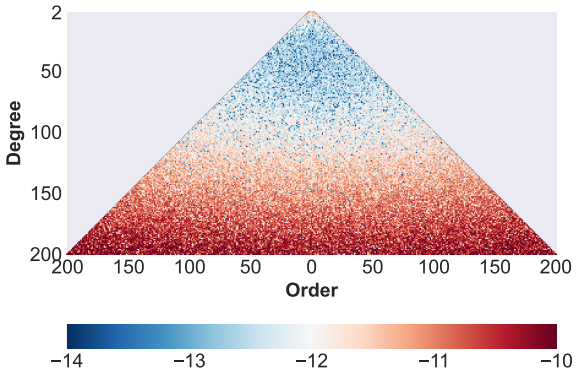
(a) ll-SST: EA at a noise level of $1 \times 10^{-12}\,\mathrm{m/s^2}$



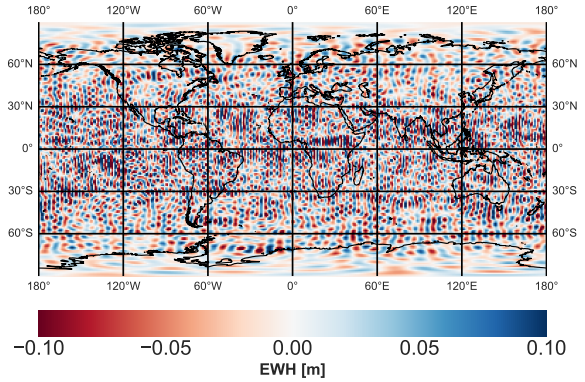
(b) ll-SST: EA at a noise level of $1 \times 10^{-12}\,\mathrm{m/s^2}$



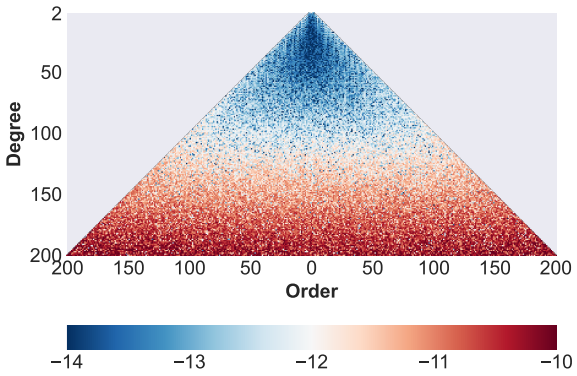
(c) Cross-track component V_{yy}: CAI gradiometer at a noise level of 0.1 mE



(d) Cross-track component V_{yy}: CAI gradiometer at a noise level of 0.1 mE

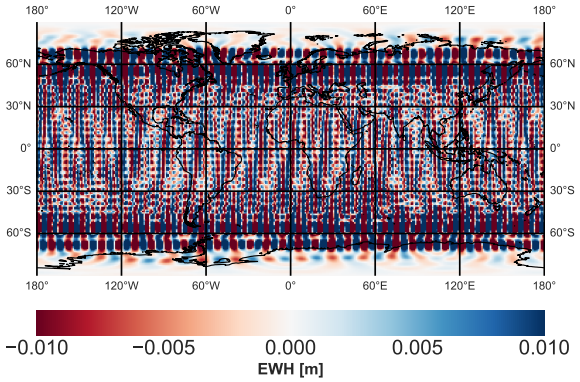


(e) Combination of ll-SST and cross-track gradiometry

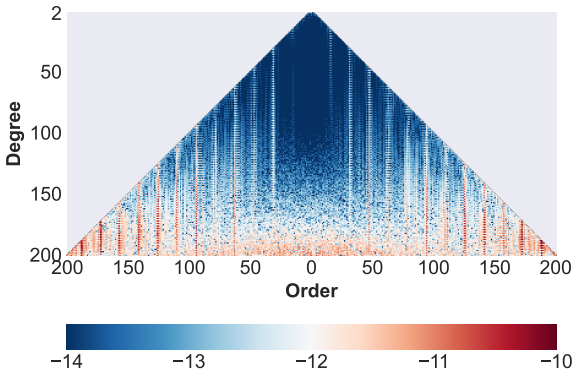


(f) Combination of ll-SST and cross-track gradiometry

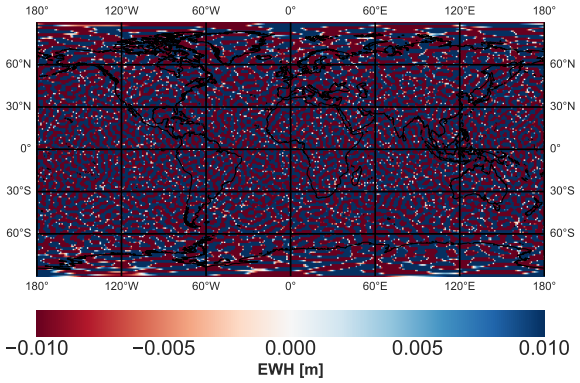
Figure A.28: Coefficient differences between recovered and reference gravity field: spatial representation in terms of EWH and pyramid representation (logarithm scale), instrument-only scenario: h=363 km, ll-SST: KBR noise and EA at a noise level of $1 \times 10^{-12}\,\mathrm{m/s^2}$, cross-track component V_{yy}: CAI gradiometer at a noise level of 0.1 mE



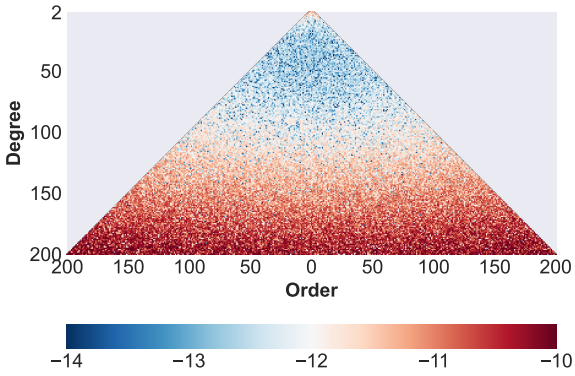
(a) ll-SST: EA at a noise level of $1 \times 10^{-12}\,\mathrm{m/s^2}$



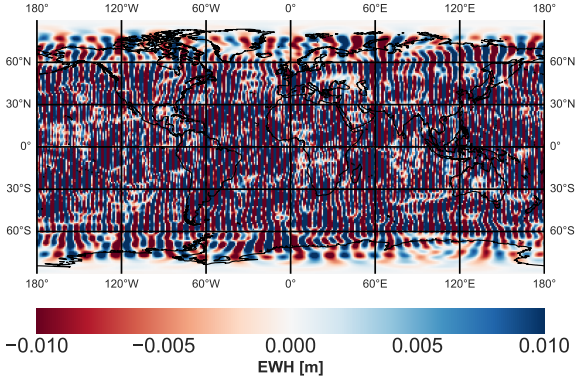
(b) ll-SST: EA at a noise level of $1 \times 10^{-12}\,\mathrm{m/s^2}$



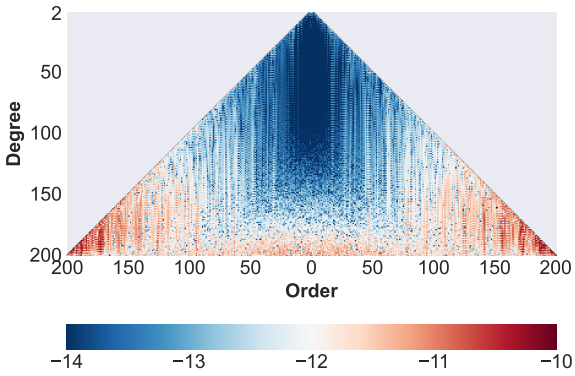
(c) Cross-track component V_{yy}: CAI gradiometer at a noise level of 0.1 mE



(d) Cross-track component V_{yy}: CAI gradiometer at a noise level of 0.1 mE

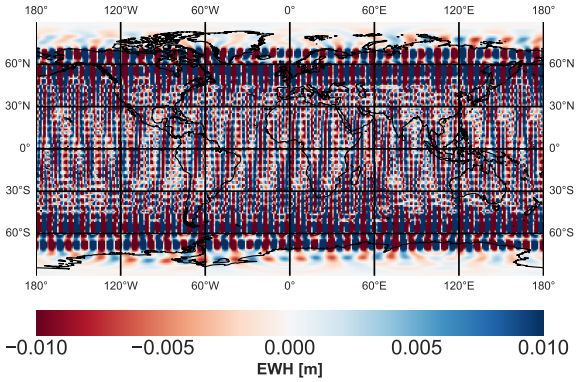


(e) Combination of ll-SST and cross-track gradiometry

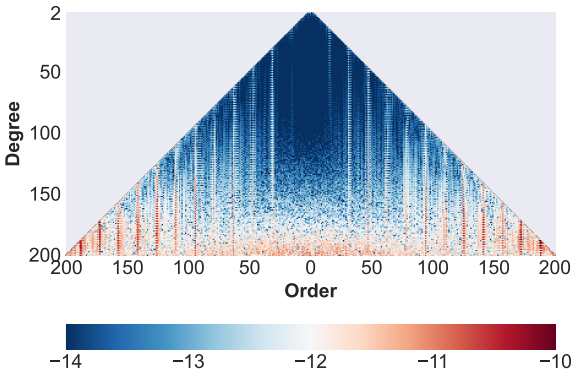


(f) Combination of ll-SST and cross-track gradiometry

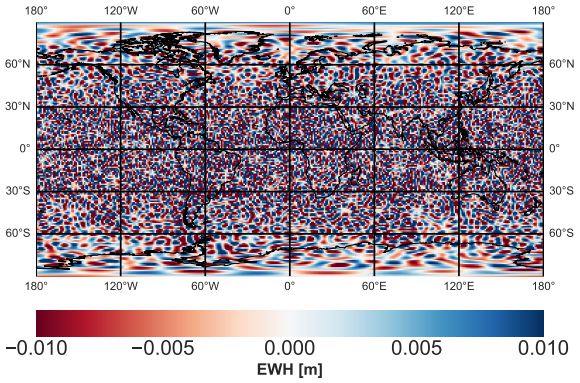
Figure A.29: Coefficient differences between recovered and reference gravity field: spatial representation in terms of EWH and pyramid representation (logarithm scale), instrument-only scenario: h=363 km, ll-SST: LRI noise and EA at a noise level of $1 \times 10^{-12}\,\mathrm{m/s^2}$, cross-track component V_{yy}: CAI gradiometer at a noise level of 0.1 mE



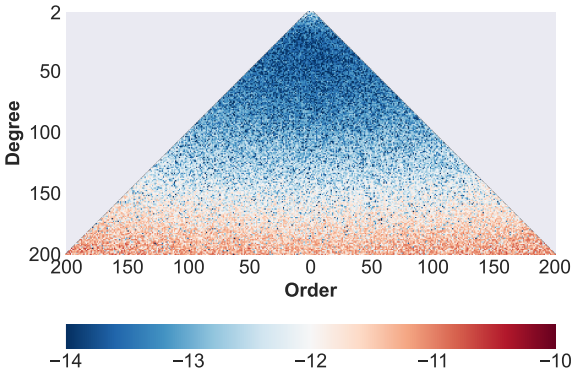
(a) ll-SST: EA at a noise level of $1 \times 10^{-12}\,\mathrm{m/s^2}$



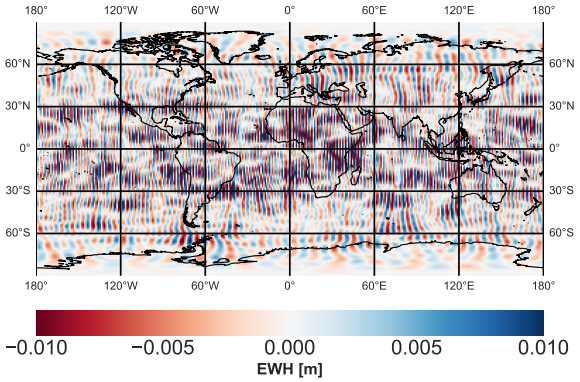
(b) ll-SST: EA at a noise level of $1 \times 10^{-12}\,\mathrm{m/s^2}$



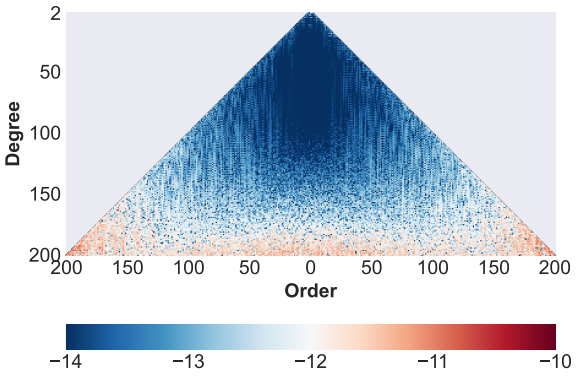
(c) Cross-track component V_{yy}: CAI gradiometer at a noise level of 0.01 mE



(d) Cross-track component V_{yy}: CAI gradiometer at a noise level of 0.01 mE



(e) Combination of ll-SST and cross-track gradiometry



(f) Combination of ll-SST and cross-track gradiometry

Figure A.30: Coefficient differences between recovered and reference gravity field: spatial representation in terms of EWH and pyramid representation (logarithm scale), instrument-only scenario: h=363 km, ll-SST: LRI noise and EA at a noise level of $1 \times 10^{-12}\,\mathrm{m/s^2}$, cross-track component V_{yy}: CAI gradiometer at a noise level of 0.01 mE

Bibliography

Abend, S., Allard, B., Arnold, A. S., Ban, T., Barry, L., Battelier, B., Bawamia, A., Beaufils, Q., Bernon, S., Bertoldi, A., Bonnin, A., Bouyer, P., Bresson, A., Burrow, O. S., Canuel, B., Desruelle, B., Drougakis, G., Forsberg, R., Gaaloul, N., Gauguet, A., Gersemann, M., Griffin, P. F., Heine, H., Henderson, V. A., Herr, W., Kanthak, S., Krutzik, M., Lachmann, M. D., Lammegger, R., Magnes, W., Mileti, G., Mitchell, M. W., Mottini, S., Papazoglou, D., Pereira dos Santos, F., Peters, A., Rasel, E., Riis, E., Schubert, C., Seidel, S. T., Tino, G. M., Van Den Bossche, M., von Klitzing, W., Wicht, A., Witkowski, M., Zahzam, N., and Zawada, M. (2023). "Technology roadmap for cold-atoms based quantum inertial sensor in space". In: *AVS Quantum Science* 5.1. 019201. DOI: 10.1116/5.0098119.

Abich, K., Abramovici, A., Amparan, B., Baatzsch, A., Okihiro, B. B., Barr, D. C., Bize, M. P., Bogan, C., Braxmaier, C., Burke, M. J., Clark, K. C., Dahl, C., Dahl, K., Danzmann, K., Davis, M. A., de Vine, G., Dickson, J. A., Dubovitsky, S., Eckardt, A., Ester, T., Barranco, G. F., Flatscher, R., Flechtner, F., Folkner, W. M., Francis, S., Gilbert, M. S., Gilles, F., Gohlke, M., Grossard, N., Guenther, B., Hager, P., Hauden, J., Heine, F., Heinzel, G., Herding, M., Hinz, M., Howell, J., Katsumura, M., Kaufer, M., Klipstein, W., Koch, A., Kruger, M., Larsen, K., Lebeda, A., Lebeda, A., Leikert, T., Liebe, C. C., Liu, J., Lobmeyer, L., Mahrdt, C., Mangoldt, T., McKenzie, K., Misfeldt, M., Morton, P. R., Müller, V., Murray, A. T., Nguyen, D. J., Nicklaus, K., Pierce, R., Ravich, J. A., Reavis, G., Reiche, J., Sanjuan, J., Schütze, D., Seiter, C., Shaddock, D., Sheard, B., Sileo, M., Spero, R., Spiers, G., Stede, G., Stephens, M., Sutton, A., Trinh, J., Voss, K., Wang, D., Wang, R. T., Ware, B., Wegener, H., Windisch, S., Woodruff, C., Zender, B., and Zimmermann, M. (2019). "In-orbit performance of the GRACE Follow-On Laser Ranging Interferometer". In: *Physical Review Letters* 123.3, 031101. ISSN: 0031-9007, 1079-7114. DOI: 10.1103/PhysRevLett.123.031101.

Abrykosov, P., Pail, R., Gruber, T., Zahzam, N., Bresson, A., Hardy, E., Christophe, B., Bidel, Y., Carraz, O., and Siemes, C. (2019). "Impact of a novel hybrid accelerometer on satellite gravimetry performance". In: *Advances in Space Research* 63.10, pp. 3235–3248. ISSN: 0273-1177. DOI: 10.1016/j.asr.2019.01.034.

Allasio, A., Anselmi, A., Catastini, G., Cesare, S., Dumontel, M., Saponara, M., Sechi, G., Tramutola, A., Vinai, B., André, G., Fehringer, M., and Muzi, D. (2010). "GOCE mission: design phases and in-flight experiences". In: *Advances in the Astronautical Sciences* 137.53.

Alvarez, A. D., Bevilacqua, R., Hollis, H., Mueller, G., Knudston, A., Patel, U., Sanjuan, J., Wass, P., and Conklin, J. W. (2022). "A Simplified Gravitational Reference Sensor for Satellite Geodesy". In: *Journal of Geodesy* 96.70. DOI: 10.1007/s00190-022-01659-0.

Bandikova, T. and Flury, J. (2014). "Improvement of the GRACE star camera data based on the revision of the combination method". In: *Advances in Space Research* 54.9, pp. 1818–1827. ISSN: 0273-1177. DOI: 10.1016/j.asr.2014.07.004.

Bender, P., Wiese, D., and Nerem, R. (2008). "A possible dual-GRACE mission with 90 degree and 63 degree inclination orbits". In: *Proceedings of the third international symposium on formation flying, missions and technologies*. ESA/ESTEC Noordwijk, pp. 1–6.

Brockmann, J., Schubert, T., and Schuh, W.-D. (2021). "An Improved Model of the Earth's Static Gravity Field Solely Derived from Reprocessed GOCE Data". In: *Surveys in Geophysics* 42, pp. 277–316. DOI: 10.1007/s10712-020-09626-0.

Canuto, E. and Andreis, D. (2003). "Robust Digital Control of Drag-Free Satellites". In: *IFAC Proceedings Volumes* 36.11, pp. 353–358. ISSN: 14746670. DOI: 10.1016/S1474-6670(17)35689-6.

Canuto, E., Molano, A., and Massotti, L. (2010). "Drag-Free Control of the GOCE Satellite: Noise and Observer Design". In: *IEEE Transactions on Control Systems Technology* 18.2, pp. 501–509. ISSN: 1063-6536. DOI: 10.1109/TCST.2009.2020169.

Canuto, E., Novara, C., Carlucci, D., Montenegro, C. P., and Massotti, L. (2018). *Spacecraft Dynamics and Control: The Embedded Model Control Approach*. Butterworth-Heinemann. ISBN: 978-0-08-100700-6.

Carraz, O., Siemes, C., Massotti, L., Haagmans, R., and Silvestrin, P. (2014). "A spaceborne gravity gradiometer concept based on cold atom interferometers for measuring Earth's gravity field". In: *Microgravity Science and Technology* 26.3, pp. 139–145. DOI: 10.1007/s12217-014-9385-x.

Carrère, L., Lyard, F., Cancet, M., Guillot, A., Picot, N., et al. (2016). "FES 2014, a new tidal model — Validation results and perspectives for improvements". In: *Proceedings of the ESA living planet symposium*, pp. 9–13.

Case, K., Kruizinga, G., and Wu, S. (2010). *GRACE level 1B Data Product User Handbook*. Tech. rep. JPL D-22027. Jet Propulsion Laboratory, California Institute of Technology.

Christophe, B., Boulanger, D., Foulon, B., Huynh, P. .-., Lebat, V., Liorzou, F., and Perrot, E. (2015). "A new generation of ultra-sensitive electrostatic accelerometers for GRACE Follow-on and towards the next generation gravity missions". In: *Acta Astronautica* 117, pp. 1–7. DOI: 10.1016/j.actaastro.2015.06.021.

Christophe, B., Foulon, B., Liorzou, F., Lebat, V., Boulanger, D., Huynh, P.-A., Zahzam, N., Bidel, Y., and Bresson, A. (2018). "Status of Development of the Future Accelerometers for Next Generation Gravity Missions". In: *International Symposium on Advancing Geodesy in a Changing World*. Ed. by J. T. Freymueller and L. Sánchez. Cham: Springer International Publishing, pp. 85–89. ISBN: 978-3-030-12914-9. DOI: 10.1007/1345_2018_42.

Christophe, B., Marque, J.-P., and Foulon, B. (2010). "In-orbit data verification of the accelerometers of the ESA GOCE mission". In: *SF2A-2010: Proceedings of the Annual meeting of the French Society of Astronomy and Astrophysics*. Ed. by S. Boissier, M. Heydari-Malayeri, R. Samadi, and D. Valls-Gabaud. Marseille, France, pp. 113–116.

Colombo, O. L. (1984). *The global mapping of gravity with two satellites*. Delft: Netherlands Geodetic Commission. ISBN: 978 90 6132 230 6.

Dahle, C., Flechtner, F., Gruber, C., König, D., König, R., Michalak, G., and Neumayer, K.-H. (2014). "GFZ RL05: An Improved Time-Series of Monthly GRACE Gravity Field

Solutions". In: *Observation of the System Earth from Space - CHAMP, GRACE, GOCE and future missions: GEOTECHNOLOGIEN Science Report No. 20*. Ed. by F. Flechtner, N. Sneeuw, and W.-D. Schuh. Berlin, Heidelberg: Springer Berlin Heidelberg, pp. 29–39. ISBN: 978-3-642-32135-1. DOI: 10.1007/978-3-642-32135-1_4.

Daras, I. and Pail, R. (2017). "Treatment of temporal aliasing effects in the context of next generation satellite gravimetry missions". In: *Journal of Geophysical Research: Solid Earth* 122.9, pp. 7343–7362. DOI: 10.1002/2017JB014250.

Darbeheshti, N., Wegener, H., Müller, V., Naeimi, M., Heinzel, G., and Hewitson, M. (2017). "Instrument data simulations for GRACE Follow-on: observation and noise models". In: *Earth System Science Data* 9, pp. 833–848. DOI: 10.5194/essd-9-833-2017.

Dobslaw, H., Bergmann-Wolf, I., Dill, R., Poropat, L., Thomas, M., Dahle, C., Esselborn, S., König, R., and Flechtner, F. (July 2017). "A new high-resolution model of non-tidal atmosphere and ocean mass variability for de-aliasing of satellite gravity observations: AOD1B RL06". In: *Geophysical Journal International* 211.1, pp. 263–269. ISSN: 0956-540X. DOI: 10.1093/gji/ggx302.

Dobslaw, H., Bergmann-Wolf, I., Forootan, E., Dahle, C., Mayer-Gürr, T., Kusche, J., and Flechtner, F. (2016). "Modeling of present-day atmosphere and ocean non-tidal de-aliasing errors for future gravity mission simulations". In: *Journal of Geodesy* 90, pp. 423–436. DOI: 10.1007/s00190-015-0884-3.

Douch, K., Knabe, A., Wu, H., Müller, J., and Heinzel, G. (2018a). "What is required to recover the time-variable gravitational field using satellite gradiometry?" Gravity, Geoid and Height Systems (GGHS) 2, Copenhagen, Denmark, Sep 17-21, 2018.

Douch, K., Wu, H., Schubert, C., Müller, J., and dos Santos, F. P. (2018b). "Simulation-based evaluation of a cold atom interferometry gradiometer concept for gravity field recovery". In: *Advances in Space Research* 61.5, pp. 1307–1323. DOI: 10.1016/j.asr.2017.12.005.

Drinkwater, M. R., Haagmans, R., Muzi, D., Popescu, A., Floberghagen, R., Kern, M., and Fehringer, M. (2007). "The GOCE gravity mission: ESA's first core Earth explorer". In: *Proceedings of the 3rd international GOCE User Workshop,6-8 November, 2006, Frascati, Italy, ESA SP-627*, pp. 1–8. ISBN: 92-9092-938-3.

Eicker, A., Jensen, L., Wöhnke, V., Dobslaw, H., Kvas, A., Mayer-Gürr, T., and Dill, R. (2020). "Daily GRACE satellite data evaluate short-term hydro-meteorological fluxes from global atmospheric reanalyses". In: *Scientific Reports* 10.1, pp. 1–10. DOI: 10.1038/s41598-020-61166-0.

Elsaka, B. (2010). "Simulated Satellite Formation Flights for Detecting the Temporal Variations of the Earth's Gravity Field". PhD thesis.

Elsaka, B., Raimondo, J.-C., Brieden, P., Reubelt, T., Kusche, J., Flechtner, F., Pour, S. I., Sneeuw, N., and Müller, J. (2014). "Comparing seven candidate mission configurations for temporal gravity field retrieval through full-scale numerical simulation". In: *Journal of Geodesy* 88.1, pp. 31–43. DOI: 10.1007/s00190-013-0665-9.

Flechtner, F., Dahle, C., Hauk, M., Wilms, J., Murböck, M., Nyenhuis, M., and Schaadt, P. (2022). *GRACE-I: A joint US-German mission for continued mass transport monitoring and enabling global biodiversity monitoring,* GRACE/GRACE-FO Science Team Meeting 2022, Potsdam, Germany, 18–20 Oct 2022, GSTM2022-13. DOI: 10.5194/gstm2022-13.

Förste, C., Bruinsma, S., Abrykosov, O., Lemoine, J.-M., Marty, J. C., Flechtner, F., Balmino G.and Barthelmes, F., and Biancale, R. (2014). "EIGEN-6C4 The latest combined global

gravity field model including GOCE data up to degree and order 2190 of GFZ Potsdam and GRGS Toulouse". In: *GFZ Data Services* 10. DOI: 10.5880/icgem.2015.1.

Freier, C., Hauth, M., Schkolnik, V., Leykauf, B., Schilling, M., Wziontek, H., Scherneck, H.-G., Müller, J., and Peters, A. (2016). "Mobile quantum gravity sensor with unprecedented stability". In: *Journal of Physics: Conference Series* 723, p. 012050. DOI: 10.1088/1742-6596/723/1/012050.

Frommknecht, B., Lamarre, D., Bigazzi, A., Meloni, M., and Floberghagen, R. (2011). "GOCE Level 1b Data Processing". In: *Journal of Geodesy* 85.11, pp. 759–775. DOI: 10.1007/s00190-011-0497-4.

Frommknecht, B. (2007). "Integrated sensor analysis of the GRACE mission". PhD thesis. Technische Universität München.

Frommknecht, B., Fackler, U., and Flury, J. (2006). "Integrated sensor analysis GRACE". In: *Observation of the Earth system from space*. Springer, pp. 99–113. DOI: 10.1007/3-540-29522-4_8.

Frye, K., Abend, S., Bartosch, W., Bawamia, A., Becker, D., Blume, H., Braxmaier, C., Chiow, S.-W., Efremov, M. A., Ertmer, W., Fierlinger, P., Franz, T., Gaaloul, N., Grosse, J., Grzeschik, C., Hellmig, O., Henderson, V. A., Herr, W., Israelsson, U., Kohel, J., Krutzik, M., Kürbis, C., Lämmerzahl, C., List, M., Lüdtke, D., Lundblad, N., Marburger, J. P., Meister, M., Mihm, M., Müller, H., Müntinga, H., Nepal, A. M., Oberschulte, T., Papakonstantinou, A., Perovsek, J., Peters, A., Prat, A., Rasel, E. M., Roura, A., Sbroscia, M., Schleich, W. P., Schubert, C., Seidel, S. T., Sommer, J., Spindeldreier, C., Stamper-Kurn, D., Stuhl, B. K., Warner, M., Wendrich, T., Wenzlawski, A., Wicht, A., Windpassinger, P., Yu, N., and Wörner, L. (2021). "The Bose-Einstein condensate and cold atom laboratory". In: *EPJ Quantum Technology* 8.1, p. 1. DOI: 10.1140/epjqt/s40507-020-00090-8.

Gillot, P., Cheng, B., Imanaliev, A., Merlet, S., and Pereira Dos Santos, F. (2016). "The LNE-SYRTE cold atom gravimeter". In: *2016 European Frequency and Time Forum (EFTF)*.

Gruber, T., Murböck, M., Baldesarra, M., Brieden, P., Danzmann, K., Daras, I., Doll, B., Feili, D., Flechtner, F., Flury, J., Heinzel, G., Iran Pour, S., Kusche, J., Langemann, M., Löcher, A., Müller, J., Müller, V., Naeimi, M., Pail, R., Raimondo, J., Reiche, J., Reubelt, T., Sheard, B., Sneeuw, N., and Wang, X. (2014a). *e^2.motion: Earth System Mass Transport Mission (Square) - Concept for a Next Generation Gravity Field Mission - Final report of project "Satellite Gravimetry of the Next Generation (NGGM-D)"*. Vol. Heft Nr. 318. Deutsche Geodätische Kommission bei der Bayerischen Akademie der Wissenschaften Reihe B, Angewandte Geodäsie. München: Verlag der Bayerischen Akademie der Wissenschaften and in Kommission beim Verlag C.H. Beck. ISBN: 9783769685978.

Gruber, T., Oikonomidou, X., Bruinsma, S., Visser, P., and Mulet, S. (2019). *GOCE High Level Processing Facility Technical Note - Release 6 GOCE Gravity Field Models Validation Report*. Tech. rep. The European GOCE Gravity Consortium.

Gruber, T., R. Rummel, R., Abrikosov, O., and van Hees, R. (2014b). *GOCE Level 2 Product Data Handbook*. Tech. rep. GO-MA-HPF-GS-0110, Issue 5.0. European GOCE Gravity Consortium EGG-C.

Haagmans, R., Siemes, C., Massotti, L., Carraz, O., and Silvestrin, P. (2020). "ESA's next-generation gravity mission concepts". In: *Rendiconti Lincei. Scienze Fisiche e Naturali* 31.1, pp. 15–25. ISSN: 1720-0776. DOI: 10.1007/s12210-020-00875-0.

Herman, J., Presti, D., Codazzi, A., and Belle, C. (2004). "Attitude control for GRACE - The first low-flying satellite formation". In: *18th International Symposium on Space Flight Dynamics*. Vol. 548, p. 27.

Hewitson, M., Armano, M., Benedetti, M., Bogenstahl, J., Bortoluzzi, D., Bosetti, P., Brandt, N., Cavalleri, A., Ciani, G., Cristofolini, I., Cruise, M., Danzmann, K., Diepholz, I., Dolesi, R., Fauste, J., Ferraioli, L., Fertin, D., Fichter, W., García, A., García, C., Grynagier, A., Guzmán, F., Fitzsimons, E., Heinzel, G., Hollington, D., Hough, J., Hueller, M., Hoyland, D., Jennrich, O., Johlander, B., Killow, C., Lobo, A., Mance, D., Mateos, I., McNamara, P. W., Monsky, A., Nicolini, D., Nicolodi, D., Nofrarias, M., Perreur-Lloyd, M., Plagnol, E., Racca, G. D., Ramos-Castro, J., Robertson, D., Sanjuan, J., Schulte, M. O., Shaul, D. N. A., Smit, M., Stagnaro, L., Steier, F., Sumner, T. J., Tateo, N., Tombolato, D., Vischer, G., Vitale, S., Wanner, G., Ward, H., Waschke, S., Wand, V., Wass, P., Weber, W. J., Ziegler, T., and Zweifel, P. (2009). "Data analysis for the LISA Technology Package". In: *Classical and Quantum Gravity* 26.9. DOI: 10.1088/0264-9381/26/9/094003.

Hofmann-Wellenhof, B. and Moritz, H. (2006). *Physical geodesy*. Springer Science & Business Media.

HosseiniArani, A., Tennstedt, B., Schilling, M., Knabe, A., Wu, H., Schön, S., and Müller, J. (2022). "Kalman-filter Based Hybridization of Classic and Cold Atom Interferometry Accelerometers for Future Satellite Gravity Missions". In: *Proceedings of the International Association of Geodesy Symposia, Beijing, China, June 28–July 2, 2021*. Ed. by J. Freymueller. Berlin, Heidelberg: Springer. DOI: 10.1007/1345_2022_172.

Hudson, D. G. (2003). "In-flight characterization and calibration of the SuperSTAR accelerometer". MA thesis. University of Texas at Austin.

Jekeli, C. (1981). *Alternative methods to smooth the Earth's gravity field*. Tech. rep. 327. Reports of the Department of Geodetic Science and Surveying. Columbus: Ohio State University.

— (1999). "The determination of gravitational potential differences from satellite-to-satellite tracking". In: *Celestial Mechanics and Dynamical Astronomy* 75.2, pp. 85–101. DOI: 10.1023/A:1008313405488.

Johannessen, J. and Aguirre-Martinez, M. (1999). "The Four Candidate Earth Explorer Core Missions–Gravity Field and Steady-State Ocean Circulation". In: *ESA SP* 1233.1.

Kasevich, M. and Chu, S. (1991). "Atomic interferometry using stimulated Raman transitions". In: *Physical review letters* 67.2, p. 181. DOI: 10.1103/PhysRevLett.67.181.

Kim, J. (2000). "Simulation study of a low-low satellite-to-satellite tracking mission". PhD thesis. The University of Texas at Austin.

Klees, R., Revtova, E., Gunter, B., Ditmar, P., Oudman, E., Winsemius, H., and Savenije, H. (Oct. 2008). "The design of an optimal filter for monthly GRACE gravity models". In: *Geophysical Journal International* 175, pp. 417–432. DOI: 10.1111/j.1365-246X.2008.03922.x.

Klinger, B. and Mayer-Gürr, T. (2016). "The role of accelerometer data calibration within GRACE gravity field recovery: Results from ITSG-Grace2016". In: *Advances in Space Research* 58.9, pp. 1597–1609. DOI: 10.1016/j.asr.2016.08.007.

Knabe, A., Schilling, M., Wu, H., HosseiniArani, A., Müller, J., Beaufils, Q., and Pereira dos Santos, F. (2022). "The Benefit of Accelerometers based on Cold Atom Interferometry for Future Satellite Gravity Missions". In: *Proceedings of the International Association of*

Geodesy Symposia, Beijing, China, June 28–July 2, 2021. Ed. by J. Freymueller. Berlin, Heidelberg: Springer. DOI: 10.1007/1345_2022_151.

Koch, K.-R. and Kusche, J. (2001). "Regularization of geopotential determination from satellite data by variance components". In: *Journal of Geodesy* 76.5, pp. 259–268. DOI: 10.1007/s00190-002-0245-x.

Koch, K., Kuhlmann, H., and Schuh, W. (2010). "Approximating covariance matrices estimated in multivariate models by estimated auto-and cross-covariances". In: *Journal of Geodesy* 84.6, pp. 383–397. DOI: 10.1007/s00190-010-0375-5.

Koch, K.-R. (1999). *Parameter estimation and hypothesis testing in linear models*. Springer-Verlag Berlin Heidelberg. ISBN: 978-3-642-08461-4. DOI: 10.1007/978-3-662-03976-2.

Kornfeld, R. P., Arnold, B. W., Gross, M. A., Dahya, N. T., Klipstein, W. M., Gath, P. F., and Bettadpur, S. (2019). "GRACE-FO: The Gravity Recovery and Climate Experiment Follow-On Mission". In: *Journal of Spacecraft and Rockets* 56.3, pp. 931–951. DOI: 10.2514/1.A34326.

Lachmann, M. D., Ahlers, H., Becker, D., Dinkelaker, A. N., Grosse, J., Hellmig, O., Müntinga, H., Schkolnik, V., Seidel, S. T., Wendrich, T., Wenzlawski, A., Carrick, B., Gaaloul, N., Lüdtke, D., Braxmaier, C., Ertmer, W., Krutzik, M., Lämmerzahl, C., Peters, A., Schleich, W. P., Sengstock, K., Wicht, A., Windpassinger, P., and Rasel, E. M. (2021). "Ultracold atom interferometry in space". In: *Nature communications* 12.1317, pp. 1–6. DOI: 10.1038/s41467-021-21628-z.

Landerer, F. W., Flechtner, F. M., Save, H., Webb, F. H., Bandikova, T., Bertiger, W. I., Bettadpur, S. V., Byun, S. H., Dahle, C., Dobslaw, H., Fahnestock, E., Harvey, N., Kang, Z., Kruizinga, G. L. H., Loomis, B. D., McCullough, C., Murböck, M., Nagel, P., Paik, M., Pie, N., Poole, S., Strekalov, D., Tamisiea, M. E., Wang, F., Watkins, M. M., Wen, H.-Y., Wiese, D. N., and Yuan, D.-N. (2020). "Extending the Global Mass Change Data Record: GRACE Follow-On Instrument and Science Data Performance". In: *Geophysical Research Letters* 47.12. DOI: 10.1029/2020GL088306.

Lautier, J., Volodimer, L., Hardin, T., Merlet, S., Lours, M., Pereira Dos Santos, F., and Landragin, A. (2014). "Hybridizing matter-wave and classical accelerometers". In: *Applied Physics Letters* 105.14, p. 144102.

Lévèque, T., Fallet, C., Lefebve, J., Piquereau, A., Gauguet, A., Battelier, B., Bouyer, P., Gaaloul, N., Lachmann, M., Piest, B., Rasel, E., Müller, J., Schubert, C., Beaufils, Q., and Pereira Dos Santos, F. (2022). "CARIOQA: Definition of a Quantum Pathfinder Mission". In: *arXiv preprint arXiv:2211.01215*. DOI: 10.48550/arXiv.2211.01215.

Liu, X. (2008). "Global gravity field recovery from satellite-to-satellite tracking data with the acceleration approach". PhD thesis. TU Delft.

Lyard, F. H., Allain, D. J., Cancet, M., Carrère, L., and Picot, N. (2021). "FES2014 global ocean tide atlas: design and performance". In: *Ocean Science* 17.3, pp. 615–649. DOI: 10.5194/os-17-615-2021.

Markley, F. L. and Crassidis, J. L. (2014). *Fundamentals of Spacecraft Attitude Determination and Control*. New York, NY: Springer New York. ISBN: 978-1-4939-0801-1. DOI: 10.1007/978-1-4939-0802-8.

Marque, J.-P., Christophe, B., and Foulon, B. (2010). "Accelerometers of the GOCE mission: return of experience from one year of in-orbit". In: *ESA Living Planet Symposium, Bergen, Norway 28 June - 2 July 2010*. Vol. 686.

Marque, J., Christophe, B., Liorzou, F., Bodovillé, G., Foulon, B., Guérard, J., and Lebat, V. (2008). "The ultra sensitive accelerometers of the ESA GOCE mission". In: *59th International Astronautical Congress (IAC-08-B1. 3.7)*. Vol. 137. Glasgow, Scotland, UK.

Massotti, L., Cara, D., Gonzalez del Amo, J., Haagmans, R., Jost, M., Siemes, C., and Silvestrin, P. (Aug. 2013). "The ESA Earth Observation Programmes Activities for the Preparation of the Next Generation Gravity Mission". In: *AIAA Guidance, Navigation, and Control (GNC) Conference*, p. 4637. ISBN: 978-1-62410-224-0. DOI: 10.2514/6.2013-4637.

Massotti, L., Amata, G. B., Anselmi, A., Cesare, S., Martimort, P., and Silvestrin, P. (2020). "Next generation gravity mission: status of the design and discussion on alternative drag compensation scenarios". In: *Sensors, Systems, and Next-Generation Satellites XXIV*. Ed. by S. P. Neeck, A. Hélière, and T. Kimura. Vol. 11530. International Society for Optics and Photonics. SPIE, pp. 15–30. DOI: 10.1117/12.2573924.

Massotti, L., Siemes, C., March, G., Haagmans, R., and Silvestrin, P. (2021). "Next Generation Gravity Mission Elements of the Mass Change and Geoscience International Constellation: From Orbit Selection to Instrument and Mission Design". In: *Remote Sensing* 13.19, p. 3935. DOI: 10.3390/rs13193935.

Mayer-Gürr, T., Savcenko, R., Bosch, W., Daras, I., Flechtner, F., and Dahle, C. (2012). "Ocean tides from satellite altimetry and GRACE". In: *Journal of Geodynamics* 59–60. DOI: 10.1016/j.jog.2011.10.009.

Mayer-Gürr, T., Behzadpour, S., Eicker, A., Ellmer, M., Koch, B., Krauss, S., Pock, C., Rieser, D., Strasser, S., Süsser-Rechberger, B., Zehentner, N., and Kvas, A. (2021). "GROOPS: A software toolkit for gravity field recovery and GNSS processing". In: *Computers and Geosciences* 155. DOI: 10.1016/j.cageo.2021.104864.

Mayer-Gürr, T., Behzadpur, S., Ellmer, M., Kvas, A., Klinger, B., Strasser, S., and Zehentner, N. (2018). *ITSG-Grace2018 - Monthly, Daily and Static Gravity Field Solutions from GRACE*. GFZ Data Services. DOI: 10.5880/ICGEM.2018.003.

McGirr, R., Tregoning, P., Allgeyer, S., McQueen, H., and Purcell, A. (2022). "Mitigation of thermal noise in GRACE accelerometer observations". In: *Adv Space Res* 69.1, pp. 386–401. ISSN: 0273-1177. DOI: 10.1016/j.asr.2021.10.055.

Meister, J., Bremer, S., HosseiniArani, A., Leipner, A., List, M., Müller, J., and Schilling, M. (2022). "Reference mirror misalignment of cold atom interferometers on satellite-based gravimetry missions". In: *International Astronautical Congress 2022*. URL: https://elib.dlr.de/188580/.

Ménoret, V., Vermeulen, P., Le Moigne, N., Bonvalot, S., Bouyer, P., Landragin, A., and Desruelle, B. (2018). "Gravity measurements below 10- 9 g with a transportable absolute quantum gravimeter". In: *Scientific reports* 8.1, pp. 1–11. DOI: 10.1038/s41598-018-30608-1.

Migliaccio, F., Reguzzoni, M., Batsukh, K., Tino, G. M., Rosi, G., Sorrentino, F., Braitenberg, C., Pivetta, T., Barbolla, D. F., and Zoffoli, S. (2019). "MOCASS: A Satellite Mission Concept Using Cold Atom Interferometry for Measuring the Earth Gravity Field". In: *Surveys in Geophysics* 40.5, pp. 1029–1053. DOI: 10.1007/s10712-019-09566-4.

Montenbruck, O. and Gill, E. (2000). *Satellite Orbits*. 1st ed. Berlin Heidelberg: Springer. ISBN: 978-3-642-63547-2. DOI: 10.1007/978-3-642-58351-3.

Müller, J. and Wu, H. (2020). "Using quantum optical sensors for determining the Earth's gravity field from space". In: *Journal of Geodesy* 94.8, pp. 1–14. DOI: 10.1007/s00190-020-01401-8.

Murböck, M. (2015). "Virtual constellations of next generation gravity missions". PhD thesis. Technische Universität München.

Murböck, M., Pail, R., Daras, I., and Gruber, T. (2013). "Optimal orbits for temporal gravity recovery regarding temporal aliasing". In: *Journal of Geodesy* 88.2, pp. 113–126. ISSN: 0949-7714. DOI: 10.1007/s00190-013-0671-y.

Pail, R., Bamber, J., Biancale, R., Bingham, R., Braitenberg, C., Eicker, A., Flechtner, F., Gruber, T., Güntner, A., Heinzel, G., Horwath, M., Longuevergne, L., Müller, J., Panet, I., Savenije, H., Seneviratne, S., Sneeuw, N., van Dam, T., and Wouters, B. (2019). "Mass variation observing system by high low inter-satellite links (MOBILE)–a new concept for sustained observation of mass transport from space". In: *Journal of Geodetic Science* 9.1, pp. 48–58. DOI: 10.1515/jogs-2019-0006.

Pail, R., Bingham, R., Braitenberg, C., Dobslaw, H., Eicker, A., Güntner, A., Horwath, M., Ivins, E., Longuevergne, L., Panet, I., et al. (2015). "Science and user needs for observing global mass transport to understand global change and to benefit society". In: *Surveys in Geophysics* 36.6, pp. 743–772. DOI: 10.1007/s10712-015-9348-9.

Pereira dos Santos, F. and Landragin, A. (2007). "Getting the measure of atom interferometry". In: *Phys. World* 20.11, pp. 32–37. DOI: 10.1088/2058-7058/20/11/38.

Petit, G. and Luzum, B. (2010). *IERS Technical Note ; 36*. Tech. rep. Verlag des Bundesamts für Kartographie und Geodäsie, Frankfurt am Main: International Earth Rotation and Reference Systems Service (IERS) Conventions Centre.

Purkhauser, A. F., Siemes, C., and Pail, R. (2020). "Consistent quantification of the impact of key mission design parameters on the performance of next-generation gravity missions". In: *Geophysical Journal International* 221.2, pp. 1190–1210. DOI: 10.1093/gji/ggaa070.

Reigber, C. (1989). "Gravity field recovery from satellite tracking data". In: *Theory of satellite geodesy and gravity field determination*. Springer, pp. 197–234. DOI: 10.1007/BFb0010546.

Reigber, C., Lühr, H., Schwintzer, P., and Wickert, J. (2005). *Earth Observation with CHAMP*. Berlin Heidelberg: Springer. ISBN: 3-540-22804-7.

Reissner, A., Buldrini, N., Seifert, B., Plesescu, F., Scharlemann, C., Gonzalez del Amo, J., and Massotti, L. (May 2014). "Detailed Performance Characterization of the mN-FEEP Thruster". In: *Space Propulsion Conference*.

Reubelt, T. (2009). "Harmonische Gravitationsfeldanalyse aus GPS-vermessenen kinematischen Bahnen niedrig fliegender Satelliten vom Typ CHAMP, GRACE und GOCE mit einem hoch auflösenden Beschleunigungsansatz". PhD thesis.

Reubelt, T., Sneeuw, N., Pour, S., Hirth, M., Fichter, W., Müller, J., Brieden, P., Flechtner, F., Raimondo, J.-C., Kusche, J., Elsaka, B., Gruber, T., Pail, R., Murböck, M., Doll, B., Sand, R., Wang, X., Klein, V., Lezius, M., and Pelivan, I. (Nov. 2014). "Future Gravity Field Satellite Missions". In: Springer-Verlag Berlin Heidelberg. Chap. III, pp. 165–230. ISBN: 978-3-642-32135-1. DOI: 10.1007/978-3-642-32135-1.

Rodell, M., Famiglietti, J. S., Wiese, D. N., Reager, J., Beaudoing, H. K., Landerer, F. W., and Lo, M.-H. (2018). "Emerging trends in global freshwater availability". In: *Nature* 557.7707, pp. 651–659.

Romanazzo, M., Steiger, C., Sechi, G., Saponara, M., Rezazad, M., Piris Niño, A., Da Costa, A., Fehringer, M., Floberghagen, R., André, G., et al. (2011). "In-orbit Experience with the Drag-Free Attitude and Orbit Control system of ESA's Gravity Mission GOCE". In: *GNC 2011: 8th International ESA Conference on Guidance, Navigation and Control Systems*. ESA Noordwijk, The Netherlands, pp. 1–17.

Rummel, R. (1986). "Satellite gradiometry". In: *Mathematical and Numerical Techniques in Physical Geodesy*. Ed. by H. Sünkel. Berlin, Heidelberg: Springer Berlin Heidelberg, pp. 317–363. ISBN: 978-3-540-47059-5. DOI: 10.1007/BFb0010135.

Rummel, R., Yi, W., and Stummer, C. (2011). "GOCE gravitational gradiometry". In: *Journal of Geodesy* 85.11, pp. 777–790. ISSN: 0949-7714. DOI: 10.1007/s00190-011-0500-0.

Savcenko, R. and Bosch, W. (2012). "EOT11a-empirical ocean tide model from multi-mission satellite altimetry". In: *Deutsches Geodätisches Forschungsinstitut (DGFI) Report* 89. DOI: 10.1594/PANGAEA.834232.

Schilling, M. (2019). "Kombination von klassischen Gravimetern mit Quantensensoren". PhD thesis. Hannover: Leibniz Universität Hannover.

Schilling, M., Timmen, L., and Müller, J. (2012). "Einsatz der Atominterferometrie in der Geodäsie". In: *zfv* 137.3/2012, pp. 185–194. DOI: 10.15488/3097.

Schrama, E. J. O., Wouters, B., and Lavallée, D. A. (2007). "Signal and noise in Gravity Recovery and Climate Experiment (GRACE) observed surface mass variations". In: *J. Geophys. Res* 112.B08407. DOI: 10.1029/2006JB004882.

Sechi, G., Buonocore, M., Cometto, F., Saponara, M., Tramutola, A., Vinai, B., Andrè, G., and Fehringer, M. (2011). "In-Flight Results from the Drag-Free and Attitude Control of GOCE Satellite". In: *IFAC Proceedings Volumes* 44.1, pp. 733–740. ISSN: 14746670. DOI: 10.3182/20110828-6-IT-1002.02966.

Seeber, G. (2003). *Satellite geodesy*. 2nd ed. Berlin: de Gruyter. ISBN: 3-11-017549-5.

Sheard, B., Heinzel, G., Danzmann, K., Shaddock, D., Klipstein, W., and Folkner, W. (2012). "Intersatellite laser ranging instrument for the GRACE follow-on mission". In: *Journal of Geodesy* 86.12, pp. 1083–1095. DOI: 10.1007/s00190-012-0566-3.

Siemes, C. (2012). *GOCE gradiometer calibration and Level 1b data processing*. Tech. rep. ESA working paper EWP-2384, Noordwijk.

Siemes, C., Haagmans, R., Kern, M., Plank, G., and Floberghagen, R. (2012). "Monitoring GOCE gradiometer calibration parameters using accelerometer and star sensor data: methodology and first results". In: *Journal of Geodesy* 86.8, pp. 629–645. ISSN: 0949-7714. DOI: 10.1007/s00190-012-0545-8.

Steiger, C., Mardle, N., and Emanuelli, P. (2014). "GOCE end-of-mission operations report". In: *ESA2014*.

Stummer, C. (2012). "Gradiometer data processing and analysis for the GOCE mission". PhD thesis. Technische Universität München.

Stummer, C., Siemes, C., Pail, R., Frommknecht, B., and Floberghagen, R. (2012). "Upgrade of the GOCE Level 1b gradiometer processor". In: *Advances in Space Research* 49.4, pp. 739–752. ISSN: 02731177. DOI: 10.1016/j.asr.2011.11.027.

Tapley, B. D., Bettadpur, S., Watkins, M., and Reigber, C. (2004). "The gravity recovery and climate experiment: Mission overview and early results". In: *Geophysical research letters* 31.9. DOI: 10.1029/2004GL019920.

Tapley, B. D., Watkins, M. M., Flechtner, F., Reigber, C., Bettadpur, S., Rodell, M., Sasgen, I., Famiglietti, J. S., Landerer, F. W., Chambers, D. P., Reager, J. T., Gardner, A. S.,

Save, H., Ivins, E. R., Swenson, S. C., Boening, C., Dahle, C., Wiese, D. N., Dobslaw, H., Tamisiea, M. E., and Velicogna, I. (2019). "Contributions of GRACE to understanding climate change". In: *Nature Climate Change* 9.5, pp. 358–369. DOI: 10.1038/s41558-019-0456-2.

Tino, G. M. (2021). "Testing gravity with cold atom interferometry: results and prospects". In: *Quantum Science and Technology* 6.2. DOI: 10.1088/2058-9565/abd83e.

Torge, W. and Müller, J. (2012). *Geodesy*. 4th ed. Berlin/Boston: Walter de Gruyter. ISBN: 978-3-11-020718-7.

Touboul, P., Métris, G., Sélig, H., Le Traon, O., Bresson, A., Zahzam, N., Benavent, C., and Rodrigues, M. (2016). "Gravitation and Geodesy with Inertial Sensors, from Ground to Space". In: *AerospaceLab Journal* 12. DOI: 10.12762/2016.AL12-11.

Touboul, P., Foulon, B., Christophe, B., and Marque, J. P. (2012). "CHAMP, GRACE, GOCE Instruments and Beyond". In: *Geodesy for Planet Earth*. Ed. by S. Kenyon, M. C. Pacino, and U. Marti. Vol. 136. Berlin, Heidelberg: Springer, pp. 215–221. DOI: 10.1007/978-3-642-20338-1_26.

Touboul, P., Foulon, B., and Willemenot, E. (1999). "Electrostatic space accelerometers for present and future missions". In: *Acta Astronautica* 45.10, pp. 605–617. DOI: 10.1016/S0094-5765(99)00132-0.

Touboul, P., Métris, G., Rodrigues, M., André, Y., Baghi, Q., Bergé, J., Boulanger, D., Bremer, S., Carle, P., Chhun, R., Christophe, B., Cipolla, V., Damour, T., Danto, P., Dittus, H., Fayet, P., Foulon, B., Gageant, C., Guidotti, P.-Y., Hagedorn, D., Hardy, E., Huynh, P.-A., Inchauspe, H., Kayser, P., Lala, S., Lämmerzahl, C., Lebat, V., Leseur, P., Liorzou, F. ç., List, M., Löffler, F., Panet, I., Pouilloux, B., Prieur, P., Rebray, A., Reynaud, S., Rievers, B., Robert, A., Selig, H., Serron, L., Sumner, T., Tanguy, N., and Visser, P. (2017). "MICROSCOPE Mission: First Results of a Space Test of the Equivalence Principle". In: *Phys. Rev. Lett.* 119 (23), p. 231101. DOI: 10.1103/PhysRevLett.119.231101.

Trimeche, A., Battelier, B., Becker, D., Bertoldi, A., Bouyer, P., Braxmaier, C., Charron, E., Corgier, R., Cornelius, M., Douch, K., Gaaloul, N., Herrmann, S., Müller, J., Rasel, E., Schubert, C., Hu, W., and Pereira dos Santos, F. (Sept. 2019). "Concept study and preliminary design of a cold atom interferometer for space gravity gradiometry". In: *Classical and Quantum Gravity* 36. DOI: 10.1088/1361-6382/ab4548.

Tröbs, M. and Heinzel, G. (2006). "Improved spectrum estimation from digitized time series on a logarithmic frequency axis". In: *Measurement* 39.2, pp. 120–129. ISSN: 0263-2241. DOI: 10.1016/j.measurement.2005.10.010.

Vielberg, K., Forootan, E., Lück, C., Löcher, A., Kusche, J., and Börger, K. (2018). "Comparison of accelerometer data calibration methods used in thermospheric neutral density estimation". In: *Annales Geophysicae* 36, pp. 761–779. DOI: 10.5194/angeo-36-761-2018.

Wahr, J., Molenaar, M., and Bryan, F. (1998). "Time variability of the Earth's gravity field: Hydrological and oceanic effects and their possible detection using GRACE". In: *Journal of Geophysical Research: Solid Earth* 103.B12, pp. 30205–30229. DOI: 10.1029/98JB02844.

Wegener, H. (2022). "Analysis of tilt-to-length coupling in the GRACE follow-on laser ranging interferometer". PhD thesis. Leibniz Universität Hannover.

Weigelt, M. (2017). "The Acceleration Approach". In: *Global Gravity Field Modeling from Satellite-to-Satellite Tracking Data*. Ed. by M. Naeimi and J. Flury. Springer, pp. 97–126. DOI: 10.1007/978-3-319-49941-3_4.

Weigelt, M., Sneeuw, N., Schrama, E., and Visser, P. N. (2013). "An improved sampling rule for mapping geopotential functions of a planet from a near polar orbit". In: *Journal of Geodesy* 87.2, pp. 127–142. DOI: 10.1007/s00190-012-0585-0.

Wen, H. Y., Kruizinga, G., Paik, M., Landerer, F., Bertiger, W., Sakumura, C., Bandikova, T., and Mccullough, C. (2019). *Gravity Recovery and Climate Experiment Follow-On (GRACE-FO) Level-1 Data Product User Handbook*. Tech. rep. NASA Jet Propulsion Laboratory, California Institute of Technology.

Wöske, F. (2021). "Gravity Field Recovery from GRACE Satellite Data and Investigation of Sensor, Environment and Processing-Option Influences by Closed Loop Mission Simulation". PhD thesis. Universität Bremen.

Wöske, F., Kato, T., List, M., and Rievers, B. (2016). "Development of a high precision simulation tool for gravity recovery missions like GRACE". In: *Proceedings of the 26th AAS/AIAA Space Flight Mechanics Meeting held February 14-18, 2016*. Ed. by R. Zanetti, R. P. Russel, M. T. Ozimek, and A. L. Bowes. Vol. 158. Advances in the Astronautical Sciences, pp. 2445–2457.

Wöske, F., Kato, T., Rievers, B., and List, M. (2018). "GRACE accelerometer calibration by high precision non-gravitational force modeling". In: *Advances in Space Research* 63. DOI: 10.1016/j.asr.2018.10.025.

Wu, H. (2016). "Gravity field recovery from GOCE observations". PhD thesis. Fachrichtung Geodäsie und Geoinformatik der Leibniz Universität Hannover.

Zhu, Z., Zhou, Z., Cai, L., Bai, Y., and Luo, J. (2013). "Electrostatic gravity gradiometer design for the future mission". In: *Advances in Space Research* 51.12, pp. 2269–2276. DOI: 10.1016/j.asr.2013.01.031.

List of Figures

2.1 Scheme of the different measurement concepts: ll-SST, hl-SST and SGG . . . 8
2.2 Servo-control channel of an electrostatic accelerometer for one axis, Figure modified from (Johannessen & Aguirre-Martinez, 1999; Touboul et al., 1999) 10
2.3 Servo-control channel of an electrostatic accelerometer for one axis with addition of a laser interferometer . . . 17
2.4 Mach-Zehnder atom interferometer, modified from (Schilling, 2019) . . . 18

3.1 Simulation procedure for range accelerations . . . 24
3.2 Simulation procedure for gradiometry . . . 24
3.3 Non-gravitational forces of the different effects acting on a GRACE-like shaped satellite body; note the different scaling of the plots . . . 25
3.4 Noise performance models of the GOCE and the GRACE-FO accelerometer 27
3.5 Response in the time domain of the transfer function for the phase shift to acceleration conversion . . . 28
3.6 Anticipated ASD of a space CAI accelerometer noise . . . 29
3.7 Anticipated ASD of a space CAI accelerometer noise filtered with the response function in the time domain . . . 29
3.8 Model of a hybrid accelerometer . . . 30
3.9 Noise performance models of the KBR instrument and the LRI instrument . 30
3.10 Different noise performance models of the LRI instrument and expectations for the future . . . 31
3.11 Flowchart of the drag-free control system . . . 32
3.12 ASD of thruster noise . . . 33
3.13 Models for AOD error for April 2006 . . . 36
3.14 Models for ocean-tide error for April 2006 . . . 36
3.15 ASD of different assumptions for AOD error and ocean-tide error . . . 37
3.16 Degree RMS of the coefficient differences between recovered gravity and reference gravity and formal errors for iteration results; parameters: altitude of 246 km, hybrid accelerometer, KBR noise . . . 40
3.17 Evaluation of the de-correlation filter by coefficient differences between recovered and reference gravity field as pyramid representation (logarithm scale); parameters: altitude of 246 km, EA noise at the level of $1 \times 10^{-10}\,\mathrm{m/s^2}$, LRI noise . . . 41

3.18 Evaluation of the de-correlation filter by coefficient differences between recovered and reference gravity field as pyramid representation (logarithm scale); parameters: gradiometry component V_{yy}, altitude of 246 km, EA noise at a level of $2 \times 10^{-12}\,\mathrm{m/s^2}$, $L_y = 0.5\,\mathrm{m}$ 43
3.19 Degree RMS of the coefficient differences between recovered gravity and reference gravity and formal errors for iteration results; parameters: gradiometry component V_{yy}, altitude of 246 km, electrostatic accelerometer noise at a level $2 \times 10^{-12}\,\mathrm{m/s^2}$, $L_y = 0.5\,\mathrm{m}$ 44
3.20 Degree RMS of the coefficient differences between recovered and reference gravity field for the iterative variance component estimation 45

4.1 Interaction between components of a satellite gravity mission 48
4.2 ASD of the non-gravitational acceleration signal in along-track direction for the altitude of 246 km (blue lines) and the requirement is based on scale factor knowledge of 0.2 % (dotted line) 50
4.3 ASD of the non-gravitational acceleration signal in along-track direction for different altitudes (colored lines) and the requirement with different assumptions for the scale factor knowledge (dotted lines), July 2000 representing solar cycle maximum 51
4.4 ASD of the non-gravitational acceleration signal in along-track direction for different altitudes (colored lines) and the requirement with different assumptions for the scale factor knowledge (dotted lines), January 2006 representing solar cycle minimum 52
4.5 ASD of the non-gravitational acceleration signal in cross-track direction for different altitudes (colored lines) and the requirement with different assumptions for the scale factor knowledge (dotted lines), July 2000 representing solar cycle maximum 52
4.6 ASD of the non-gravitational acceleration signal in cross-track direction for different altitudes (colored lines) and the requirement with different assumptions for the scale factor knowledge (dotted lines), January 2006 representing solar cycle minimum 53
4.7 ASD of the non-gravitational acceleration signal in radial direction for different altitudes (colored lines) and the requirement with different assumptions for the scale factor knowledge (dotted lines), July 2000 representing solar cycle maximum 53
4.8 ASD of the non-gravitational acceleration signal in radial direction for different altitudes (colored lines) and the requirement with different assumptions for the scale factor knowledge (dotted lines), January 2006 representing solar cycle minimum 54
4.9 ASD of the non-gravitational acceleration signal in along-track direction for different altitudes (colored lines) and the requirement with different assumptions for differential scale factor knowledge (dotted lines), July 2000 representing solar cycle maximum 56

4.10 ASD of the non-gravitational acceleration signal in along-track direction for different altitudes (colored lines) and the requirement with different assumptions for differential scale factor knowledge (dotted lines), January 2006 representing solar cycle minimum 57
4.11 ASD of the non-gravitational acceleration signal in cross-track direction for different altitudes (colored lines) and the requirement with different assumptions for differential scale factor knowledge (dotted lines), July 2000 representing solar cycle maximum 57
4.12 ASD of the non-gravitational acceleration signal in cross-track direction for different altitudes (colored lines) and the requirement with different assumptions for differential scale factor knowledge (dotted lines), January 2006 representing solar cycle minimum 58
4.13 ASD of the non-gravitational acceleration signal in radial direction for different altitudes (colored lines) and the requirement with different assumptions for differential scale factor knowledge (dotted lines), July 2000 representing solar cycle maximum 58
4.14 ASD of the non-gravitational acceleration signal in radial direction for different altitudes (colored lines) and the requirement with different assumptions for differential scale factor knowledge (dotted lines), January 2006 representing solar cycle minimum 59
4.15 ASD of the residual non-gravitational acceleration using drag compensation (colored lines) and the requirement with different assumptions for the scale factor knowledge (dotted lines) 59
4.16 Non-gravitational accelerations in along-track direction for different orbit altitudes and saturation limit 60
4.17 Non-gravitational accelerations in along- and cross-track direction for different orbit altitudes and saturation limit 60
4.18 Control system using constant thrust levels, calculation for January 1st, 2006 61
4.19 Propellant consumption of the ion thrusters for a mission duration of 10 years 63
4.20 Variation of non-gravitational accelerations within one interferometer cycle for two different altitudes: 462 km (red) and 303 km (blue) for January 1st, 2006 64
4.21 ASD of the variation of non-gravitational accelerations within one interferometer cycle (acc. var. - solid lines) and corresponding error contribution to the CAI measurements (error - dotted lines) for two different altitudes: 462 km and 303 km for January 1st, 2006 64
4.22 Acceleration variation and its error estimation for various time epochs 65
4.23 Acceleration variation and its error estimation under drag compensation; orbit altitude of 303 km 66
4.24 Error contribution due to acceleration variation and sensitivity of the atom interferometer 66
4.25 ASD of considered noise sources 67
4.26 Degree RMS of the coefficient differences for different accelerometer noise models, ranging noise models for the altitudes of (a) 246 km, (b) 303 km, (c) 363 km and (d) 462 km including AOD and ocean-tide error 68

4.27 Degree RMS of the coefficient differences for different accelerometer noise models with an LRI noise model for the altitude of 462 km including different error assumptions for AOD and ocean-tide error 69
4.28 Coefficient differences between recovered and reference gravity field: spatial representation in terms of EWH and pyramid representation (logarithm scale); parameters: h=303 km, KBR measurement noise and different accelerometer noise models 71
4.29 Coefficient differences between recovered and reference gravity field: spatial representation in terms of EWH and pyramid representation (logarithm scale); parameters: h=303 km, LRI measurement noise and different accelerometer noise models 72
4.30 Coefficient differences between recovered and reference gravity field: spatial representation in terms of EWH and pyramid representation (logarithm scale); parameters: h=462 km, KBR measurement noise and different accelerometer noise models 73
4.31 Coefficient differences between recovered and reference gravity field: spatial representation in terms of EWH and pyramid representation (logarithm scale); parameters: h=462 km, LRI measurement noise and different accelerometer noise models 74
4.32 Degree RMS of the coefficient differences for different accelerometer noise models and ranging noise models for altitudes of (a) 246 km, (b) 303 km, (c) 363 km and (d) 462 km for the instrument-only scenarios 75
4.33 Coefficient differences between recovered and reference gravity field: spatial representation in terms of EWH and pyramid representation (logarithm scale); parameters: h=303 km, only instrument noise, KBR measurement noise and different accelerometer noise models 76
4.34 Coefficient differences between recovered and reference gravity field: spatial representation in terms of EWH and pyramid representation (logarithm scale); parameters: h=303 km, only instrument noise, LRI measurement noise and different accelerometer noise models 77
4.35 Coefficient differences between recovered and reference gravity field: spatial representation in terms of EWH and pyramid representation (logarithm scale); parameters: h=462 km, only instrument noise, KBR measurement noise and different accelerometer noise models 78
4.36 Coefficient differences between recovered and reference gravity field: spatial representation in terms of EWH and pyramid representation (logarithm scale); parameters: h=462 km, only instrument noise, LRI measurement noise and variation of accelerometer noise 79
4.37 Degree RMS of the coefficient differences between recovered and reference gravity field solutions with various LRI noise models for an orbit altitude of 462 km 80
4.38 Degree RMS of the coefficient differences between recovered and reference gravity field solutions of the cross-track component for different gradiometer noise models 83

4.39 Degree RMS of the coefficient differences between recovered and reference gravity field using KBR noise and EA noise at a level of $1 \times 10^{-10}\,\mathrm{m/s^2}$ for ll-SST and different gradiometer noise levels for the cross-track gradiometer, altitude of 246 km 84
4.40 Degree RMS of the coefficient differences between recovered and reference gravity field using KBR noise and EA noise at a level of $1 \times 10^{-10}\,\mathrm{m/s^2}$ for ll-SST and different gradiometer noise levels for the cross-track gradiometer, altitude of 246 km 85
4.41 Degree RMS of the coefficient differences between recovered and reference gravity field using LRI noise and EA noise at a level of $1 \times 10^{-10}\,\mathrm{m/s^2}$ for ll-SST and different gradiometer noise levels for the cross-track gradiometer, altitude of 246 km 85
4.42 Degree RMS of the coefficient differences between recovered and reference gravity field using and EA noise at a level of $1 \times 10^{-12}\,\mathrm{m/s^2}$ for ll-SST and different gradiometer noise levels for the cross-track gradiometer, altitude of 246 km 86
4.43 Coefficient differences between recovered and reference gravity field: spatial representation in terms of EWH and pyramid representation (logarithm scale), instrument-only scenario: h=246 km, ll-SST: KBR noise and EA at a noise level of $1 \times 10^{-10}\,\mathrm{m/s^2}$, cross-track component V_{yy}: EG at a noise level of 1 mE 87
4.44 Coefficient differences between recovered and reference gravity field: spatial representation in terms of EWH and pyramid representation (logarithm scale), instrument-only scenario: h=246 km, ll-SST: LRI noise and EA at a noise level of $1 \times 10^{-10}\,\mathrm{m/s^2}$, cross-track component V_{yy}: CAI gradiometer at a noise level of 1 mE 88
4.45 Coefficient differences between recovered and reference gravity field: spatial representation in terms of EWH and pyramid representation (logarithm scale), instrument-only scenario: h=246 km, ll-SST: KBR noise and EA at a noise level of $1 \times 10^{-12}\,\mathrm{m/s^2}$, cross-track component V_{yy}: CAI gradiometer at a noise level of 1 mE 89
4.46 Coefficient differences between recovered and reference gravity field: spatial representation in terms of EWH and pyramid representation (logarithm scale), instrument-only scenario: h=246 km, ll-SST: KBR noise and EA at a noise level of $1 \times 10^{-12}\,\mathrm{m/s^2}$, cross-track component V_{yy}: CAI gradiometer at a noise level of 0.1 mE 90
4.47 Coefficient differences between recovered and reference gravity field: spatial representation in terms of EWH and pyramid representation (logarithm scale), instrument-only scenario: h=246 km, ll-SST: LRI noise and EA at a noise level of $1 \times 10^{-12}\,\mathrm{m/s^2}$, cross-track component V_{yy}: CAI gradiometer at a noise level of 0.1 mE 91
4.48 Degree RMS of the coefficient differences between recovered and reference gravity field for combinations of ll-SST and cross-track gradiometry, instrument-only and and scenarios including AOD and ocean-tide errors for different sensor combinations, altitudes of 246 km and 363 km 93

4.49 Coefficient differences between recovered and reference gravity field: spatial representation in terms of EWH and pyramid representation (logarithm scale), scenario including AOD and ocean-tide errors: h=246 km, ll-SST: KBR noise and EA at a noise level of $1 \times 10^{-10}\,\mathrm{m/s^2}$, cross-track component V_{yy}: EG at a noise level of 1 mE 95
4.50 Coefficient differences between recovered and reference gravity field: spatial representation in terms of EWH and pyramid representation (logarithm scale), scenario including AOD and ocean-tide errors: h=246 km, ll-SST: KBR noise and EA at a noise level of $1 \times 10^{-12}\,\mathrm{m/s^2}$, cross-track component V_{yy}: CAI gradiometer at a noise level of 1 mE 96

A.1 Coefficient differences between recovered and reference gravity field: spatial representation in terms of EWH and pyramid representation (logarithm scale); parameters: h=246 km, only instrument noise, KBR measurement noise and different accelerometer noise models 105
A.2 Coefficient differences between recovered and reference gravity field: spatial representation in terms of EWH and pyramid representation (logarithm scale); parameters: h=246 km, only instrument noise, LRI measurement noise and different accelerometer noise models 106
A.3 Coefficient differences between recovered and reference gravity field: spatial representation in terms of EWH and pyramid representation (logarithm scale); parameters: h=363 km, only instrument noise, KBR measurement noise and different accelerometer noise models 107
A.4 Coefficient differences between recovered and reference gravity field: spatial representation in terms of EWH and pyramid representation (logarithm scale); parameters: h=363 km, only instrument noise, LRI measurement noise and variation of accelerometer noise 108
A.5 Coefficient differences between recovered and reference gravity field: spatial representation in terms of EWH and pyramid representation (logarithm scale); parameters: h=246 km, KBR measurement noise and different accelerometer noise models 109
A.6 Coefficient differences between recovered and reference gravity field: spatial representation in terms of EWH and pyramid representation (logarithm scale); parameters: h=246 km, LRI measurement noise and different accelerometer noise models 110
A.7 Coefficient differences between recovered and reference gravity field: spatial representation in terms of EWH and pyramid representation (logarithm scale); parameters: h=363 km, KBR measurement noise and different accelerometer noise models 111
A.8 Coefficient differences between recovered and reference gravity field: spatial representation in terms of EWH and pyramid representation (logarithm scale); parameters: h=363 km, LRI measurement noise and different accelerometer noise models 112
A.9 Degree RMS of the coefficient differences between recovered and reference gravity field for different sensor combinations for an orbit altitude of 303 km 113

A.10 Coefficient differences between recovered and reference gravity field: spatial representation in terms of EWH and pyramid representation (logarithm scale), instrument-only scenario: h=246 km, ll-SST: KBR noise and EA at a noise level of $1 \times 10^{-10}\,\mathrm{m/s^2}$, cross-track component V_{yy}: EG at a noise level of 6.5 mE 114
A.11 Coefficient differences between recovered and reference gravity field: spatial representation in terms of EWH and pyramid representation (logarithm scale), instrument-only scenario: h=246 km, ll-SST: KBR noise and EA at a noise level of $1 \times 10^{-10}\,\mathrm{m/s^2}$, cross-track component V_{yy}: CAI gradiometer at a noise level of 6.5 mE 115
A.12 Coefficient differences between recovered and reference gravity field: spatial representation in terms of EWH and pyramid representation (logarithm scale), instrument-only scenario: h=246 km, ll-SST: KBR noise and EA at a noise level of $1 \times 10^{-10}\,\mathrm{m/s^2}$, cross-track component V_{yy}: CAI gradiometer at a noise level of 1 mE 116
A.13 Coefficient differences between recovered and reference gravity field: spatial representation in terms of EWH and pyramid representation (logarithm scale), instrument-only scenario: h=246 km, ll-SST: KBR noise and EA at a noise level of $1 \times 10^{-10}\,\mathrm{m/s^2}$, cross-track component V_{yy}: CAI gradiometer at a noise level of 0.1 mE 117
A.14 Coefficient differences between recovered and reference gravity field: spatial representation in terms of EWH and pyramid representation (logarithm scale), instrument-only scenario: h=246 km, ll-SST: LRI noise and EA at a noise level of $1 \times 10^{-10}\,\mathrm{m/s^2}$, cross-track component V_{yy}: EG at a noise level of 1 mE 118
A.15 Coefficient differences between recovered and reference gravity field: spatial representation in terms of EWH and pyramid representation (logarithm scale), instrument-only scenario: h=246 km, ll-SST: LRI noise and EA at a noise level of $1 \times 10^{-10}\,\mathrm{m/s^2}$, cross-track component V_{yy}: CAI gradiometer at a noise level of 0.1 mE 119
A.16 Coefficient differences between recovered and reference gravity field: spatial representation in terms of EWH and pyramid representation (logarithm scale), instrument-only scenario: h=246 km, ll-SST: LRI noise and EA at a noise level of $1 \times 10^{-12}\,\mathrm{m/s^2}$, cross-track component V_{yy}: CAI gradiometer at a noise level of 0.01 mE 120
A.17 Coefficient differences between recovered and reference gravity field: spatial representation in terms of EWH and pyramid representation (logarithm scale), instrument-only scenario: h=303 km, ll-SST: KBR noise and EA at a noise level of $1 \times 10^{-10}\,\mathrm{m/s^2}$, cross-track component V_{yy}: EG at a noise level of 1 mE 121
A.18 Coefficient differences between recovered and reference gravity field: spatial representation in terms of EWH and pyramid representation (logarithm scale), instrument-only scenario: h=303 km, ll-SST: KBR noise and EA at a noise level of $1 \times 10^{-10}\,\mathrm{m/s^2}$, cross-track component V_{yy}: CAI gradiometer at a noise level of 1 mE 122

A.19 Coefficient differences between recovered and reference gravity field: spatial representation in terms of EWH and pyramid representation (logarithm scale), instrument-only scenario: h=303 km, ll-SST: LRI noise and EA at a noise level of 1×10^{-10} m/s^2, cross-track component V_{yy}: CAI gradiometer at a noise level of 0.1 mE 123
A.20 Coefficient differences between recovered and reference gravity field: spatial representation in terms of EWH and pyramid representation (logarithm scale), instrument-only scenario: h=303 km, ll-SST: KBR noise and EA at a noise level of 1×10^{-12} m/s^2, cross-track component V_{yy}: CAI gradiometer at a noise level of 1 mE 124
A.21 Coefficient differences between recovered and reference gravity field: spatial representation in terms of EWH and pyramid representation (logarithm scale), instrument-only scenario: h=303 km, ll-SST: KBR noise and EA at a noise level of 1×10^{-12} m/s^2, cross-track component V_{yy}: CAI gradiometer at a noise level of 0.1 mE 125
A.22 Coefficient differences between recovered and reference gravity field: spatial representation in terms of EWH and pyramid representation (logarithm scale), instrument-only scenario: h=303 km, ll-SST: LRI noise and EA at a noise level of 1×10^{-12} m/s^2, cross-track component V_{yy}: CAI gradiometer at a noise level of 0.1 mE 126
A.23 Coefficient differences between recovered and reference gravity field: spatial representation in terms of EWH and pyramid representation (logarithm scale), instrument-only scenario: h=303 km, ll-SST: LRI noise and EA at a noise level of 1×10^{-12} m/s^2, cross-track component V_{yy}: CAI gradiometer at a noise level of 0.01 mE 127
A.24 Coefficient differences between recovered and reference gravity field: spatial representation in terms of EWH and pyramid representation (logarithm scale), instrument-only scenario: h=363 km, ll-SST: KBR noise and EA at a noise level of 1×10^{-10} m/s^2, cross-track component V_{yy}: EG at a noise level of 1 mE 128
A.25 Coefficient differences between recovered and reference gravity field: spatial representation in terms of EWH and pyramid representation (logarithm scale), instrument-only scenario: h=363 km, ll-SST: KBR noise and EA at a noise level of 1×10^{-10} m/s^2, cross-track component V_{yy}: CAI gradiometer at a noise level of 1 mE 129
A.26 Coefficient differences between recovered and reference gravity field: spatial representation in terms of EWH and pyramid representation (logarithm scale), instrument-only scenario: h=363 km, ll-SST: LRI noise and EA at a noise level of 1×10^{-10} m/s^2, cross-track component V_{yy}: CAI gradiometer at a noise level of 0.1 mE 130
A.27 Coefficient differences between recovered and reference gravity field: spatial representation in terms of EWH and pyramid representation (logarithm scale), instrument-only scenario: h=363 km, ll-SST: KBR noise and EA at a noise level of 1×10^{-12} m/s^2, cross-track component V_{yy}: CAI gradiometer at a noise level of 1 mE 131

A.28 Coefficient differences between recovered and reference gravity field: spatial representation in terms of EWH and pyramid representation (logarithm scale), instrument-only scenario: h=363 km, ll-SST: KBR noise and EA at a noise level of 1×10^{-12} m/s^2, cross-track component V_{yy}: CAI gradiometer at a noise level of 0.1 mE 132
A.29 Coefficient differences between recovered and reference gravity field: spatial representation in terms of EWH and pyramid representation (logarithm scale), instrument-only scenario: h=363 km, ll-SST: LRI noise and EA at a noise level of 1×10^{-12} m/s^2, cross-track component V_{yy}: CAI gradiometer at a noise level of 0.1 mE 133
A.30 Coefficient differences between recovered and reference gravity field: spatial representation in terms of EWH and pyramid representation (logarithm scale), instrument-only scenario: h=363 km, ll-SST: LRI noise and EA at a noise level of 1×10^{-12} m/s^2, cross-track component V_{yy}: CAI gradiometer at a noise level of 0.01 mE 134

List of Tables

2.1 Orbit parameters of previous satellite gravity missions 7
2.2 Accelerometer performances 11

3.1 Transfer function parameters of the thrusters of the GOCE mission 33
3.2 Characterization of the two thruster types 34

4.1 Orbit parameters of selected scenarios 49
4.2 Maximum absolute value of the non-gravitational acceleration signals for different altitudes and measurement directions 61
4.3 Cumulative geoid error up to degree and order 90; observations of one month with sampling frequency of 0.2 Hz; instrument-only scenarios 80
4.4 Cumulative geoid error up to degree and order 90; observations of one month with sampling frequency of 0.2 Hz; scenarios including AOD and ocean-tide error 81
4.5 Cumulative geoid error up to degree and order 200; observations of one month with sampling frequency of 0.2 Hz; instrument-only scenarios 92
4.6 Cumulative geoid error up to degree and order 200; observations of one month with sampling frequency of 0.2 Hz; scenarios including AOD and ocean-tide errors 94
4.7 Cumulative geoid error up to degree and order 133; observations of one month with sampling frequency of 0.2 Hz; scenarios including AOD and ocean-tide errors 94

Acronyms

AOD	Atmosphere and Ocean De-aliasing
ASD	Amplitude Spectral Density
CAI	Cold Atom Interferometry
CARIOQA	Cold Atom Rubidium Interferometer in Orbit for Quantum Accelerometry
CHAMP	Challenging Minisatellite Payload
CMRR	Common Mode Rejection Ratio
DLR	Deutsches Zentrum für Luft- und Raumfahrt
EA	Electrostatic Accelerometer
EG	Electrostatic Gradiometer
ERF	Earth-fixed Reference Frame
ESA	European Space Agency
EWH	Equivalent Water Height
GAST	Greenwich Apparent Sideral Time
GNSS	Global Navigation Satellite System
GOCE	Gravity Field and Steady-State Ocean Circulation Explorer
GPS	Global Positioning System
GRACE	Gravity Recovery and Climate Experiment
GRACE-FO	GRACE Follow-On
GRF	Gradiometer Reference Frame
hl-SST	high-low Satellite-to-Satellite Tracking
IMU	Inertial Measurement Unit
IRF	Inertial Reference Frame
KBR	K-band Ranging System
LAGEOS	Laser Geodynamics Satellite
LASD	Logarithmic frequency resolution axis Amplitude Spectral Density
LEO	Low Earth Orbit
LISA	Laser Interferometer Space Antenna
ll-SST	low-low Satellite-to-Satellite Tracking

LNORF	Local North-Oriented Reference Frame
LOS	Line-of-Sight
LRI	Laser Ranging Interferometer
LTPDA	LISA Technology Package Data Analysis
MAGIC	Mass change And Geosciences International Constellation
MBW	Measurement Bandwidth
MEO	Medium Earth Orbit
NASA	National Aeronautics and Space Administration
NGGM	Next Generation Gravity Mission
ONERA	Office National d'Etudes et de Recherches Aérospatiales
ORF	Orbit Reference Frame
PSD	Power Spectral Density
PID	Proportional-Integral-Derivative
RMS	Root Mean Square
SGG	Satellite Gravity Gradiometry
SH	Spherical Harmonic
SST	Satellite-to-Satellite Tracking
XHPS	eXtended High Performance Satellite Dynamics Simulator
ZARM	Zentrum für angewandte Raumfahrttechnologie und Mikrogravitation

Acknowledgments

I would like to thank Prof. Jürgen Müller for giving me the opportunity to work on my PhD at the Institut für Erdmessung (IfE). I appreciate his support and encouraging discussions. I would like to thank Dr. Hamza Alkhatib and Prof. Wolf-Dieter Schuh for being the reviewers and for their useful comments.
I would like to thank all colleagues at the Institut für Erdmessung for the great time. In particular, I would like to thank Dr. Manuel Schilling for being very helpful from my first day at work. Many thanks also to Dr. Karim Douch, Dr. Matthias Weigelt and Dr. Hu Wu for sharing their deep knowledge about gravity field recovery with me and to Dr. Quentin Beaufils and Dr. Franck Pereira dos Santos for their explanations about atom interferometry. I feel lucky having some colleagues as good friends of mine. Thus, I would like to express my gratitude to Yannick Breva, Johannes Kröger and Thomas Maschke for constant mental support and many discussions after office hours. I am also grateful to be part of the research programs geoQ, TerraQ and QuantumFrontiers for giving me great opportunity for networking with other researchers.
Last but not least, my very deep gratitude goes to my family and my friends for their understanding, support and love.